Characterisation of Magnetic Field Effects Through Sensitive Spectroscopic Measurement

Patrick Murton
Magdalen College, University of Oxford

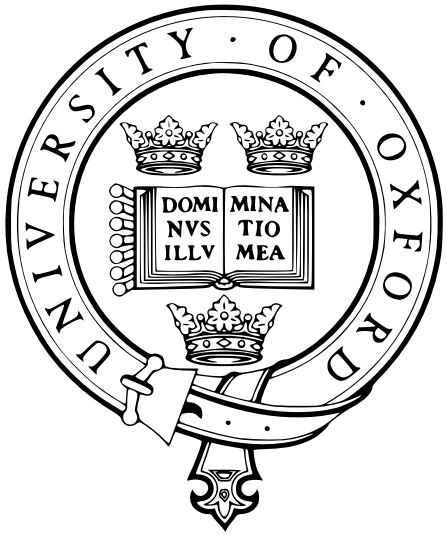

A thesis submitted for the degree of
Doctor of Philosophy

Physical and Theoretical Chemistry
Laboratory South Parks Road, Oxford
April 30, 2024

You're not really an adult at all. You're a tall child holding a beer, having a conversation you don't understand.

– D. Moran

Abstract

Avian magnetoreception, the ability of birds to perceive and navigate using the Earth's magnetic field, is a phenomenon whose basis has intrigued scientists for decades. One leading hypothesis is the radical pair mechanism (RPM) which has been proposed as a possible magneto-sensing mechanism in biological systems such as the magnetoreception of night migratory songbirds (**Chapter 1**). In particular, the retinal cryptochrome 4a proteins of these birds are believed to exhibit the key features necessary for magneto-sensing. That is, the formation of photoinduced radical pairs (RPs) whose interaction with magnetic fields, due to their quantum spin dynamics, causes variations in the yields of their photoproducts, known as a magnetic field effect (MFE). The quantum mechanics of spin, the RPM and its manifestation in cryptochrome 4a proteins is introduced in **Chapter 2**.

The RPM in cryptochrome 4a proteins occurs over a time scale spanning several orders of magnitude (ps - min) with the photoproducts formed exhibiting significant spectral overlap in their absorption (**Chapter 2**). Consequently, a variety of spectroscopic techniques are required to probe the entirety of the photocycle. Furthermore, the MFEs generated in these proteins tend to be small and as such require specialised sensitive spectroscopic techniques to reliably detect them. One such set of techniques are optical cavity experiments which provide significant sensitivity gains over traditional single-pass measurements. These methods, in particular the technique known as broad-band cavity enhanced absorption spectroscopy (BBCEAS), form the bulk of experimental results in this thesis and are introduced in **Chapter 3**.

Thanks to recent advances in the expression of cryptochrome 4a proteins,[1] their photochemistry (*in vitro*) and efficacy as a potential magnetoreceptor can now be explored. In **Chapter 4** the ability of these proteins to develop MFEs is demonstrated for a variety of

avian species prior to exploration in **Chapters 6** and **7** of the role of particular amino acid residues which are highly evolutionarily conserved in the night-migratory passerines.

Historically, the use of the reoxidant potassium ferricyanide (FC) has been used in the spectroscopic study of proteins (in **Chapter 4** for example) to aid in sample recovery following irradiation. **Chapter 5** presents a study on the photochemistry of FC itself and highlights some potential problems it can cause when studying the RPM in cryptochrome 4a. Furthermore, **Chapter 5** demonstrates that MFEs in these proteins can be studied using the more biologically relevant molecular oxygen as an alternative reoxidant.

Due to the small MFEs produced in crpytochrome proteins, their relatively poor stability and time-consuming and costly expression, new techniques with improved sensitivity and which allow faster data acquisition or reduced sample consumption are highly sought after. Therefore, in a shift of focus, **Chapters 8** and **9** introduce two newly developed techniques, optical cavity enhanced transient absorption spectroscopy (OCTAS) and microdroplet fluorescence magnetically altered reaction yield (μDF-MARY) spectroscopy. The former offers improved sensitivity and spectral resolution in absorption measurements over the ns-μs time scale while the latter significantly reduces the amount of sample required to measure continuous fluorescence MFEs and minimises laser induced sample degradation.



Figure 1: A "quantum" robin generated in microsoft Copilot.

Acknowledgments

As someone who is somewhat lactose intolerant to the metaphorical cheese, I find these a challenge to write, but, I'll give it a bash. First and foremost I'd like to thank Prof. Stuart Mackenzie for his guidance and support throughout the DPhil, for bringing me here in the first place and allowing me to generally lower the tone without repercussion. I would also like to thank Prof. Peter Hore for his help and guidance, for allowing me to bother him with questions about theory and putting up with my inability to write in the English language (it's, its?..). Of course, a thanks goes out to my unofficial third supervisor Prof. Christiane Timmel for her support, insight and love of a good laugh. I'll look back fondly on many a Timmel anecdote! I've thoroughly enjoyed my time here, not least because the group has been so welcoming and fun. I believe much of this can attributed to the supportive atmosphere created by three main quantum birds Professors Stuart, Peter and Chris. It has been a privilege!

To the people I spent more-or-less all of my time with over the past few years, the Mackenzie/Timmel collective (the Oxford Mafia). Thanks for being an absolute blast to work with and hang out with. The group wouldn't be the same without you lot and the pub would be much more lonely and tragic. Thanks to the super Dr. Kevin Henbest, the project would be no-where without your handwork and limitless knowledge. It was fun to chat all things science and chess with you. To the new postdoc Dr. Lewis Antill, although I've been writing basically the whole time you've been here, it has still been a good laugh. Although, I fear our shared sense of humour will get us both in trouble one day!

To the DPhils, thanks to Tommy Pitcher, the voice of reason, your choice in football team is as good as your choice of favoured Star wars film is bad. Good luck with your final year and writing up, it'll only take you a week or two, so relax! To Ana Štuhec my favourite eastern European, thanks for the chats, all of the cake and Lindor chocolate bribery. Although you won't need it (data looks great!), good luck with the rest of your DPhil. To Daniel Cubbin, my original protege and fellow pub frequenter, I'm sure the pleasure has all been yours. I will defeat you at foosball if it kills me. But seriously, it has been fun, good luck with the rest of your DPhil, I hope your lasers outlast you for a change! To Carl Olavesen, in whose capable hands I leave BBCEAS and OCTAS. Thanks for the fun chats about random science, I hope you continue to enjoy your DPhil and maybe see you in Belfast some time! To Laurynas Paskevicius in whose capable hands I leave μDF-MARY, it has been fun to work with you. I can only apologies I wasn't around as much this year but you've done well with a difficult project. I wish you good luck wherever you end up next!

A special thanks goes out to my fellow 2019 DPhil students, Jamie Gravell, my pollo hermano, Angela Gehrckens, a vegan, Ashley Redman, Ötzi the iceman and Sebastian Kopp, monster energy's favourite German. Jamie, it has been fun and I'm glad I had a comrade, fellow Celt and enjoyer of the pub(eg) for the journey. Together we nearly made a decent DPhil student (red-Kevin, chimera cry)! Good luck in London and finishing up your thesis. No doubt I'll see you around! Angela, my first friend in Oxford, lunch won't be the same without you. I may not have made it to deepest darkest Cowley ever but perhaps I'll manage to make it to the moderately closer Marseille, I'll still never karaoke though. Anyways, I hope Marseille is brilliant and you can enjoy the sun (being part plant and all). Ashley, thanks for making us excellent food, sharing my mild obsession with coffee and giving me many a film to add to my never ending list of must watches. I hope Freiburg is a blast! Seb, it has been a jolly old time, thanks for providing a wealth of excellent catch phrases and a generally positive vibe. You were a great late night companion during the madness of thesis writing etc. In your own words, "goodbye good sir", enjoy your new life at Northwestern with your favourite supervisor. I hope we can share a shisha in the near future!

Last but not least thanks to the rest of the Mackenzie (clusters) and Timmel (EPR) groups who now tragically have to share an office space with that rabble. I can only apologies for the noise!

Contents

Abstract v

Acknowledgments vii

1 Introduction 1

2 Spin Chemistry 3
- 2.1 Quantum Mechanics of Spin . . . 3
- 2.2 Spin Hamiltonian . . . 7
  - 2.2.1 Zeeman Interaction . . . 8
  - 2.2.2 Hyperfine Interaction . . . 9
  - 2.2.3 Dipolar Interaction . . . 11
  - 2.2.4 Exchange Interaction . . . 11
- 2.3 Density Matrix Formalism . . . 12
  - 2.3.1 Liouville von-Neumann Equation . . . 13
  - 2.3.2 Liouville Space . . . 14
- 2.4 The Radical Pair Mechanism . . . 16
  - 2.4.1 Coherent Evolution . . . 17
  - 2.4.2 Electron Transfer . . . 19
  - 2.4.3 Magnetic Field Effects . . . 21
  - 2.4.4 Relaxation . . . 27
- 2.5 The Radical Pair Mechanism in Cryptochromes . . . 31

3 Optical Cavity Spectroscopy 35
- 3.1 The Optical Cavity . . . 36
  - 3.1.1 Pulsed Light . . . 41
  - 3.1.2 Continuous Light . . . 42
- 3.2 Broad-band Cavity Enhanced Absorption Spectroscopy . . . 45

4 Comparison of the Magnetic Field Effects From Wild Type Avian Cryptochromes 51
- 4.1 Methods . . . 52
- 4.2 Results and Discussion . . . 52
- 4.3 Conclusion . . . 56

5 Ferricyanide Photochemistry and Its Influence on The Radical Pair Mechanism in Cryptochromes 59

5.1 Potassium Ferricyanide Photochemistry . . . 62
5.1.1 Methods . . . 63
5.1.2 Results . . . 64
5.1.3 Discussion . . . 69
5.2 Potassium Ferricyanide Influence on Cryptochrome Magnetic Field Effects . 72
5.2.1 Methods . . . 72
5.2.2 Results . . . 73
5.2.3 Influence on Kinetics . . . 78
5.2.4 Influence on Spin Dynamics . . . 86
5.3 Conclusion . . . 94

6 Exploring The MFE Mechanism in Cryptochromes One Mutation at a Time 95
6.1 Methods . . . 97
6.1.1 Transient Absorption Spectroscopy . . . 97
6.1.2 Broad-band Cavity Enhanced Absorption Spectroscopy . . . 99
6.1.3 Continuous Illumination . . . 99
6.2 Results . . . 99
6.2.1 Transient Absorption Spectroscopy . . . 102
6.2.2 BBCEAS . . . 107
6.2.3 Continuous Blue Light Irradiation . . . 110
6.3 Discussion . . . 112
6.4 Conclusion . . . 116

7 Single Point Mutations of the Electron Transfer Chain in *Gallus gallus* Cryptochrome 4a 119
7.1 Methods . . . 120
7.2 Results and Discussion . . . 121
7.2.1 *Gg*Cry4a W369F Y319F and *Gg*Cry4a Y319F . . . 121
7.2.2 *Gg*Cry4a W318F and *Gg*Cry4a W372F . . . 129
7.3 Conclusion . . . 133

8 Optical Cavity-Enhanced Transient Absorption Spectroscopy 135
8.1 Introduction to OCTAS . . . 135
8.2 OCTAS Working Principles . . . 139
8.2.1 Experimental Apparatus . . . 145
8.2.2 Experimental Protocol and Data Analysis . . . 146
8.3 Magnetic Field Effects in FMN/HEWL . . . 147
8.3.1 Pulsed Photoexcitation . . . 148
8.3.2 Continuous Photoexcitation . . . 151
8.4 Magnetic Field Effects in FAD . . . 154
8.5 Magnetic Field Effects in a CPF Triad . . . 158
8.6 Magnetic Field Effects in *Gg*Cry4a W369F Y319F . . . 163

8.7 Conclusions and Outlook . . . 167

9 Development of a New Instrument for Microdroplet Fluorescence Magnetic Field Effects 171

9.1 Microfluidics - A Brief Introduction . . . 172
9.1.1 Fluid Particles and Fields . . . 172
9.1.2 The Continuity Equation . . . 174
9.1.3 The Navier-Stokes Equation . . . 175
9.1.4 Microdroplet formation . . . 177
9.2 μDF-MARY Working Principles . . . 183
9.2.1 Experimental Apparatus and Protocol . . . 185
9.2.2 Data Analysis . . . 187
9.3 Microfluidic Magnetic Field Effects in FAD . . . 192
9.4 Magnetic Field Effect on FMN/Ascorbic Acid . . . 195
9.5 Microdroplet Size and Magnetic Field Effects . . . 199
9.6 Conclusion and Outlook . . . 202

10 Summary and Outlook 205

Bibliography 209

A Appendices 229

A.1 Appendix 1 . . . 229
A.1.1 *Er*Cry4a, *Cc*Cry4a, *Cl*Cry4a and *Gg*Cry4a BBCEAS ΔA Spectra . . . 229
A.1.2 Potassium Ferricyanide $\Delta\Delta A$ Spectrum . . . 230
A.1.3 *Er*Cry4a, *Cc*Cry4a, *Cl*Cry4a and *Gg*Cry4a BBCEAS $\Delta\Delta A$ Spectral Fits 231
A.1.4 *Er*Cry4a, *Cc*Cry4a, *Cl*Cry4a and *Gg*Cry4a Sequence Alignments . . . 232
A.2 Appendix 2 . . . 233
A.2.1 Glycerol and Tris Structures . . . 233
A.2.2 Potential Potassium Ferricyanide Degradation Product Calculated IR Spectra . . . 233
A.2.3 Kinetic Modelling Details . . . 233
A.2.4 FAD and Tryptophan HFC Atom Labels . . . 237
A.2.5 Kinetic Parameters for Spin Dynamics Simulations . . . 237
A.2.6 Electron Hopping Spin Dynamics . . . 237
A.3 Appendix 3 . . . 239
A.3.1 Global Analysis Methods . . . 239
A.3.2 Time Dependent Spin Dynamics Simulations . . . 240
A.4 Appendix 4 . . . 242
A.4.1 Basis States for Characteristic ST Mixing Rate Estimation . . . 242
A.4.2 FMN HEWL Global Fit Results . . . 242
A.5 Appendix 5 . . . 243

A.5.1 FAD Kinetic Model Used In Simulation 243
A.5.2 Allan Deviation 244

Abbreviations **245**

List of Figures **249**

List of Tables **253**

Chapter 1

Introduction

The way some animals detect the Earth's magnetic field, magnetoreception, and utilise it for navigation remains one of the least well understood natural senses. Several theories including electromagnetic induction and ferrimagnetism have been proposed as possible sensing mechanisms with the precise mechanism likely to be species dependent.[2]

One of the oldest documented cases of migrating animals is that of birds with references to their migration dating as far back as the Iliad.[3] Birds are known to use a variety of tools to navigate during migration such as the sun, stars and geographical land marks.[4] However, the observation that some birds were able to navigate during poor weather conditions hinted at an alternative additional navigation mechanism, the magnetic sense.[5] This was later confirmed by Wiltschko and Wiltschko who demonstrated that some migratory birds could orientate with the Earth's magnetic field.[6] Additionally, further behavioural studies demonstrated that the magnetic sense was light-dependent with European robins unable to orientate when exposed to red light, whilst able to orientate under blue light.[7] This light-dependence hinted at a magnetoreceptor located in the retina with information passed to the brain *via* the thalamofugal visual pathway. Neurological studies corroborated this with the retinal ganglion cells and Cluster N found to be the most active parts of the nervous system when birds orientate using a magnetic field.[4,a] Subsequent research showed that degradation of Cluster N in European robins rendered them incapable of using their magnetic sense.[8]

A family of proteins known as cryptochromes was proposed as a potential magnetoreceptor and later found localised in the double cones of retinal cells in European robins.[4,9,10] The magnetic sensitivity of these proteins is proposed to arise from the quantum spin dynamics of photoinduced radical pairs (RPs, a pair of molecules with unpaired electrons whose spins

[a]Cluster N is a forebrain area which processes some visual stimuli.

are correlated), a process known as the radical pair mechanism (RPM).[4,9,11] Specifically, the quantum spin dynamics of RPs is known to be sensitive to external magnetic fields with variations in an external field causing changes in the rates and yields of chemical reactions.[4,11,12] These effects are known as magnetic field effects (MFEs) and they form the foundation of the RPM hypothesis by which birds detect variations in the photoinduced reaction yields in photoreceptor proteins. Crucially, due to the non-equilibrium nature of the RPM, MFEs below the thermal energy, $k_B T$, are theoretically viable and have been experimentally reported in model systems at geomagnetic field strengths (50 μT).[13] This forms the topic of discussion in the following thesis which explores the RPM in cryptochromes and the development of novel techniques with which to study them.

Chapter 2

Spin Chemistry

Spin chemistry, as its name suggests, is the study of magnetic and quantum spin effects in chemical reactions and processes.[14] Originating in the 1960s, spin chemistry was first used to understand the observation of non-equilibrium nuclear magnetic resonance (NMR) peaks in chemically reacting systems, a process now known as chemically induced dynamic nuclear polarisation (CIDNP).[14–16] Since then, spin chemistry has expanded into a broad interdisciplinary field with applications in photochemistry and photophysics, organic semiconductors, NMR sensitivity enhancement and, in particular, quantum information technology.[14] Of special importance to the research discussed here is the interplay between magnetic fields and the outcome of radical pair reactions, termed magnetic field effects (MFEs). Discussed in the following is the theoretical background behind MFEs and their application to the radical pair mechanism and avian magnetoreception.

2.1 Quantum Mechanics of Spin

Naturally, the field of spin chemistry relies on the quantum mechanics of spin, a fundamental property of all elementary particles (*i.e.* electrons, quarks, photons, nucleons *etc.*). Generally speaking, spin describes a particle's quantised intrinsic angular momentum (even at rest for massive particles) characterised by the spin quantum number s. First discovered in the 1920s, the concept of electron spin was introduced by George Uhlenbeck and Samuel Goudsmit to simplify interpretation of atomic spectra, additionally explaining the results from Stern and Gerlach's famous experiment.[17,b] Specifically, they stated that electrons could exist in two states $m_s = +1/2$ (spin up, α) or $m_s = -1/2$ (spin down, β).[17] The term spin arises by analogy with the rotation of classical bodies. However, this is somewhat of a misnomer as particles are not actually spinning on an axis. In fact, for an electron

[b]The Stern-Gerlach experiment comprised of passing a beam of silver atoms through an inhomogeneous magnetic field. Atoms passing through the magnetic field were found to be deflected in one of two directions.[17]

spinning on its axis to account for the observed intrinsic angular momentum, the surface of the electron (in so far as one can be claimed)[c] would have to be travelling ten times faster than the speed of light.[18,19]

In 1927 Pauli phenomenologically formalised the theory of electron spin using quantum mechanics. To do this he redefined the electron's wavefunction to consist of a pair of wavefunctions (α or β), known as a two-component spinor, $\mathbf{\Psi}$.[20] This is given formally by[21]

$$\mathbf{\Psi} = \psi_1(\mathbf{r})\alpha + \psi_2(\mathbf{r})\beta = \psi_1(\mathbf{r}) \begin{bmatrix} 1 \\ 0 \end{bmatrix} + \psi_2(\mathbf{r}) \begin{bmatrix} 0 \\ 1 \end{bmatrix} = \begin{bmatrix} \psi_1(\mathbf{r}) \\ \psi_2(\mathbf{r}) \end{bmatrix} \tag{2.1}$$

Later, when Dirac combined quantum mechanics and special relativity to derive his famous equation the electron spin appeared naturally, providing theoretical justification for Pauli's treatment. For completeness, the Dirac equation is given by[22,23]

$$(i\hbar\gamma^\mu\partial_\mu - mc)\psi \;=\; 0 \tag{2.2}$$

where ψ is a four-component spinor, known as a bispinor,[d] ∂_μ is the gradient over space and time, γ^μ represents the 4×4 gamma matrices which ensure ∂_μ acts on the correct components of ψ, m is the mass and c is the speed of light.[22] In the non-relativistic limit the Dirac equation reproduces Pauli's theory of spin.[23] Therefore, since relativistic effects can be safely ignored in all of the following, Pauli's interpretation will be applied.

The spin of a particle is described by the spin quantum number, s, and the spin projection quantum number m_s. States defined by s and m_s are eigenstates of the total spin angular

[c]The standard model of particle physics treats all fundamental particles as point-like. Their properties are defined by the fields around them.

[d]The bispinor is composed of two Pauli spinors one with negative energies and one with positive energies. The appearance of the former predicted the existence of anti-matter.

momentum operator, $\hat{S}^2$ and their projection onto an arbitrary axis, $\hat{S}_z$.[17,24]

$$\hat{S}^2 |s, m_s\rangle = s(s+1)\hbar^2 |s, M_s\rangle \tag{2.3a}$$

$$\hat{S}_z |s, m_s\rangle = \hbar m_s |s, M_s\rangle \tag{2.3b}$$

The spin quantum number can take any positive integer or half integer value while $m_s = s,\ s-1, ..., -s+1,\ -s$, such that the state space of a particle with spin s is $2s+1$. Therefore, for an $s = 1/2$ particle, such as an electron, $m_s = \pm 1/2$ which yields a state space of 2 (*i.e.* spin up and spin down, *cf* equation 2.1). Due to the prevalence of $s = 1/2$ particles, their spin states are commonly denoted[17,24]

$$\left|\frac{1}{2}, \frac{1}{2}\right\rangle = |\alpha\rangle, \qquad \left|\frac{1}{2}, -\frac{1}{2}\right\rangle = |\beta\rangle \tag{2.4}$$

where $|\alpha\rangle$ and $|\beta\rangle$ are orthogonal vectors as indicated in equation 2.1. Setting $\hbar = 1$ and using equations 2.3a and 2.1, the matrix representation of $\hat{S}^2$ for an $s = 1/2$ particle may be inferred as[24,e]

$$\hat{S}^2 \left(\begin{bmatrix} 1 \\ 0 \end{bmatrix}, \begin{bmatrix} 0 \\ 1 \end{bmatrix} \right) \Longrightarrow \hat{S}^2 = \begin{pmatrix} 3/4 & 0 \\ 0 & 3/4 \end{pmatrix} \tag{2.5}$$

Similarly, by noting that $|\alpha\rangle$ and $|\beta\rangle$ should be lowered and raised into one another, matrix representations for the raising, $\hat{S}_+$, and lowering, $\hat{S}_-$, operators may be defined as[24]

$$\hat{S}_+ = \begin{pmatrix} 0 & 1 \\ 0 & 0 \end{pmatrix}, \qquad \hat{S}_- = \begin{pmatrix} 0 & 0 \\ 1 & 0 \end{pmatrix} \tag{2.6}$$

By then applying the definition $\hat{S}_\pm = \hat{S}_x \pm i\hat{S}_y$, the remaining Cartesian spin projection operators may be constructed. The resulting set of operators has the form, $\hat{S}_i = \frac{1}{2}\sigma_i$ where σ_i represents a Pauli matrix ($i = x, y, z$). The three Pauli matrices are[24]

$$\sigma_x = \begin{pmatrix} 0 & 1 \\ 1 & 0 \end{pmatrix}, \qquad \sigma_y = \begin{pmatrix} 0 & -i \\ i & 0 \end{pmatrix}, \qquad \sigma_z = \begin{pmatrix} 1 & 0 \\ 0 & -1 \end{pmatrix} \tag{2.7}$$

[e] $\hbar = 1$ will be applied throughout the following discussion.

The same logic may be employed to derive the set of spin operators for any value of s. For example, the spin operators for $s = 1$ (^{14}N for example) are,

$$\hat{S}_x = \frac{1}{\sqrt{2}}\begin{pmatrix} 0 & 1 & 0 \\ 1 & 0 & 1 \\ 0 & 1 & 0 \end{pmatrix}, \quad \hat{S}_y = \frac{1}{\sqrt{2}}\begin{pmatrix} 0 & -i & 0 \\ i & 0 & -i \\ 0 & i & 0 \end{pmatrix}, \quad \hat{S}_z = \begin{pmatrix} 1 & 0 & 0 \\ 0 & 0 & 0 \\ 0 & 0 & -1 \end{pmatrix} \tag{2.8}$$

Together, the spin projection operators constitute the components of the spin angular momentum operator, $\hat{S}$, such that $\hat{S}^2 = \hat{S} \cdot \hat{S} = \hat{S}_x^2 + \hat{S}_y^2 + \hat{S}_z^2$. Importantly, all of the spin projection operators commute with $\hat{S}^2$ and obey the following commutation relations

$$\left[\hat{S}_x, \hat{S}_y\right] = i\hat{S}_z \quad \left[\hat{S}_y, \hat{S}_z\right] = i\hat{S}_x \quad \left[\hat{S}_z, \hat{S}_x\right] = i\hat{S}_y \tag{2.9}$$

where, $[A, B] = AB - BA$. Consequently, one can observe a particle's total spin angular momentum and its projection onto an axis precisely and simultaneously. However, no two spin projections can be known precisely and simultaneously.[f]

For a system comprised of two particles, the total spin operator is simply $\hat{S} = \hat{S}_1 + \hat{S}_2$ and obeys the commutation relations above (equation 2.9) and thus equations 2.3a and 2.3b. The total spin quantum number, S, for the composite system follows the Clebsch-Gordan series,[17]

$$S = s_1 + s_2, s_1 + s_2 - 1, ..., |s_1 - s_2| \tag{2.10}$$

Therefore, for two spin-1/2 particles, the total spin can either be $S = 0$ or $S = 1$ with $M_S = -S, -S+1, ..., S$. This leads to four possible states, one singlet ($S = 0$, $M_S = 0$)

$$|0,0\rangle \;=\; \frac{1}{\sqrt{2}}\left(|\alpha_1\beta_2\rangle - |\beta_1\alpha_2\rangle\right) \;=\; |S\rangle \tag{2.11}$$

[f] This is due to the uncertainty principle which states that the product of the uncertainties in the observables, A and B, is given by, $\sigma_A\sigma_B \geq \frac{\hbar}{2}\left|\left\langle\left[\hat{A}, \hat{B}\right]\right\rangle\right|$, where $\sigma_A = \sqrt{\left\langle\hat{A}^2\right\rangle - \left\langle\hat{A}\right\rangle^2}$.[17]

and three triplet states ($S = 1,\ M_S = 0, \pm 1$)

$$|1,1\rangle \ = \ |\alpha_1\alpha_2\rangle \ = \ |T_+\rangle \tag{2.12a}$$

$$|1,0\rangle \ = \ \frac{1}{\sqrt{2}}\left(|\alpha_1\beta_2\rangle + |\beta_1\alpha_2\rangle\right) \ = \ |T_0\rangle \tag{2.12b}$$

$$|1,-1\rangle \ = \ |\beta_1\beta_2\rangle \ = \ |T_-\rangle \tag{2.12c}$$

where a state $|ab\rangle = |a\rangle \otimes |b\rangle$. Obviously, such systems describe the behaviour of the coupled electron spins that drive the RPM and will thus be particularly important in the following.

2.2 Spin Hamiltonian

As shown in equation 2.1, the total wavefunction of a particle may be separated into spatial, $|\psi_n(\boldsymbol{r})\rangle$, and spin components, $|s_n\rangle$[23]

$$\boldsymbol{\Psi}(\boldsymbol{r},s) = \sum_n a_n \, |\psi_n(\boldsymbol{r})\rangle \otimes |s_n\rangle \tag{2.13}$$

Since the spin states are assumed to be orthonormal, the Hamiltonian for the system can be factorised into a sum of direct products of spatial operators, $\hat{H}_{pq}$, and spin state projections, $|s_p\rangle \langle s_q|$.[23]

$$\hat{H} \ = \ \sum_{pq} \hat{H}_{pq} \otimes |s_p\rangle \langle s_q| \tag{2.14}$$

By then calculating the energy expectation value, the spatial degrees of freedom can be removed as follows,[23]

$$\begin{aligned} E \ &= \ \langle \boldsymbol{\Psi}(\boldsymbol{r},s)| \, \hat{H} \, |\boldsymbol{\Psi}(\boldsymbol{r},s)\rangle \\ &= \sum_{knpq} a_k^* \langle s_k| \otimes \langle \psi_k(r)| \left(\hat{H}_{pq} \otimes |s_p\rangle \langle s_q|\right) a_n \, |\psi_n(r)\rangle \otimes |s_n\rangle \\ &= \sum_{knpq} a_k^* a_n \langle s_k|s_p\rangle \langle \psi_k(r)| \, \hat{H}_{pq} \, |\psi_n(r)\rangle \langle s_q|s_n\rangle \\ &= \sum_{kn} a_k^* a_n \langle \psi_k(r)| \, \hat{H}_{kn} \, |\psi_n(r)\rangle \ = \ \sum_{kn} a_k^* h_{kn} a_n \end{aligned} \tag{2.15}$$

where h_{kn} are the matrix elements for an effective Hamiltonian known as the spin Hamiltonian, $\hat{H}_S$, which only acts on the spin sub-space of the total wavefunction.

The spin Hamiltonian represents a weak perturbation to the total system Hamiltonian and is a strong approximation which breaks down when spin interactions become comparable in energy to the spatial part of the total Hamiltonian.[23] Nonetheless, the approximation holds for the systems considered in this work and the total system energy can be written as a Taylor series[24]

$$E = E_0 + \sum_n \frac{\partial E}{\partial s_n} s_n + \frac{1}{2} \sum_{nk} \frac{\partial^2 E}{\partial s_n \partial s_k} s_n s_k + \ldots \tag{2.16}$$

where E_0 is the spin-independent (spatial) energy and s_n represents either spin or external magnetic field components. The 1st and 2nd order terms in equation 2.16 describe spin, spin-external field and spin-spin interactions and thus represent different contributions to the spin Hamiltonian.[23] Below a few of the most relevant contributions to the spin Hamiltonian are stated while their derivations can be found in the textbook "Spin" by Ilya Kuprov.[23]

2.2.1 Zeeman Interaction

As spin is an angular momentum, charged particles possessing spin produce a magnetic moment, $\hat{\mu}$, given by

$$\hat{\mu} = \gamma \hat{S} \tag{2.17}$$

The proportionality constant γ is known as the magnetogyric ratio and is $\gamma_e = -g_e \mu_B$ for a free electron where μ_B is the Bohr magneton ($\approx 9 \times 10^{-24}$ J T^{-1}) and g_e is the free electron g-factor (≈ 2).

This magnetic moment will interact with external magnetic fields, thus altering the energy of the system in a way that depends on its spin state (*cf.* **Fig. 2.1**). This effect is known as the Zeeman interaction and, for an electron, is described by the following Hamiltonian, $\hat{H}_{zee}$

$$\hat{H}_{zee} = \mu_B \hat{S} \cdot \boldsymbol{g} \cdot \vec{B} \tag{2.18}$$

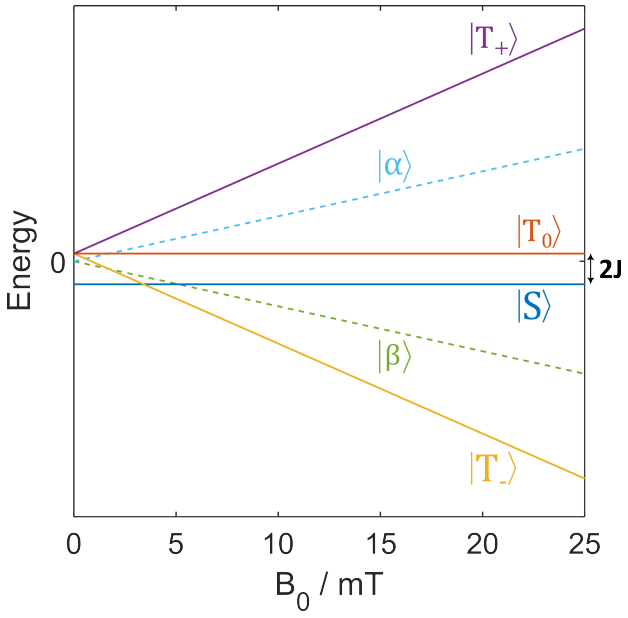

Figure 2.1: Eigenvalues of the Zeeman interaction Hamiltonian as a function of applied external magnetic field, in the $\hat{S}_z$ direction, for a system consisting of a single spin, dashed lines, and a system consisting of two coupled spins, solid lines (including the exchange interaction, see section 2.2.4). In the single spin system increasing the field linearly separates the $|\alpha\rangle$ and $|\beta\rangle$ states, raising the energy of the former and lowering the latter. In the composite system, the energy of the $|S\rangle$ and $|T_0\rangle$ states are invariant to the external magnetic field. Meanwhile, the $|T_+\rangle$ and $|T_-\rangle$ states are split analogously to the single spin $|\alpha\rangle$ and $|\beta\rangle$ states. Inclusion of the exchange interaction lifts the degeneracy between $|S\rangle$ and $|T_0\rangle$, separating them by $2J$ (*cf.* equation 2.28).

where $\vec{B}$ is the external magnetic field vector and $\boldsymbol{g}$ is a 3×3 matrix called the g-tensor.[g] In all of the systems considered here the g-tensor is isotropic such that equation 2.18 becomes

$$\hat{H}_{zee} = \mu_B g \hat{S} \cdot \vec{B} \tag{2.19}$$

where g is the isotropic g-value and is typically around 2 for organic radicals. The nuclear equivalent of the g-tensor is the chemical-shielding tensor.

2.2.2 Hyperfine Interaction

Just as the electron's spin magnetic moment can interact with an external field, so too can it interact with the spin magnetic moments of other particles such as nuclei. This coupling between electron and nuclear spins is the hyperfine coupling (HFC). The Hamiltonian describing this interaction is

$$\hat{H}_{HF} = \sum_{i}^{N} \hat{S} \cdot \boldsymbol{A}_i \cdot \hat{I}_i \tag{2.20}$$

[g]The components of the g-tensor are determined by taking the second derivative of the ground state energy with respect to the electron magnetic moment and external magnetic field.[23]

where $\hat{I}$ is the nuclear spin, $\boldsymbol{A}$ is the 3×3 HFC tensor and the sum is over all, N, spin active nuclei coupled to the electron spin, $\hat{S}$.

The HFC tensor has both isotropic (a_{iso}) and anisotropic components ($\boldsymbol{A}_{ani}$). The former arises from the small probability of the electron existing within the nuclear volume where the spherical average of the magnetic field produced from the nuclear spin is non zero. This is known as the Fermi contact interaction where the isotropic HFC constant is given by,[17,25]

$$a_{iso} = -\frac{2\mu_0 \gamma_e \gamma_N}{3} |\psi(0)|^2 \tag{2.21}$$

where μ_0 is the vacuum permeability, γ_e is the electron magnetogyric ratio, γ_N is the magnetogyric ratio of the nucleus and $|\psi(0)|^2$ is the probability density for the electron being located at the nucleus.

The anisotropic part of the HFC tensor describes the dipole-dipole interaction between the magnetic moments of the two spins. This is directly obtained from classical electromagnetism[17,26] and has the general form

$$\boldsymbol{A}_{ani} = \frac{\mu_0 \gamma_e \gamma_N}{4\pi} \left(\frac{r^2 \hat{E} - 3\boldsymbol{r}\boldsymbol{r}^{\mathrm{T}}}{r^5} \right) \tag{2.22}$$

where $\boldsymbol{r}$ is the x, y, z electron-nucleus separation with magnitude r, $\hat{E}$ is the identity operator and ^{T} indicates the transpose. The total HFC tensor is therefore,[17,24,27]

$$\boldsymbol{A} = a_{iso}\hat{E} + \boldsymbol{A}_{ani} \tag{2.23}$$

Due to the orientational dependence, the anisotropic HFC interaction will average to zero when the radical tumbles rapidly. As a result, only the isotropic HFC interaction typically contributes to solution phase spectroscopic measurements. However, for an immobilised system, the anisotropic HFC interaction causes the total spin Hamiltonian to depend on both the external magnetic field's magnitude and direction. This is of central importance to the radical pair mechanism hypothesis of magnetoreception.

2.2.3 Dipolar Interaction

In exactly the same way that electron and nuclear spins interact, so do two electron spins. However, unlike the HFC interaction, the dipolar interaction between two electron spins has no isotropic component. The Hamiltonian describing the electron-electron dipole interaction is,[17,23]

$$\hat{H}_{Dip} = \hat{S}_1 \cdot \boldsymbol{D} \cdot \hat{S}_2 \tag{2.24}$$

where $\boldsymbol{D}$ is the dipolar coupling tensor and is defined by equation 2.22 except that the collection of constants contains γ_e^2 in place of $\gamma_e \gamma_N$. Once again, this interaction is typically averaged to zero in non-viscous solution.[h]

2.2.4 Exchange Interaction

The final interaction that will be considered here is the exchange interaction. This contribution to the spin Hamiltonian arises from the Pauli exclusion principle and is a purely quantum mechanical effect. The exchange interaction represents the non-classical contribution to the inter-electron Coulomb repulsion and works to remove the degeneracy between the singlet and triplet states of coupled spins (**Fig. 2.1**).[17,24] The Hamiltonian describing this interaction is,

$$\hat{H}_{Ex} = -2J\hat{S}_1 \cdot \hat{S}_2 \tag{2.25}$$

where J is the exchange integral, defined by

$$J = \left\langle \psi_1(\alpha)\psi_2(\beta) \left| \frac{1}{r} \right| \psi_1(\beta)\psi_2(\alpha) \right\rangle \tag{2.26}$$

where ψ_i is the wavefunction for electron 1 or 2 with spin state α or β and r is the distance between the two electrons. The exchange integral is often difficult to solve but is expected to have an exponential dependence on r and as such is typically approximated to

$$J = j_0 \exp(-\beta r) \tag{2.27}$$

[h] This is not generally true for larger systems like large proteins.

where j_0 determines the magnitude of the interaction and β determines how strongly the interaction depends on inter-electron separation.

The energy separation between singlet and triplet states subject to the exchange interaction is[17,24]

$$\Delta E = \langle S|\hat{H}_{Ex}|S\rangle - \langle T_{0,\pm}|\hat{H}_{Ex}|T_{0,\pm}\rangle = \pm 2J \tag{2.28}$$

Importantly, the sign of the energy separation depends on the system. For two electrons in distinct orbitals but close spatial proximity (*e.g.* excited state of a molecule), the probability of finding the electrons in the same point in space is zero if the two electrons are in the same spin state (*i.e.* a triplet state). This is known as a Fermi hole and causes the two electrons to remain further apart, on average, and thus experience less repulsion. Consequently, the triplet states lie lower in energy than the singlet state. Alternatively, exchange can occur between two spatially separated electron spins (*i.e.* their wavefunctions do not overlap) *via* orbitals from other bridging atoms or molecules.[28,29] This process is called superexchange and can have either positive or negative contributions to the exchange coupling. Therefore, if the superexchange contribution is positive and more significant than the "direct" exchange contribution, the singlet state can be lower in energy than the triplet states. Such a scenario is observed in the exchange interaction between radicals in a radical pair.

2.3 Density Matrix Formalism

Now that the various pertinent spin interactions have been defined the radical pair mechanism can be discussed in detail. However, first it is necessary to introduce the density matrix formalism as it is the dominant method for the study of spin systems. This is in part due to its ability to readily describe ensembles and thus mixed states (a distribution of pure states).[30,i] This additionally enables the inclusion of relaxation theories (see section 2.4.4) which, in a loose sense, typically convert a system from a pure state into a mixed state. Therefore, the density matrix formalism is much more reflective of real world experiments.[24]

[i] For example, a pure state would be the ensemble of spins where every spin is in the $|\alpha\rangle$ state. Conversely, a mixed state would be the ensemble of spins where there is a Boltzmann distribution of $|\alpha\rangle$ and $|\beta\rangle$ states.

The quantum statistical ensemble of a system is described by its density matrix, $\hat{\rho}$.[31] For a system in the arbitrary basis,

$$|\psi\rangle = \sum_n c_n |\phi_n\rangle \tag{2.29}$$

the density matrix describing this system is defined as[30,31]

$$\hat{\rho} = |\psi\rangle\langle\psi| = \sum_{nk} c_k^* c_n |\phi_n\rangle\langle\phi_k| = \begin{pmatrix} |c_1|^2 & c_1 c_2^* & \cdots & c_1 c_k^* \\ c_2 c_1^* & |c_2|^2 & \cdots & c_2 c_k^* \\ \vdots & \vdots & \ddots & \vdots \\ c_n c_1^* & c_n c_2^* & \cdots & |c_{n=k}|^2 \end{pmatrix} \tag{2.30}$$

where the diagonal elements are known as populations and reflect the probabilities of finding the system in a given state. Consequently, the sum of diagonal elements (*i.e.* the trace) must be one. The off-diagonal elements of $\hat{\rho}$ are called coherences and lead to time-dependent evolution.[23] These are thus a vital component of the RPM.

2.3.1 Liouville von-Neumann Equation

The equation of motion for $\hat{\rho}$ is readily obtained from the time-dependent Schrödinger equation. That is, if the evolution of a non-relativistic quantum system is dictated by the time-dependent Schrödinger equation

$$\frac{d}{dt}|\psi(t)\rangle = -i\hat{H}(t)|\psi(t)\rangle \tag{2.31}$$

then the evolution of the corresponding density matrix is[24]

$$\frac{d\hat{\rho}(t)}{dt} = -i\left[\hat{H}(t), \hat{\rho}(t)\right] \tag{2.32}$$

This is known as the Liouville von-Neumann (LvN) equation and is the key equation in spin dynamics. Repeated integration and substitution of equation 2.32 yields[31]

$$\hat{\rho}(t) = \hat{U}(t)\hat{\rho}(0)\hat{U}(t)^\dagger \tag{2.33}$$

where $\hat{\rho}(0)$ is the density matrix at $t = 0$ and $\hat{U}$ is the time propagation operator

$$\hat{U}(t) = \hat{T}\exp\left(-i\int_0^t \hat{H}(t)dt\right) \tag{2.34}$$

where $\hat{T}$ is called the time ordering operator.[j] In most systems considered here the Hamiltonian is time independent and thus the time propagation operator is simply

$$\hat{U}(t) = \exp\left(-i\hat{H}t\right) \tag{2.35}$$

Together with a system's evolution, measurable observables may be expressed in terms of the density matrix as follows

$$\begin{aligned}\langle\hat{O}\rangle = \langle\psi|\hat{O}|\psi\rangle &= \sum_{nk}\psi_n^*\hat{O}_{nk}\psi_k = \sum_{nk}\psi_n^*\psi_k\hat{O}_{nk} \\ &= \sum_{nk}\psi_k\psi_n^*\hat{O}_{nk} = \mathrm{Tr}\left[\hat{\rho}(t)\hat{O}\right]\end{aligned} \tag{2.36}$$

where Tr denotes the trace.

2.3.2 Liouville Space

The density matrix description is a powerful tool for understanding ensemble systems, however, the LvN equation becomes difficult to solve when there are non-linear terms (*e.g.* relaxation) in the equation of motion. To overcome this issue it is often convenient to work in Liouville space when dealing with incoherent evolution.[23,30,31]

[j] $\hat{T}$ reorders $\hat{H}$ such that the time arguments descend in order. This enables the integration limits in the iterative integration and substitution of equation 2.32 to decouple, leading to equation 2.34.[24,32]

The Liouville space (or state vector) formalism involves vectorisation (row-wise flattening) of the density matrix such that[24]

$$|\rho\rangle = \begin{bmatrix} \rho_{11} \\ \rho_{12} \\ \vdots \\ \rho_{21} \\ \rho_{22} \\ \vdots \\ \rho_{nn} \end{bmatrix} \tag{2.37}$$

Accordingly, operators must be recast to operate on the correct elements of $\hat{\rho}$. These are known as Liouvillian superoperators, $\hat{\hat{L}}$, with the Hamiltonian in Liouville space given by[24]

$$\hat{\hat{L}}(t) = \hat{H}(t) \otimes \hat{E} - \hat{E} \otimes \hat{H}(t)^{\mathrm{T}} \tag{2.38}$$

The equation of motion in Liouville space thus becomes

$$\frac{d\,|\rho(t)\rangle}{dt} = -i\hat{\hat{L}}(t)\,|\rho(t)\rangle \tag{2.39}$$

In this representation both coherent and incoherent terms are now linear. Analogously to equation 2.32, equation 2.39 has the general solution.

$$|\rho(t)\rangle = \hat{T} \exp\left(-i \int_0^t \hat{\hat{L}}(t')dt'\right) |\rho(0)\rangle \xrightarrow{\hat{\hat{L}}(t)=\hat{\hat{L}}} \exp\left(-i\hat{\hat{L}}t\right) |\rho(0)\rangle \tag{2.40}$$

with observables now determined by

$$\langle \hat{O} \rangle = \langle O|\rho(t)\rangle \tag{2.41}$$

where $|O\rangle$ is the row-wise flattened Hilbert space operator $\hat{O}$.



Figure 2.2: Generic example of the RPM for a singlet born SCRP. Absorption of light by an acceptor, A, prompts electron transfer from some donor, D, to the excited singlet state of A. This thus forms an $[A^{\bullet-}\ D^{\bullet+}]$ SCRP in the singlet state. The SCRP oscillates between singlet and triplet states (ST mixing) and either recombines *via* the singlet state or proceeds onto some long-lived product, P, *via* the triplet state.

2.4 The Radical Pair Mechanism

Discovered by Kaptein and Oosterhoff,[16] the radical pair mechanism (RPM) describes the magnetic field dependent behaviour of reactions which proceed *via* an intermediate state consisting of a pair of spatially separated radicals, termed a radical pair (RP). A generic example of a system undergoing the RPM is provided in **Fig. 2.2** where some molecule, A, absorbs a photon to form its excited singlet state, ^{1}A*, prompting electron transfer (ET) from a donor molecule, D. This thus forms a pair of radical ions ($[A^{\bullet-}\ D^{\bullet+}]$) whose spins are correlated in a singlet state due to the spin conservation rule ($\Delta S = 0$). These states are termed spin correlated radical pairs (SCRPs). Spin couplings such as the HFC interaction cause the SCRP to oscillate coherently between singlet and triplet states in a process called singlet-triplet (ST) mixing. The SCRP can then either undergo back-electron transfer (BET) *via* the singlet state or go on to form some product, P, *via* the triplet state. Crucially, the application of external magnetic fields influences the ST mixing dynamics. This thus alters the relative amounts of BET and product formation causing variations in the concentrations of the SCRP, products and ground state. These concentration variations are termed magnetic field effects (MFEs) and represent the central argument for the RPM hypothesis of magnetoreception.

The following section will detail each of the major processes contributing to the formation of MFEs in the RPM due to the evolution of SCRPs subject to the following equation of

motion,

$$\frac{d\hat{\rho}(t)}{dt} = -i\left[\hat{H}(t),\hat{\rho}(t)\right] - \left\{\hat{K},\hat{\rho}(t)\right\} + \hat{R}\hat{\rho}(t) \tag{2.42}$$

where $\{a,b\} = ab + ba$, $\hat{H}$ is the Hamiltonian and describes the coherent evolution of the SCRP, $\hat{K}$ is the recombination operator and describes the reaction kinetics and $\hat{R}$ is the relaxation operator which characterises decoherence and population relaxation. Following on from this, the RPM in cryptochrome proteins will be introduced.

2.4.1 Coherent Evolution

As mentioned above, the SCRP can undergo ST mixing when certain interactions are included in the Hamiltonian. In a crude sense, this can be thought of as arising from different local magnetic fields, B_{loc}, around the individual radicals, causing them to exhibit different Larmor frequencies, $\omega \propto \mu_B g B_{loc}$, and thus mixing states by altering the relative phase of the two spins. A more precise explanation can be achieved by considering the time-dependent probability of finding the system in the singlet state. This is given by,[33]

$$P_S(t) = \mathrm{Tr}\left[\hat{P}_S\hat{\rho}(t)\right] \tag{2.43}$$

where

$$\hat{P}_S = |S\rangle\langle S| \tag{2.44}$$

is the singlet projection operator and $|S\rangle$ is the singlet state. In the absence of recombination and relaxation, equation 2.44 can be re-written in terms of the Hamiltonian eigenstates, $|n\rangle$, and eigenvalues, ϵ_m to yield,[33,34,k]

$$P_S(t) = \frac{1}{Z}\sum_{nm} P_0^{nm} P_S^{mn} \exp(i\epsilon_{nm}t) \tag{2.45}$$

where $\epsilon_{nm} = \epsilon_n - \epsilon_m$ is the energy separation between states n and m, Z is the dimensionality of the nuclear spin space and $P_0^{nm} = \langle n|\hat{P}_0|m\rangle$ and $P_S^{nm} = \langle n|\hat{P}_S|m\rangle$ are the matrix elements of the initial (*i.e.* singlet or triplet) state projection operator and singlet projection operator, respectively. It is clear from equation 2.45 that evolution only occurs if states $|n\rangle$ and $|m\rangle$

[k] This is achieved by taking advantage of the identity operator $\sum_n |a_n\rangle\langle a_n| = \hat{E}$.

are non-degenerate and if the matrix element for the projection of that state is non zero. Therefore, the populations of $\hat{\rho}(t)$ (in the Hamiltonian eigenbasis) are time invariant while the coherences oscillate at a frequency determined by the energy gap between the two eigenstates. The system therefore oscillates between singlet and triplet states at a number of frequencies. This process is demonstrated in **Fig. 2.3** which shows the time-dependent singlet probability for a SCRP where each radical experiences HFC with a spin-1 nucleus.

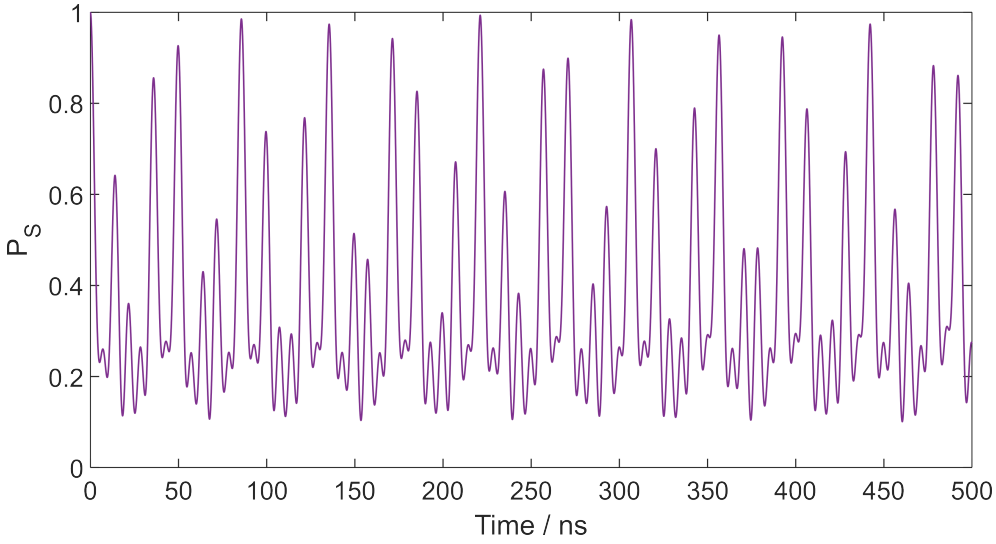

Figure 2.3: Time evolution of the singlet probability, P_S, for a singlet born SCRP where each electron is coupled to a single spin-1 nucleus ($a_1 = 1.4$ mT, $a_2 = 1.9$ mT). Recombination and relaxation have been ignored. The probability of finding the system in the singlet state oscillates as the system moves between the singlet and triplet states at a defined sum of frequencies dictated by the HFC interactions. Only the HFC interaction is included in the Hamiltonian.

What makes this evolution coherent? To understand this, coherence must first be defined. The term coherence comes from classical wave mechanics and describes the phase relationship between two waves. More specifically, two waves are considered to be coherent if their phase relationship is fixed in time (or space). This concept naturally carries over to quantum mechanics where coherence describes the phase relationship between two states and their probability distributions. Therefore, if the phase relationship between two states is fixed then they are said to be coherent. Coherent evolution is thus the evolution of a system where the phase relationship between states is conserved and the system simply oscillates between states. This can be seen from equation 2.45 where any pair of non-degenerate states (with non-zero projection operator elements) oscillate at a frequency defined by ϵ_{nm}. The whole system thus oscillates between states at a sum of

frequencies whose relative phases to one another are fixed in time and determined by ϵ_{nm}. The evolution of the system is therefore coherent.

2.4.2 Electron Transfer

Once the SCRP is formed and undergoing ST mixing, the singlet and triplet states can undergo forward reactions such as electron transfer and (de)protonation. Importantly, any ET reactions involving both radicals will be spin-selective and thus the singlet SCRP state must form a singlet product by ET. Similarly, the triplet SCRP state must form a triplet ET product. It is this spin-selectivity that gives rise to observable MFEs in the RPM, as the application of fields alters the SCRP singlet and triplet populations and thus the relative proportion of SCRP undergoing the singlet and triplet state reactions. The specifics of this will be discussed further below (section 2.4.3). For now, the spin-selective reaction term in the SCRP equation of motion (equation 2.42) will be introduced.

Typically, electron transfer (and proton transfer)[35] reactions in chemistry are described by Marcus theory.[36] Marcus theory is a semi-classical theory which combines Fermi's golden rule with classical thermodynamics. In Marcus theory, the rate constant for electron transfer, k_{DA}, is

$$k_{DA} = \frac{2\pi}{\hbar}\frac{|H_{DA}|^2}{\sqrt{4\pi\lambda k_B T}}\exp\left(-\frac{(\lambda+\Delta G^o)^2}{4\lambda k_B T}\right) \tag{2.46}$$

where H_{DA} is the matrix element for the electronic coupling between the initial and final states, λ is the reorganisation energy,[l] ΔG^o is the standard Gibbs free energy between the initial and final states, T is the temperature and k_B is the Boltzmann constant.[36]

Marcus theory does not, however, explicitly include electron spin but rather assumes that the spin selection rule is obeyed.[m] Thus, any ET reaction with a rate constant defined by equation 2.46 only describes either the singlet or triplet state reaction. To incorporate these reactions into the SCRP equation of motion, the phenomenological Haberkorn

[l] energetic cost due to changes in things like solvation and/or molecular vibrations etc.

[m] This comes from applying the Born-Oppenheimer approximation to Fermi's golden rule where the rate of transfer would be zero if it was between two states of different spin multiplicity.

recombination operator was defined as[37]

$$\hat{K} = \frac{k_S}{2}\hat{P}_S + \frac{k_T}{2}\hat{P}_T \tag{2.47}$$

where k_S and k_T are the reaction rate constants for the SCRP singlet and triplet states and $\hat{P}_S$ and $\hat{P}_T$ are their respective projection operators. Equation 2.47 works to decay the singlet and triplet populations exponentially at a rate of k_S or k_T respectively. Additionally, the coherences decay exponentially, with a rate of $(1/2)(k_S + k_T)$.[37] The effect of this operator on the singlet probability of a model SCRP is demonstrated in **Fig. 2.4**.

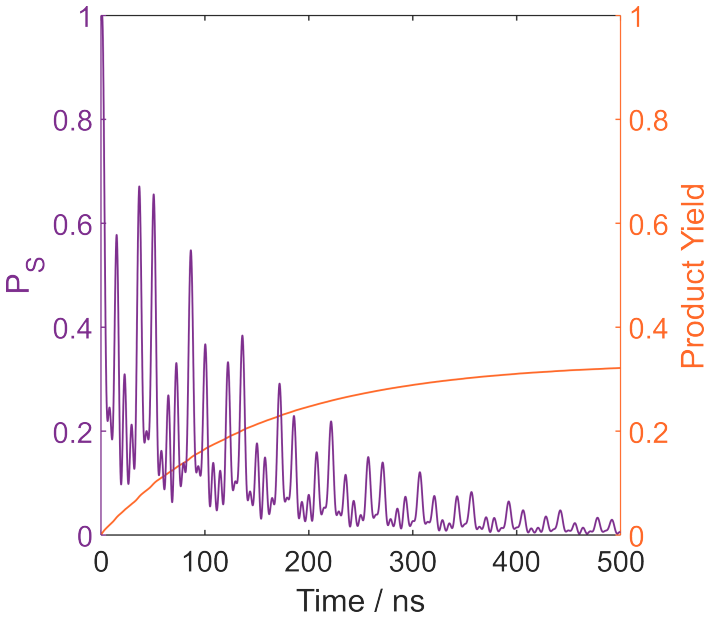

Figure 2.4: Purple line (left axis) - singlet probability, P_S, for a singlet born SCRP subject to the Haberkorn recombination operator ($k_S = 10\ \mu s^{-1}$, $k_T = 5\ \mu s^{-1}$) where each electron is coupled to a single spin-1 nucleus ($a_1 = 1.4$ mT, $a_2 = 1.9$ mT). Orange line (right axis) - proportion of the SCRP which forms the triplet product (*cf.* **Fig. 2.2**). Relaxation has been ignored and only the Zeeman and HFC interactions are included in the Hamiltonian.

Recently, a more rigorous derivation of spin-selective electron transfer in non-adiabatic radical ion pairs, using chemical reaction rate theory, proved the validity of the Haberkorn equation with an additional correction to the equation of motion.[38,n] The resulting operator is defined as,

$$\hat{K} = \frac{k_S}{2}\hat{P}_S + \frac{k_T}{2}\hat{P}_T - i2J_R\hat{S}_1 \cdot \hat{S}_2 \tag{2.48}$$

[n]The master equation derived by Fay *et al.* exhibits a perturbative expansion term where truncation to second order yields equation 2.48. Higher order truncation leads to additional terms.

where the new term $-i2J_R\hat{S}_1 \cdot \hat{S}_2$ contributes to the coherent part of the spin Hamiltonian and is a reactive spin coupling term which describes the effect that the coupling between spins has on the energy levels of the states. This shift in energy levels is quantified by $J_R = J_R^S - J_R^T$ where J_R^S and J_R^T are the contributions from the singlet and triplet reaction pathways, respectively. In the classical approximation $J_R^{S/T}$ is defined as

$$J_R^{S/T} = \frac{2\pi}{4}\frac{|H_{DA}|^2}{\sqrt{4\pi\lambda k_B T}}\exp\left(-\frac{(\lambda+\Delta G^o)^2}{4\lambda k_B T}\right)\mathrm{erfi}\left(\frac{\Delta G^o - \lambda}{\sqrt{4\lambda k_B T}}\right) \tag{2.49}$$

where

$$\mathrm{erfi}(x) = \frac{2}{\sqrt{\pi}}\int_0^x \exp(z^2)dz \tag{2.50}$$

is the complex error function. For the derivation and detailed discussion of equation 2.48, the reader is referred to Fay *at al.*[38] In any case, the contribution from reactive electron spin coupling correction is small in the systems considered here and as such ignored.[38] Consequently, equation 2.47 is used in all simulations presented in this work.

2.4.3 Magnetic Field Effects

At this point, the effect the application of external magnetic fields has on the ST mixing dynamics can be discussed. As mentioned, this effect combined with the spin selective reactions discussed above marks the origin of the MFEs which are central to the RPM hypothesis of magnetoreception. Specifically, MFEs are the change in concentration of species involved in the RPM in response to an external magnetic field. This is often quantified by the $\%MFE$ which is given by

$$\%MFE = 100 \cdot \frac{[RPM\ Species]_B - [RPM\ Species]_{B=0}}{[RPM\ Species]_{B=0}} \tag{2.51}$$

where $[RPM\ Species]$ is the concentration of any species formed during the RPM process (*cf.* **Fig. 2.2**). The subscript indicates the presence (B) or absence ($B = 0$) of an externally applied magnetic field.

The effect of applying external magnetic fields to a singlet born SCRP where each of the electrons is coupled to a spin-1 nucleus and the singlet and triplet states decay at a rate of

$k_S = 10\ \mu s^{-1}$ and $k_T = 5\ \mu s^{-1}$, respectively, is shown in **Fig. 2.5**. The time evolution of the change in SCRP probability, ΔRP, is shown in **Fig 2.5 b** where the application of a 25 mT magnetic field causes a drop in the SCRP concentration which subsequently decays away in conjunction with the decay of the SCRP itself. This decrease in SCRP concentration is a result of the external magnetic field impeding the ST mixing efficiency thus causing greater BET and a reduction in the SCRP, and product, concentration. This effect is known as the high field effect (HFE). The field dependence of the %MFE (integrated over all time) in **Fig 2.5 a** is called a magnetically altered reaction yield (MARY) and exhibits a Lorentzian-like profile. In addition to the HFE, the MARY highlights two important features; the low field effect (LFE) and $B_{1/2}$. The LFE region is where the application of external magnetic fields enhances the ST mixing dynamics. Thus, for a singlet born SCRP there is a greater proportion of triplet state and suppressed BET, leading to an increase in the SCRP concentration (and product formation).

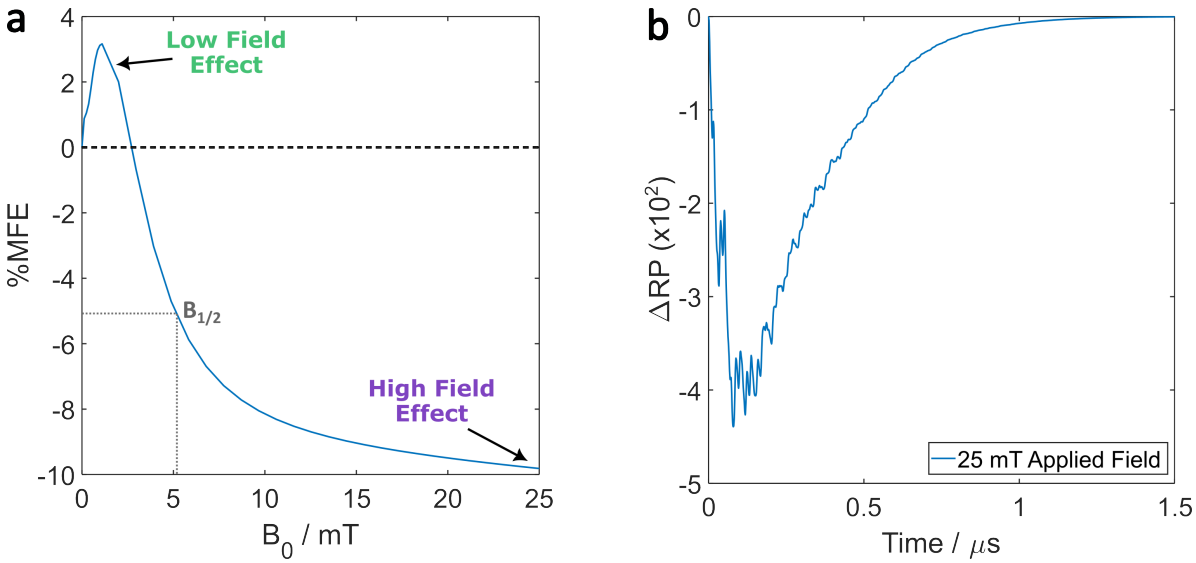

Figure 2.5: a) %MFE (integrated over all time) as a function of applied magnetic field strength, termed magnetically altered reaction yield. Three key features are highlighted; the low field effect, the high field effect and the $B_{1/2}$. These are discussed in detail in the main text. b) Time evolution of the change in the total SCRP probability (P_T), $\Delta RP = P_T(B = 25\ \text{mT}) - P_T(B = 0\ \text{mT})$, at 25 mT. The SCRP concentration is decreased by the application of the magnetic field with the magnitude of ΔRP peaking within the first *ca* 200 ns before decaying away along with the decay of the SCRP itself. Both plots are results from simulating a singlet born SCRP subject to the Haberkorn recombination operator ($k_S = 10\ \mu s^{-1}$, $k_T = 5\ \mu s^{-1}$) with each electron coupled to a single spin-1 nucleus ($a_1 = 1.4$ mT, $a_2 = 1.9$ mT). Relaxation was ignored and only the Zeeman and HFC interactions are included in the Hamiltonian.

The $B_{1/2}$ is the magnetic field at half of the saturated %MFE (%MFE($B \to \infty$)). Importantly, the $B_{1/2}$ is empirically linked to the HFC interactions within the SCRP *via* the Weller

formula[39]

$$B_{1/2} = \sqrt{3}\frac{B_1^2 + B_2^2}{B_1 + B_2} \tag{2.52}$$

where

$$B_i = \sqrt{\frac{4}{3}\sum_k a_{ik}^2 I_{ik}(I_{ik}+1)} \tag{2.53}$$

is the effective HFC, a_{ik} is the isotropic HFC between electron i and the kth nucleus, I_{ik} is the spin of the kth nucleus coupled to electron i and the sum is over all k nuclei coupled to electron i. Deviations from the Weller formula indicate significant spin relaxation during the SCRP lifetime and thus the $B_{1/2}$ can be used as a (qualitative) measure of spin relaxation.[40,41,o]

The origin of the MFE can be understood from the time-dependent probabilities of the singlet and triplet states of the SCRP. Following Lewis *et al.*,[34] consider a SCRP, formed in the singlet state, where one of the electrons is coupled to a spin-1/2 nucleus, I. The Hamiltonian describing this system is

$$\hat{H} = \mu_B g B_0 \left(\hat{S}_{1z} + \hat{S}_{2z}\right) + a_{iso}\hat{S}_1 \cdot \hat{I} \tag{2.54}$$

[o]It is worth noting that recent work by Wong *et al.*[40] found that the Weller formula is only valid for small, short-lived, radical pairs. For longer-lived SCRPs the theoretically calculated $B_{1/2}$ was found to be smaller. Therefore, values above the Weller formula are a strong indication of spin relaxation.

and has eight eigenstates

$$\begin{aligned}
|1\rangle &= |T_+\alpha\rangle \\
|2\rangle &= \frac{1}{\sqrt{2}}(|T_0\alpha\rangle + |S\alpha\rangle) \\
|3\rangle &= \frac{c_-}{2}(|T_0\alpha\rangle - |S\alpha\rangle) + \frac{c_+}{\sqrt{2}}|T_+\beta\rangle \\
|4\rangle &= \frac{c_+}{2}(|T_0\alpha\rangle - |S\alpha\rangle) - \frac{c_-}{\sqrt{2}}|T_+\beta\rangle \\
|5\rangle &= \frac{c_-}{2}(|T_0\beta\rangle + |S\beta\rangle) - \frac{c_+}{\sqrt{2}}|T_-\alpha\rangle \\
|6\rangle &= \frac{c_+}{2}(|T_0\beta\rangle + |S\beta\rangle) + \frac{c_-}{\sqrt{2}}|T_-\alpha\rangle \\
|7\rangle &= \frac{1}{\sqrt{2}}(|T_0\beta\rangle - |S\beta\rangle) \\
|8\rangle &= |T_-\beta\rangle
\end{aligned} \tag{2.55}$$

and eigenvalues

$$\begin{aligned}
\epsilon_1 &= \omega + \frac{a_{iso}}{4} \\
\epsilon_2 &= \frac{a_{iso}}{4} \\
\epsilon_3 &= \frac{\omega + \kappa}{2} - \frac{a_{iso}}{4} \\
\epsilon_4 &= \frac{\omega - \kappa}{2} - \frac{a_{iso}}{4} \\
\epsilon_5 &= -\frac{\omega + \kappa}{2} - \frac{a_{iso}}{4} \\
\epsilon_6 &= -\frac{\omega - \kappa}{2} - \frac{a_{iso}}{4} \\
\epsilon_7 &= \frac{a_{iso}}{4} \\
\epsilon_8 &= -\omega + \frac{a_{iso}}{4}
\end{aligned} \tag{2.56}$$

where $c_\pm = \sqrt{1 \pm \omega/\kappa}$, $\kappa = \sqrt{\omega^2 + a_{iso}^2}$ and $\omega = \mu_B g B_0$.

Since the SCRP is singlet born and thus depends on the initial singlet projection operator ($P_0^{nm} = P_S^{nm}$, *cf.* equation 2.45), and the different nuclear spin states are orthogonal, the application of a magnetic field can only introduce new time-dependent terms into the

singlet and triplet probabilities between states $|2\rangle$ to $|4\rangle$ and $|5\rangle$ to $|7\rangle$.[34] Consequently, the application of a magnetic field lifts degeneracies between states $|2\rangle$ and $|3\rangle$ and states $|6\rangle$ and $|7\rangle$. This thus leads to additional time-dependent terms provided the matrix elements for the relevant spin state projections are non-zero. The only spin states for which this is true are $|T_0\rangle$ and $|S\rangle$. Their corresponding projection operator matrix elements between states $|2\rangle$ and $|3\rangle$ and states $|6\rangle$ and $|7\rangle$ are given by[34]

$$P_{T_0}^{23} = -P_S^{23} = \frac{c_-}{2\sqrt{2}} \tag{2.57a}$$

$$P_{T_0}^{67} = -P_S^{67} = \frac{c_+}{2\sqrt{2}} \tag{2.57b}$$

and alter the time-dependent probability of finding the system in $|T_0\rangle$ and $|S\rangle$ by equal and opposite amounts. Therefore, the application of a magnetic field lifts degeneracies, inducing additional mixing terms between $|S\rangle$ and $|T_0\rangle$ thus altering their time-dependent probabilities. Importantly, these new time-dependent terms do not affect the $|T_+\rangle$ or $|T_-\rangle$ probabilities.

In addition to these new mixing terms, although already non-degenerate, the application of a magnetic field reduces the probability amplitude for mixing between states $|3\rangle$ and $|4\rangle$ and states $|5\rangle$ and $|6\rangle$. This results in a reduction in the probability of finding the RP in the $|T_+\rangle$ and $|T_-\rangle$ states as the field is increased. Broadly speaking, the mixing between $|S\rangle$ and $|T_0\rangle$ increases with increasing applied magnetic field strength while the $|S\rangle$ to $|T_\pm\rangle$ transfer efficiency decreases with increasing applied magnetic field strength.[34]

At low field strengths, the increased $|S\rangle$ to $|T_0\rangle$ population transfer out-competes the decreased $|S\rangle$ to $|T_\pm\rangle$ transfer. This results in an overall increase in the ST mixing efficiency giving rise to the LFE. Conversely, at high field strengths $|T_\pm\rangle$ become energetically inaccessible (*cf.* **Fig. 2.1**) such that the decreased $|S\rangle$ to $|T_\pm\rangle$ transfer outcompetes the increased $|S\rangle$ to $|T_0\rangle$ mixing. This results in a net decrease in the ST mixing efficiency, yielding the HFE.[34]

The effect of applying a 50 μT magnetic field on the singlet state probability of a singlet born SCRP where each of the electrons is coupled to a spin-1 nucleus (in the absence of

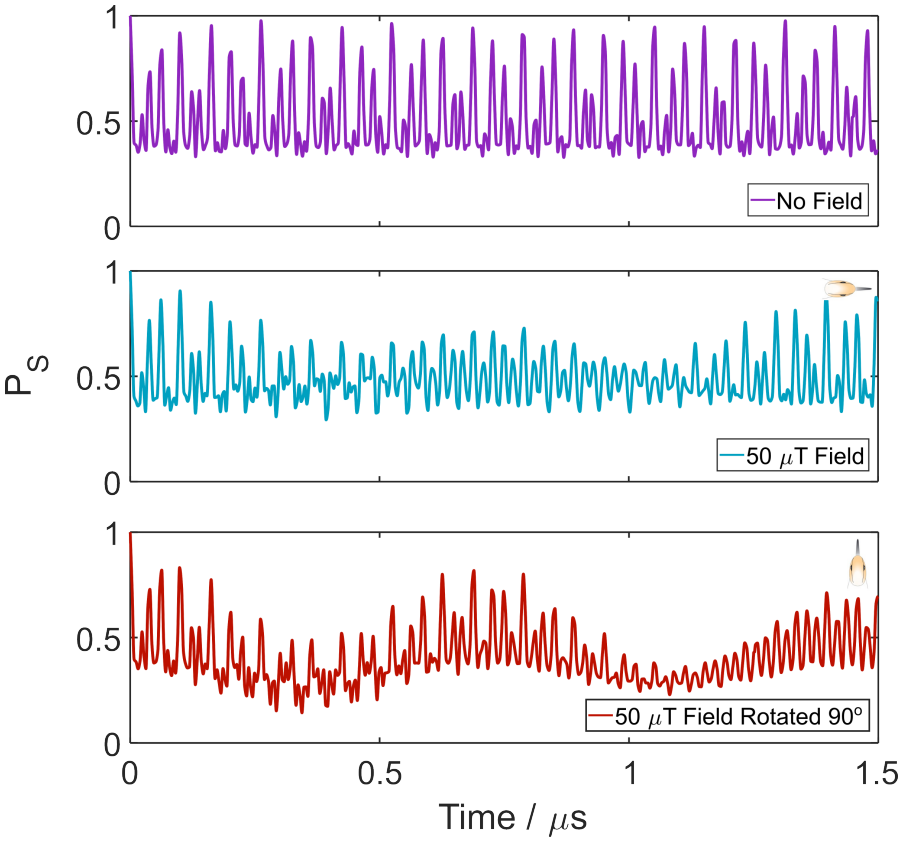

Figure 2.6: Top panel - Time evolution of the singlet probability, P_S, in the absence of an applied magnetic field. Middle panel - Time evolution of the singlet probability, P_S, in the presence of a 50 μT magnetic field. The applied field has induced additional, slow, oscillations in the singlet probability at the Larmor frequency (1.4 MHz). Bottom panel - Time evolution of the singlet probability, P_S, where the 50 μT magnetic field has been rotated 90° relative to the field in the middle panel. This alters the behaviour of the additional, slow, modulations in the singlet probability induced by the 50 μT. Once again, these plots are the result of simulating a singlet born SCRP where each of the electrons are coupled to a single spin-1 nucleus. Recombination, relaxation and the exchange interaction have been ignored. The anisotropic HFC and dipolar coupling tensors were taken from Fay *et al.*[42]

reaction kinetics) is shown in **Fig. 2.6**. In the absence of an applied field (top panel) the singlet probability oscillates in a complex manner dictated by the HFC interactions present. However, when a 50 μT field is applied (middle panel) an additional, slowly evolving, modulation is observed due to the presence of new mixing terms which arise from the lifting of degeneracies as described above. In the case where the HFC interactions are anisotropic and the system is immobilised, the direction and magnitude of the field become important. This is highlighted in the bottom panel of **Fig. 2.6** where rotating the 50 μT external magnetic field 90° relative to the HFC tensor alters the frequency and magnitude of the additional modulations arising from the presence of the magnetic field. This shift

in the ST mixing dynamics due only to field orientation forms the basis of the quantum compass, the magnetic sense believed to be utilised by some migratory birds.[1,4,6,11]

2.4.4 Relaxation

In addition to coherent evolution between pure states within a system, incoherent evolution can occur, driving the system to an equilibrium state where all coherences are lost, thus destroying any magnetic sensitivity. This is known as relaxation and arises from the coupling of the system to the environment.[24,30,43] That is, stochastic thermal motion causes time-dependent fluctuating interactions, through rotational motion or collisions with solvent molecules for example, which induce random transitions between states, spin flips.[24,43] This type of relaxation, termed spin-lattice relaxation (T_1), thus effects the populations of states and leads to the formation of mixed states. Additionally, this stochastic motion induces random fluctuations in the orientation and separation of spins which causes variations in the local magnetic field, *i.e.* modulates interactions such as HFC and exchange. This is termed spin-spin relaxation (T_2) and results in varying time-evolution throughout the system which causes a decay in the coherences between spins, thus stopping coherent evolution.[24,43]

The field of spin relaxation, and open quantum systems in general, is vast and complex. Therefore, this section will only introduce the equations relevant to the following work in a heuristic fashion, highlighting the key conceptual steps and approximations. Much more detailed discussion can be found in the tutorial paper by Manzano[30] and chapter 2 and 3 of "The Theory of Open Quantum Systems" by Breuer and Petruccione.[31]

The evolution of a system of interest and its environment is given by

$$\frac{d\hat{\rho}_T(t)}{dt} = -i\left[\hat{H}_T(t), \hat{\rho}_T(t)\right] \tag{2.58}$$

where $\hat{H}_T$ is the total Hamiltonian for the system and environment and $\hat{\rho}_T$ is the density matrix for the system and environment. The Hamiltonian

$$\hat{H}_T = \hat{H}_S \otimes \hat{E}_E + \hat{E}_S \otimes \hat{H}_E + \hat{H}_I(t) = \hat{H}_0 + \hat{H}_I(t) \tag{2.59}$$

is the sum of contributions from the system, $\hat{H}_S$, environment , $\hat{H}_E$, and the interaction between them, $\hat{H}_I$.

At this point it is useful to move to the interaction picture where the evolution of the density matrix depends only on the interaction Hamiltonian while the time evolution of operators depend on the system and environment Hamiltonians.[30,31,p] Therefore, the equation of motion becomes

$$\frac{d\hat{\rho}'_T(t)}{dt} = -i\left[\hat{H}'_I(t), \hat{\rho}'_T(t)\right] \tag{2.60}$$

where $'$ denotes the interaction picture.

Integrating equation 2.60 yields

$$\hat{\rho}'_T(t) = \hat{\rho}'_T(0) - i\int_0^t \left[\hat{H}'_I(\tau), \hat{\rho}'_T(\tau)\right] d\tau \tag{2.61}$$

and provides a route to an exact solution of the total system density matrix. However, this involves solving an integral over the total Hilbert space. Additionally, solving the integral requires knowledge of the total system density matrix at all previous times. This is, in general, too difficult and is thus avoided by substituting equation 2.61 into equation 2.60 and integrating. The result of which is again substituted into equation 2.60 to yield

$$\frac{d\hat{\rho}'_T(t)}{dt} = -i\left[\hat{H}'_I(t), \hat{\rho}'_T(0)\right] - \int_0^t \left[\hat{H}'_I(t), \left[\hat{H}'_I(\tau), \hat{\rho}'_T(t)\right]\right] d\tau \tag{2.62}$$

Truncating the iterative integration and substitution here marks the first approximation. Namely the interaction between system and environment is assumed to be small such that higher order terms from further integration and substitution can be ignored. This has the benefit of removing the requirement of knowledge of previous states of the system as they are only present in higher order terms.[30]

Equation 2.62 still depends on the total density matrix for the system of interest and the environment. To extract the dynamics of just the system of interest several assumptions must be made. First, at $t = 0$ there are no correlations between the system and environment (*i.e.*

[p] An operator, $\hat{O}$, in the interaction picture is given by $\hat{O}'(t) = \exp(i\hat{H}_0 t)\hat{O}\exp(-i\hat{H}_0 t)$.

they are separable, $\hat{\rho}_T(0) = \hat{\rho}_s(0) \otimes \hat{\rho}_E(0)$). Secondly, the initial state of the environment is at thermal equilibrium. Finally, and most significantly, the timescale for the correlation and relaxation of the environment, due to interaction with the system of interest, is assumed to be much smaller than the time scale of the system of interest. Therefore, the environment is always in thermal equilibrium and can be decoupled. Together, these approximations lead to, skipping several steps, the Redfield equation[30,31]

$$\frac{d\hat{\rho}'_s(t)}{dt} = -\int_0^\infty \mathrm{tr}_E\left[\hat{H}'_I(t), \left[\hat{H}'_I(\tau - t), \hat{\rho}'_s(t) \otimes \hat{\rho}'_E(0)\right]\right] d\tau \tag{2.63}$$

where tr_E indicates the partial trace over the environmental degrees of freedom.[q]

Equation 2.63 describes the time evolution of the system of interest which is interacting with its environment. This interaction is characterised by the interaction Hamiltonian which is typically modelled as a stochastically varying interaction from the spin Hamiltonian ($\hat{H}_S$), such as hyperfine or dipole-dipole coupling.[24] Some of the frequencies of this stochastic modulation may be resonant with transitions within the system, thus causing relaxation.[24] However, although widely used to model relaxation processes in spin chemistry, the Redfield equation has a problem with occasionally producing non-positive density matrices (*i.e.* negative eigenvalues and thus probabilities). To overcome this the rotating wave approximation[r] is applied. Once again skipping several steps, this approximation, after returning to the Schrödinger picture, produces the Lindblad equation[30,31]

$$\begin{aligned} \frac{d\hat{\rho}_s(t)}{dt} &= -i\left[\hat{H}_0(t), \hat{\rho}_s(t)\right] + \sum_i k_i \left(\hat{L}_i \hat{\rho}_s(t) \hat{L}_i^\dagger - \frac{1}{2}\left\{\hat{L}_i^\dagger \hat{L}_i, \hat{\rho}_s(t)\right\}\right) \\ &= -i\left[\hat{H}_0(t), \hat{\rho}_s(t)\right] + \hat{R}\hat{\rho}_s(t) \end{aligned} \tag{2.64}$$

where $\hat{L}_i$ are known as Lindblad operators.[s]

[q] The partial trace of a system with subspaces a and b over the subspace b is defined as, $\mathrm{tr}_b\left[\sum_{ijkl} |a_i\rangle\langle a_j| \otimes |b_k\rangle\langle b_l|\right] = \sum_{ij} |a_i\rangle\langle a_j| \,\mathrm{Tr}\left[\sum_{kl} |b_k\rangle\langle b_l|\right]$

[r] Rotating wave approximation is the assumption that terms oscillating sufficiently rapidly will average to zero on any appreciable time scale and may thus be neglected from the systems dynamics.[31]

[s] The Lindblad operators are obtained by decomposition of the interaction Hamiltonian into system and environment contributions and represent the system's contribution to the system environment interaction.[30,44]

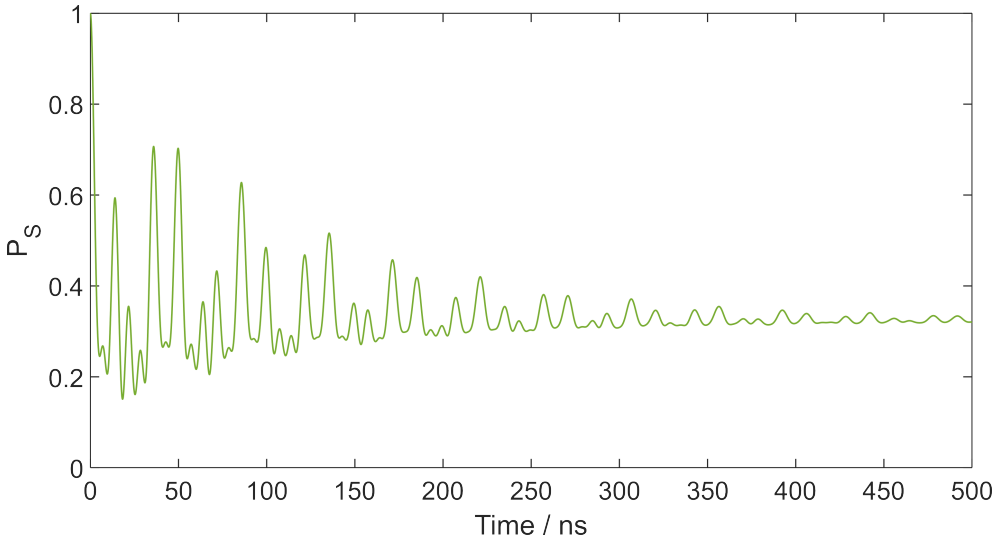

Figure 2.7: Demonstration of the effect singlet-triplet dephasing (STD) has on the evolution of the singlet probability, P_S. As the coherence terms are decayed by STD, the coherent evolution of the singlet probability is damped and the singlet probability tends to a constant value. Similarly, the evolution of the triplet state probability will be damped and tend to a constant value of $1-P_S$. Each electron of the SCRP used in this simulation is coupled to a single spin-1 nucleus ($a_1 = 1.4$ mT, $a_2 = 1.9$ mT). Recombination has been ignored and only the HFC interaction was included in the Hamiltonian.

The Lindblad equation, like the Redfield equation, describes the evolution of a system of interest which is coupled to its environment except now, the equation of motion is completely positive (*i.e.* no negative probabilities) and the relaxation of the system due to the environment is described by the Lindblad operators. Unfortunately, these operators are often unknown or difficult to define.[30,31] As a result, they are regularly defined phenomenologically to achieve a specific system dynamic. For example, setting $\hat{L}_i$ to singlet and or triplet projection operators (dropping the s subscript) yields[t]

$$\begin{aligned}\hat{R}\hat{\rho}(t) &= k_R \sum_{i=S,T} \left(\hat{P}_i \hat{\rho}(t) \hat{P}_i^\dagger - \frac{1}{2} \left\{ \hat{P}_i^\dagger \hat{P}_i, \hat{\rho}_s(t) \right\} \right) \\ &= -k_R \left(\hat{P}_S \hat{\rho}(t) \hat{P}_T + \hat{P}_T \hat{\rho}(t) \hat{P}_S \right)\end{aligned} \tag{2.65}$$

This is known as the singlet-triplet dephasing (STD) operator and works to decay the density matrix coherences, at a rate constant k_R, without influencing the populations. The effect STD has on the singlet probability of a RP is demonstrated in **Fig. 2.7**. Although phenomenological, this mechanism can arise from modulation of the exchange interaction between the radicals in a SCRP. The STD mechanism is thought to be particularly relevant

[t]Projection operator properties $\hat{P}_S + \hat{P}_T = \hat{E}$ and $\hat{P}_i \hat{P}_i^\dagger = \hat{P}_i$ have been used.

to the behaviour of MFEs in cryptochrome proteins and will be discussed in more detail in later chapters.

2.5 The Radical Pair Mechanism in Cryptochromes

The radical pair mechanism was proposed as a potential explanation for the magnetic sense of migratory birds by Schulten *et al.*[11] in 1978. This was based on the observation that the magnetic sense depended on the inclination of the magnetic field rather than the polarity.[6] Schulten thus proposed that this could be explained by anisotropic HFC interactions present in a SCRP formed *via* photon absorption and subsequent spin conserved electron transfer.[11] This hypothesis was later lent additional weight by the further observation that the magnetic sense in European robins appeared to be light sensitive.[45] It was thus necessary to find a suitable photoreceptor that could form spatially separated SCRPs where one or both of the radicals has anisotropic HFC interactions. Importantly, these SCRPs must be blue (or green) light activated[7,11] and live long-enough such that MFEs may develop (sufficient time for ST mixing). Furthermore, the receptor must be immobilised or exhibit net alignment from a collection of receptors *in vivo* so as to prevent the averaging out of anisotrpic HFC interactions.[4] In 2000 Ritz *et al*.[9] suggested that cryptochrome proteins could fulfil the criteria required for such an avian magnetoreceptor. Since then growing evidence has supported this proposal with cryptochrome proteins found localised in the retina of migratory birds.[4,6,7,10,46–50]

Cryptochrome proteins are blue light photoreceptor flavoproteins that exhibit several functional roles, most notably in regulating the circadian rhythm in animals and plants.[51] They are closely related to photolyase, a protein responsible for DNA repair, which is believed to be their evolutionary ancestor.[51] As a result, cryptochrome proteins share structural similarities with photolyase. For example, photolyase and most cryptochrome proteins non-covalently bind a flavin adenine dinucleotide (FAD) cofactor in close spatial proximity to a tryptophan (W) chain (**Fig. 2.8**). Importantly, FAD is a blue light absorbing chromophore which is readily reduced upon absorption of light and thus capable of forming photoinduced radical pairs.[4,9,51,52]

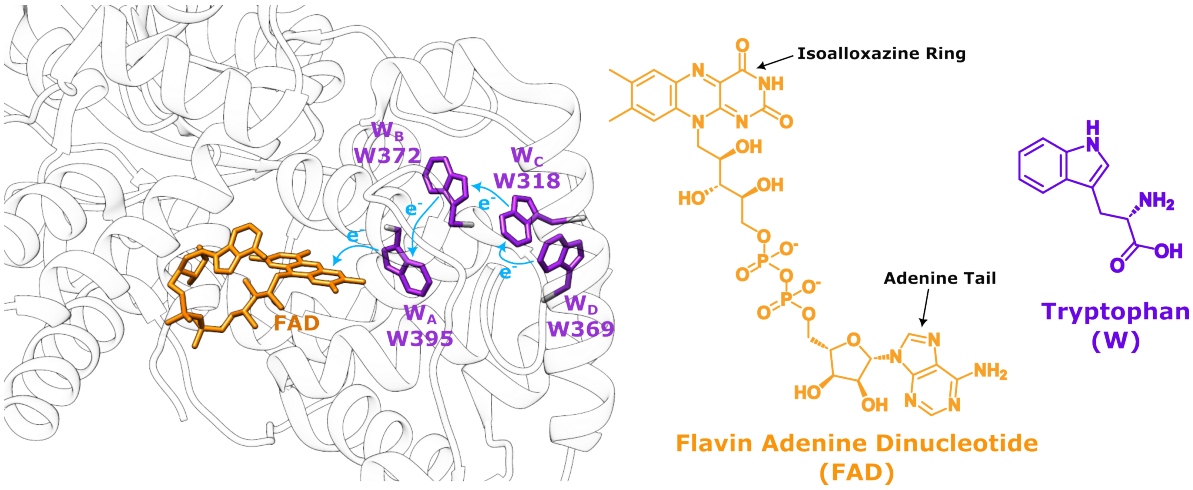

Figure 2.8: Structure of the FAD binding pocket and tryptophan tetrad in a cryptochrome 4a protein from the common pigeon *Columba livia*. Figure generated from the crystal structure determined by Zoltowski *et al.*[53] and highlights the FAD (orange) and four tryptophans (purple); W_A (W395), W_B (W372), W_C (W318) and W_D (W369). The numbers in the tryptophan labels represent their position in the protein's amino acid sequence. The molecular structures of tryptophan and FAD are additionally shown with the adenine tail and isoalloxazine ring of FAD highlighted, the latter of which is the active chromophore which absorbs blue light and is reduced by electron transfer.

There are several types of cryptochrome protein throughout nature with varying tryptophan chain lengths (typically triad or tetrad).[51,54] The specific protein implicated in avian magnetoreception is cryptochrome 4a (Cry4a) which exhibits a tryptophan tetrad adjacent to the FAD cofactor and forms SCRPs between FAD and tryptophan following a light induced electron transfer cascade.[1,55,56] Anisotropic HFC interactions on both tryptophan and the FAD isoalloxazine ring provide magnetic field sensitivity, potentially enabling a compass sense.[57]

The RPM in Cry4a is summarised in **Fig. 2.9 a** where ground state flavin adenine dinucleotide (FAD_{OX}) absorbs a photon to form the excited singlet state. Along with some fluorescence, this prompts an electron transfer cascade down the tryptophan tetrad, reducing the isoalloxazine ring on FAD (*cf.* **Fig. 2.8**) and forming an $FAD^{\bullet-}$-$W_DH^{\bullet+}$ SCRP. Due to the close spatial proximity of W_A to FAD (*cf.* **Fig. 2.8**), the initial electron transfer is fast (<1 ps)[56] and out-competes intersystem crossing to the FAD triplet state thus leading to singlet born SCRPs. These SCRPs subsequently undergo HFC driven ST mixing, as described above, before either recombining back to the ground state (GS) *via* back electron transfer (BET) from the singlet state or go on to form long-lived (s - min), uncorrelated, neutral $FADH^{\bullet}$ and $W^{\bullet}$ radicals *via* (de)protonation processes from either the singlet or

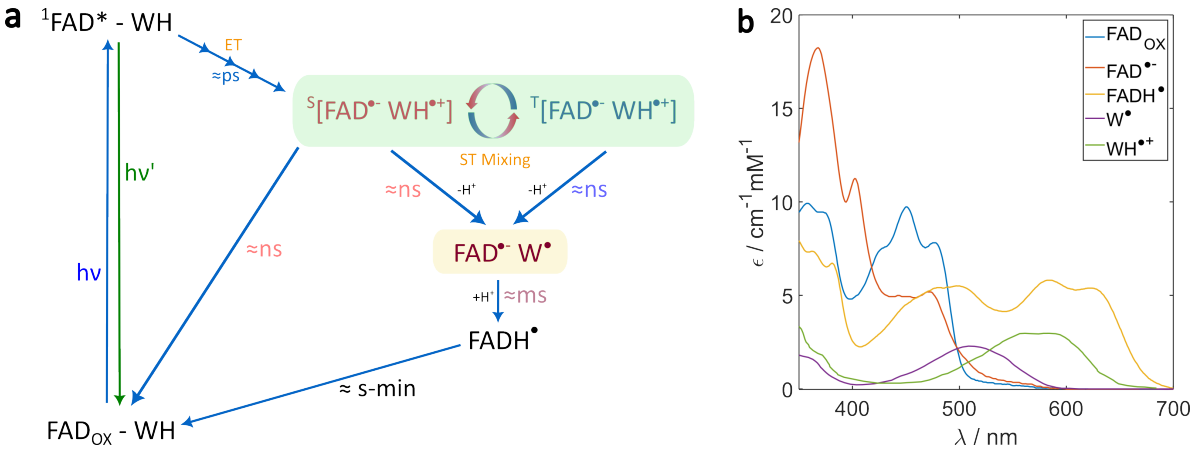

Figure 2.9: a) Proposed radical pair mechanism in Cry4a proteins where SCRPs are generated following photon absorption by FAD_{OX} and electron transfer along the tryptophan tetrad. The SCRP then mixes between singlet and triplet states, either recombining *via* singlet state or forming long-lived products, *via* (de)protonation processes, from both the singlet and triplet state. b) Absorption spectra for all of the species thought to be involved in the Cry4a RPM.[58]

triplet SCRP state. Variations in the magnitude or direction of external magnetic fields induce changes in the ST mixing dynamics of the SCRP thus inducing MFEs in downstream photoproducts such as FAD_{OX} and the long-lived $FADH^{\bullet}$ and $W^{\bullet}$ radicals. These long-lived radicals have been suggested as a potential signalling state of the protein by inducing structural changes in the C-terminus.[4] Therefore, modification in the concentrations of these long-lived radicals could be transmitted, *via* a signalling partner, to the brain thus forming the magnetic sense.

The absorption profiles of all of the species thought to be involved in the Cry4a RPM are shown in **Fig. 2.9 b**.[58] Clearly there is significant spectral overlap between the various photoproducts. Additionally, the RPM operates over a timescale spanning several orders of magnitude (ps-min). It is, therefore, necessary to employ a variety of sensitive spectroscopic techniques to adequately study the photochemistry and magnetic field sensitivity of these Cry4a proteins. While several such techniques will be discussed, an important subset are optical cavity based techniques which form the majority of experimental results in this work. As such, these techniques will be introduced in the following chapter.

Chapter 3

Optical Cavity Spectroscopy

An optical cavity is simply a well defined region of space where light is confined by reflective walls thus generating spatial interference as the radiation is reflected back and forth.[59,u] This broadly has the effect of enhancing light-matter interactions which induce transitions (*e.g.* vibrational or electronic) within molecules and materials.[60–62] This is taken advantage of in a variety of fields, most famously in the development of lasers where a gain medium, usually some form of semiconductor, is contained within an optical cavity and excited (either by light or electronically).[59] The subsequent emission couples into the optical cavity and causes stimulated emission from the excited gain medium thus forming a high powered coherent beam of light. Alternatively, when light is confined on the μm scale its quantum properties cannot be ignored. Under the right conditions, this causes strong light-matter coupling such that neither can be treated as perturbing the other. This can lead to the formation of novel pseudo-particles, such as polaritons,[v] and a breakdown of quantum chemical selection rules.[60,63–67]

On a much larger scale, in the absence of intracavity material, the interference properties of optical cavities has been employed to study gravitational waves at the laser interferometer gravitational-wave observatory (LIGO). Specifically, gravitational waves (5 Hz - 20 kHz) cause small changes in the lengths of two extremely long (4 km), mutually perpendicular, (linear)[w] optical cavities. This alters the interference pattern generated between the two cavities which can be detected and related directly back to the wavelength of the incident gravitational wave.[68–70]

[u] The behaviour of radiation in free space can be thought of as light confined in an infinitely large cavity.
[v] A polariton is a photon-matter quasi state where the interaction between light and a material is resonant with some transition within said material such that the state of the material cannot be separated from the light process generating it.
[w] Two opposite-facing mirrors which trap light in a single axis. This is discussed in more detail below.

Of relevance here is the field of optical cavity spectroscopy where the enhanced coupling between light and matter is taken advantage of to boost the sensitivity of measurements, such as absorption, from intracavity samples.[62] In a loose sense, this is due to the optical cavity forcing a beam of light to pass through a sample many times thus increasing the effective pathlength and enhancing sensitivity compared to conventional single-pass techniques.[x] Since D. A. Jackson first documented recordings of intra-cavity absorption in 1961 and O'Keefe *et al*. demonstrated significant sensitivity enhancement in 1988,[62,71,72] optical cavity spectroscopy has been successfully used in a wide range of applications. To name a few, optical cavity spectroscopy has been used in the detection of trace atmospheric pollutants,[73] glucose sensing,[74] the study of molecule chirality[75] and, most importantly in the current context, the study of weak MFEs in radical pair reactions.[1,76,77] In light of the latter, this chapter will (very) briefly introduce the theory of optical cavities and cavity spectroscopy before detailing the primary technique used throughout this thesis.

3.1 The Optical Cavity

Optical cavities can come in a variety of structures, such as cuboidal, spherical, bow-tie and ring cavities.[62,78,79] However, the simplest, and most common, is a two-sided cavity composed of opposite-facing highly reflective mirrors. Such a cavity is known as a Fabry–Pérot type optical cavity and will form the basis of the following discussion.

Light inside an optical cavity is reflected by the cavity walls and thus interacts with itself, creating a spatial interference pattern. This is described by the spatial component of the electric field, $\boldsymbol{U}(\boldsymbol{r})$, which is characterised by the Helmholtz equation[59]

$$\nabla^2 \boldsymbol{U}(\boldsymbol{r}) + k^2 \boldsymbol{U}(\boldsymbol{r}) = 0 \tag{3.1}$$

where $k = \omega/c$ is the wavenumber, ω is the angular frequency of light and c is the speed of light. Solving equation 3.1 for a Fabry–Pérot type optical cavity, with square mirrors and the cavity axis in the z-direction, yields the following allowed frequencies (modes) of

[x] Since in Beer-Lambert law absorption is proportional to pathlength.

light sustained by the cavity[59,80]

$$\nu_{lmp} = \frac{c}{2L_C} p \left[1 + \frac{l^2 + m^2}{2p^2} \left(\frac{L_C}{a} \right)^2 + \ldots \right] \tag{3.2}$$

where L_C is the separation between the two mirrors, a is the length of the side of the mirrors and l, m and p are positive integers which together define a mode of the cavity. More specifically, a cavity mode refers to the spatial distribution of the electric field produced by one round trip around the cavity (propagation along the cavity in both directions). For a mode, and thus wavelength of light, to be sustained by a cavity the total phase accumulated from one round trip must be $2\pi p$. That is, the amplitude and phase of the electric field at a given point within the cavity must remain unchanged.[59]

The influence of the first term in equation 3.2 can be seen by considering the simple case of a propagating plane wave where l and m are zero. Under this condition the wavelengths of light sustained within the optical cavity are $\lambda = 2L_C/p$. Thus, for a real plane wave, the spatial variation along the axis of propagation, z, is described by $\sin(\frac{\pi p}{L_c} z)$ where the phase of the wave depends on p. Therefore, p describes interference along the cavity axis and, for any given pair of integers l and m, defines a series of standing waves known as longitudinal modes. The second term in equation 3.2 represents an additional phase shift due to the finite extent of the beam in xy plane, perpendicular to the cavity axis. For a given value of p this additional phase shift is determined by the integers l and m which together characterise the inference pattern in the xy plane, and define a series of transverse modes for each longitudinal mode.[y]

Under the paraxial approximation,[z] equation 3.1 is solved to yield a Gaussian beam[59]

$$\begin{aligned} U = {} & U_0 \frac{w(z_0)}{w(z)} \exp\left(-\frac{x^2 + y^2}{w(z)^2} \right) \mathrm{H}_l \left[\sqrt{2} \frac{x}{w(z)} \right] \mathrm{H}_m \left[\sqrt{2} \frac{y}{w(z)} \right] \\ & \times \exp\left(i \left[kz + \frac{k(x^2 + y^2)}{2r(z)} - (l + m + 1)\alpha(z) \right] \right) \end{aligned} \tag{3.3}$$

[y] The presence of higher order terms in equation 3.2 (indicated by +...) arise from application of a binomial series in the derivation and contribute little.[59,80]

[z] The paraxial approximation assumes that a beam of light within the optical cavity propagates at a small angle to the cavity axis.

where U is the spatial component of the electric field, U_0 is the amplitude of the electric field, $r(z)$ is the radius of curvature of the beam front, $w(z)$ is the width of the beam (in the xy plane), $w(0)$ is the beam width at a focal point and is the narrowest the beam can get, $\alpha(z)$ is a phase factor which determines the resonant longitudinal modes sustained by the cavity and $\mathrm{H}_l(x)$ and $\mathrm{H}_m(y)$ are Hermite polynomials of order l and m, respectively. Equation 3.3 is the fundamental equation describing laser radiation where the Hermite polynomials define the transverse modes (spatial profile, *cf.* equation 3.2) of the beam, denoted TEM_{lm}. A few of these modes are shown below in **Fig. 3.1** which maps the intensity profile of a cross section (xy) from a beam.

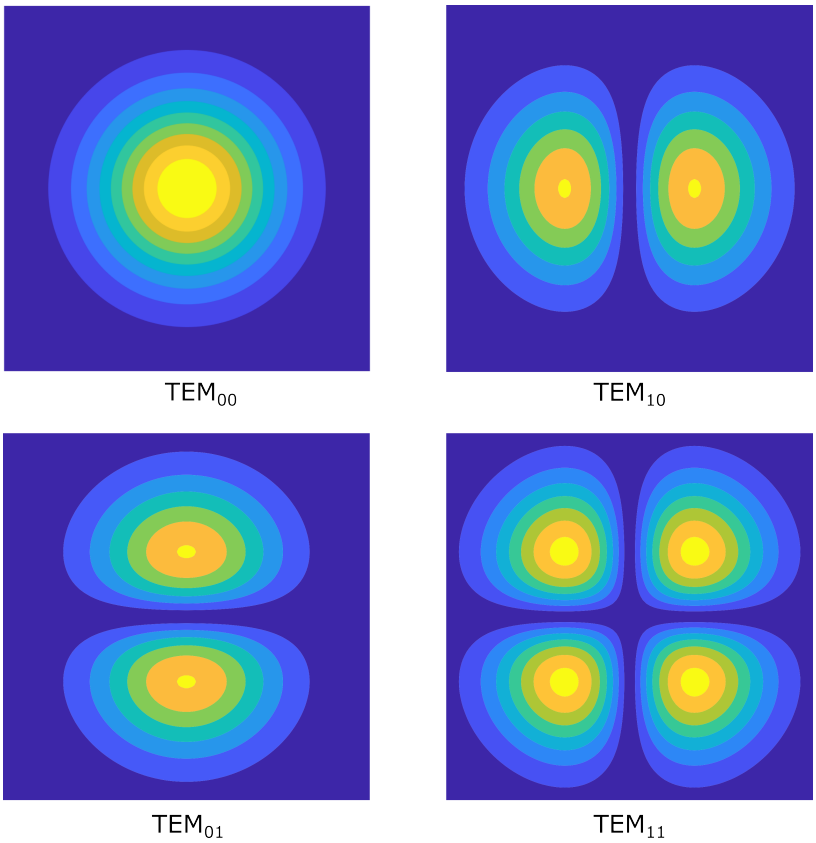

Figure 3.1: Absolute value of the electric field for the first three transverse modes of a Gaussian beam. The lowest order mode, TEM_{00}, is a simple Gaussian profile.

Of course, a perfectly reflective mirror does not exist and thus light is lost through the cavity walls as the light cycles back and forth. Additionally, depending on the alignment and geometry (*i.e.* curvature) of the cavity mirrors, light can be lost out of the open sides of the cavity (x and y). For equation 3.3 to be a valid solution for a Fabry–Pérot type optical cavity, the radius of curvature of the beam front at a cavity mirror must equal that of the cavity mirror such that the beam is reflected directly back along its propagation

path.[59] If this is the case then the light is in one of the cavity modes and losses only occur through the mirrors. Such a cavity is said to be stable with the stability of a cavity directly related to the its geometry (*i.e.* mirror separation and radius of curvature). A two-sided optical cavity is stable (low-loss) if it satisfies the following criteria[59,aa]

$$0 < g_1 g_2 < 1 \tag{3.4}$$

where the subscripts 1 and 2 refer to each of the two mirrors and

$$g_i = 1 - \frac{L_C}{r_i} \tag{3.5}$$

where r_i is the mirrors radius of curvature.

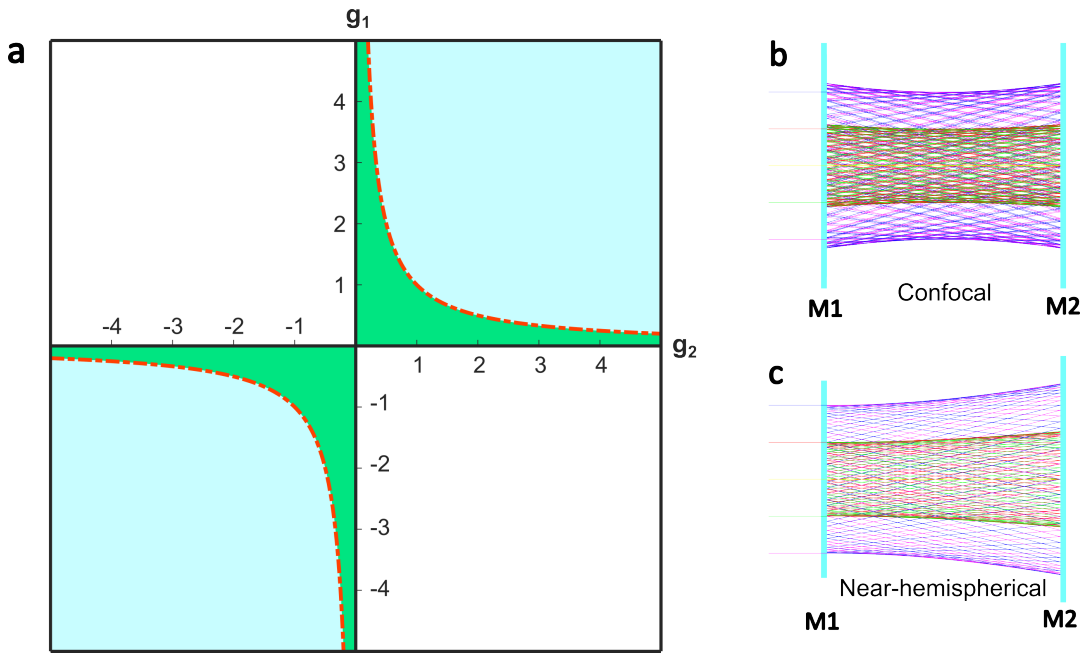

Figure 3.2: a) g_1 *vs.* g_2 plot detailing the cavity stability criteria ($0 < g_1 g_2 < 1$) curve. The low-loss stable region is indicated by the green shaded areas ($g_1 g_2 < 1$). The unstable, high-loss, region is indicated by the light blue areas ($g_1 g_2 > 1$). b) and c) show a stable confocal and near-hemispherical cavity, respectively.

Fig. 3.2 shows the condition for a stable optical cavity as a function of g_1 and g_2 where cavities within the green shaded region are low loss. Additionally, two examples of common stable cavity structures are shown, one with two curved cavity mirrors which refocus the beam back into the cavity and one with a flat mirror (M1) and a curved mirror (M2) that

[aa] The stability of any arbitrary cavity structure is determined by the eigenvalues of the transfer matrix (M) which must be less than 1. This is calculated from $\lambda = \frac{1}{2}\left(Tr(M) \pm \sqrt{Tr(M)^2 - 4\det(M)}\right)$

focuses the beam to some point behind M1. The former, and most common, is termed a confocal cavity structure and the latter a near-hemispherical cavity structure. The coloured lines within the cavities indicate the behaviour of rays of light oscillating within them with the overall structure formed representing the shape of a cavity mode.[ab]

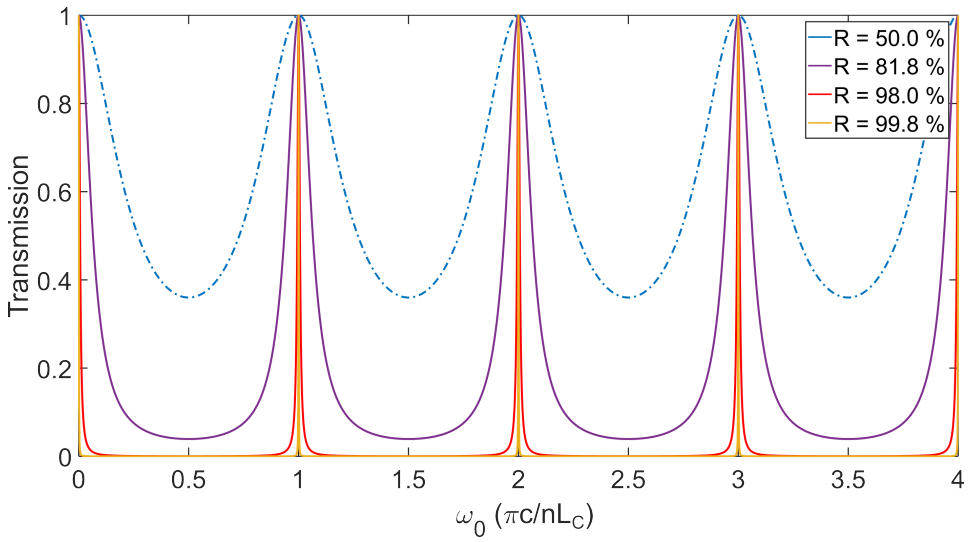

Figure 3.3: Transmission of light through an optical cavity as given by equation 3.6 where each trace represents a different mirror reflectivity and thus finesse. Increasing finesse is found to narrow the mode bandwidth. ω_0 is the normalised angular frequency where n is the refractive index.

As mentioned, mirrors are not 100% reflective and therefore a stable cavity with incident radiation through one of its mirrors, parallel to the cavity axis, will transmit light. The light transmitted through an optical cavity with equally reflective mirrors ($R_1 = R_2 = R$) is given by,[59,81]

$$T_{cav} = \frac{1}{1 + F \sin^2\left(\frac{\pi\nu}{\Delta\nu_{FSR}}\right)} \tag{3.6}$$

where

$$F = \frac{4R}{(1-R)^2} \tag{3.7}$$

ν is the frequency of light and $\Delta\nu_{FSR} = c/2L_C$ is called the free spectral range (FSR). Equation 3.6 represents an Airy distribution of longitudinal modes separated by the FSR (*cf.* equation 3.2). The bandwidth, $\Delta\nu_{1/2}$, of each mode transmitted through the cavity is determined by the cavity length and mirror reflectivity and is given by[59]

$$\Delta\nu_{1/2} = \frac{c}{L_C}\frac{1-R}{\sqrt{R}} \tag{3.8}$$

[ab]Ray tracing of beams of light within the optical cavities calculated using ABCD matrices.[59]

Together the FSR and mode bandwidth defines the finesse, $\mathscr{F}$, of a cavity

$$\mathscr{F} = \frac{\Delta\nu_{FSR}}{\Delta\nu_{1/2}} = \frac{\pi\sqrt{F}}{2} = \frac{\pi\sqrt{R}}{1-R} \tag{3.9}$$

where a cavity with a high finesse exhibits narrower, better resolved, longitudinal modes. Consequently, finesse is often used as a measure of a cavity's quality. The effect of a cavity's mirror reflectivity, and thus finesse, on the light transmitted through it is demonstrated in **Fig. 3.3** where a higher mirror reflectivity produces narrower modes.[ac]

3.1.1 Pulsed Light

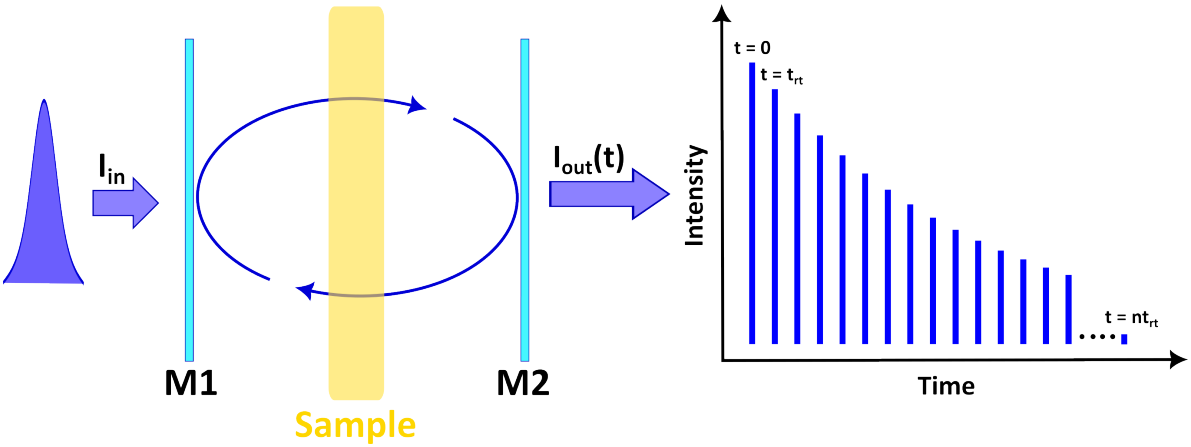

Figure 3.4: Schematic detailing the behaviour of a pulse of light incident on an optical cavity containing a sample. The light exiting the cavity decays exponentially with each round trip at a rate determined by the cavity ring-down constant which depends on the mirror reflectivity and sample absorption.

The light incident on a cavity whose transmission is described by equation 3.6 can, of course, be either continuous or pulsed. This distinction forms two broad categories within optical cavity spectroscopy with the former of particular relevance to the work herein. Nonetheless, it is worth characterising the behaviour of both pulsed and continuous light incident on an optical cavity. In that vein, consider a pulse of light whose frequency satisfies the mode conditions discussed above, incident on an optical cavity composed of two mirrors of equal reflectivity. If some sample with transmission T is placed in the

[ac] As an aside, it is worth mentioning that the characteristics of optical cavities discussed above can be derived from quantum mechanics.[60,65,81,82] In fact, this must be done if the cavities are sufficiently small or the coupling between light and matter sufficiently strong. There are several approaches to describing optical cavity phenomena quantum mechanically with the approach depending on the specific system. For example, strong-light matter coupling is typically described by the Pauli-Fierz Hamiltonian which treats the light with relativistic and the matter with non-relativistic quantum mechanics.[60]

middle of the cavity then the pulse oscillating backwards and forwards decays in intensity by R^2T^2 for every round trip which takes $t_{rt} = 2L_C/c$ seconds (see **Fig. 3.4**). Therefore, if the initial intensity transmitted through M2 ($t = 0$) is 1, after the nth round trip the light leaving M2, I_{out}, has intensity $R^{2n}T^{2n}$ after nt_{rt} seconds. This can be written as an exponential decay

$$I_{out}(t) = I_{in}(1-R)^2 \exp\left(-\frac{t}{\tau_{rd}}\right) \tag{3.10}$$

where

$$\tau_{rd} = \frac{L_C}{c(1-R+\alpha l)} \tag{3.11}$$

is the cavity ring-down time, I_{in} is the intensity of light incident on M1 at ($t = 0$), l is the optical path length through the sample and α is the sample's absorption coefficient.[61,83–85,ad] Since, τ_{rd} depends on αl, the absorption of a species within the cavity can thus be determined by comparison with an empty cavity (*i.e.* $\alpha l = 0$). If coupled with pulsed photoexcitation (not into a cavity mode), this method can be used to map out the kinetic evolution of transient photoinduced species by carefully delaying the pulse into the cavity (probe pulse) after the photoexcitation (pump) pulse. This forms the basis of cavity ring-down spectroscopy (CRDS) which has been successfully used to study MFEs in avian cryptochromes.[1]

3.1.2 Continuous Light

For a continuously driven cavity, at steady state, containing a sample with transmission T, the intensity of the output from M2 can be thought of as the sum of a series of light pulses separated by t_{rt} where each pulse decays as dictated by equation 3.10. Therefore, each pulse in the sum has undergone a different number of round trips with the contribution after n round trips, $R^{2n}T^{2n}$ times the initial intensity (*cf.* CRDS). This thus forms the following geometric expansion[72,83]

$$I_{out} = I_{in}(1-R)^2 T \sum_{n=0}^{\infty} (RT)^{2n} \tag{3.12}$$

[ad]Note, since R is taken to be near unity the approximation $\ln(R) \approx (R-1)$ has been applied.

Taking the limit as $n \to \infty$, equation 3.12 converges to

$$I_{out} = I_{in}\frac{(1-R)^2 T}{1-R^2T^2} \tag{3.13}$$

The time taken for the cavity output intensity to achieve a steady state is obtained by considering the time-dependent decay of light within the cavity subject to a constant source of radiation (*i.e.* continuous incident light coupling into the cavity). This is described by the following rate equation[83,84]

$$\frac{dI_{cav}}{dt} = \frac{c}{2L_C}\left[I_{in}\eta(1-R) - 2I_{cav}(1-RT)\right] \tag{3.14}$$

which is solved to yield[83,84]

$$I_{out} = I_{in}\frac{\eta(1-R)^2}{2(1-RT)}\left[1-\exp\left(-\frac{t}{\tau_{ru}}\right)\right] \tag{3.15}$$

where $I_{cav} = I_{out}/(1-R)$ is the intensity of light inside the cavity and η is a scaling constant which accounts for the coupling of incident light into the optical cavity. The intensity of light leaving the cavity thus builds up (**Fig. 3.5**) with a ring-up time constant, $\tau_{ru} = L_c/c(1-RT)$, similar to the cavity ring-down constant (*cf.* equation 3.11). As $t \to \infty$ equation 3.15 reduces to equation 3.13 with

$$\eta = \frac{2T}{1+RT} \tag{3.16}$$

Up until this point the transmittance through the sample and thus sample cell and cavity has been assumed to only arise from absorption processes. However, of course the sample cell and imperfections in the cavity mirror surfaces will scatter light. Therefore, to determine the single pass absorbance from the sample, these scattering processes must be accounted for. This is done by defining an effective reflectivity $R_{eff} = RT_L$ which is the mirror reflectivity scaled by non-sample transmission losses, T_L, while the transmission through the cavity is given by the product of sample, T_A, and non-sample transmission losses,

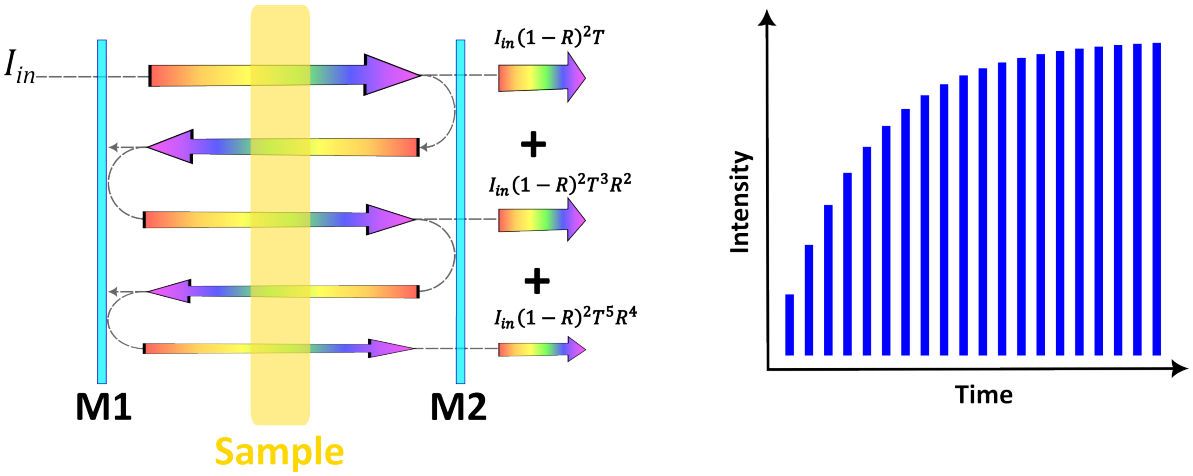

Figure 3.5: Schematic detailing the behaviour of a continuous beam of light incident on an optical cavity containing a sample. The light escaping the cavity builds up to a steady state at a rate determined by the cavity ring-up constant , $\tau_{ru} = L_c/c(1-RT)$. The amplitude of the steady state at any given time is the sum of output intensities for every round trip that a pulse would make and depends on the mirror reflectivity and sample absorbance.

$T = T_A T_L$. Equation 3.13 thus becomes

$$I_{out} = I_{in} \frac{\left(1 - \frac{R_{eff}}{T_L}\right)^2 (T_L T_A)}{1 - \left(\frac{R_{eff}}{T_L}\right)^2 (T_L T_A)^2} \tag{3.17}$$

The scattering contribution to the cavity transmission can then be removed by measuring the intensity, I_0, from a cavity with an empty sample cell (*e.g.* filled with solvent) such that $T_A = 1$. Taking the ratio of equation 3.17 and I_0 yields

$$\frac{I_{out}}{I_0} = \frac{(1 - R_{eff}^2) T_A}{1 - R_{eff}^2 T_A^2} \tag{3.18}$$

where the dependence on the input laser intensity has been removed and the cavity scattering transmission approximated with R_{eff}. Solving equation 3.18 for T_A thus provides an expression for the single pass absorption of the sample within the cavity

$$A = -\log_{10}\left(\frac{R_{eff}^2 - 1 + \sqrt{1 + \left(2\left(\frac{I_{out}}{I_0}\right)^2 - 1\right)2R_{eff}^2 + R_{eff}^4}}{2\left(\frac{I_{out}}{I_0}\right)R_{eff}^2}\right) \tag{3.19}$$

Equation 3.19 forms the basis of cavity enhanced absorption spectroscopy (CEAS), the principal technique employed in this thesis. Therefore, the following section will outline

experimental details of CEAS. More specifically, the variant, first introduced by Fiedler *et al.*,[86] where the cavity is irradiated with white light, termed broad-band cavity enhanced absorption spectroscopy (BBCEAS) will be introduced.

3.2 Broad-band Cavity Enhanced Absorption Spectroscopy

Since the RPM systems studied in this research are photoinduced, their behaviour following photoexcitation must be monitored. Consequently, BBCEAS is a pump-probe technique where a sample placed inside an optical cavity is continuously photoexcited by an excitation laser (pump) while its absorption is measured by a white light super-continuum (SC) laser (probe) which irradiates the optical cavity as described above. MFEs within the system can then be studied by applying magnetic fields during these illumination periods and observing changes in the absorption of photoinduced species.

The BBCEAS experimental apparatus is shown in the simplified schematic in **Fig. 3.6 a**. The optical cavity employed is formed of two opposite-facing broad-band mirrors (Layertec GmbH) with mean reflectivities of, $R > 0.9978$ (400 nm - 800 nm). The front mirror (M1) has a radius of curvature of 0.5 m while the back mirror (M2) has radius of curvature of 2 m. The cavity length is 20 cm providing a stable Fabry-Pérot-like resonator with $g_1 g_2 = 0.54$ (*cf.* equation 3.4). The sample cell placed at the centre of the cavity is a quartz cell (Hellma analytics, QS 165-40) with a 1 mm pathlength and liquid cooling jacket.

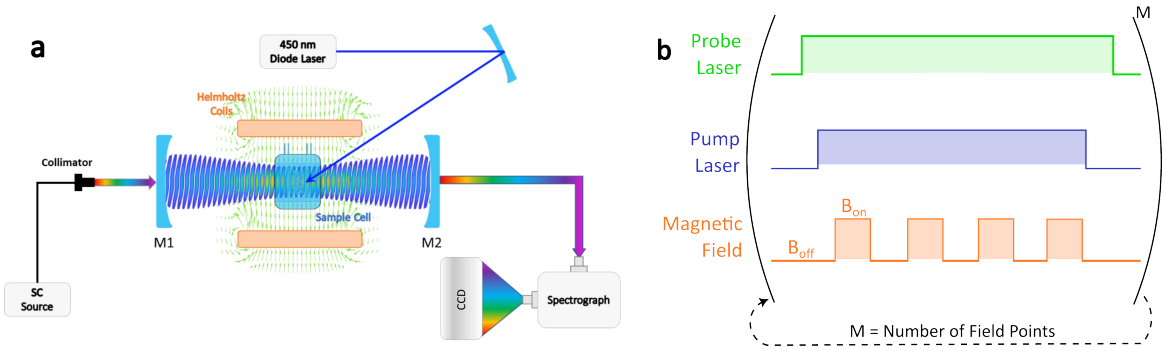

Figure 3.6: a) Simplified schematic of the BBCEAS experiment. b) Triggering sequence for a single magnetic field point measurement where the probe initially measures the ground state absorption before the pump beam is turned on, photoexciting the sample. During this photoexcitation period a magnetic field is symmetrically modulated on and off with a frequency of 5 Hz. The CCD camera detecting the cavity output acquires data during the whole process at a fixed exposure time of 1 - 3 ms.

The cavity is pseudo-continuously probed by a 78 MHz white light SC source (NKT SuperK Extreme) with 700 ps pulse widths with the IR wavelengths (> 900 nm) dumped using a set of hot/cold mirrors (NKT Super Split). To improve signal throughput, a coupling lens is placed in front of the cavity to enhance the coupling of the SC source into the lowest order transverse mode of the cavity. Photoexcitation is provided by a 450 nm continuous wave (cw) diode laser (Oxxius LBX-450, up to 70 mW) and is focused into the sample at an acute angle relative to the cavity axis such that there is minimal coupling of the pump beam into the cavity.

Magnetic fields are applied to the system *via* a set of Helmholtz coils manufactured by the University of Oxford Physical and Theoretical Chemistry Electronic and Mechanical Workshops. The coils are spaced 7.5 cm apart and have an inner diameter of 15 cm. A constant current power supply drives the coils with up to 7 A at 16-bit resolution, yielding homogeneous magnetic fields up to approximately ± 31.5 mT. The coils are accurate to ± 0.1 mT and are calibrated before each experiment. This is done by measuring the magnetic field at the sample, using a 3D Gauss meter, over a series of voltages between -5 V and 5 V and fitting a polynomial. Additionally, the coils are actively water-cooled to avoid significant power heating.

Light exiting M2 is directed into a Czerny-Turner type spectrograph (Andor Shamrock SR303i) which subsequently disperses the light, *via* a 150 lines/mm diffraction grating, onto a charged coupled device (CCD) detector (Andor Newton). The CCD is a 1024×256 array of 26×26 μm pixels providing BBCEAS with a spectral resolution up to 0.5 nm per pixel.

All timing and triggering is controlled by a digital delay generator (DDG, Stanford Research Systems DG645) which itself is triggered by a computer to initialise an experiment. A diagram of the experimental control sequence and acquisition is provided in **Fig. 3.6 b**. The whole experiment is controlled *via* a custom-written LabView program (National Instruments, 2015 SP1)[ae] which initiates and logs data acquisition and allows the user

[ae]LabView program written by previous DPhil student Dr. Marcin Konowalczyk.

to set experimental parameters such as applied magnetic fields, number of averages and illumination time *etc*.

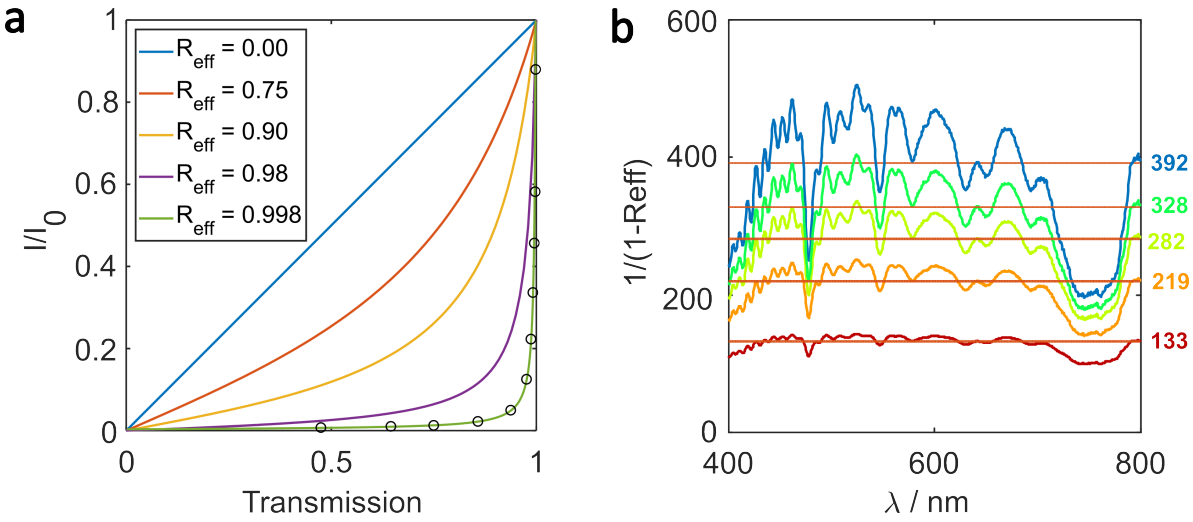

Figure 3.7: a) BBCEAS cavity calibration curves for different effective reflectivities, at 605 nm. Curves are typically fitted to the data points (black circles) from a series of dye mixture dilutions at every wavelength to estimate the R_{eff} spectrum. b) Several example cavity enhancement factor (CEF) spectra characterising the wavelength-dependent R_{eff} used to calculate single-pass absorption spectra. The straight horizontal lines indicate the median CEF.

The intensity of light detected by the CCD is converted into sample absorbance, as a function of time and wavelength, by way of equation 3.19. To do this the parameters I_0 and R_{eff} must be determined first. Of course, I_0 is simply measured as the intensity output of the optical cavity in the absence of an absorbing sample (*i.e.* sample cell filled with water). On the other hand, R_{eff} is estimated *via* a cavity calibration procedure where the intensity of light leaving M2 is measured for a series of dilutions from a dye mixture of known absorbance.[af] As the single-pass absorbance of each dye mixture dilution is known, the R_{eff} is estimated by minimising the least square error between the measured dye mixture intensities and equation 3.17 with respect to R_{eff}. This is shown in **Fig. 3.7 a** for a single wavelength where the data points (black circles) are the measured dye mixture dilutions and the solid lines are plots of equation 3.17 for a variety of different R_{eff} values. Performing this fitting procedure for every acquired wavelength point yields a cavity enhancement factor (CEF $= 1/(1-R_{eff})$, **Fig. 3.7 b**) spectrum which is thus used to calculate absorption spectra. The R_{eff} dependence in **Fig. 3.7 a** demonstrates the origin of the improved sensitivity of BBCEAS. Due to the non-linearity of equation 3.17, for

[af]This dye mixture consists of Acid Red 27 (Amaranth), Acid Green 25 and Acid Green 1 such that the absorption spectrum adequately covers the full 400 nm - 800 nm reflectivity range of the cavity mirrors.

weakly absorbing samples, a small change in their concentration (and thus transmission) corresponds to a large change in the experimental observable I_{out}/I_0. Therefore, BBCEAS is ideally suited for measuring small effects (such as MFEs) in weakly absorbing samples.

Following cavity calibration a typical BBCEAS experiment is run as follows. First, the probe laser measures the transmission through the optical cavity, and thus sample, in the absence of photoexcitation (*i.e.* ground state absorption). The pump laser is then turned on for some illumination period set by the user (typically 10 s) while the probe laser, and CCD, continually monitor the transmission through the cavity at a time-resolution determined by the CCD exposure time (usually 1 ms). During this illumination period, a magnetic field is symmetrically modulated on and off at a frequency of 5 Hz. The applied field strength and polarities are varied for each illumination cycle and randomly selected from a set of desired field values. After each illumination period samples are left to recover in the dark for a delay set by the user. The whole process is repeated for every desired field point and number of averages to yield a wavelength by time by magnetic field data array for every acquired average. The averages are then converted into absorption data and combined into a single averaged wavelength by time by magnetic field absorption array.

The formation and accumulation of photoinduced products is monitored by the change in absorption (ΔA) with ($A_{h\nu}$) and without (A_{GS}) photoexcitation

$$\Delta A = A_{h\nu} - A_{GS} \tag{3.20}$$

This produces a wavelength by time ΔA surface where positive signals correspond to the formation of photoproducts while negative signals reflect the depletion of ground state species, known as a ground state bleach (GSB). An example of such a ΔA surface can be found in **Fig. 3.8 b** which shows the formation of a long-lived radical species ($>$ 500 nm) in a 30 μM thale cress cryptochrome (*Arabidopsis thaliana*, *At*Cry1) sample. Taking slices of the ΔA surface at a constant time or wavelength yields ΔA spectra (**Fig. 3.8 a**) or kinetic traces (**Fig. 3.8 c**), respectively. From the former the absorption spectra of photoinduced

species is characterised while the latter characterises the accumulation dynamics under a given illumination condition.

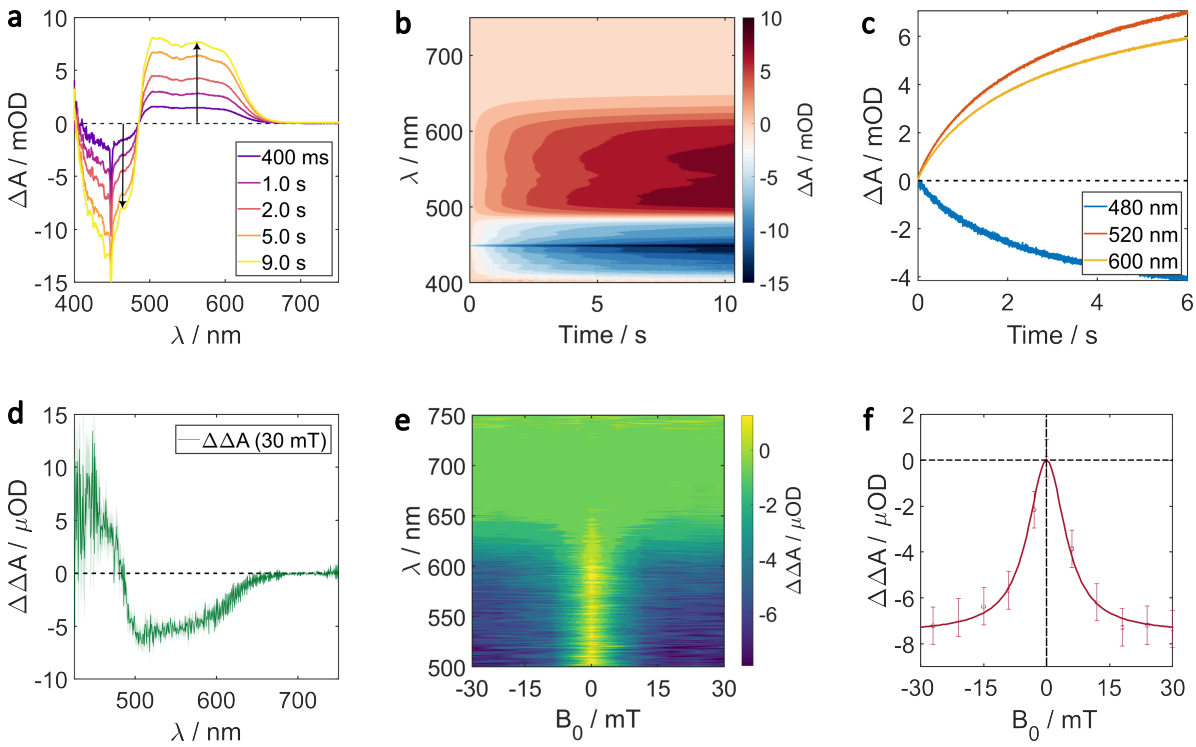

Figure 3.8: Example BBCEAS data from a 30 μM *At*Cry1 sample. a) ΔA spectra at several time points following the start of photoexcitation. The positive absorption band above 500 nm indicates the formation and accumulation of a long-lived radical species while the negative band below 500 nm indicates the depletion of FAD_{OX} (GSB). Each line represents a different time slice from the ΔA surface in (b). c) Kinetic traces indicating the accumulation dynamics of the long-lived radical species (520 nm and 600 nm) and depletion dynamics of FAD_{OX} (480 nm). Each trace is a single wavelength slice through the ΔA surface in (b). d) Time-averaged (over 10 s) $\Delta\Delta A$ spectrum at 30 mT characterising the MFEs on the formation of the long-lived radical species and GSB. The negative sign of the $\Delta\Delta A$ spectrum above 500 nm indicates a singlet-born SCRP. e) Time-averaged $\Delta\Delta A$ surface as a function of wavelength and time where a slice at constant field (30 mT) yields the $\Delta\Delta A$ spectrum in (d) and a slice at constant wavelength (530 nm) yields the MARY curve in (f). The width (HWHM) of the MARY curve in (f) indicates some spin-relaxation during the SCRP lifetime as the $B_{1/2}$ is greater than the Weller-predicted 3 mT.

The effect of applied magnetic fields on the formation and accumulation of photoproducts is characterised by calculating the change in the ΔA with (ΔA_B) and without ($\Delta A_{B=0}$) an applied field. This produces a MFE, $\Delta\Delta A$

$$\Delta\Delta A = \Delta A_B - \Delta A_{B=0} \tag{3.21}$$

surface which is typically time-averaged to improve signal-to-noise. The time-averaged wavelength by applied magnetic field *At*Cry1 $\Delta\Delta A$ surface is shown **Fig. 3.8 e**. Similarly

to the ΔA surface, the $\Delta\Delta A$ surface can be sliced at a constant wavelength or magnetic field to yield $\Delta\Delta A$ spectra (**Fig. 3.8 d**) or MARY curves (**Fig. 3.8 f**, *cf.* **Chapter 2**) which together characterise which species experience MFEs, the extent to which they do so and the presence of any spin-relaxation. In this instance, the negative $\Delta\Delta A$ spectrum at 30 mT indicates a MFE on the accumulation of the long-lived radical species ($>$ 500 nm) due to the formation of a singlet-born SCRP. This corresponds to a positive $\Delta\Delta A$ signal below 500 nm which indicates a positive MFE on the GSB, again suggesting the formation of a singlet-born SCRP. Furthermore, the MARY curve at 530 nm exhibits a $B_{1/2}$ greater than 3 mT, the Weller formula-estimated value for an FAD-W SCRP, thus indicating the presence of spin relaxation during the SCRP lifetime.

As can be seen from **Fig. 3.8 d**, the magnitudes of MFEs in cryptochrome proteins, under continuous illumination, are very small (μOD). As such, conventional single-pass absorption techniques generally lack the sensitivity required for detecting such small effects. This together with the low concentration, and thus absorption, of protein samples[ag] makes BBCEAS uniquely suited to studying their weak MFEs.

[ag] Low concentrations must be used since the proteins are difficult, time-consuming and expensive to make and tend to aggregate at high concentrations.

Chapter 4

Comparison of the Magnetic Field Effects From Wild Type Avian Cryptochromes

In **Chapter 2**, the plausibility of a cryptochrome based magnetoreceptor was demonstrated from a theoretical stand-point whereby MFEs on the products of photoinduced reactions arose from the spin dynamics of a coherent, photoinduced, radical pair between an FAD cofactor and a tryptophan residue, a process known as the radical pair mechanism (RPM). As discussed, such a magnetoreceptor agrees well with behavioural, biological and neurological studies carried out on European robins (*Erithacus rubecula*, *Er*), a member of the night-migratory passerines.[4,6,7,46–49] Furthermore, the discovery of cryptochrome proteins in the retina of night-migratory passerines added weight to this hypothesis.[10,49,50] However, for the avian cryptochrome protein (Cry4a) to be truly considered as a candidate magnetoreceptor, MFEs must be experimentally demonstrated, *in vitro* at the very least. Reassuringly, MFEs have been successfully detected in cryptochrome proteins from the plant thale cress (*Arabidopsis thaliana*, *At*Cry1)[87] and fruit fly (*Drosophila melanogaster*, *Dm*Cry),[76] in addition to the closely related DNA photolyase.[88] Now, thanks to the successful expression and purification of Cry4a proteins[1] from a number of avian species, the *in vitro* magnetic sensing capabilities of these systems can be experimentally examined. Of particular interest is whether cryptochromes from night-migratory passerines, known to have a magnetic sense (*i.e.* *Er*Cry4a), exhibit different field dependent behaviour than proteins from other avian species?

In the following, four species with varied migratory behaviour were chosen for study and comparison; the European robin, common quail, common pigeon and domestic chicken. Their scientific and sample names are defined in **Table 4.1**. Like the European robin, the common quail is a night-migratory bird known to migrate around Europe, northern Africa and the Levant.[89–92] In spite of this, the common quail is more closely related to the obviously non-migratory domestic chicken than it is to the European robin.[93–95] On the

other hand, the common pigeon, although non-migratory, is a renowned navigator and is believed to have some form of magnetic sense.[96,97]

Common Name	Scientific Name	Sample Name
European Robin	*Erithacus rubecula*	*Er*Cry4a
Common quail	*Coturnix coturnix*	*Cc*Cry4a
Common pigeon	*Columba livia*	*Cl*Cry4a
Domestic chicken	*Gallus gallus domesticus*	*Gg*Cry4a

Table 4.1: Naming convention for various avian cryptochrome samples.

4.1 Methods

BBCEAS was used to study the proteins discussed above where samples were continuously photoexcited by a 450 nm diode laser at *ca.* 3.8 kW m^{-2} (3 mW with a $\approx$ 1 mm beam spot) over a period of 10 s. Simultaneously, the optical cavity, and thus sample, was probed by a super continuum source while a symmetrically modulated (200 ms on-off period) magnetic field was applied. The light transmitted through the cavity was detected by a CCD camera with an exposure time, and thus time resolution, of 1 ms. The single-pass sample absorbance was calculated using equation 3.19, from which changes in absorption and thus MFEs ($\Delta\Delta A$s) could be determined. See **Chapter 3** for the full BBCEAS experimental details and protocol.

Cryptochrome samples of each of the four proteins, expressed by collaborators at the University of Oldenburg, were prepared to a concentration of *ca.* 30 μM (0.3 OD @ 450 nm) in pH 8 tris buffer (20 mM Tris, 250 mM NaCl and 20% glycerol (V/V)). In addition, 5 mM potassium ferricyanide ($K_3[Fe(III)(CN_6)]$) was added to the samples to aid in sample reoxidation following photoexcitation.[76] The samples were kept at 278 K throughout the experiments and left to reoxidise, in the dark, for 20 min after each 10 s illumination cycle.

4.2 Results and Discussion

Due to competing photochemistry from potassium ferricyanide (FC) little information can be garnered from analysis of the ΔA spectra, however, for completeness the ΔA spectra are included in **Appendix A.1**. The FC photochemistry and role in the RPM is addressed in

the **Chapter 5**. Regardless, since FC photochemistry exhibits no magnetic field sensitivity (**Appendix A.2**), MFEs may still be determined for each of the four proteins. These results are summarised in **Fig. 4.1**.

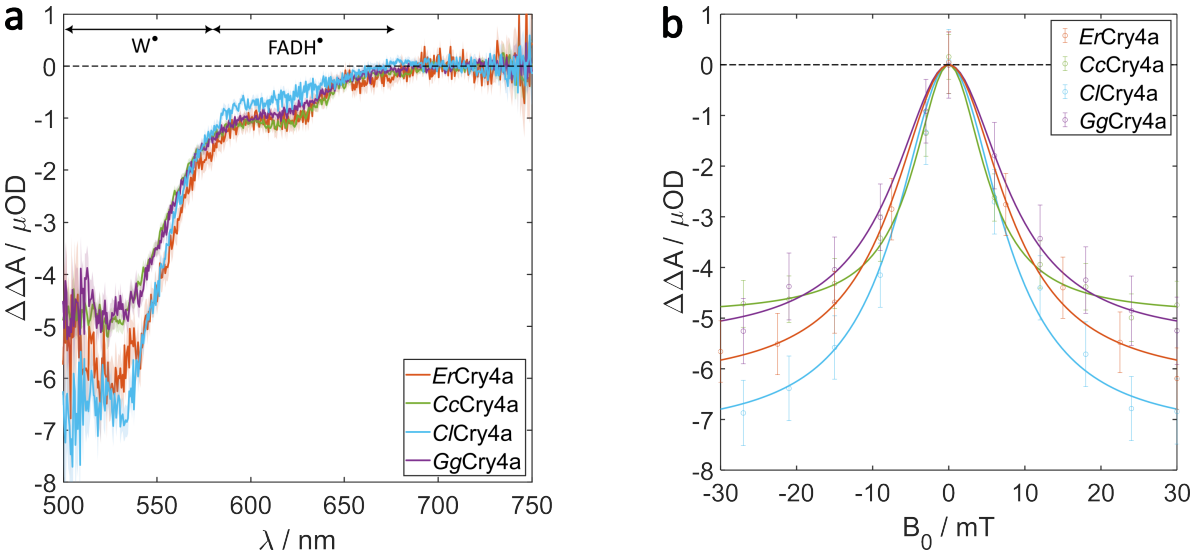

Figure 4.1: a) 30 mT time averaged $\Delta\Delta A$ spectra for *Er*Cry4a, *Cc*Cry4a, *Cl*Cry4a and *Gg*Cry4a. Each spectrum consists of a major peak at *ca.* 520 nm, attributed predominantly to a $W^{\bullet}$ MFE, with a smaller shoulder from *ca.* 580 nm - 700 nm, attributed to $FADH^{\bullet}$. $W^{\bullet}$ and $FADH^{\bullet}$ regions indicated at the top of the spectra. b) Time averaged MARY curves for the four proteins in (a). Curves are wavelength averaged between 500 nm and 530 nm. Experimental data indicated by errorbars while the solid lines are Lorentzian fits to the experimental data using equation 4.2. Fit results are summarised in **Table 4.2**. Generally, all four species exhibit similar magnetic sensitivity.

The time averaged $\Delta\Delta A$ (*cf.* equation 3.21) spectra, at 30 mT, of all four proteins (**Fig. 4.1 a**) are strikingly similar in both spectral shape and magnitude. In each case, the spectrum is characterised by a large negative $\Delta\Delta A$, peaking at *ca.* 520 nm, which is accompanied by a much smaller shoulder between 580 nm and 700 nm. Upon comparison with the individual species spectra in **Fig. 2.9 b**, the former is assigned, predominantly, to a MFE on the accumulation of $W^{\bullet}$ while the latter is assigned to a MFE on the formation of $FADH^{\bullet}$.

This assignment was confirmed by spectral deconvolution of the $\Delta\Delta A$ spectra. Given the $\Delta\Delta A$ spectrum is a linear combination of MFEs arising from, N, different species defined by

$$\Delta\Delta A(\lambda) = \sum_{i=1}^{N} c_i S_i(\lambda) = \mathbf{c} \cdot \mathbf{S}(\lambda) \tag{4.1}$$

where $S_i(\lambda)$ is an individual species absorption spectrum and c_i is a scaling coefficient which determines the sign of $S_i(\lambda)$ (positive or negative MFE) and how much it contributes to the $\Delta\Delta A$ spectrum. The contribution from each species can be determined by minimising the least-square error between the experimental data and $\mathbf{c}\cdot\mathbf{S}(\lambda)$ with respect to $\mathbf{c}$. The results of this analysis for *Er*Cry4a are displayed in **Fig. 4.2** where the $\Delta\Delta A$ spectrum is shown to consist of a large negative $W^{\bullet}$ MFE with a smaller negative $FADH^{\bullet}$ and positive FAD_{OX} MFE, validating the assignment above. On account of the BBCEAS time scale, only the FAD_{OX}, $FAD^{\bullet-}$, $FADH^{\bullet}$ and $W^{\bullet}$ spectra were included in $S(\lambda)$. Similar analysis of *Cc*Cry4a, *Cl*Cry4a and *Gg*Cry4a yielded essentially the same results and can be found in **Appendix A.3**.

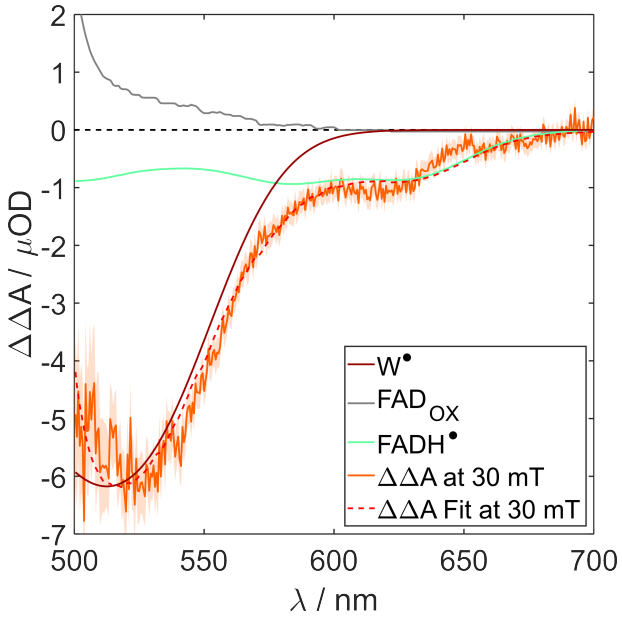

Figure 4.2: *Er*Cry4a spectral fitting results, estimated by minimising the least-square error between the experimental data and equation 4.1. $\Delta\Delta A$ spectrum consists of large negative $W^{\bullet}$ MFE with smaller contributions from $FADH^{\bullet}$ and FAD_{OX}. $FAD^{\bullet-}$ contribution was found to be zero.

It is known that the application of magnetic fields stronger than the RPs' effective HFC (*ca.* 1 mT) will impede singlet-triplet interconversion (*cf.* **Chapter 2**). Therefore, if a SCRP is formed in the singlet state, this will increase the amount of singlet recombination, leading to a reduction in the concentration of the SCRP and any following photoproducts (*i.e.* $W^{\bullet}$ and $FADH^{\bullet}$). Consequently, the negative sign of the $\Delta\Delta A$ spectra in **Fig. 4.1 a** is indicative of a singlet-born SCRP, as expected for a cryptochrome FAD-W RP (*cf.* **Fig. 2.9**).

The field dependences of the MFEs are characterised by the time averaged MARY plots in **Fig. 4.1 b** where the $\Delta\Delta A$ at each field point has been wavelength averaged from 500

nm - 530 nm. All four of the proteins' MFEs exhibit a Lorentzian-like field dependence, indicating HFC driven spin mixing (*cf.* **Chapter 2**). To better characterise the MARY plots, each curve was fit with the following Lorentzian function

$$\mathscr{L}(B_0|MFE_{Sat},B_{1/2}) = MFE_{Sat}\frac{B_{1/2}^2}{B_0^2+B_{1/2}^2} - MFE_{Sat} \tag{4.2}$$

where B_0 is the applied external magnetic field, MFE_{Sat} is the $\Delta\Delta A$ when $B_0 \to \infty$ and $B_{1/2}$ is the half width at half maximum. The fit results are shown in **Table 4.2**.

Sample Name	MFE_{Sat} / μOD	$B_{1/2}$ / mT
*Er*Cry4a	−6.32 ± 0.07	8.71 ± 0.26
*Cc*Cry4a	−4.94 ± 0.04	5.62 ± 0.16
*Cl*Cry4a	−7.31 ± 0.09	8.23 ± 0.24
*Gg*Cry4a	−5.48 ± 0.07	8.68 ± 0.24

Table 4.2: Results from fitting equation 4.2 to the field dependent $\Delta\Delta A$ data in **Fig. 4.1** with respect to MFE_{Sat} and $B_{1/2}$. MFE_{Sat} is the $\Delta\Delta A$ when $B_0 \to \infty$ and $B_{1/2}$ is the half width at half maximum. Errors were estimated using the inverse Hessian method.

Recalling that the $B_{1/2}$ for an FAD-W RP is predicted to be *ca.* 3 mT and that the $B_{1/2}$ is related to HFC interactions (equation 2.52) and relaxation processes within the SCRP, it is clear from **Table 4.2** that all four of the proteins experience significant spin relaxation during the SCRP lifetime. This could arise from singlet-triplet dephasing or the interaction of the solvent exposed terminal tryptophan, W_D (W369, *cf.* **Fig. 2.8**), with the solvent, causing T_1 and T_2 type relaxation. Additionally, the presence of paramagnetic FC could perturb the spin dynamics, causing broadening of the MARY curves. This will be explored in more detail in **Chapter 5**.

With the exception of *Cc*Cry4a, the $B_{1/2}$ values in **Table 4.2** are near identical and well within batch-to-batch sample variations. This implies the SCRP HFC interactions and local environment are markedly similar in these systems. The similarity in the $\Delta\Delta A$ spectra (**Fig. 4.1 a**) supports this observation with the $\text{W}^\bullet$ and $\text{FADH}^\bullet$ negative MFEs indicating a singlet-born $\text{FAD}^{\bullet-}$-$\text{WH}^{\bullet+}$ SCRP in all cases (since $\text{W}^\bullet$ and $\text{FADH}^\bullet$ are formed *via* (de)protonation processes from $\text{FAD}^{\bullet-}$ and $\text{WH}^{\bullet+}$). Furthermore, the similarity in the MFE magnitudes

conveys a similarity in the photocycle rate processes and thus RP environment.[ah] Although these observations contradict recent results by Xu *et al.*[1] they agree well with a molecular dynamics study by Hanić *et al.* where the intramolecular interaction energies from several avian cryptochromes (including *Er*Cry4a, *Cl*Cry4a and *Gg*Cry4a) were found to be broadly similar.[98]

The cause of the reduced $B_{1/2}$ in *Cc*Cry4a has no immediately obvious rationale. Naturally it either indicates a shift in HFC interactions and or spin relaxation. As mentioned above, the contributing species to the $\Delta\Delta A$ spectrum indicate an $FAD^{\bullet-}$-$WH^{\bullet+}$ SCRP and thus equivalent HFC interactions for all four proteins. Therefore, the change in $B_{1/2}$ likely comes from a change in spin relaxation, without greatly influencing the MFE magnitude. However, given the similarities in the structures and interactions of the Cry4a proteins studied by Hanić *et al.*[98] it is reasonable to expect these similarities to carry through to *Cc*Cry4a and thus the SCRP environment and spin relaxation. One possible explanation is that variations in the amino acid sequence, while not greatly influencing the protein structure, effect protein-solvent or protein-FC interactions around the terminal tryptophan, leading to a change in spin relaxation.[ai] However, in contradiction to this line of thought, the amino acid sequences of the quail and chicken cryptochromes are remarkably similar (97.2 %), especially around the terminal tryptophan (*cf.* **Appendix A.1**). Either way, the cause of *Cc*Cry4a $B_{1/2}$ remains ambiguous with additional experiments (such as electron paramagnetic resonance and transient absorption spectroscopy) required before any meaningful conclusions can be drawn.

4.3 Conclusion

From the results presented here, it is clear that avian Cry4a proteins *in vitro* can sense weak applied magnetic fields, albeit much larger than the Earth's magnetic field (≈ 50 μT). Interestingly, the MFEs produced by the four cryptochromes were strikingly similar, regardless of the migratory behaviour of the species from which they came. Considering

[ah] MFE magnitudes are arguably within bath-to-batch variations.

[ai] In fact, following a shift to molecular oxygen as a sample reoxidant (see **Chapter 5**), the *Gg*Cry4a and *Cc*Cry4a $B_{1/2}$ values became comparable, suggesting that interaction with FC was causing the initial discrepancy.

the MFEs observed in *Dm*Cry, *At*Cry1 and DNA photolyase,[76,87,88] it seems probable that any flavoprotein with a tryptophan chain in close spatial proximity to the flavin cofactor can form SCRPs and generate MFEs. This suggests that night-migratory passerines such as the European robin have not evolutionarily optimised the Cry4a protein in development of their magnetic sensing capabilities, hinting at evolutionary optimisation elsewhere in the sensing process. For example, night-migratory passerines may have optimised the signal transduction and amplification process. Thus, while all of these species have proteins that exhibit a magnetic response, perhaps they cannot all process that information. Alternatively, it could be that all of these species can sense magnetic fields. For example, the quail is a night-migratory bird and some (contested) behavioural experiments by Wiltschko *et al.*[99] have suggested pigeons do have a magnetic compass sense. However, given the ubiquity of cryptochromes throughout the biosphere[51] and relative rarity of a known magnetic sense, it seems more likely that a species' ability to convert cryptochrome MFEs into a neurological signal defines its magnetic sensing capabilities. Nevertheless, these results clearly demonstrate that cryptochromes from migratory birds do develop MFEs adding legitimacy to the cryptochrome RPM hypothesis of avian magnetoreception.

Chapter 5

Ferricyanide Photochemistry and Its Influence on The Radical Pair Mechanism in Cryptochromes

In the study of redox proteins it is common practice to add some form of oxidative or reductive agent as a tractable redox partner or to aid in sample recovery.[76,88,100,101] This is no less true than in the study of cryptochromes where potassium ferricyanide (FC), $K_3[Fe(III)(CN)_6]$, has been used to reoxidise the long-lived $FADH^\bullet$ that forms following photoexciation.[1,76,87,102–104]

Ferricyanide is a paramagnetic low-spin d^5 complex with octahedral symmetry (O_h).[aj,107–110] Importantly, FC readily acts as an electron acceptor, forming the low-spin diamagnetic $[Fe(II)(CN)_6]^{4-}$ octahedral complex, ferrocyanide.[105,109] It is based on this property that FC has found use as a reoxidant in the study of redox processes.

In the study of cryptochromes, FC was chosen for a variety of reasons. Firstly, the redox potentials of FC (*ca.* 0.4 V)[111] and $FADH^\bullet$ (*ca.* -0.3 V)[112] match suitably. Secondly, FC is chemically stable due to the strong Fe-CN bond and, finally, for FC's low extinction coefficient at 450 nm ($\epsilon \approx 250$ M^{-1} cm^{-1}). It was thus judged that FC would only play a spectator role in the RPM and influence the recovery of long-lived radicals while exhibiting little or no photochemistry itself.

Despite this, FC was found to exhibit significant photochemistry, especially under the continuous illumination conditions utilised by techniques such as BBCEAS. Remarkably, this process, or at least the extent of its occurrence, has gone unnoticed for over a decade of studying MFEs in photolyase and cryptochromes. It was only discovered when the group shifted to a static oxygen environment to reoxidise the system following concerns about the biological relevance of FC. In the case of BBCEAS, which is inherently more sensitive

[aj] In some literature[105] the unevenly populated t_{2g} orbitals is thought to induce a minor Jahn-Teller distortion leading to D_{4h} or D_{3d}[106] symmetry. Nonetheless, an octahedral symmetry is assumed in following analysis.

to minor photoproducts which accumulate slowly, this may have led to the erroneous assignment of FC spectral features to cryptochrome photoproducts.

The influence FC has on the photoinduced absorption spectra (ΔA) obtained by BBCEAS can be seen in **Fig. 5.1** which shows the evolution of the ΔA spectra from a 30 μM *Er*Cry4a wild type (WT, natural unmutated protein) sample in pH 8 tris buffer (10 mM tris, 250 mM NaCl in 20 % glycerol/water V/V) with (**Fig. 5.1 b**) and without (**Fig. 5.1 a**) the addition of 5 mM FC. In both cases, experiments were run at 278 K and photoexcited at 450 nm with 3 mW (*ca.* 3.82 kW m^2) of power.

For the sample without FC, the absorption band above 500 nm reflects the formation and accumulation of, primarily, $FADH^{\bullet}$ while the negative signal between 420 nm and 500 nm indicates the ground state bleach of FAD_{OX}. The positive absorption band below 420 nm is believed to be $FAD^{\bullet-}$ however the spectrum is distorted in this region due to the low probe intensity at this wavelength.

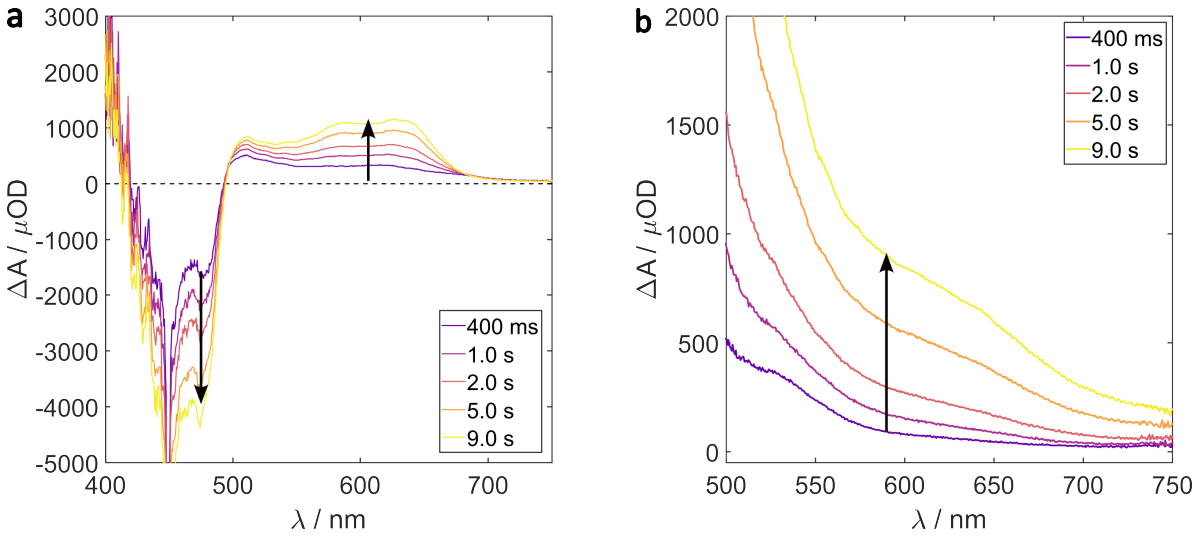

Figure 5.1: BBCEAS ΔA spectra from 30 μM *Er*Cry4a WT without (a) and with (b) 5 mM potassium ferricyanide. Both experiments were run in pH 8 tris buffer (10 mM tris, 250 mM NaCl in 20 % glycerol/water V/V) at 278 K and photoexcited at 450 nm with 3 mW of power.

On the other hand, the sample with 5 mM FC has a markedly different spectral shape at every time point with the ΔA spectra now dominated by a large photoinduced absorption (PIA) which peaks at some wavelength below 500 nm. Unfortunately this peak cannot be resolved due to a combination of high FC absorption, relative to protein, (due to the high FC concentration) and low probe laser intensity below 500 nm. Nonetheless, it is evident

that the addition of FC has changed the accumulation behaviour of the sample due to the loss of the large $FADH^{\bullet}$ signal (*cf.* **Fig. 5.1 a**). This suppression of $FADH^{\bullet}$ accumulation is logical since the intended role of FC is to reoxidise this species. However, the new large dominant peak is more mysterious and had previously been assigned to $FAD^{\bullet-}$.

Naturally, upon discovery of this shift in the data, a solution of 5 mM FC (without cryptochrome) was measured under the same experimental conditions. The results are shown below in **Fig. 5.2**. Upon comparison with **Fig. 5.1 b** it is clear that most of the signal in **Fig. 5.1 b** comes from a FC PIA with a relatively minimal cryptochrome contribution (*vs.* **Fig. 5.2**) characterised by the enhanced absorption above 550 nm and the slight shoulder at 530 nm at early times (*e.g.* 400 ms). It thus appears that FC reacts to form and accumulate small amounts of some photoproduct, difficult to detect with conventional pump-probe spectroscopy, upon illumination at 450 nm despite its weak absorption and high chemical stability.

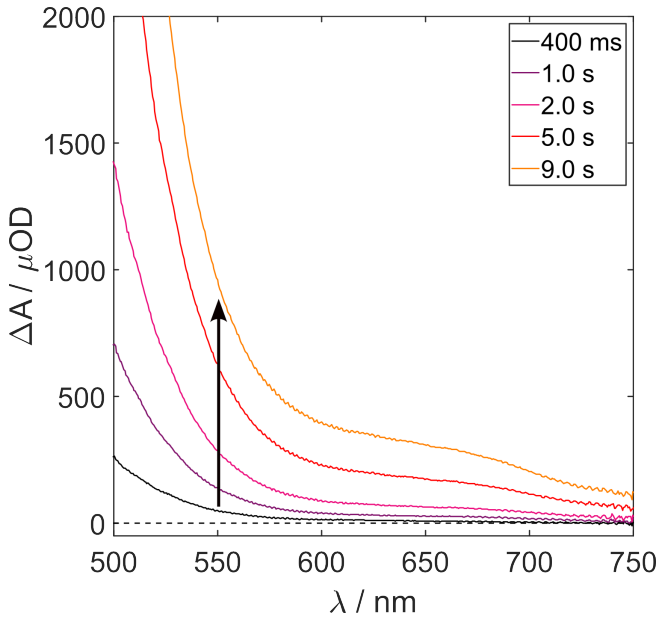

Figure 5.2: BBCEAS photoinduced absorption spectra from 5 mM FC in pH 8 tris buffer (10 mM tris, 250 mM NaCl in 20 % glycerol/water V/V). Sample was run at 278 K with 3 mW of 450 nm excitation.

In light of these results we sought to understand a couple of open questions. Namely, what is the FC photoproduct and how is it formed? And, how, if at all, does this influence the spin dynamics and development of MFEs in cryptochromes? This chapter presents our attempts to answer these questions.

5.1 Potassium Ferricyanide Photochemistry

Despite its use in the study of cryptochrome and photolyase MFEs, FC is known to undergo a degree of photochemistry when excited at or below 420 nm, albeit largely on the ps time scale. Specifically, photoexcitation of FC leads to ligand-to-metal charge transfer (LMCT, $^2T_{2g} \rightarrow {}^2T_{1u}$) followed by rapid (*ca.* ≤ 0.5 ps) recombination.[105,109,110] However, when dissolved in water, a small (< 2 %) proportion of the excited state undergoes ligand dissociation and loss of a cyano radical ($CN^\bullet$) followed by aquation to form the stable $[Fe(II)(CN)_5OH_2]^{3-}$ photoproduct.[107,109,110]

Due to its low yield and the use of 450 nm excitation when studying flavoproteins, the formation of $[Fe(II)(CN)_5OH_2]^{3-}$ should have little impact on pulsed experiments (*i.e.* CRDS and TA spectroscopy) where the PIA from the protein is significantly higher. This appears to be the case as FC PIA has never been reported when used in flavoprotein studies by these techniques.[1,76,87,102–104] However, due to the continuous illumination and high sensitivity of BBCEAS, the formation of stable photodegradation products, even in low yield, will accumulate significantly, becoming the major signal over transient species. This certainly seems to be the case as indicated in **Fig. 5.1**

The majority of photochemistry studies on FC (and ferrocyanide) have employed ultra-fast (fs - ps) pump-probe techniques due to the time scale of the known processes involved. As such, little is known about FC under long, continuous, photoexcitation conditions. Furthermore, the majority of FC photochemistry studies have focused on its degradation when dissolved in water rather than the conditions employed in the study of cryptochromes (*i.e.* pH 8 tris buffer). Therefore, to identify the process observed in BBCEAS when FC is used, and whether the photoproduct forming was indeed $[Fe(II)(CN)_5OH_2]^{3-}$ or something else more specific to our experimental conditions, a series of continuous irradiation experiments was carried out in conjunction with density functional theory (DFT) calculations. The experimental results presented here were done in collaboration with Dr. Patricia Rodriquez-Maciá.

5.1.1 Methods

Irradiation experiments involve a sample being continuously illuminated with a light emitting diode (LED) and probed spectrally over a long time period (seconds-hrs). In this instance, a 450 nm LED was used to match the excitation employed when studying cryptochromes. The system was then probed in the visible (UV/Vis, Agilent Cary 60) or infrared (IR, Bruker Vertex 80v) spectral regions. The former monitors the formation of degradation products while the latter monitors the oxidation state of those photoproducts. The experimental set-up is summarised in the schematic shown in **Fig. 5.3**. In all cases, 5 mM FC (Sigma Aldrich) was used and the samples were illuminated with approximately 20 mW of light. It should be noted that due to the different spatial restrictions for attaching the LED between the two spectrometers, the precise irradiance differed slightly between the UV/Vis and IR experiments. In general the UV/Vis spectrometer allowed for more even illumination. Additionally, the pathlengths for light passing through the samples differ significantly between the spectrometers with a 1 cm pathlength used in the UV/Vis experiments and a 50 μm pathlength used in the IR experiments (due to the fact it is an interferometer).

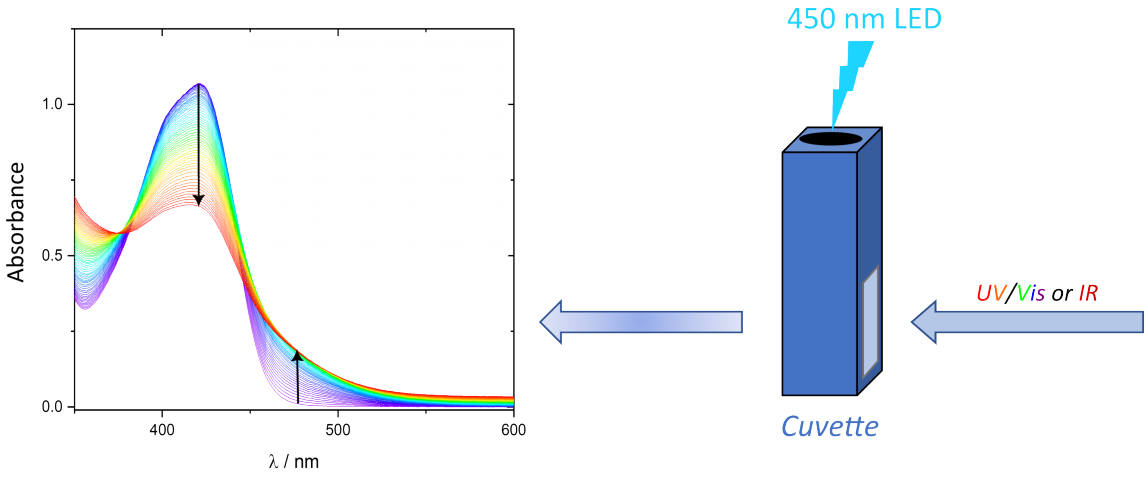

Figure 5.3: Schematic of the irradiation experiments where a 450 nm LED is used to continuously illuminate a sample which is simultaneously probed by UV/Vis or IR light to monitor changes in the sample's absorbance. For all experiments, approximately 20 mW of light was used to illuminate the sample. The example spectra on the left is taken from a UV/Vis irradiation experiment of 5 mM potassium ferricyanide dissolved in tris buffer (10 mM tris, 250 mM NaCl in 20 % glycerol/water V/V). The arrows indicate change in absorption as a function of irradiation time.

DFT calculations were done following a similar procedure to that employed by Ross *et al.*[113] Namely, the PBE0 exchange-correlation functional was employed in conjunction with the 6-311G** basis set for all non-metal atoms. The Stuttgart/Dresden electron core potential basis set was used for the Fe atom. The solvent was accounted for by a simple polarisation continuum model (SMD), with water used in each case. All calculations were run in Gaussian16 on the University of Oxford's ARC high-performance computing clusters.

5.1.2 Results

Before carrying out any irradiation experiments the ground state UV/Vis and IR absorption of FC and ferrocyanide were measured. The results are shown in **Fig. 5.4 a** and **b** respectively.

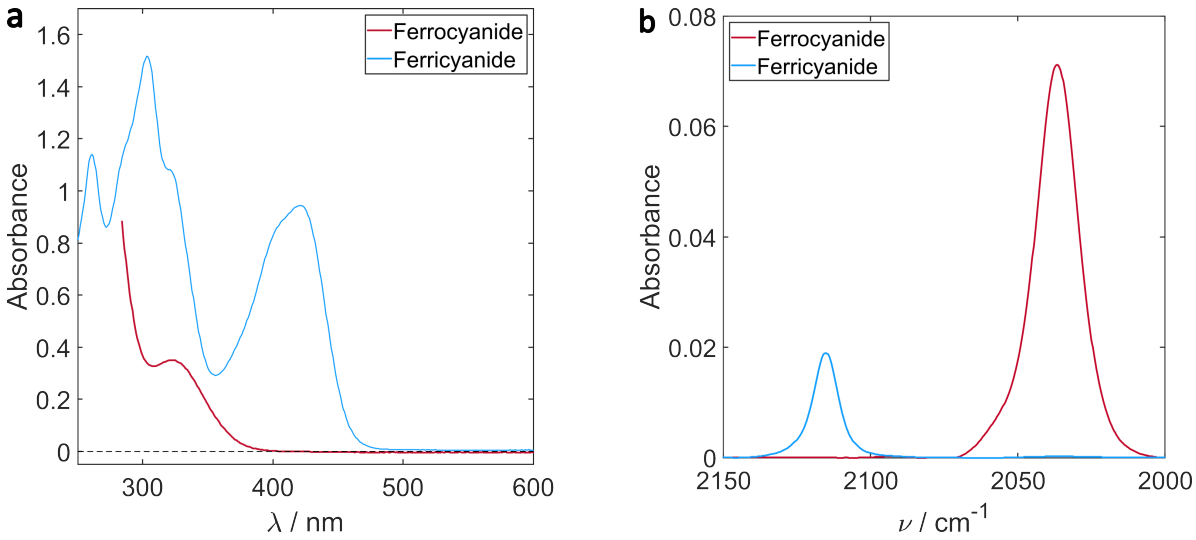

Figure 5.4: UV/Vis (a) and IR (b) reference spectra of 5 mM potassium ferricyanide and 5 mM potassium ferrocyanide .

The absorption band peaking at 420 nm in the FC UV/Vis spectrum in **Fig. 5.4 a** arises due to the LMCT mentioned above. For ferrocyanide, the absorption band peaking at 340 nm reflects an $^1A_{1g} \longrightarrow {}^1T_{1g}$ transition.[108,114,115] In both cases, the absorption peak in their IR spectra arises from the T_{1u} CN stretch.[105,107–110,114] The red shift in the ferrocyanide CN stretch (*vs.* FC) reflects the longer equilibrium Fe-CN bond length in ferrocyanide.[116]

Ferricyanide in Water

In an effort to extend the wealth of ultra-fast studies to slow continuous conditions, initial irradiation experiments were run in deionised water. The point being, assuming

$[Fe(II)(CN)_5OH_2]^{3-}$ is formed, what does this process look like under these different conditions and does the photodegradation stop there?

The UV/Vis results of a long-term irradiation experiment are shown in **Fig. 5.5**. Over an illumination period of 16 hrs (**Fig. 5.5 a**), it appears that the system exhibits A⟶B⟶C type behaviour with some photoproduct, likely $[Fe(II)(CN)_5OH_2]^{3-}$, initially forming within the first hour (**Fig. 5.5 b**) before decaying into something else.

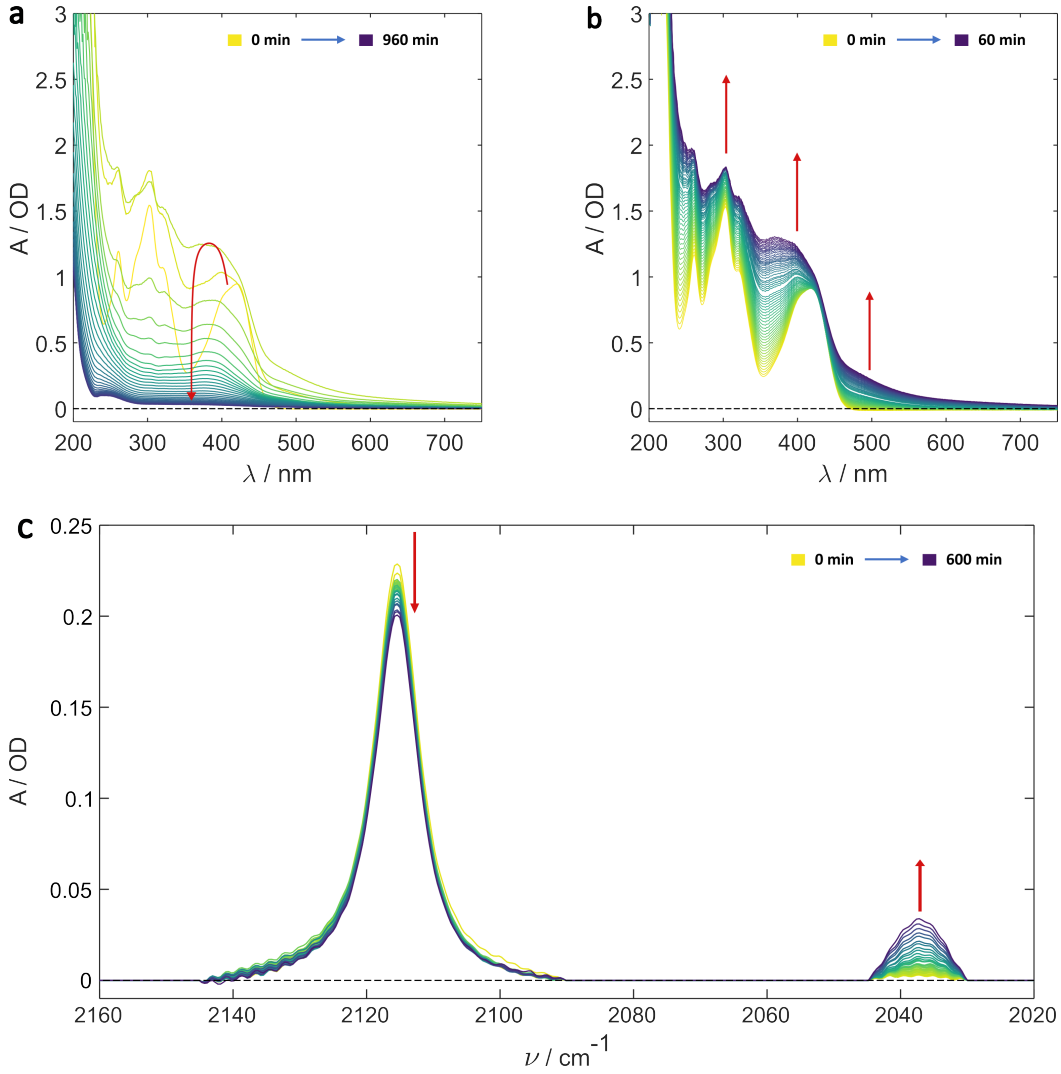

Figure 5.5: Potassium ferricyanide spectra in water. a) UV/Vis irradiation over a 16 hr period with a spectrum taken every 30 min. The dynamics of the spectral profile appears to be A⟶B⟶C. b) UV/Vis irradiation over the first hr with a spectrum taken every minute. c) IR detected irradiation over a 10 hr period with a spectrum taken every 15 min. Clear formation of Fe(II) from Fe(III), however, Fe(II) accumulation is minimal. In all figures, arrows indicate direction of intensity change (*i.e.* growth or decays).

Reduction of the metal centre is confirmed by the IR detected irradiation experiment, the results of which are shown in **Fig. 5.5 c**. The appearance and growth of the peak centred at 2037 cm^{-1} clearly indicates the formation of Fe(II). However, as indicated by the relative

peak amplitudes of ferricyande and ferrocyanide in **Fig. 5.4 b**, the Fe(II) CN stretch has a much higher extinction coefficient and yet, little of this oxidation state accumulates. This could arise from the A⟶B⟶C behaviour observed in **Fig. 5.5 a** and **b**, where B is $[Fe(II)(CN)_5OH_2]^{3-}$ and gives rise to the IR band at 2037 cm^{-1}. If $[Fe(II)(CN)_5OH_2]^{3-}$ decays *via* loss of CN^- ligands, then the amplitude of the Fe(II) CN stretch peak will also decay, leading to a suppression in the growth of this peak under these conditions.

Although undetected in the results shown in **Fig. 5.5**, another degradation mechanism to consider is the formation of Prussian blue ($Fe(III)_4[Fe(II)(CN)_6]_3 \cdot \times H_2O$) which is known to occur in aqueous mixtures of FC and ferrocyanide. It follows that, if a photoaquated Fe(II) ferrous cyano complex is forming, Prussian blue will eventually form. This is a known problem when doing photochemistry on FC[110] since the insoluble Prussian blue causes scattering of measurement lasers.

In any case, it is abundantly clear that substantial FC photochemistry occurs over these prolonged time scales and under these illumination conditions. The process was confirmed to be photoinduced following "irradiation" experiments without photoexcitation which showed no change in the UV/Vis or IR spectral signatures over a period of 10 hrs.

Ferricyanide in Tris Buffer

Moving on to conditions more reflective of cryptochrome MFE experiments, **Fig. 5.6** shows the irradiation results of FC in pH 8 tris buffer in 20 % glycerol (V/V). The UV/Vis irradiation data in **Fig. 5.6 a** clearly show the formation of some photoproduct with what appears to be A⟶B behaviour. The spectral shape change in **Fig. 5.6 a** is clearly different from that formed in the sample in water (*cf.* **Fig. 5.5 a** and **b**) thus indicating the formation of a different photoproduct.

Similarly to the sample without tris, photoproduct formation is accompanied by reduction of the metal centre from Fe(III) to Fe(II). As indicated by the growth of the IR band centred at 2037 cm^{-1}. However, unlike the aqueous case, this new peak is significantly larger (*cf.* **Fig. 5.5 c**). This could be due to the A⟶B behaviour observed in the UV/Vis irradiation

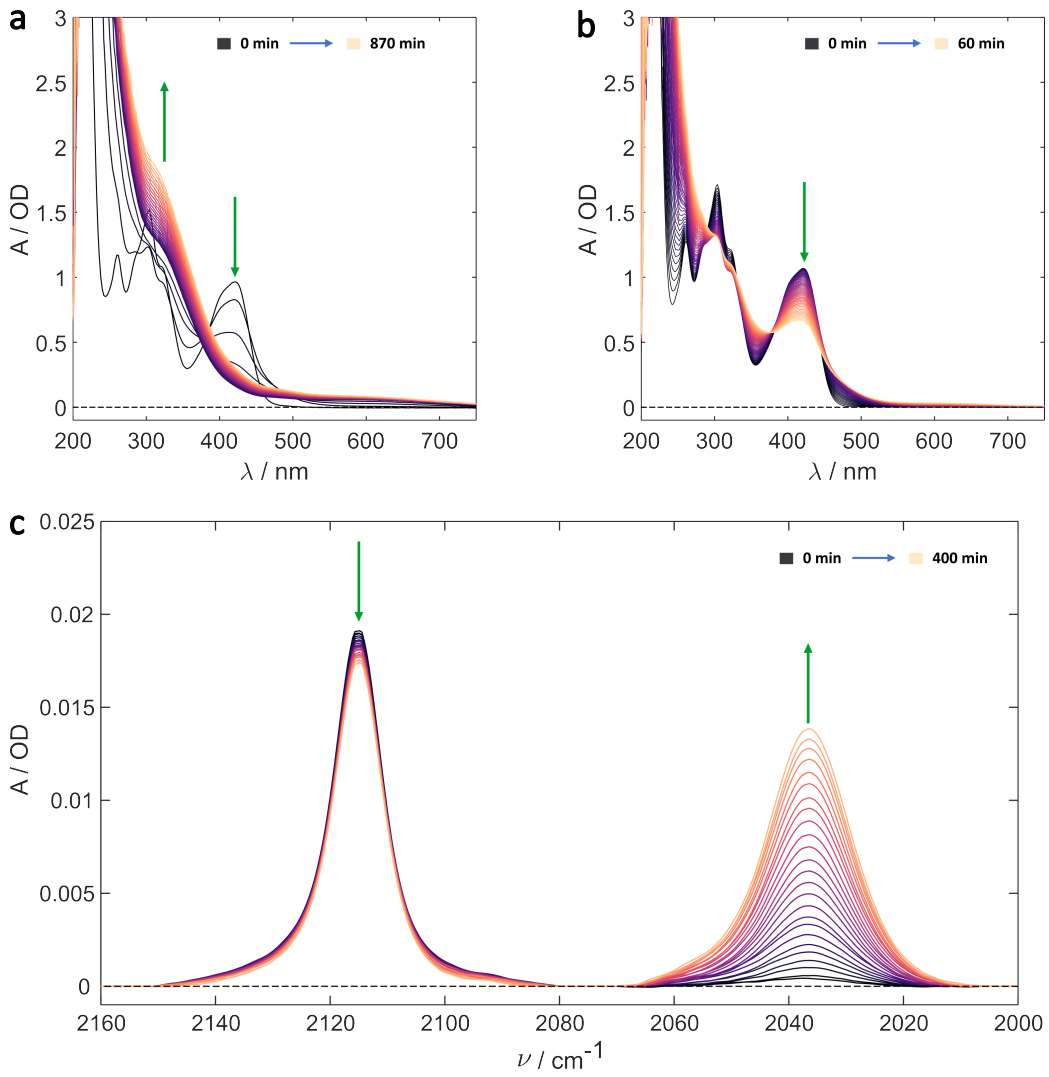

Figure 5.6: Results of irradiation experiments on potassium ferricyanide in tris buffer. a) UV/Vis irradiation over a 14.5 hr period with a spectrum taken every 30 min. The dynamics of the spectral profile appears to be A⟶B. b) UV/Vis irradiation over the first hr with a spectrum taken every minute. c) IR detected irradiation over a 7 hr period with a spectrum taken every 15 min. Clear formation of Fe(II) from Fe(III). In all figures, arrows indicate direction of intensity shift (*i.e.* growth or decays).

where the photodegradation product is formed, reducing the metal centre, without further degradation and loss of cyano groups leading to a weaker CN stretch absorption band.

Control experiments without LED illumination showed no change in the UV/Vis or IR spectral signatures over a period of 10 hrs, thus confirming the process observed in **Fig. 5.6** is photoinduced. Evidently, the photochemistry is rather different in 20 % glycerol (V/V) tris buffer than in pure water. In both cases, photoexcitation leads to reduction of the metal centre, presumably from LMCT, followed by ligand dissociation. However, where aquation occurs in water, an alternative ligand seems to bind in tris buffer. Given the buffer composition, the two candidate ligands are glycerol and tris, both of which could bind *via*

hydroxy groups (and/or an amine group in tris). Their structures are shown **Appendix A.2**.

Ferricyanide in 20 % Glycerol (V/V)

To determine whether tris was solely responsible for the change in photoproduct, experiments were done on FC in 20 % glycerol (V/V). The results are shown in **Fig. 5.7**. Once again, the process was confirmed to be photoinduced following "irradiation" experiments without photoexcitation which showed no change in the UV/Vis or IR spectral signatures over a period of 10 hrs.

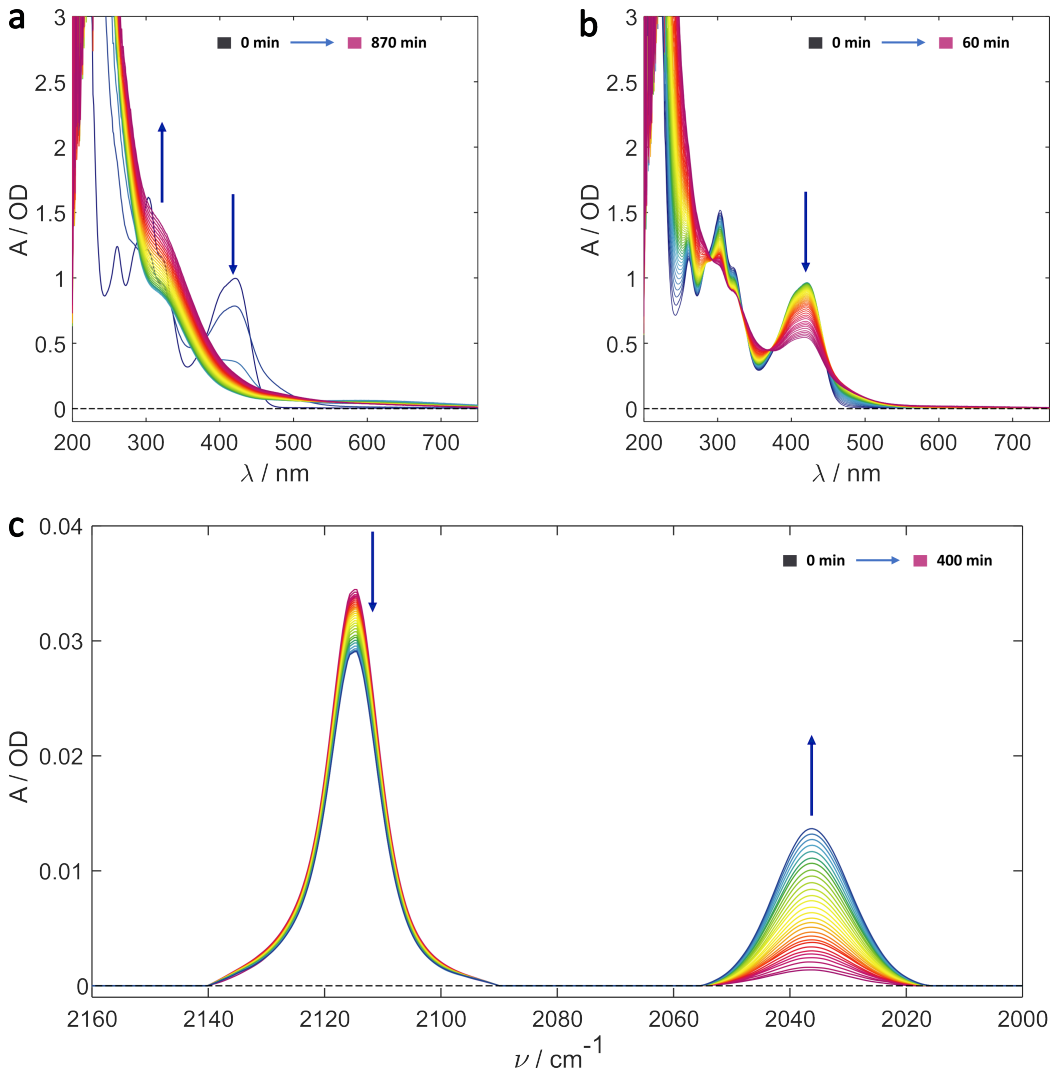

Figure 5.7: Potassium ferricyanide in 20 % glycerol/water (V/V) irradiation experiment results. a) UV/Vis irradiation over a 14.5 hr period with a spectrum taken every 30 min. The dynamics of the spectral profile appears to be A⟶B. b) UV/Vis irradiation over the first hr with a spectrum taken every minute. c) IR detected irradiation over a 7 hr period with a spectrum taken every 15 min. Clear formation of Fe(II) from Fe(III). In all figures, arrows indicate direction of intensity shift (*i.e.* growth or decays).

Both the UV/Vis and IR irradiation data are nearly identical to the sample in tris buffer, with glycerol, above (*cf.* **Fig. 5.6**). That is, irradiation seems to induce photodegradation into a stable product which persists and accumulates in the UV/Vis spectra. This photoproduct forms following photoinduced LMCT and ligand dissociation as indicated by the IR peak at 2037 cm^{-1}. Thus it appears the same photoproduct is forming here, even in the absence of tris, and therefore likely arises from the binding of a glycerol molecule.

5.1.3 Discussion

Evidently, photodegradation of FC occurs in all systems measured. However, it is clear that a different degradation process occurs in the presence of glycerol *vs* pure water. This shift is likely due to preferential binding of glycerol over water with DFT calculations confirming that the IR stretch observed at 2037 cm^{-1} could come from any of the potential degradation products discussed above (*cf.* **Appendix A.2**). The preferential glycerol binding can be understood by comparing DFT calculations of the photoaquated product and glycerol-bound product(s) .

The electronic energies of a variety of potential degradation products are shown in **Fig. 5.8 a**. As can be seen, the singly bound glycerol products ($[Fe(CN)_5(C_3H_8O_3)]^{3-}$) are much more stable than the photoaquated product. Thus, in the presence of a high glycerol concentration, assuming the barrier for binding is not significantly higher, glycerol is expected to bind over water, following cyano radical dissociation. The proposed photochemical scheme leading to solvent-ligand exchange is summarised in **Fig. 5.8 b** where photon absorption induces LMCT which leads to $CN^{\bullet}$ dissociation followed by glycerol binding or H_2O binding if glycerol is not present.

The DFT calculations also predict that the tris-bound photoproduct ($[Fe(CN)_5(C_4H_{11}NO_3)]^{3-}$) is more stable than both the photoaquated and glycerol-bound photoproducts. However, considering the relatively similar electronic energies of the glycerol and tris-bound products, the much higher concentration of glycerol present could lead to the glycerol-bound product being kinetically favourable. Regardless, the results do suggest that tris could also bind following $CN^{\bullet}$ dissociation. In light of which, additional irradiation experiments of

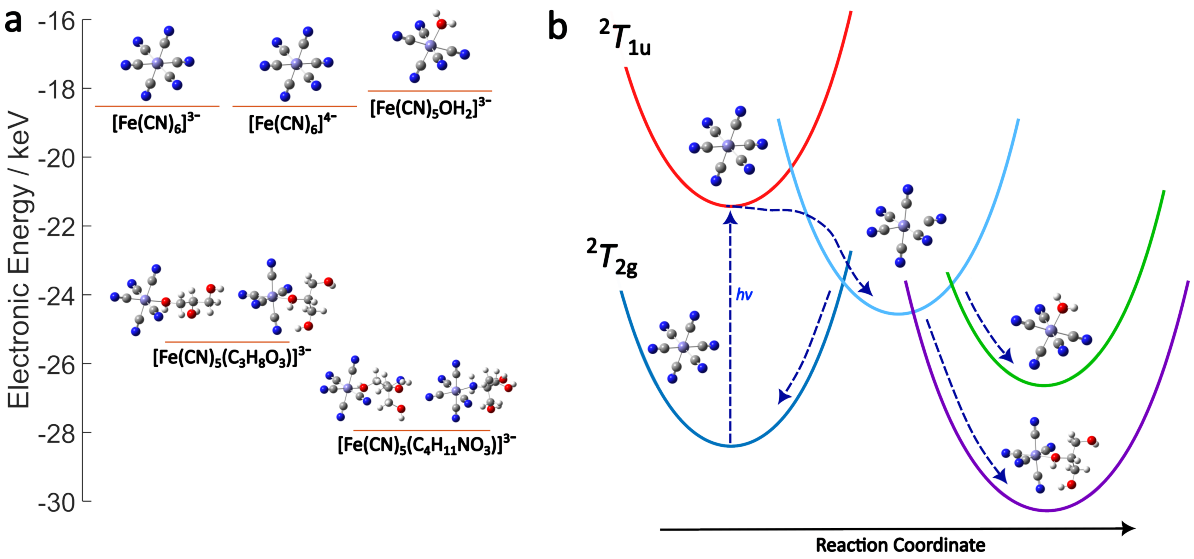

Figure 5.8: a) Calculated electronic energies of ferricyanide ($[Fe(CN)_6]^{3-}$), ferrocyanide ($[Fe(CN)_6]^{4-}$), singly photoaquated product ($[Fe(CN)_5(OH_2)]^{3-}$), singly bound glycerol product ($[Fe(CN)_5(C_3H_8O_3)]^{3-}$) and singly bound tris products ($[Fe(CN)_5(C_4H_{11}NO_3)]^{3-}$). Both the singly bound glycerol and tris products could bind in two ways however, these different binding options yielded near identical electronic energies. Glycerol can bind *via* the central or a terminal hydroxy group whereas, tris can bind *via* a hydroxy group or the amine group. b) Proposed photodegradation mechanism. Photoinduced LMCT followed by dissociation of cyano radical and solvent molecule binding.

tris and FC solutions, without glycerol present, would be prudent and remain the subject of future work.

As discussed, for FC in water, the process does not seem to stop after a single ligand exchange. The further degradation could arise due to the similar stabilities of ferrocyanide and the photoaquated product. More specifically, ferrocyanide is known to undergo a similar photoaquation reaction as FC, albeit *via* loss of CN^-.[108,114,115] It is thus reasonable to expect further solvent-ligand exchange, leading to multiply substituted ferrous complexes. This process likely follows a similar pathway to that of ferrocyanide and can be understood from symmetry arguments. As described by Cruz *et al.*,[115] following $[Fe(II)(CN)_6(OH_2)]^{3-}$ formation, the molecular symmetry shifts to C_{2v}. The covalently bound water molecule acts as a σ donor and primarily mixes with the iron d_{z^2} orbital, lowering its energy. This additional orbital interaction together with a reduction of the molecular symmetry splits the d_{z^2} energy level due to contributions from H_2O and CN σ donation and π^* back-donation. Meanwhile, the $d_{x^2-y^2}$ orbital and formally t_{2g} orbitals are largely unaffected, mixing minimally with the water orbitals. This results in more pronounced absorption > 500

nm from a metal-centred (MC) transition into an anti-bonding orbital which still absorbs reasonably strongly under 450 nm illumination, thus promoting further ligand dissociation. Given the $[Fe(II)(CN)_6(OH_2)]^{3-}$ ground state absorption is known with the MC transition peaking close to 450 nm,[108,115] the above argument agrees well with both the UV/Vis and IR irradiation data for this system. However, little work has been done here or in the literature to explore the stability and continued degradation behaviour of the aquated product. As such, more experiments and theoretical calculations are required to adequately determine the continued irradiation dynamics after $[Fe(II)(CN)_6(OH_2)]^{3-}$ formation.

Conversely, the photodegradation reaction of FC in the presence of glycerol appears to stop after reduction of the metal centre and formation of a, potentially, glycerol-bound degradation product. This can be understood by considering the greater stability of this product *vs.* the aquated product and FC. That is, the increased stability leads to a blue shift in the absorption spectra such that the degradation product absorbs minimally at 450 nm. Therefore, any potential electronic transitions into anti-bonding orbitals etc. will not occur to any meaningful extent under these illumination conditions. This coupled with the greater stability and thus potentially higher ligand dissociation energy could explain why the photoinduced degradation of FC, in the presence of glycerol, under 450 nm illumination stops after a single ligand-solvent exchange. However, more DFT calculations must be done to determine the ligand dissociation energies while more spectroscopic experiments, particularly ultrafast IR and X-ray, are required to properly determine the degradation pathway under these conditions.

In summary, it suffices to conclude that FC undergoes photoinduced degradation under experimental conditions regularly employed in the study of cryptochrome proteins. Specifically, the evidence suggests the formation of a glycerol-bound Fe(II) degradation product which accumulates significantly under prolonged illumination. Whether this photochemistry occurs independently to that of the cryptochrome or directly influences it remains to be seen. However, the degradation of FC will interfere (and certainly has interfered) with measurements made using it.

5.2 Potassium Ferricyanide Influence on Cryptochrome Magnetic Field Effects

Now that the FC photochemistry has been examined, its influence on the cryptochrome protein and, most importantly, the development of MFEs must be addressed. Some TA experiments from the group[ak] have already shown FC to quench the flavin triplet state, thus destroying intermolecular MFEs, and to slightly influence the $FAD^{\bullet-}$ lifetime. However, since the most pronounced effect in cryptochromes is expected to be on the long-lived $FADH^{\bullet}$ lifetime, BBCEAS was deemed the most suitable technique for examining the influence of FC on cryptochrome photochemsitry and MFEs. To do this, a series of cryptochrome MFE experiments were carried out with varying concentrations of FC, the results of which were coupled with kinetic modelling and spin dynamics simulations.

The sample chosen for this study was *Gg*Cry4 W369F due to its good stability, reproducible data and relatively large MFEs.[117] The *Gg*Cry4 W369F protein is a chicken (*Gallus gallus domesticus, Gg*) cryptochrome where the terminal tryptophan in the electron transfer chain (W369) has been replaced with a phenylalanine (F).[al] Consequently, RPs are formed between FAD and W_C (W318). Such a mutation has been shown to markedly increase the MFE in chicken, European robin and quail cryptochromes (see **Chapter 6**).[1,117] The structure of *Gg*Cry4 W369F is shown in **Fig. 5.9**.

5.2.1 Methods

All samples were prepared to a concentration of *ca.* 30 μM (0.3 OD at 450 nm) in pH 8 tris buffer (10 mM Tris, 250 mM NaCl and 20 % glycerol in water V/V). The series of FC concentrations employed were: 0 mM, 0.5 mM, 1 mM, 2 mM, 3.5 mM and 5 mM. For the sample with 0 mM Fe(III) an oxygen atmosphere (applied by an O_2 filled balloon) was used to aid in sample recovery.

[ak] Measured by Dr. Kevin Henbest in collaboration with DPhil student Jamie Gravell

[al] Note, this is the convention for any mutated cryptochrome, where A123B represents the substitution of amino acid A with B in position 123.

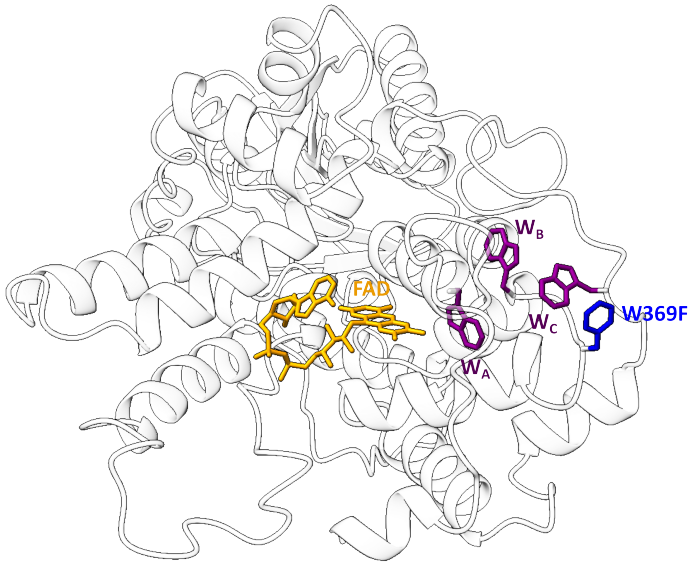

Figure 5.9: Homology model of *Gg*Cry4 W369F protein generated using SWISS-MODEL with the pigeon (*Columba livia*, ClCry4) crystal structure used as a template.[53,118–122] The electron transfer chain and mutation are highlighted with the FAD chromophore shown in orange, tryptophans A (W_A, W395), B (W_B, W372) and C (W_C, W318) shown in purple and the phenylalanine (W369F) mutation shown in blue.

As mentioned, BBCEAS was utilised in this study. The working principles behind BBCEAS have already been discussed extensively in **Chapter 3**. All that needs mentioning here is that all samples were run at 278 K and continuously photoexcited at 450 nm with an excitation power of 3 mW. All kinetic modelling and quantum dynamics simulations were carried out in Matlab, the details of which may be found in **Appendix A.2** unless explicitly discussed in the main text.

The BBCEAS experiments and kinetic modelling presented in this section were done in collaboration with Part II student Madeleine Buffet.

5.2.2 Results

The BBCEAS ΔA spectra from *Gg*Cry4a W369F under an oxygen atmosphere and with 5 mM FC are shown in **Fig. 5.10 a** and **c** respectively. The change in the ΔA spectra matches that of *Er*Cry4a WT discussed above. In the absence of FC the spectrum is dominated by the accumulation of $FADH^{\bullet}$ whereas the sample with FC is dominated by the formation of the Fe(II) photoproduct, with a minor contribution from the protein primarily visible at early times ($\leq$ 400 ms, 530 nm peak).

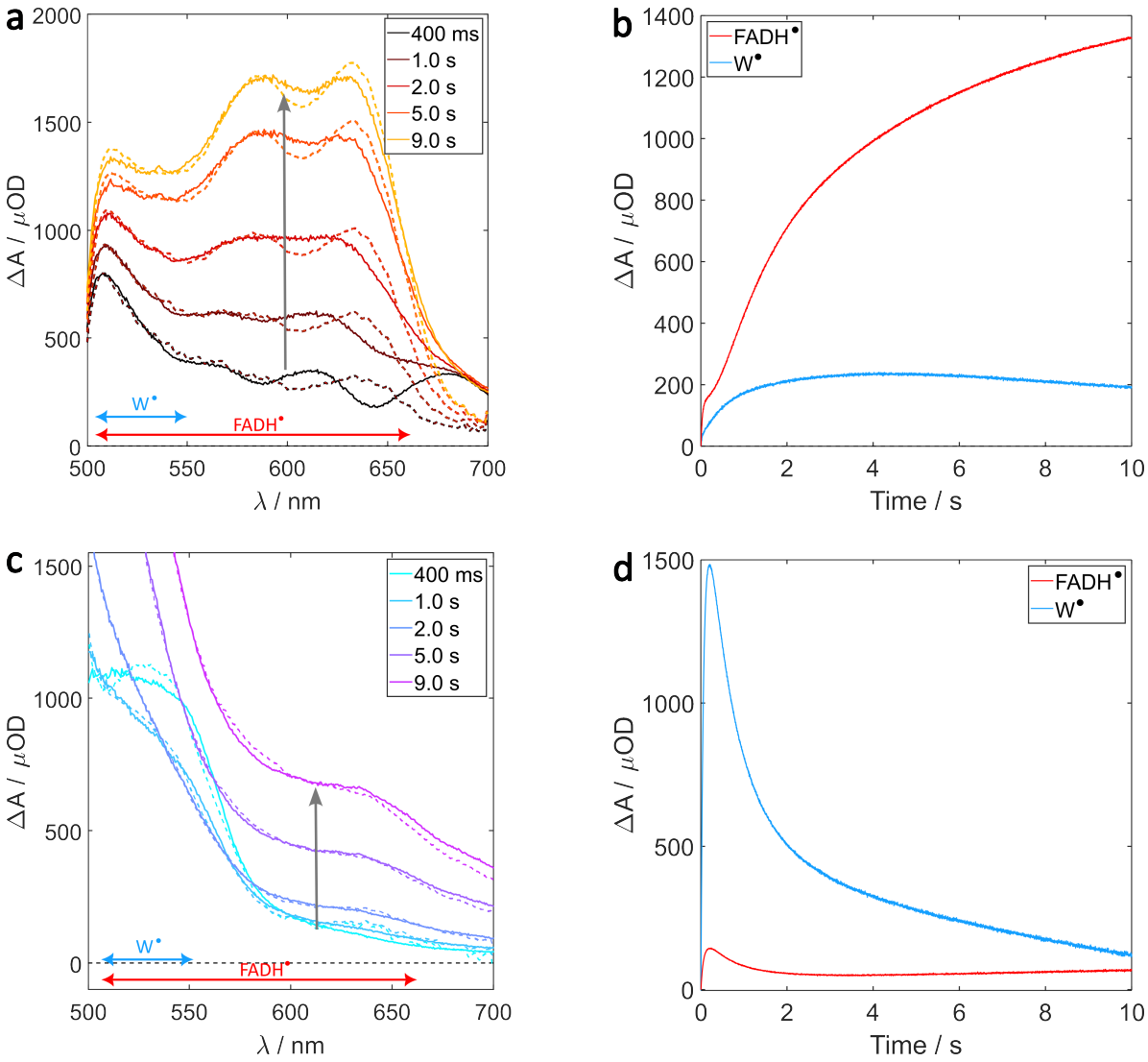

Figure 5.10: a) BBCEAS ΔA spectra of *Gg*Cry4 W369F under an oxygen atmosphere (solid lines). Formation and accumulation of FADH$^\bullet$ is observed. The dotted lines indicate the fit result from global analysis. b) FADH$^\bullet$ and W$^\bullet$ kinetics extracted from (a) *via* global analysis. c) BBCEAS ΔA spectra of *Gg*Cry4 W369F with 5 mM potassium ferricyanide (solid lines). Early formation of W$^\bullet$ is observed (520 nm peak at 400 ms) before the spectrum is dominated by ferricyanide degradation processes. Once again, the dotted lines indicate the fit result from global analysis. d) FADH$^\bullet$ and W$^\bullet$ kinetics extracted from (c) *via* global analysis.

With the now known PIA of FC, it was possible to carry out global target analysis (**Appendix A.3**) on both the FC-containing sample and the oxygen-saturated sample, extracting the kinetic behaviour of the long-lived cryptochrome radicals. The results of this analysis are shown in **Fig. 5.10 b** (oxygen atmosphere) and **d** (5 mM FC). As expected, FC suppresses the accumulation of FADH$^\bullet$ resulting in a much lower yield and thus contribution to the ΔA spectra. However, interestingly, FC also seems to significantly alter the neutral tryptophan radical yield and kinetic evolution. That is, the slowly evolving and relatively low yield W$^\bullet$ in oxygen becomes the dominant species in the presence of FC with its yield peaking within

the first *ca.* 400 ms before decaying significantly over the remaining experimental run time. This result is surprising since FC is believed to only influence the flavin and because $FADH^{\bullet}$ and $W^{\bullet}$ are believed to have independent recovery pathways.[123] Nonetheless, it is clear that the dominant radical species shifts from $W^{\bullet}$ to $FADH^{\bullet}$ when moving from FC to O_2 as the reoxidant. In both oxygen and FC samples, the tryptophan radical cation is too short lived (*ca.* 300 ns)[117] to contribute significantly to the ΔA spectra.

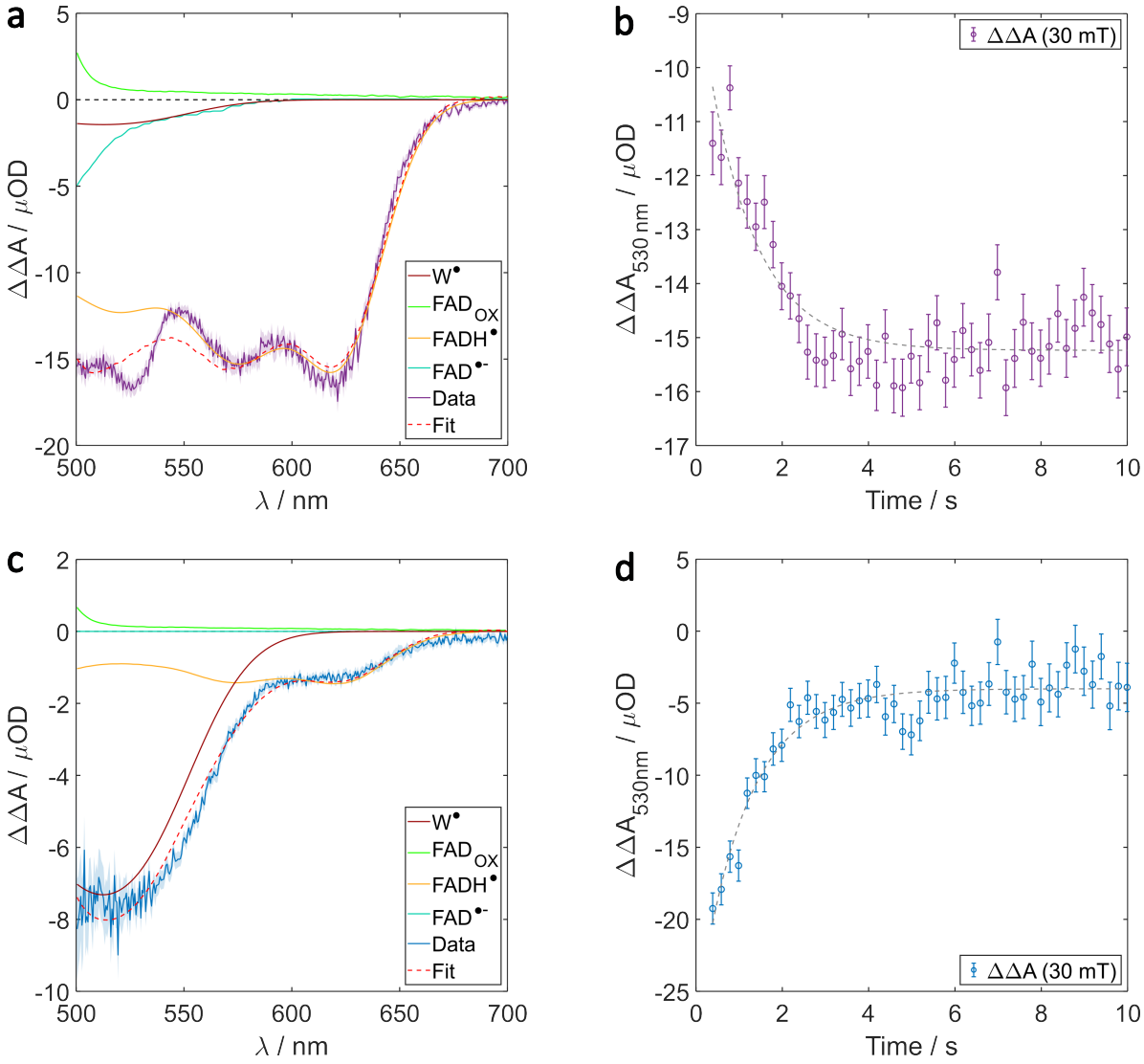

Figure 5.11: a) BBCEAS time averaged $\Delta\Delta A$ spectrum and spectral fitting results of *Gg*Cry4 W369F under an oxygen atmosphere. Spectral fitting indicates a predominantly $FADH^{\bullet}$ MFE. b) kinetic evolution of the $\Delta\Delta A$ spectrum in (a) at 530 nm. c) BBCEAS time averaged $\Delta\Delta A$ spectrum and spectral fitting results of *Gg*Cry4 W369F with 5 mM potassium ferricyanide. Spectral fitting indicates a predominantly $W^{\bullet}$ MFE. d) Kinetic evolution of the $\Delta\Delta A$ spectrum in (c) at 530 nm. All figures were measured with a 30 mT applied magnetic field. Dashed lines in (b) and (d) are monoexponential fits to the data.

This shift in the dominant radical species in the ΔA spectra is reflected in the spectral shape change in the time averaged $\Delta\Delta A$ spectra (30 mT) shown in **Fig. 5.11**. This is confirmed

following spectral fitting which shows that, as expected, the MFE under an O_2 atmosphere (**Fig. 5.11 a**) is dominated by $FADH^\bullet$ while the $\Delta\Delta A$ spectrum with 5 mM FC (**Fig. 5.11 c**) is dominated by a $W^\bullet$ MFE. Additionally, the time evolution of the MFEs at 530 nm (*cf.* **Fig. 5.11 c** and **d**) match the dominant radical species kinetics extracted from the ΔA spectra above.[am] This change in the ΔA and $\Delta\Delta A$ likely depends on kinetic considerations and will be discussed in more detail below (**Section 5.2.3**). In any case, **Fig. 5.11** clearly shows that cryptochrome MFEs can be measured, for the first time, without the use of FC. While MFEs could not be detected in the absence of a reoxidant, due to inefficient cycling of the system leading to the flavin stuck in $FADH^\bullet$ without passing back through the SCRP, molecular oxygen proved to be an effective reoxidant, enabling MFE experiments under more biologically relevant conditions.

The primary results from the FC concentration dependence study are shown in **Fig. 5.12** where the $\Delta\Delta A$ spectra (**Fig. 5.12 a**) have been normalised to the transmission of the photoexcitation laser through the FC present (*i.e.* how much of the photoexcitation laser has been attenuated by FC absorption). Notably, the 30 mT time averaged $\Delta\Delta A$ spectral shape of all FC containing samples is remarkably consistent *i.e.* they are dominated by a large $W^\bullet$ MFE centred at *ca.* 520 nm with a smaller $FADH^\bullet$ shoulder above 600 nm (**Fig. 5.12 a**). Despite this, the magnitude of the time averaged MFEs, at 30 mT, varies with FC concentration and generally increases as the Fe(III) concentration is reduced. The exception being the 3.5 mM Fe(III) sample which warrants repeating,[an] especially since its $W^\bullet$ ΔA yield is considerably lower than the rest (*cf.* **Fig. 5.12 b**). In line with this observation, the trend in the $\Delta\Delta A$ variation loosely follows the variation in the $W^\bullet$ yield extracted from the ΔA spectra (*cf.* **Fig. 5.12 b**). With the exception of the sample without Fe(III).

It thus seems that FC reduces the yield of both $W^\bullet$ and $FADH^\bullet$, influencing their subsequent MFEs. Qualitatively, all of the $W^\bullet$ ΔA dynamics in the presence of Fe(III) follow a similar

[am] Note that the $W^\bullet$ initial growth observed in the ΔA is not observed in the $\Delta\Delta A$ because the first field-on step is not acquired until after this peak. Thus, only the subsequent $W^\bullet$ decay is reflected in the $\Delta\Delta A$ results.

[an] A repeat of all experiments was attempted, however this protein batch was unhealthy (aggregated) with all resulting data unusable. Further repeats were not possible due to time limitations.

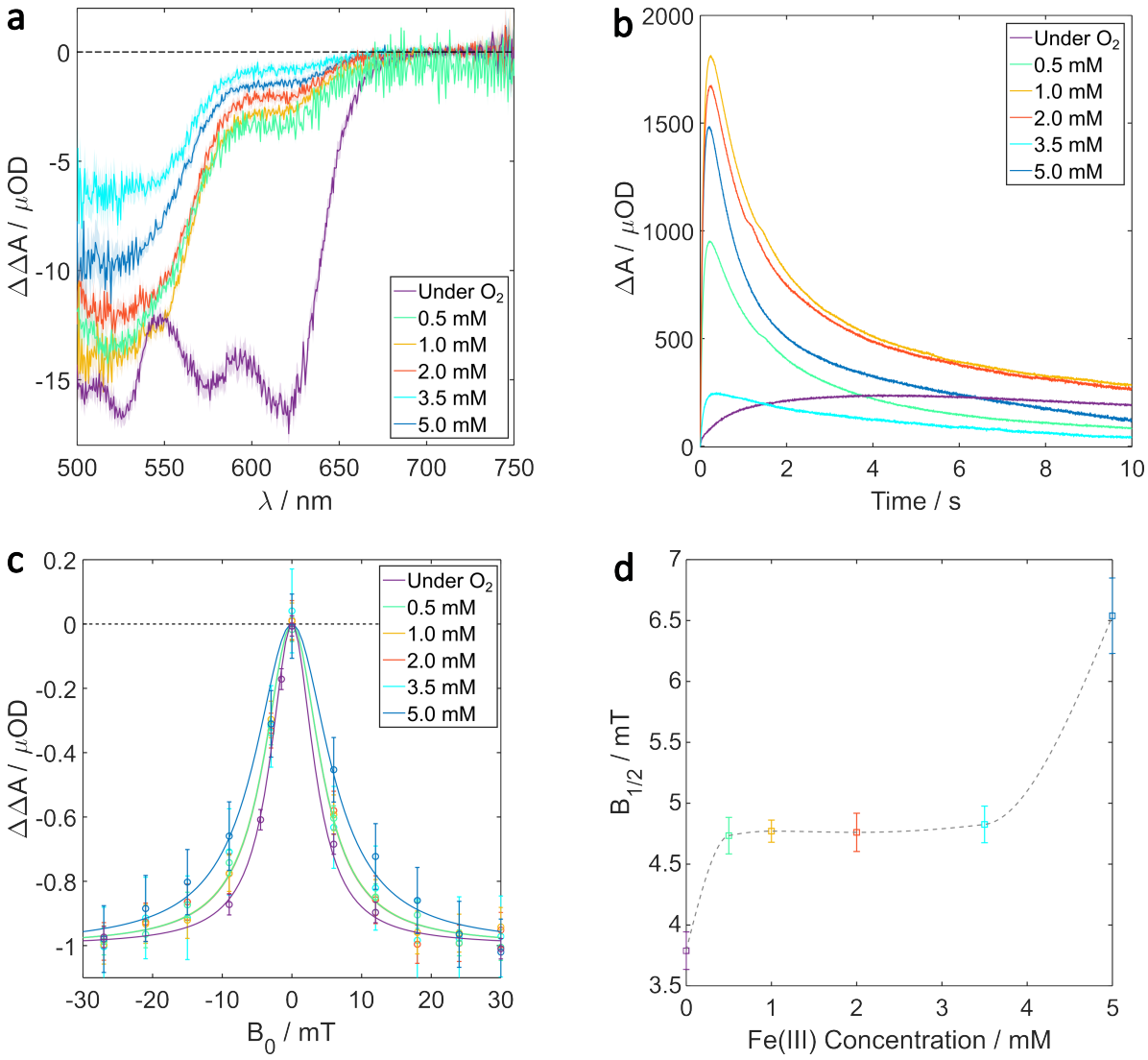

Figure 5.12: a) Time averaged $\Delta\Delta A$ spectra of *Gg*Cry4 W369F measured at a variety of ferricyanide concentrations. All ferricyanide containing samples exhibit $W^{\bullet}$ dominated MFEs. b) Extracted $W^{\bullet}$ ΔA kinetics with the yield loosely dictating the magnitude of the MFE observed in (a). c) Normalised *Gg*Cry4 W369F MARY plots and their corresponding $B_{1/2}$ values (d). The MARYs were normalised by $\Delta\Delta A_{sat}$ which is the $\Delta\Delta A$ when the MFE no longer depends on the applied magnetic field.

kinetic profile (**Fig. 5.12 b**). As such, the influence FC plays on the $W^{\bullet}$ yield must come from a change in its formation dynamics, a process which occurs prior to the BBCEAS timescale. Additionally, the effect FC has on $W^{\bullet}$ and $FADH^{\bullet}$ is not symmetric as indicated by the shift in the relative contributions of each radical to MFE. As the Fe(III) concentration is reduced, the $FADH^{\bullet}$ contribution to the $\Delta\Delta A$ spectrum increases. This is explicitly shown in **Fig. 5.13** which shows the $W^{\bullet}/FADH^{\bullet}$ concentration ratio from the $\Delta\Delta A$ spectra. Thus, the smaller the ratio, the greater the $FADH^{\bullet}$ contribution. Regardless, it seems that, provided any amount of FC in excess, the dominant long-lived radical species is $W^{\bullet}$.

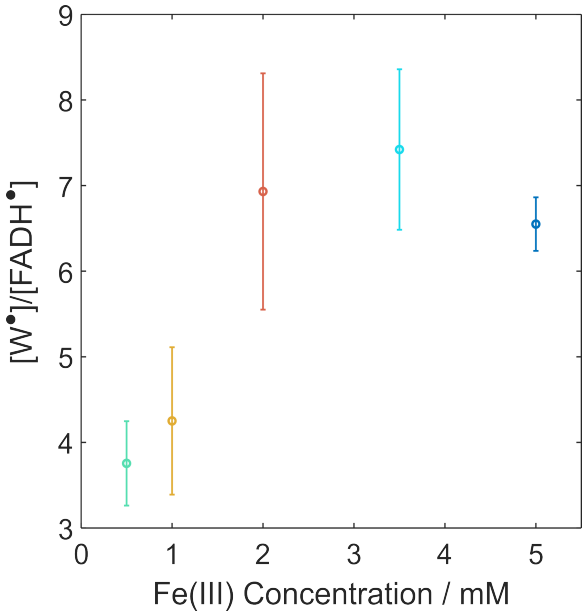

Figure 5.13: Ratio of $W^{\bullet}$ and $FADH^{\bullet}$ concentrations in **Fig. 5.12 a**. $FADH^{\bullet}$ contribution increases with decreasing Fe(III) concentration.

The normalised MARY curves in **Fig. 5.12 c** show a clear dependence on the presence of FC. Notably, the width of the MARY curves increase in the presence of FC but do not greatly depend on the Fe(III) concentration until a sharp increase at 5 mM FC. This is further highlighted in **Fig. 5.12 d** which shows the extracted $B_{1/2}$ dependence on FC concentration. As mentioned in **Chapter 2**, the $B_{1/2}$ depends strongly on the HFC interactions within the SCRP and on the extent of spin relaxation within the SCRP lifetime. Assuming FC does not change the species involved in the SCRP and thus alter the HFC interactions, it must influence the spin relaxation. This is perhaps unsurprising given the paramagnetism of FC which may induce diffusion-controlled fluctuations in local magnetic fields experienced by the SCRP. However, if this was the case and the effect was diffusion-controlled, *only*, then the $B_{1/2}$ dependence ought to depend more clearly on the FC concentration. Of course, FC could be in sufficient excess such that the process is no longer diffusion-controlled, however, this wouldn't account for the sharp $B_{1/2}$ increase at 5mM. It thus appears that the effect on spin relaxation is more complex and will be discussed in more detail below (**Section 5.2.4**).

5.2.3 Influence on Kinetics

The with and without FC ΔA comparison shown in **Fig. 5.10** indicated a change in the dominant long-lived radical and thus in its absolute and relative lifetime. To better

understand this change, cryptochrome kinetic models were constructed and used to predict how the presence of FC affects the lifetimes of $FADH^{\bullet}$ and $W^{\bullet}$.[123,124] The photocycles used with and without FC are shown in **Fig. 5.14 b** and **a**, respectively. The processes induced by FC are shown in orange. The known or calculated rate constants used in both models can be found in **Table 5.1** leaving 3 unknown rate constants for the system under oxygen and 5 unknown rate constants for the system with FC.

The rate constant for ST mixing is approximated by a single rate constant, k_{HFM}, which describes the interconversion of the singlet and all three triplet states in the absence of a magnetic field and the singlet and T_0 state in the presence of a strong magnetic field. Following Murakami *et al.*, k_{HFM} was estimated *via* the following expression.[124,125]

$$k_{HFM} \approx \frac{g_e \mu_B B_{1/2}}{h} \tag{5.1}$$

where g_e is the free electron g-factor, μ_B is the Bohr magneton, h is Planck's constant and $B_{1/2}$ is the $B_{1/2}$ extracted from the MARY plots shown in **Fig. 5.12**. The resulting ST mixing rate constants for the sample under oxygen and the sample with 5 mM Fe(III) are $k_{HFM} = 1.01 \times 10^8\ s^{-1}$ and $k_{HFM} = 1.83 \times 10^8\ s^{-1}$ respectively.

$k_{h\nu}$ / s^{-1}	k_{ET} / s^{-1}	k_r / s^{-1}	k_{DP} / s^{-1}	k_P / s^{-1}
32.2	1.8×10^{10}	5.0×10^6	5.0×10^6	5.0

Table 5.1: Known or calculated rate constants used in the kinetic models. $k_{h\nu}$ is the excitation rate and was calculated as a first order process. k_{ET} is the electron transfer rate and was taken from the work of Lacombat *et al.*[58]. k_P is the protonation rate and was estimated by Otsuka *et al.*[126] k_r and k_{DP} were estimated from transient absorption measurements (see **Chapter 6**). Of course these rate constants are estimates and as such their reliability in the context of BBCEAS is debatable.

The resulting sets of coupled ordinary differential equations were solved using Matlab's ODE15s solver for stiff systems of equations. By minimising the least-square error in the calculated $FADH^{\bullet}$ and $W^{\bullet}$ kinetics with those extracted from the global analysis above (**Fig. 5.10**), estimates could be made for their lifetimes. This fitting was achieved by

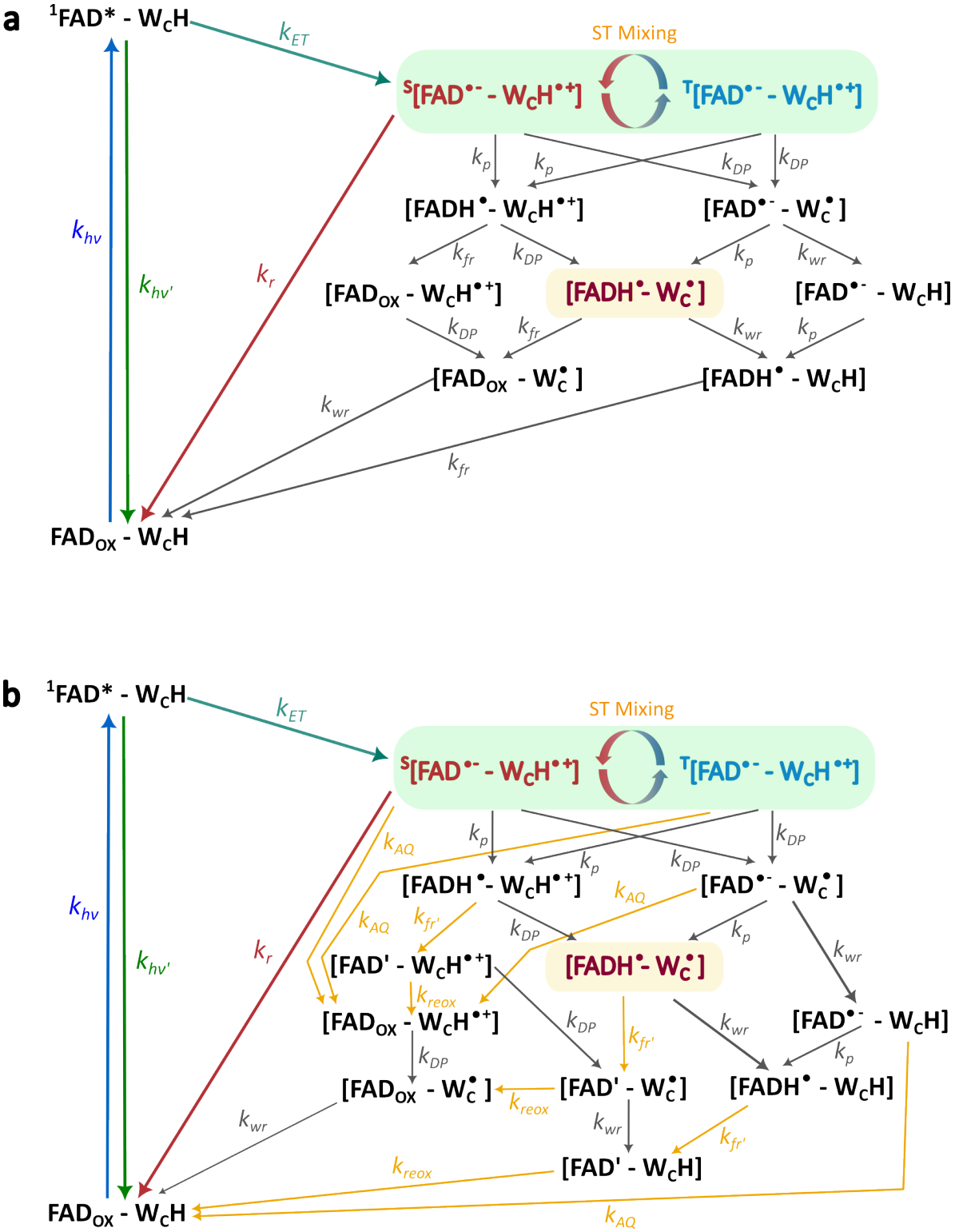

Figure 5.14: Kinetic cycles used to model *Gg*Cry4a W369F photochemistry occurring in BBCEAS with (b) and without (a) potassium ferricyanide. Models based on the work by Kattnig *et al.*[123] k_{hv} is the excitation rate constant, $k_{hv'}$ is the emission rate constant, k_{ET} is the rate constant of electron transfer (forming an FAD$^{\bullet-}$-W$_C$H$^{\bullet+}$ RP), k_r the rate constant for singlet recombination, k_p and k_{DP} are the rate constants for FAD$^{\bullet-}$ protonation and WH$^{\bullet+}$ deprotonation and k_{fr} and k_{wr} are the rate constants of FADH$^\bullet$ and W$^\bullet$ decay respectively. Additional processes induced by Fe(III) are shown in orange in (b) where k_{AQ} is the rate constant of FAD$^{\bullet-}$ quenching by Fe(III), $k_{fr'}$ is rate constant in the first step of FADH$^\bullet$ reoxidation in the presence of Fe(III) while k_{reox} is the rate constant in the second step of FADH$^\bullet$ reoxidation in the presence of Fe(III). FAD' is the intermediate species between FADH$^\bullet$ and FAD$_{OX}$.

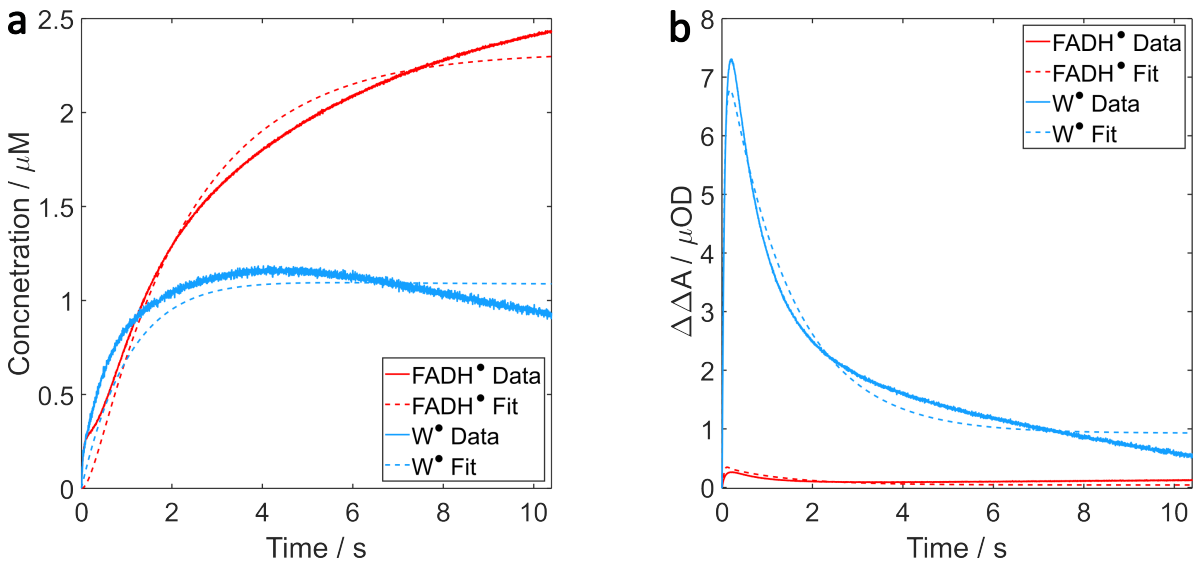

Figure 5.15: a) Kinetic model fit results for *Gg*Cry4 W369F under an oxygen atmosphere. b) Kinetic model fit results for *Gg*Cry4 W369F with 5 mM ferricyanide.

implementing a Nedler-Mead (simplex) optimisation algorithm in Matlab's fminsearch function.[ao] The full details of the kinetic modelling may be found in **Appendix A.2**.

The optimised fits are shown in **Fig. 5.15** with the resulting $FADH^{\bullet}$ and $W^{\bullet}$ decay rate constants shown in **Table 5.2**. During the fitting procedure, the emission rate constant was allowed to vary between 1×10^{8} s^{-1} and 1×10^{15} s^{-1} in an attempt to capture both the fluorescence rate and to account for the fact that the electron transfer chain has been approximated to a single rate constant. In reality, the SCRP is formed following an electron transfer cascade with the first electron transfer estimated to be 1 ps.[56] Additionally, the electron transfer does not occur with 100 % efficiency but rather has to compete with GS recombination at every step.[ap] As such, the fit results for $k_{h\nu'}$ are included in **Table 5.2** and will be discussed below.

Naturally, despite the size of the photocycles, the kinetic fits come with several assumptions. As already mentioned, the electron transfer cascade is approximated to a single step. Similarly, the ST mixing dynamics is reduced to a single average mixing rate. Furthermore, models do not allow FAD_{OX} to be re-excited until both the flavin and tryptophan have returned to the ground state which is of course not the case in reality. However, it is unlikely

[ao] Fit results were further checked by comparison with results from a genetic algorithm (Matlab's ga function) and simulated annealing (Matlab's sa function) optimisations.

[ap] Alternatively, k_{ET} could have been varied to achieve similar results since it is primarily the ratio between k_{ET} and $k_{h\nu'}$ that matters.

that a stable SCRP would form on W_B or W_A while a radical exists on W_C. Furthermore, the model employed neglects diffusion effects, sample degradation, possible side reactions and any induced photochemistry in the photoproducts. For example, $FADH^\bullet$ can be photoexcited and bleached under 450 nm illumination. Nonetheless, the fit results match the data reasonably well and allow qualitative conclusions to be made.

O_2			Fe(III)		
k_{fr} / s^{-1}	k_{wr} / s^{-1}	$k_{hv'}$ / s^{-1}	$k_{fr'}$ / s^{-1}	k_{wr} / s^{-1}	$k_{hv'}$ / s^{-1}
0.41	0.87	1.35×10^{13}	53.32	15.42	7.19×10^{10}

Table 5.2: Optimised rate constants from the kinetic modeling in **Fig. 5.15**. Note, $k_{fr'}$ is the first step in a now two step $FADH^\bullet$ recovery (see **Fig. 5.14** and discussion in text).

From **Table 5.2** it is immediately apparent that FC alters $FADH^\bullet$ and $W^\bullet$ lifetimes and their relationship to one another, consistent with the speculative discussion above (*cf.* section 5.2.2). Given FC was added to cryptochrome samples to aid in $FADH^\bullet$ oxidation, it is unsurprising that $FADH^\bullet$ decays significantly faster ($k_{fr'}$) in its presence. However, to obtain a good fit to the data, the $FADH^\bullet$ to FAD_{OX} recovery had to be separated into two steps ($FADH^\bullet \rightarrow FAD' \rightarrow FAD_{OX}$). This could be due to the fact that Fe(III) disproportionately increases the electron transfer step (*vs.* deprotonation) required for FAD_{OX} recovery thus potentially forming an $FADH^+$ intermediate which subsequently deprotonates on a slower time scale ($k_{reox} = 0.08\ s^{-1}$, *cf.* **Fig. 5.14**).

While the effect on the $FADH^\bullet$ lifetime arises from a direct process with FC, the effect on the $W^\bullet$ lifetime is harder to understand and is potentially indirect. As discussed above, photoexcitation of FC causes reduction of the metal centre and ligand dissociation. The formed Fe(II) species could now act as an electron donor aiding in WH recovery. However, recalling the fact that these ferric/ferrous compounds are highly negatively charged, upon consideration of the charge distribution around the protein (see **Fig. 5.16**) it seems unlikely that any these compounds will interact meaningfully with W_C since it lies in a net negatively charged region of the protein. Conversely, the region around FAD is net positively charged and could promote interaction with FC. One can argue that the large concentration of NaCl (250 mM) present in the buffer solution may sufficiently screen Coulombic interactions, enabling the reaction of Fe(II) photoproducts with the surface accessible W_C. However,

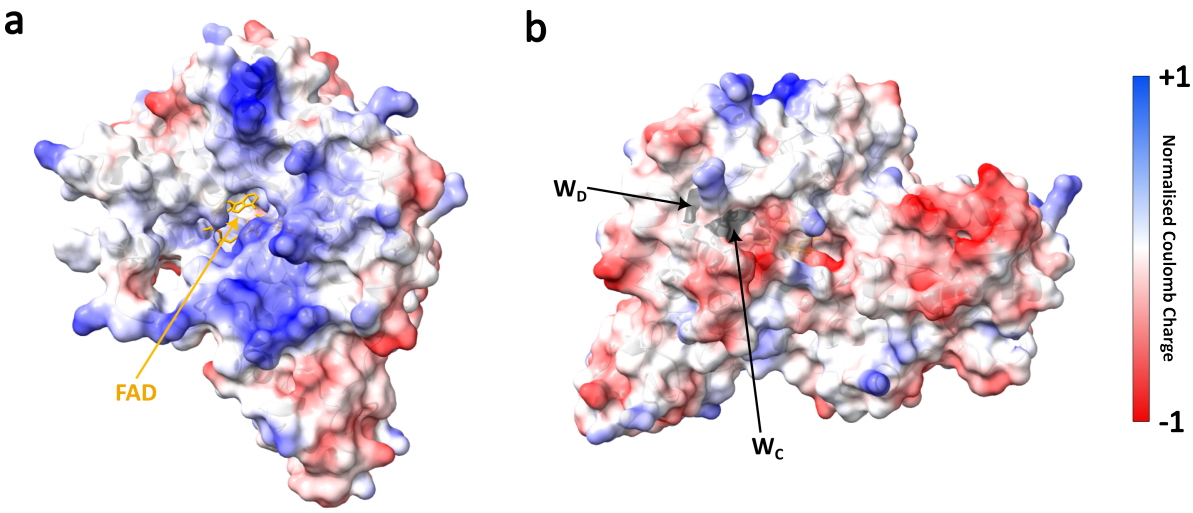

Figure 5.16: Coulombic charge surfaces of *Gg*Cry4 WT calculated using ChimeraX. a) Shows the FAD binding pocket in a net positive region of the protein. b) Shows tryptophans W_C and W_D to be in largely negative regions of the protein, apart from a positive protrusion between them. Both tryptophans are relatively surface exposed.

given the process of WH recovery is still unknown, this discussion is speculative at best and the effect Fe(III) plays on the $W^{\bullet}$ to WH process remains unclear.

In addition to a shift in the long-lived radical dynamics, the optimised $k_{hv'}$ values significantly differ. It was mentioned earlier that this rate constant was allowed to vary as it approximates both emission and electron transfer and recombination reactions along the tryptophan chain, prior to SCRP formation. Thus it comes as no surprise that $k_{hv'}$ is faster than reported FAD emission rates (1×10^8 s^{-1})[123] for both kinetic models. The large difference between the two models is more surprising. However, this can be understood by considering its influence on radical yields. That is, the ratio between the electron transfer rate k_{ET} and $k_{hv'}$ will alter the yield of the SCRP. Thus, by keeping k_{ET} fixed, variations in $k_{hv'}$ dictate the SCRP yield. As such, the kinetic models suggest higher SCRP yields when FC is added then when not (*ca.* 25.6 % *vs.* 0.4 %) while the more rapid $W^{\bullet}$ and $FADH^{\bullet}$ decays, in the presence of FC, prevent their excessive accumulation in BBCEAS. Surprisingly, this is in line with some experimental results. As recently reported by Timmer *et al.*,[56] the ET efficiency in reaching W_C in a *Er*Cry4a W369F mutant, with 1.5 mM FC, was estimated to be *ca.* 36.9 %. Conversely, air equilibrated (no FC or oxygen atmosphere) TA experiments on *Gg*Cry4a W369F (*cf.* **Chapter 6**)[117] predicted an ET transfer efficiency of *ca.* 4.17 %. This implies that the addition of FC influences the electron transfer cascade process. The

reason for this is unclear, however, one possible explanation is that FC electrostatically associates with the protein near the FAD binding pocket (see **Fig. 5.16 a**), altering the local structure and redox environment thus either promoting ET or inhibiting radical recombination during the ET cascade. Furthermore, some preliminary TA measurements within the group[aq] have shown FC to slightly alter the $FAD^{\bullet-}$ lifetime. Consequently, this process was included in the kinetic model but only on the SCRP and subsequent photoproducts thus neglecting any potential effect it may have on the ET efficiency. In any case, while the use of $k_{hv'}$ in this context is a big assumption, the role it plays in the kinetic models does potentially provide some insights into the influence Fe(III) may have on ET processes within the protein.

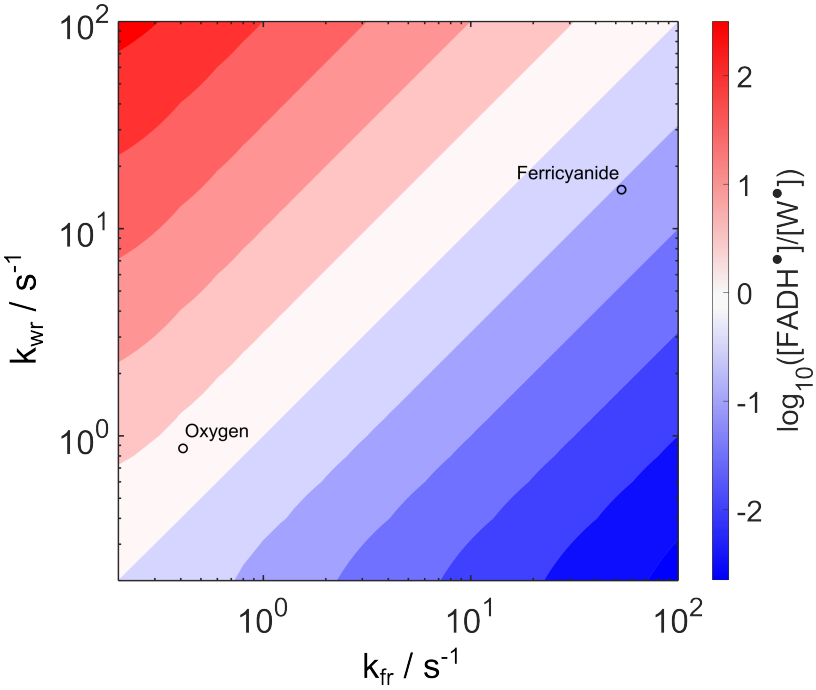

Figure 5.17: Contour plot of the steady state $FADH^{\bullet}/W^{\bullet}$ concentration ratio as a function of their decay rates (k_{fr} and k_{wr}). The positions of the fit results from **Fig. 5.15** are marked.

Despite the ambiguity in the precise long-lived radical decay mechanisms, the kinetic model does successfully capture the shift in the long-lived radical dynamics with the effect predominantly on the relative and absolute $FADH^{\bullet}$ and $W^{\bullet}$ decay rates. With this, the relationship between the two radical lifetimes and the dominant absorbing species can be demonstrated by calculating the ratio between their steady state concentrations ($[FADH^{\bullet}]/[W^{\bullet}]$). These results are shown in **Fig. 5.17** where there is a clear inversion of

[aq]Experiments by Dr. Kevin Henbest and Part II student Holly Hayward

the relative proportions of $FADH^{\bullet}$ and $W^{\bullet}$ upon inversion of the k_{fr} and k_{wr} ratio. This relationship may have some significance in the process of magnetoreception. If $FADH^{\bullet}$ is involved in some form of signalling state then *in situ* optimisation of k_{fr}/k_{wr}, and thus the $[FADH^{\bullet}]/[W^{\bullet}]$, ratio could lead to an improved magnetic sense.[123]

This shift in the dominant radical species carries neatly through into the observed BBCEAS MFEs. Using the ΔA fit results obtained above, the BBCEAS $\Delta\Delta A$ spectra, with 5 mM Fe(III) and under oxygen, were simulated by modelling the kinetic cycle with an applied magnetic field and subtracting it from the results above (**Fig. 5.15**). The difference in the kinetic model with an applied magnetic field is that the $T_{\pm}$ states are now energetically isolated. As such, coherent mixing only occurs between the singlet and T_0 state. Additionally, an incoherent mechanism (*e.g.* spin-lattice relaxation) is introduced, k_{RM}, allowing interconversion to $T_{\pm}$.[123,124] This incoherent mechanism simply scales the magnitude of any MFE without influencing the rest of the system dynamics. As such, k_{RM} was varied to fit the observed MFE magnitude. The time averaged simulated MFEs and time averaged experimental MFEs are shown in **Fig. 5.18**.

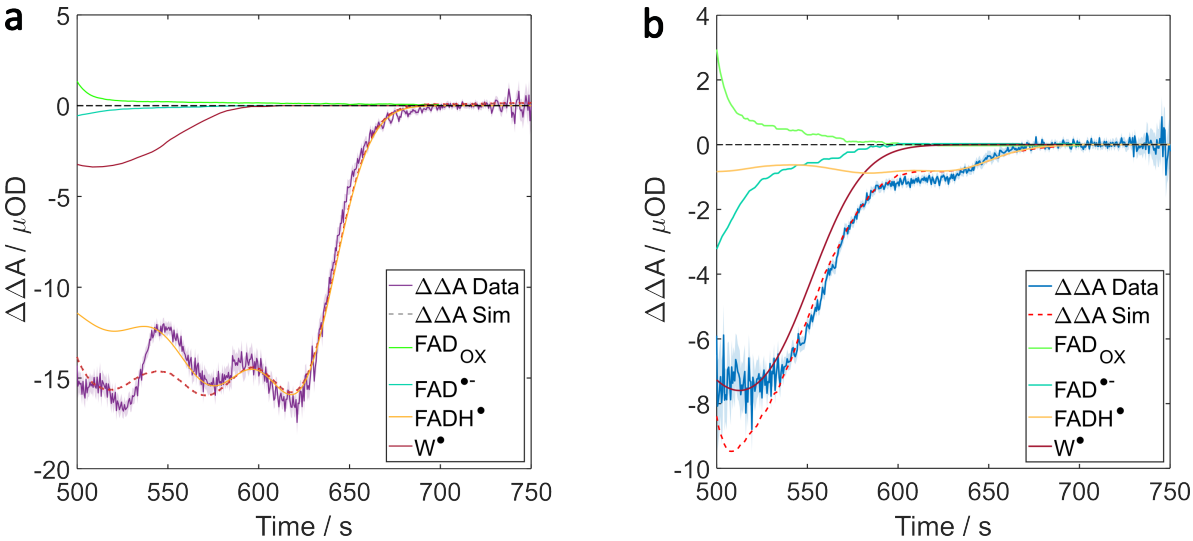

Figure 5.18: Time averaged $\Delta\Delta A$ spectrum and simulation results of *Gg*Cry4 W369F under an oxygen atmosphere (a) and with 5 mM potassium ferricyanide (b).

In both cases the modelled MFEs match reasonably well with the experimental MFEs, particularly in the relative contributions of each of the long-lived radicals. For the system under oxygen, much of the deviation between the simulated and experimental $\Delta\Delta A$ spectra arises from the reference spectra used to convert the concentration kinetics into spectra (*cf.*

Fig. 2.9 b). Indeed, this is a problem when simply spectrally fitting the $\Delta\Delta A$ spectra (*cf.* **Fig. 5.11**). On the other hand, the modelled $\Delta\Delta A$ in the presence of FC overestimates MFEs on FAD_{OX} and $FAD^{\bullet-}$. This is likely a result of approximations made in constructing the model. In particular, the approximations associated with k_{ET} and $k_{h\nu'}$ will significantly alter the FAD_{OX} and $FAD^{\bullet-}$ concentrations and dynamics and thus their MFEs. In any case, the kinetic models successfully captured the qualitative dynamic behaviour of the long-lived neutral radicals, demonstrating how the addition of FC could influence the absolute and relative lifetimes of $FADH^{\bullet}$ and $W^{\bullet}$ thus drastically altering the spectral shape of MFEs as observed by BBCEAS.

5.2.4 Influence on Spin Dynamics

In addition to the influence FC can have on kinetic processes within the RPM in cryptochromes, the results of the concentration dependence study implicate its involvement in the spin dynamics. As mentioned above, the effect FC has on the $B_{1/2}$ results suggests that spin relaxation in the SCRP is affected. This could simply arise from the addition of large amounts of a paramagnetic species causing diffusion-driven modulations of the local magnetic field. That is, stochastic modulation of inter-electron dipolar interactions between electrons in the SCRP and the unpaired electron on FC. Alternatively, modulation of the exchange interaction due to electron-hopping or fluctuations in inter-radical separation can cause singlet-triplet dephasing (STD) leading to a decay in the radical-radical coherences.[41] This could arise from association of FC with the protein causing conformational changes which alter the ET rates and thus electron hopping or alter the vibrational modes within the protein thus increasing modulations in the inter-electron separation. This association could be Coulombic as discussed above, or covalent following photoinduced ligand dissociation and binding to an amino acid (*e.g.* a surface cysteine).

Another mechanism worth considering is the role FC potentially plays as a scavenger, quenching $FAD^{\bullet-}$ from the SCRP. Not only does this influence the kinetics of the system but it can also influence the spin dynamics *via* the so called chemical Zeno effect (CZE).[127–129] This effect is an extension of the quantum Zeno effect where repeated and rapid measurements made of a system inhibit the evolution of that system and thus the outcome

of measurements.[127,130] More specifically, a quantum measurement acts as a projection operator onto some experimental basis. When measurements become so frequent so as to be essentially continuous (relative to the evolution of the system), coherent evolution of the system stops with the system continuously in the state which the measurement projects it into.[127,130] Since spin-conserved electron transfer with a radical pair involves projection (typically singlet) into the correct spin state, the process acts as a quantum measurement. Thus, with a sufficient scavenging or recombination rate, electron transfer can, in principle, influence the ST mixing evolution (not just the population kinetics).[127,129,131] This is the CZE and its influence can be understood as follows.

Consider a typical equation of motion for a SCRP

$$\frac{d\rho}{dt} = -i\left[\hat{H},\rho\right] - \frac{k}{2}\left\{\hat{P}_S,\rho\right\} \tag{5.2}$$

where ρ is the density operator, $\hat{H}$ is the RP spin Hamiltonian, k is the singlet recombination rate constant, $\hat{P}_S$ is the singlet projection operator and [,] and {,} represent the commutator and anti-commutator. Using the fact that $\hat{P}_S + \hat{P}_T = \hat{E}$, where $\hat{P}_T$ is the triplet projection operator and $\hat{E}$ is the unit operator, equation 5.2 becomes[127]

$$\frac{d\rho}{dt} = -i\left[\hat{H},\rho\right] + \frac{k}{2}\left\{\hat{P}_T,\rho\right\} - k\rho \tag{5.3}$$

Equation 5.3 describes how singlet recombination leads to the decay of all radical pairs with rate constant k coupled with the spontaneous appearance of triplet radical pairs. That is, the act of singlet recombination forces the surviving RPs into the triplet state which is observed as a decrease in the singlet-triplet conversion frequency for the surviving radicals.[127]

In the case of a paramagnetic scavenger (C) which reacts with one of the radicals (A) in the RP, electron transfer can occur in two ways[129]

$$^{2}\mathrm{A} + {}^{2S+1}\mathrm{C} \xrightarrow{k_S^{+}} {}^{1}\mathrm{A} + {}^{2S+2}\mathrm{C} \tag{5.4a}$$

$$^{2}\mathrm{A} + {}^{2S+1}\mathrm{C} \xrightarrow{k_S^{-}} {}^{1}\mathrm{A} + {}^{2S}\mathrm{C} \tag{5.4b}$$

where the superscripts denote the spin multiplicity with $S = 1/2$. As a consequence of spin conservation, the scavenger's spin must change by $\pm 1/2$. Therefore, a doublet scavenging radical can either form a singlet (5.4b) or triplet state (5.4a) following electron transfer. Under such conditions, Kattnig and Hore[129] (also Letuta and Berdinskii[128]), showed that scavenging reactions *via* equation 5.4b convert a portion of the surviving RPs into the triplet state (*cf.* equation 5.3), thus leading to the CZE. The reaction between $\mathrm{FAD}^{\bullet-}$ and FC would satisfy equation 5.4b, influencing the spin dynamics.

To gain greater insight into the potential influence FC has on the aforementioned spin dynamics and thus BBCEAS results, simulations were carried out where the SCRP concentration was assumed constant (*i.e.* $d\rho/dt = 0$). This assumption is justified due to the time scale of the BBCEAS experiments (> 10 s) *vs.* the rate processes of the SCRP (*cf.* **Table 5.1**). As such, all mechanisms were modelled following the same general procedure.

Consider a RP whose density operator, ρ, is described by the following stochastic Liouville equation

$$\frac{d\rho}{dt} = -i\left[\hat{H}, \rho\right] + \left\{\hat{K}, \rho\right\} + \frac{k_0}{Z}\hat{P}_S + \hat{R}\rho \tag{5.5}$$

where $\hat{K}$ is the recombination operator, k_0 is the rate of singlet born RP formation, Z is the number of nuclear spin states and $\hat{R}$ is the relaxation operator. Rewriting equation 5.5 in Liouville space and applying the steady state condition yields[132]

$$|\rho\rangle = \frac{k_0}{Z}\hat{\mathrm{L}}^{-1}|\hat{P}_S\rangle \tag{5.6}$$

where $|\rho\rangle$ is the row-wise flattened density matrix, $|\hat{P}_S\rangle$ is the row-wise flattened singlet projection operator and $\hat{\hat{\mathrm{L}}}$ is the Liouvillian

$$\hat{\hat{\mathrm{L}}} = i\hat{\hat{\mathbf{H}}} + \hat{\hat{\mathbf{K}}} + \hat{\hat{\mathbf{R}}} \tag{5.7}$$

Here, $\hat{\hat{\mathbf{H}}}$, $\hat{\hat{\mathbf{K}}}$ and $\hat{\hat{\mathbf{R}}}$ are the Hamiltonian, recombination and relaxation superoperators in Liouville space (see **Chapter 2**) and will depend on the specific mechanism in question. With equation 5.6, the total RP probability, P_{RP}, can be calculated from the sum of singlet and triplet probabilities using

$$P_{RP} = \frac{k_0}{Z}\left(\langle\hat{P}_S|\hat{\hat{\mathrm{L}}}^{-1}|\hat{P}_S\rangle + \langle\hat{P}_T|\hat{\hat{\mathrm{L}}}^{-1}|\hat{P}_S\rangle\right) = \frac{k_0}{Z}\langle\hat{E}|\hat{\hat{\mathrm{L}}}^{-1}|\hat{P}_S\rangle \tag{5.8}$$

where $|\hat{P}_T\rangle$ and $|\hat{E}\rangle$ are the row-wise flattened triplet projection and identity operators, respectively.

The operators used in the simulations will be simply stated and the reader will be referred to an appropriate reference for their derivations. Both random local magnetic field fluctuations (RFR) and STD mechanisms share the same spin Hamiltonian and recombination operator. The recombination operator is the Haberkorn operator (equation 2.47 in **Chapter 2**) where k_S is the sum of singlet recombination, $FAD^{\bullet-}$ protonation and $WH^{\bullet+}$ deprotonation rate constants and k_T is the sum of $FAD^{\bullet-}$ protonation and $WH^{\bullet+}$ deprotonation rate constants (*cf.* **Table 5.1**). The spin Hamiltonian is given by

$$\hat{H} = \sum_{i=A,B}\omega_i\hat{S}_{zi} + \sum_{i=A,B}\sum_{k=1}^{N_i}a_{ik}\hat{I}_{ik}\cdot\hat{S}_i - 2J\hat{S}_A\cdot\hat{S}_B \tag{5.9}$$

where the first term is the Zeeman interactions, the second term captures the HFC interactions, with N_i the number of HFCs on radical i, and the third term is the electron exchange interaction ($J = 0.3$ MHz)[117]. Since BBCEAS experiments are carried out in solution, rapid molecular tumbling minimises the dipolar interaction and thus it is neglected.

The RFR relaxation operator was modelled using a phenomenological operator which, in Liouville space, is given by[41]

$$\hat{\hat{\mathbf{R}}}_{RFR} = k_{RFR}\left(\frac{3}{2}\hat{E}\otimes\hat{E} - \sum_{i=A,B}\sum_{k=x,y,z}\hat{S}_{ik}\otimes\hat{S}_{ik}^{\mathrm{T}}\right) \tag{5.10}$$

where k_{RFR} is the relaxation rate constant and isotropically relaxes both electron spins to equilibrium.[41] While equation 5.10 is a major simplification of such a relaxation mechanism it can qualitatively capture the effect of such stochastic fluctuating field mechanisms.[41,133] A derivation of equation $\hat{\hat{\mathbf{R}}}_{RFR}$ may be found in the appendix of Kattnig *at al.*[133]

The STD operator was introduced and discussed in **Chapter 2** and in Liouville space is given by[41]

$$\hat{\hat{\mathbf{R}}}_{STD} = k_{STD}\left(\hat{P}_S\otimes\hat{P}_T + \hat{P}_T\otimes\hat{P}_S\right) \tag{5.11}$$

where k_{STD} is the rate constant of singlet triplet dephasing (decay of coherences not populations). Once again, a derivation of equation 5.11 may be found in the appendices of Kattnig *at al.*[133]

For the CZE, the spin of the scavenging radical, C, must be considered. Therefore, assuming C has no HFCs (97.6 % of natural abundance iron has no nuclear spin), the spin Hamiltonian becomes

$$\hat{H} = \sum_{i=A,B,C}\omega_i\hat{S}_{zi} + \sum_{i=A,B}\sum_{k=1}^{N_i}a_{ik}\hat{I}_{ik}\cdot\hat{S}_i - 2\sum_{i,j=A,B,C}J_{ij}\hat{S}_i\cdot\hat{S}_j \tag{5.12}$$

where the sums over the exchange interactions are such that $i \neq j$. With the additional spin selective electron transfer, the recombination superoperator becomes

$$\hat{\hat{\mathbf{K}}}_{Zeno} = \frac{1}{2}\left(k_c^-\hat{\hat{\mathbf{P}}}_{AC}^- + k_S\hat{\hat{\mathbf{P}}}_S + k_T\hat{\hat{\mathbf{P}}}_T\right) \tag{5.13}$$

where k_S and k_T are the same as for the RFR and STD mechanisms, $\hat{\hat{\mathbf{P}}}_S$ and $\hat{\hat{\mathbf{P}}}_T$ are the singlet and triplet projection superoperators for the RP (*i.e.* between spins A and B), k_c^- is the scavenging rate constant to form a singlet scavenger product and $\hat{\hat{\mathbf{P}}}_{AC}^-$ is the projection superoperator for the reaction and is derived from[129]

$$\hat{P}_{AC}^{\pm} = \frac{1}{2} \pm \frac{1}{2S+1}\left(\frac{1}{2} + 2\hat{S}_A \cdot \hat{S}_C\right) \tag{5.14}$$

where S is the spin multiplicity of the scavenging species. A derivation for equation 5.14 may be found in the supporting information of Kattnig *et al.*[129]

In all simulations, due to limited computational resources, 5 nuclear spins were included. Specifically, following Maeda *et al.*,[87] the $FAD^{\bullet-}$ radical was modelled with the largest HFC, N5 (*cf.* **Fig. A.9**) and all remaining HFCs approximated by a single spin-1/2 interaction with the HFC constant, a_{rest}, determined by the effective HFC (equation 2.53). Similarly, $WH^{\bullet+}$ was modelled with the two largest HFCs, H18 and H23 (*cf.* **Fig. A.9**), with all remaining HFC interactions approximated to a single spin half interaction, a_{rest}, determined by the effective HFC. All HFC interactions used can be found in **Table 5.3**. The reader is referred to **Appendix A.2** for the full list of parameters employed.

$FAD^{\bullet-}$		$WH^{\bullet+}$	
	HFC / mT		HFC / mT
N5	0.523	H18	1.605
a_{rest}	1.107	H23	−0.598
		a_{rest}	0.918

Table 5.3: HFC interactions used in all simulations were taken from Maeda *et al.*[87]

The effect of the outlined mechanisms on the magnitude of the MFE and the $B_{1/2}$ is shown in **Fig. 5.19** where $\Delta RP = P_{RP}(B) - P_{RP}(B=0)$ is the change in the total RP probability when a magnetic field is applied. The normalised ΔRP_{sat} in **Fig. 5.19 a** is the ΔRP at 20 mT, normalised by the ΔRP at 20 mT without any relaxation or radical scavenging mechanisms. In **Fig. 5.19 b**, the $B_{1/2}$ values when $\Delta RP_{sat} = 0$ have been omitted. Each potential mechanism was simulated independently such that the rate constants of the other three were set to zero. Details of the additional hopping mechanism included in **Fig. 5.19** can be found in **Appendix A.2**. In brief, it explicitly models the effect of one

of the electrons in the SCRP hopping between two sites with different electron exchange interactions.

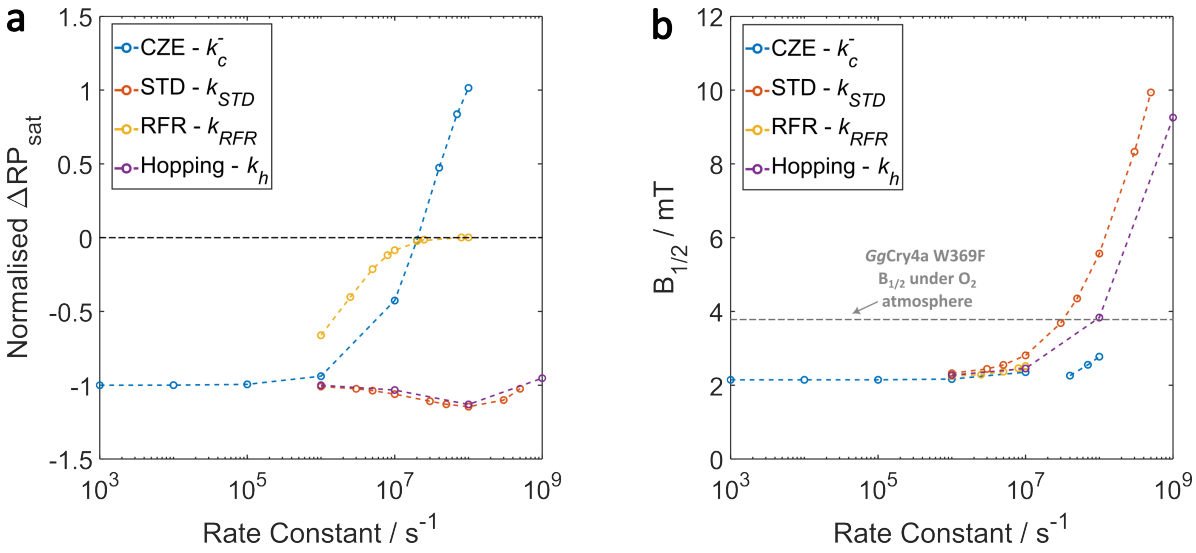

Figure 5.19: Spin dynamics simulation results on (a) the magnitude of the saturated magnetic field effects (*i.e.* when the MFE no longer depends on applied magnetic field) and (b) the $B_{1/2}$ from simulated MARY plots. The normalised ΔRP_{sat} in (a) is ΔRP_{sat} divided by ΔRP_{sat} without any relaxation or scavenging mechanisms. $\Delta RP_{sat} = P_{RP}(B = 20\ mT) - P_{RP}(B = 0)$. In both plots, the x-axis denotes different values for the rate constants highlighted in the legend where k_c^- is the scavenging rate constant for the chemical zeno effect mechanism, k_{STD} is the rate constant for singlet-triplet dephasing, k_{RFR} is the rate constant for random fields relaxation and k_h is the hopping rate from W_C to W_B. The rate constant of electron transfer from W_B to W_C was kept constant (1×10^{10} s^{-1}).

In line with recent work by Golesworthy *et al.*[41], the RFR mechanism works to decrease the magnitude of the MFE (**Fig. 5.19 a**) whilst having minimal effect on the $B_{1/2}$ (**Fig. 5.19 b**). Since this mechanism works to bring the system to equilibrium by relaxing all coherences to zero and making all states equally probable at the same rate, at any given time, the surviving (un-relaxed) population undergoes the same ST mixing dynamics as it would in the absence of relaxation. The net result is therefore the attenuation of the magnitude of the MFE without altering its field dependence (*i.e.* $B_{1/2}$).[41]

In contrast, the STD mechanism initially slightly increases the MFE before it begins to decay after $k_{STD} > 1 \times 10^8$ s^{-1} (**Fig. 5.19 a**). Additionally, STD significantly influences the $B_{1/2}$ which increases with increasing k_{STD}. This is due to the damping of singlet-triplet coherences causing a reduction in the rate of singlet-triplet interconversion which thus indirectly influences the singlet/triplet probabilities.[41] As such, while k_{STD} may rapidly quench the coherences, the effect on singlet/triplet probabilities occurs on a much slower

time scale.[41] For values of k_{STD} where the effect on the singlet/triplet probabilities occurs more slowly than SCRP recombination, the reduced S-T mixing rate leads to a more gradual MFE field dependence, and thus larger $B_{1/2}$, without significantly influencing the MFE magnitude. Once k_{STD} is sufficiently large, the coherence terms are relaxed too rapidly for any ST mixing to occur, thus reducing the MFE. The validity of the phenomenological STD mechanism was evaluated (**Fig. 5.19**) by explicitly modelling an electron hopping process with the results broadly mirroring the STD effects. The hopping mechanism initially moderately increases the magnitude of the MFE, until the hopping rate k_h exceeds 1×10^8 s^{-1}, while simultaneously increasing the $B_{1/2}$.

The radical scavenging reaction appears to primarily affect the size of the MFE. As shown in **Fig. 5.19 a**, there is little effect on the MFE until the scavenging rate constant (k_c^-) exceeds the rate of SCRP singlet recombination (5×10^6 s^{-1}), at which point the MFE magnitude begins to decrease. Once the scavenging rate greatly exceeds SCRP singlet recombination the reaction manifests the CZE leading to an inversion in the sign of the MFE. This is a direct result of the fact that the scavenging reaction converts a portion of the surviving radicals into the triplet state, thus at sufficiently rapid scavenging rates the system begins to appear triplet born, causing "inverted" MFEs. Conversely, the reaction has little effect on the $B_{1/2}$ (*cf.* **Fig. 5.19 b**). This is because the CZE mechanism considered here does not influence the spin-spin interactions between the two radicals in the SCRP and thus does not effect their coherences. One way the $B_{1/2}$ could be effected is by allowing the SCRP radicals to exchange with the scavenging radical provided a large enough J. However, the estimated exchange interaction between $FAD^{\bullet-}$ and FC, assuming FC sits in the positively charged pocket of the protein (*cf.* **Fig. 5.16 a**), is small ($J = 0.42$ MHz)[ar] and including it had little to no effect on the $B_{1/2}$.

It is clear from the simulations above that the presence of FC could influence the spin dynamics of SCRPs in cryptochrome proteins. In reality, the precise mechanism is likely a combination of a variety of processes with the net result a broadening of the $B_{1/2}$ and a reduction in the MFE. If the CZE is indeed occurring in these systems then FC, or

[ar] Estimated assuming the usual exponential decay with distance (equation 2.27). The parameter used to calculate J were, $j_0 = 3.2 \times 10^{12}$ MHz, $\beta = 0.8$ and Å, $r = 37$ Å.[134]

similar redox partners, could offer a means of experimentally exploring this phenomenon. Especially if the sign of the MFE can be inverted by controlling the rate of a scavenging reaction.

5.3 Conclusion

In this chapter UV/Vis and IR irradiation experiments and DFT calculations were used to explore the long-time scale photochemistry and degradation of FC under experimental conditions regularly employed in cryptochrome MFE experiments. From these results it is evident that FC undergoes significant photodegration in tris buffer under relatively weak 450 nm illumination. The resulting degradation product accounts for the large BBCEAS absorption signals observed above 500 nm (**Fig. 5.1**) when FC was used. Furthermore, the influence FC has on the development of MFEs in BBCEAS was explored by way of an Fe(III) concentration dependence study where FC was found to influence the spectral shape, magnitude and field dependence of MFEs.

Considering the evidence presented in this chapter it is apparent that, in spite of its prolonged use in protein MFE studies, FC is a far from ideal reoxidant for the spectroscopic study of cryptochromes. Not only does it exhibit extensive photochemistry under our experimental conditions, but directly influences kinetic and spin dynamics processes within the protein. The use of FC thus significantly influences the results obtained from spectroscopic measurements, particularly BBCEAS, of cryptochrome proteins. In light of these results and due to the successful MFE measurements made under an oxygen atmosphere, O_2 will be used as for sample reoxidation hereafter.

Chapter 6

Exploring The MFE Mechanism in Cryptochromes One Mutation at a Time

In **Chapter 4** MFEs were demonstrated in cryptochrome proteins from several avian species. Notably, comparable MFEs were observed in proteins from both migratory and non-migratory birds. This result is significant since several publications[1,95,135] have speculated over the evolutionary optimisation of Cry4a MFEs in organisms which make use of them. In particular, a cysteine (C317) and lysine residue (K320), both in close proximity to the tryptophan chain (see **Fig. 6.1**), are found to be conserved in the Cry4a proteins of night-migratory passerines,[95] while absent in chicken (*Gg*Cry4a), pigeon (*Cl*Cry4a) and quail (*Cc*Cry4a) cryptochromes.

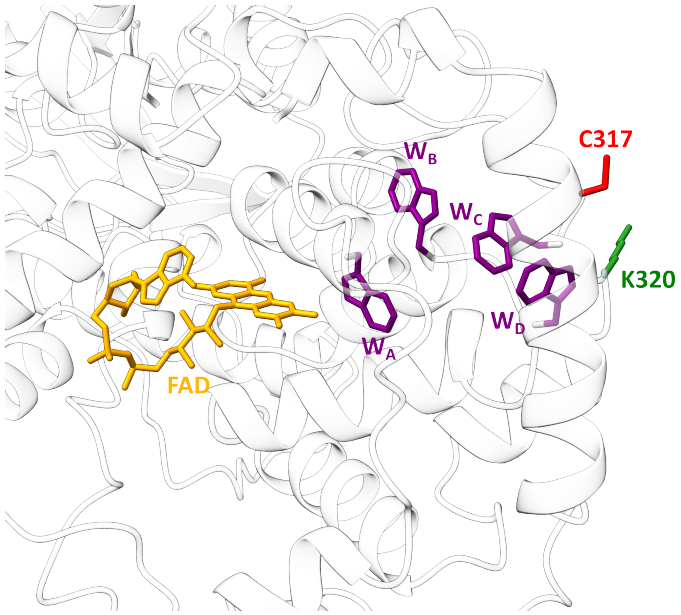

Figure 6.1: Structure of a robin wild type cryptochrome protein (*Erithacus rubecula*, *Er*Cry4a WT). Key components of electron transfer chain indicated with the FAD chromophore highlighted in orange and the four tryptophans (W_A/W395, W_B/W372, W_C/W318 and W_D/W369) highlighted in purple. The evolutionarily conserved C317 and K320 residues, present in all night-migratory passerines, are shown in red and green respectively. Both C317 and K320 lie in close proximity to W_C and W_D.

The conservation of the C317 residue is particularly noteworthy since cysteine residues have been found to influence electron and proton transfer interactions in proteins and

peptides.[136–138] Specifically, cysteine is thought to gate electron transfer in the WT *Drosophila melanogaster* cryptochrome (*Dm*Cry WT) by influencing the redox environment around FAD.[139,140] In a similar vein, the conservation of a positively charged (at physiological pH) lysine residue (K320) in night-migratory passerines versus the negatively charged glutamic acid (E320) residue observed in *Gg*Cry4a, *Cl*Cry4a and *Cc*Cry4a, marks a potential major shift in the local redox environment. Consequently, the efficiency of electron transfer, recombination and tryptophan deprotonation may be affected. Therefore, if the local environment around W_C and W_D is sufficiently different, mutations of these residues should influence radical yields, kinetics and thus MFEs.

In addition to the speculative role of C317 and K320, recent results by Xu *et al.* found that mutation of the terminal tryptophan (W_D, W369) with a phenylalanine (F), leading to FAD-W_C photoinduced RPs, resulted in markedly enhanced MFEs.[1] Naturally this prompts the question of why four tryptophans are favoured in avian cryptochromes? Wong *et. al.* attempted to address this by way of a composite RP, formed by an equilibrium between FAD-W_C and FAD-W_D RPs.[1,135] The argument generally consisting of an interplay between the magnetic sensing capabilities of the FAD-W_C RP and the potential signalling capabilities of the FAD-W_D RP. If the composite RP exists, mutations of neighbouring amino acid residues (*i.e.* positions 317 or 320) may influence the FAD-W_C/FAD-W_D equilibrium, by stabilising one RP over the other, thus altering measurable MFEs.[135]

With this in mind, the role C317 and K320 play in the cryptochrome RPM, and thus magnetic sense, was studied by way of single-point mutations of *Gg*Cry4a WT in which the arginine (R) in position 317 and the glutamic acid (E) in position 320 were exchanged for their *Er*Cry4a WT counter parts, C and K respectively. These results were compared to *Gg*Cry4a WT and *Gg*Cry4a W369F (see **Chapter 5**) measurements to see if: i) the MFE enhancements observed in *Er*Cry4a W369F occur in other cryptochromes and ii) whether the single-point mutations influence MFE development and/or any potential composite RP equilibrium.

6.1 Methods

This project was a collaborative project led by the author and fellow DPhil student Jamie Gravell. Further contributions were made by several group members with a variety of spectroscopic techniques utilised in the study. Discussed here are only techniques which the author was directly involved in. Additional techniques utilised in the study that will not be discussed in detail are EPR (DPhil student Tommy Pitcher) and fluorescence microscopy (Jamie Gravell). The detailed results from these techniques may be found in Gravell and Murton *et al.*[117]

All cryptochrome proteins were expressed and purified by our collaborators in Oldenburg.[1] Dilute spectroscopic samples were prepared in pH 8 tris buffer consisting of 20 mM Tris, 250 mM NaCl and 20% glycerol (V/V). In light of the results discussed in **Chapter 5**, molecular oxygen was used as a reoxidant throughout.

6.1.1 Transient Absorption Spectroscopy

Transient absorption (TA) spectroscopy is, perhaps, the quintessential pump-probe spectroscopic technique where a system is photoexcited (by a short-pulsed pump beam) with the resulting photophysics/photochemistry monitored by a weaker, probe, beam at some time after photoexcitation. In TA spectroscopy, ultrashort laser pulses (typically, fs - ps) are used to photoexcite a system which subsequently evolves over some period of time (Δt) before another ultrashort laser pulse, often broad-band, probes the state of the system (*e.g.* by absorption). Changes in the system, due to photoexcitation, may be characterised by the change in absorption, $\Delta A = A_{t=\Delta t} - A_{t=0}$ (*cf.* BBCEAS **Chapter 3**). By taking a series of ΔA measurements at varying pump-probe delays (PPD, Δt), the kinetic evolution of photoinduced species may be mapped out. A simplified schematic of the TA experiment is shown in **Fig. 6.2**.

TA spectroscopy data was obtained using an Ultrafast Systems EOS spectrometer following the protocol reported in the supporting information of Xu *et al.*[1] Briefly, samples were photoexcited at 450 nm by way of a mode-locked, 355 nm, Nd:YAG laser (Ekspla PL2210) pumped optical parametric generator (OPG, Ekspla PG403) which yielded 30 μJ pulses at

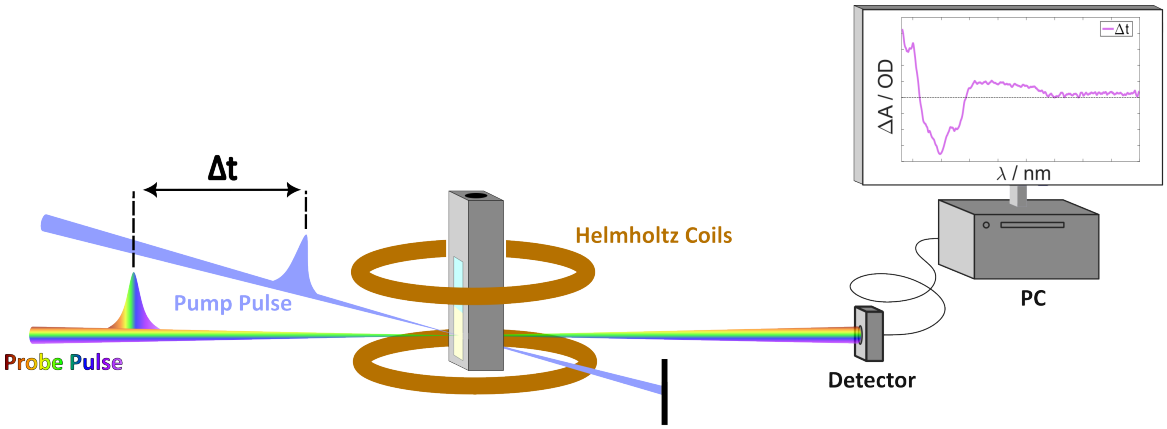

Figure 6.2: Simplified schematic of a transient absorption spectroscopy experiment. The absorption of the sample is measured, by way of a probe pulse, at some time Δt after photoexcitation from a pump pulse. Changes in the system, due to photoexcitation, are characterised by the change in absorption following photoexcitation, $\Delta A = A_{t=\Delta t} - A_{t=0}$. Kinetic profiles are constructed from a series of ΔA measurements at varying pump-probe delays (Δt). The spectrum shown inset is a ΔA spectrum from *Gg*Cry4a WT, taken from **Fig. 6.4 a**.

a rep-rate of 1 kHz. The probe beam was provided by a 2 kHz supercontinuum (SC) white light laser with a spectral range of 350 nm - 900 nm. The samples were cooled to 278 K, by an Oxford Instruments cryostat. External magnetic fields (25 mT) were provided by a set of home-built Helmholtz coils.

Measurements were made by acquiring the transmission of the SC probe through the sample prior to photoexcitation and then following photoexcitation, after some PPD, with and without an applied external magnetic field. Kinetic profiles of the resulting ΔA and $\Delta\Delta A$ (*cf.* **Chapter 3**) spectra were constructed by varying the PPD. For each data point measured (PPD and field on or field off) signals were collected for 15 s followed by a 3 min delay before moving onto the next point. In order to minimise the effects of photodegradation, field on and off measurements were made for each PPD in a sequence of (field) on-off-off-on cycles.

The protein samples measured here were prepared to a concentration of approximately 65 μM (corresponding to an absorbance at 450 nm $A_{450\,nm} = 0.65$) and air-equilibrated prior to measurement. Samples were prepared by the author and Jamie Gravell. The TA data was acquired by Dr. Kevin Henbest and analysed by the author.

6.1.2 Broad-band Cavity Enhanced Absorption Spectroscopy

Since the full details of the BBCEAS experimental procedure have already been discussed in **Chapter 3**, only specific experimental conditions will be mentioned here. All samples were photoexcited continuously with *ca.* 3.82 kW m^{-2} (3 mW, *ca.* 1 mm beam diameter) over a period of 10 s. Concurrently, the cavity and sample were continuously probed by a SC source with the light transmitted through the cavity detected by a CCD with an exposure time, and thus time resolution, of 1 ms. During the photoexcitation cycle a magnetic field was symmetrically modulated on and off with a period of 200 ms. Varying field strengths and polarities were applied randomly from the set of desired field values with a different magnetic field applied for every 10 s illumination cycle. After photoexcitation, the sample was allowed to reoxidise in the dark for 60 min. A ground state spectrum was acquired before every photoexcitation period. All BBCEAS protein samples were prepared to a concentration of approximately 30 μM and were run at 278 K under an oxygen atmosphere (applied by an O_2 filled balloon).

6.1.3 Continuous Illumination

The continuous illumination experiment set-up and general protocol was introduced in *ca.*xtbfChapter 5.3. In short, protein samples were prepared to a concentration of approximately 25 μM and air-equilibrated. Radicals were generated by 60 s of 3 mW (*ca.* 25 Wm^{-2}) illumination from a 450 nm LED (see **Fig. 5.3**). The (dark) decay of long-lived photoproducts back to their ground state was monitored with Carey 60 UV/Vis spectrometer. Spectra (300 nm - 800 nm) were recorded at 75 s intervals after illumination. Irradiation experiments were done in collaboration with Jamie Gravell.

6.2 Results

Before any samples were studied by time-resolved spectroscopic measurements, the proteins condition was evaluated by native mass spectrometry (MS)[as] and basic UV/Vis spectroscopy. The native MS confirmed that all proteins were almost exclusively monomeric with the FAD cofactor bound to the protein[117] The UV/Vis measurements (**Fig. 6.3**) provided further

[as]Measured by DPhil student Angela Gherkins

evidence of FAD binding within the protein due to the clear vibrational fine structure of their absorption profiles between 300 nm and 500 nm. Moreover, the absence of any features above 500 nm confirmed that the protein was fully oxidised prior to time resolved spectroscopic measurements.

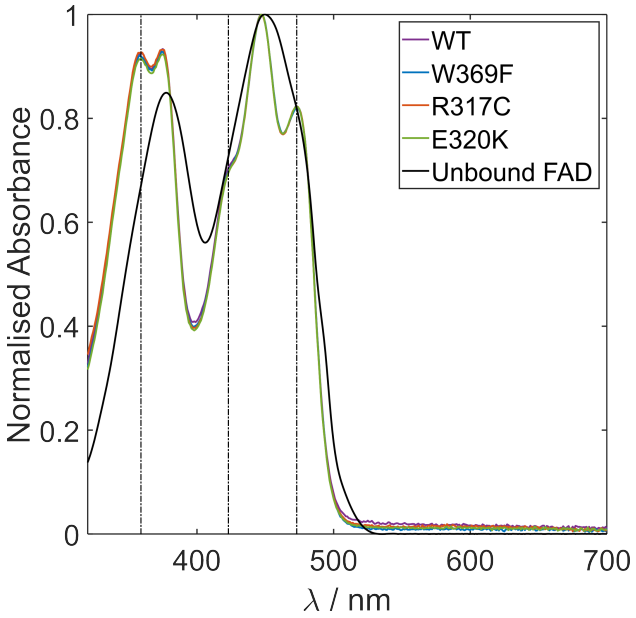

Figure 6.3: UV/Vis spetcra of *Gg*Cry4a WT (purple line), *Gg*Cry4a W369F (blue line), *Gg*Cry4a R317C (orange line) and *Gg*Cry4a E320K (green line) solutions. The spectrum of free, unbound, FAD (black line) is shown for comparison. Successful binding of FAD within the cryptochrome is indicated by the vibrational fine structure (vertical dotted lines) at approximately 359 nm, 423 nm and 474 nm.

With the condition of the proteins assessed, electron paramagnetic resonance (EPR) spectroscopy (by Tommy Pitcher) was used to identify the SCRP in each of the cryptochromes. More specifically, a combination of transient EPR (TrEPR) and out-of-phase electron spin echo envelope modulation (OOP-ESEEM) was used to determine the spin polarisation, inter-radical separation and spin-spin interactions. TrEPR operates in a similar manner to TA spectroscopy in that the system is photoexcited (thus generating a SCRP), and then probed with a secondary radiation source, microwave in this instance. The resulting spectrum exhibits absorptive and emissive features which indicate the spin polarisation of the SCRP. The fine structure of these transitions arise from the combination of spin-spin interactions, such as dipolar and exchange interactions, HFC interactions, Zeeman interactions, and the relative orientation of the two radicals in the SCRP.[1,141,142] OOP-ESEEM is a pulsed EPR technique which measures dipolar and exchange interactions. In brief,

shortly after photoexcitation, a $\pi/2$ and then π microwave pulse is applied. The intensity of the resulting echo signal[25] depends on the delay between the two microwave pulses. By incrementally varying this delay, an oscillatory OOP-ESEEM trace may be constructed where the frequency of oscillation directly depends on the strength of exchange and dipolar interactions and thus inter-radical separations $\left(r(\text{Å}) = \sqrt[3]{-7.84 \times 10^4 / D(\text{MHz})}\right)$.[143–146] Neither the TrEPR or OOP-ESEEM data is shown here since it was not measured nor analysed by the author. However, as the results are pertinent to the TA and BBCEAS discussion below, it suffices to simply state them while referring the reader to Gravell and Murton *et al.*[117]

The TrEPR for all four proteins exhibited distinctive anti-phase absorption-emission-absorption-emission signals, indicative of a singlet born SCRP.[1,147,148] Furthermore, simulations of the TrEPR spectra were consistent with an $FAD^{\bullet-}$-$WH^{\bullet+}$ SCRP.[117] Meanwhile, the OOP-ESEEM traces for all three proteins containing the full tryptophan tetrad were identical, within signal-to-noise, yielding an inter-radical separation of *ca.* 21 Å. In contrast, the OOP-ESEEM for *Gg*Cry4a W369F exhibited a higher oscillation frequency, reflecting a shorter inter-radical separation of 17.75 Å. Upon comparison with FAD and W centre-to-centre separations, estimated from a *Gg*Cry4a WT homology model, it is clear that the *Gg*Cry4a WT, *Gg*Cry4a R317C and *Gg*Cry4a E320K proteins form an FAD-W_D RP (centre-to-centre distance = 21.4 Å) while *Gg*Cry4a W369F forms an FAD-W_C RP (centre-to-centre distance = 17.7 Å). These results are summarised in **Table 6.1**.

Protein	D / MHz	r / Å
*Gg*Cry4a WT	-8.37 ± 0.03	21.04 ± 0.03
*Gg*Cry4a R317C	-8.46 ± 0.03	20.97 ± 0.03
*Gg*Cry4a E320K	-8.51 ± 0.03	20.93 ± 0.03
*Gg*Cry4a W369F	-13.95 ± 0.07	17.75 ± 0.03

Table 6.1: Dipolar (D) coupling constants, and thus radical pair separation (r), obtained from out-of-phase electron spin echo envelope modulation spectroscopy. Data measured by DPhil student Tommy Pitcher. Experimental and simulation details can be found in Gravell and Murton *et al.*[117]

6.2.1 Transient Absorption Spectroscopy

Transient Absorption spectroscopy was used to monitor the lifetimes and kinetic evolution of photoproducts, following electron transfer, on a nanosecond time scale. The ΔA spectra, at a variety of pump-probe delays (PPDs), for all four systems can be seen in **Fig. 6.4**. Immediately following the laser flash (0.3 ns - 1 ns), all four proteins are characterised by a negative ground state bleach (GSB) signal between 400 nm and 500 nm which is accompanied by positive absorption features below 400 nm and above 500 nm. Upon comparison with **Fig. 2.9 b** it is clear that these positive photoinduced absorption signals indicate the formation of RP1, *i.e.* $WH^{\bullet+}$ and $FAD^{\bullet-}$. Specifically, the positive absorption below 400 nm marks the formation of $FAD^{\bullet-}$ while the positive absorption band between 500 nm and 650 nm arises due to, predominantly, $WH^{\bullet+}$ formation (with a minor $FAD^{\bullet-}$ contribution from 500 nm - 550 nm). The broad signal above 650 nm is attributed to absorption from small amounts of ^{1}FAD* and ^{3}FAD*, the latter of which is thought to result from a minor fraction of misfolded protein in which intersystem crossing (ISC) in the excited FAD cofactor can compete with electron transfer.

In all three proteins containing the full electron transfer chain (ETC) (*Gg*Cry4a WT, *Gg*Cry4a R317C and *Gg*Cry4a E320K), the $FAD^{\bullet-}$ and $WH^{\bullet+}$ absorption features decay to zero (within signal-to-noise) within 1 μs, in conjunction with the recovery of the GSB, thus indicating efficient singlet recombination of the SCRP. Conversely, *Gg*Cry4a W369F displays a time dependant spectral shape change above 500 nm (**Fig. 6.4 d**), attributed to the deprotonation of $WH^{\bullet+}$ forming $W^{\bullet}$ which persists beyond the maximum measurement time (1 μs). Consequently, a positive $FAD^{\bullet-}$ signal ($<$ 400 nm), and thus GSB, persists due to the loss of its recombination partner. Therefore, *Gg*Cry4a W369F efficiently forms an uncorrelated $FAD^{\bullet-}/W^{\bullet}$ RP, termed RP2, and hints at a greater competition between singlet recombination and $WH^{\bullet+}$ deprotonation within this system.

This shift to efficient RP2 formation, versus singlet recombination, is reflected in the kinetic evolution of the ΔA spectra. The normalised kinetics of all four proteins, averaged between 500 nm and 550 nm to improve signal-to-noise, are shown in **Fig. 6.5**. Each trace has been

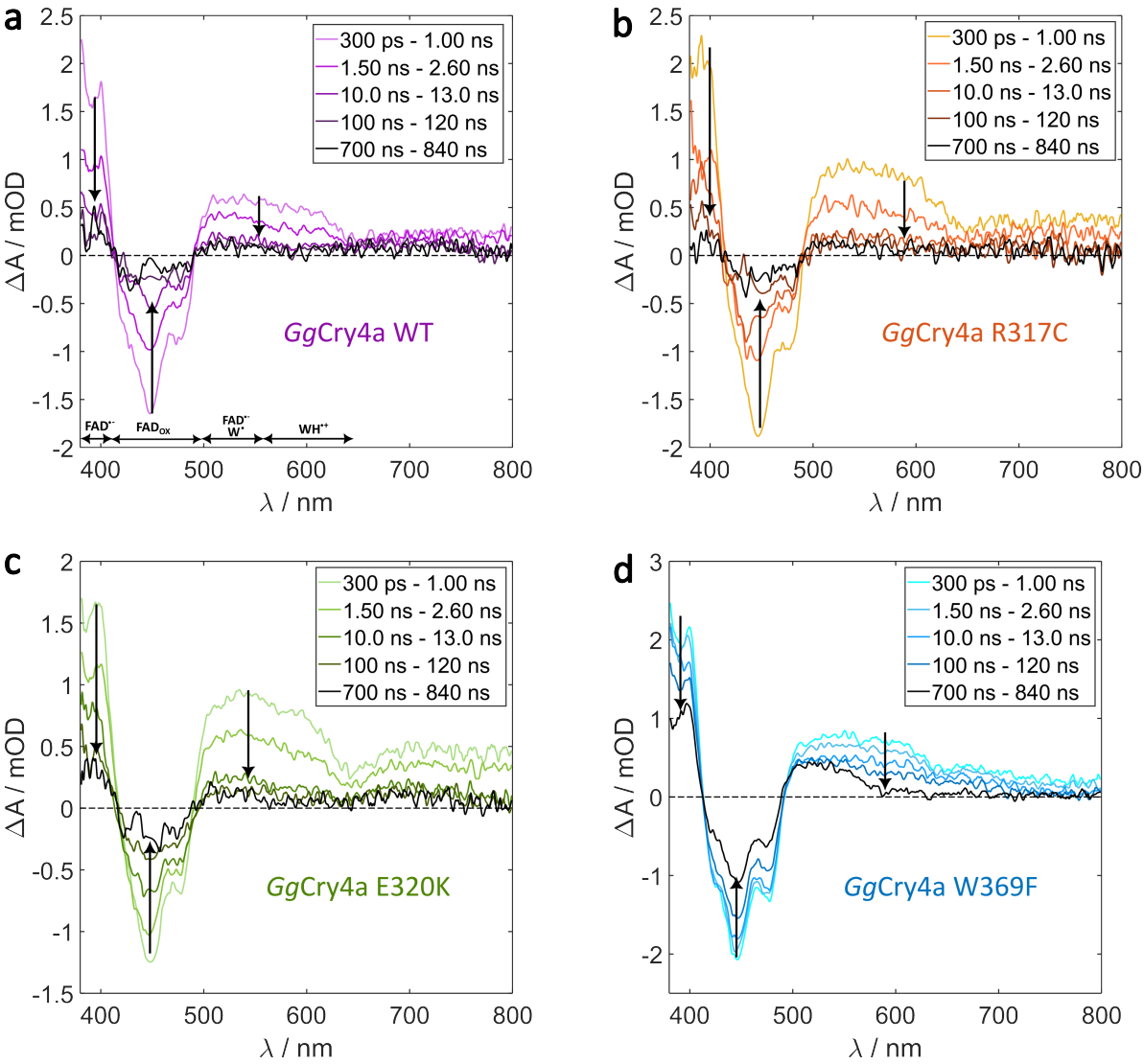

Figure 6.4: Transient absorption spectra, ΔA, at a series of pump-probe delays following 450 nm photoexcitation (80 ps pulse), for the air-equilibrated *Gg*Cry4a WT (a), *Gg*Cry4a R317C (b), *Gg*Cry4a E320K (c) and *Gg*Cry4a W369F (d) proteins. All spectra are averaged over the time-windows given in the corresponding legend. At the bottom of panel (a), a rough guide indicates which species contribute most to the spectra at a given wavelength. The feature between 500 nm and 650 nm is ascribed to absorption by $FAD^{\bullet-}$ and $WH^{\bullet+}$. The absorbance centered at 750 nm is assigned to a combination of ^{1}FAD* and ^{3}FAD*. The latter is only observed in a (minor component of) misfolded protein in which intersystem crossing out-competes electron transfer.

fit to a biexponential function with a constant offset applied to account for the formation of photoproducts whose lifetimes significantly exceed the experiment time.

Since the 500 nm - 550 nm spectral region predominantly reflects the evolution of $FAD^{\bullet-}$ and $WH^{\bullet+}/W^{\bullet}$, the lifetimes (**Table 6.2**) extracted from the biexponential fits in **Fig. 6.5** qualitatively describe the lifetimes of those species. All four proteins exhibit a fast decay ($\lesssim$ 2 ns) component followed by a significantly slower component. A recent study by Timmer *et al.* showed that the efficiency of forward electron transfer steps decreases as

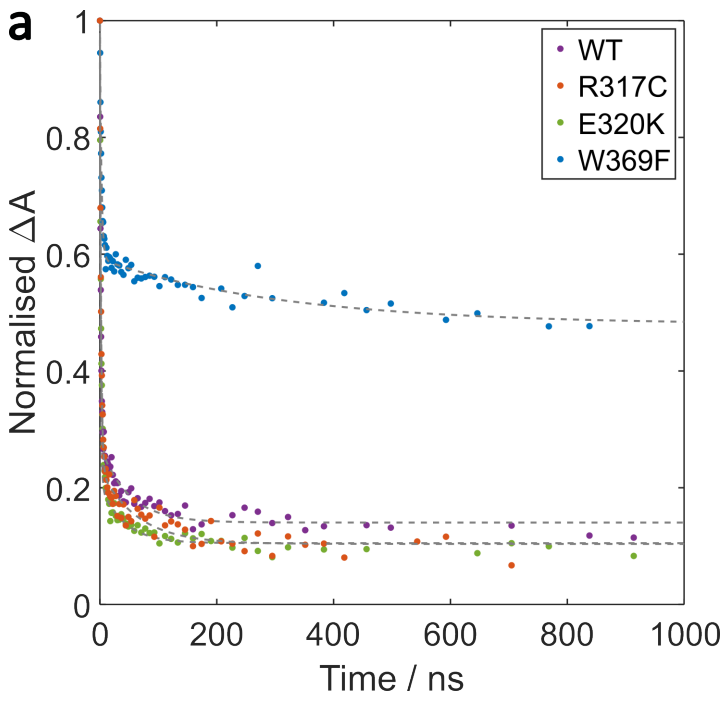

Figure 6.5: Normalised ΔA kinetics of *Gg*Cry4a WT (purple), *Gg*Cry4a W369F (blue), *Gg*Cry4a R317C (red), and *Gg*Cry4a E320K (green) proteins, wavelength-averaged between 500 nm - 550 nm. The ΔA in this region is dominated by $FAD^{\bullet-}$, $WH^{\bullet+}$ and $W^{\bullet}$ absorbance. Kinetic fits to each data set are shown in grey. Fitting parameters are provided in **Table 6.2**.

Protein	τ_1 / ns	τ_2 / ns
*Gg*Cry4a WT	1.5 ± 0.01	60 ± 4.9
*Gg*Cry4a R317C	2.0 ± 0.01	63.9 ± 5.2
*Gg*Cry4a E320K	1.9 ± 0.01	40 ± 2.4
*Gg*Cry4a W369F	1.7 ± 0.01	299 ± 15

Table 6.2: TA lifetimes of all four proteins estimated by kinetic fitting of the ΔA decay curves, averaged between 500-550 nm, shown in **Fig. 6.5**. All decays were fit to a biexponential function with a constant offset to account for long-lived photoproducts.

charge separation proceeds along the tryptophan tetrad in *Er*Cry4a WT.[56] Consequently, the decay of intermediate RPs in the ETC could contribute to the kinetic profiles observed by TA spectroscopy. Furthermore, TA measurements of *Er*Cry4 W318F, in which the third tryptophan residue has been exchanged for phenylalanine, exhibited a dominant 2.5 ns decay lifetime.[1] Naturally, this was assigned to $FAD^{\bullet-}$ and $W_BH^{\bullet+}$ (W372) recombination, due to the shortening of the ETC.[1] Therefore, it seems logical to assign the *ca.* 2 ns component observed here to $FAD^{\bullet-}/W_BH^{\bullet+}$ recombination while noting that such a lifetime approaches the time resolution of the experiment. It therefore follows that τ_2 reflects the decay of the longer-lived magnetosensitive SCRP. Interestingly, *Gg*Cry4a W369F exhibits a

significantly longer τ_2 compared to the other three proteins. As a consequence, a boost in the yield of long-lived species is observed, reflecting the efficient formation of RP2.

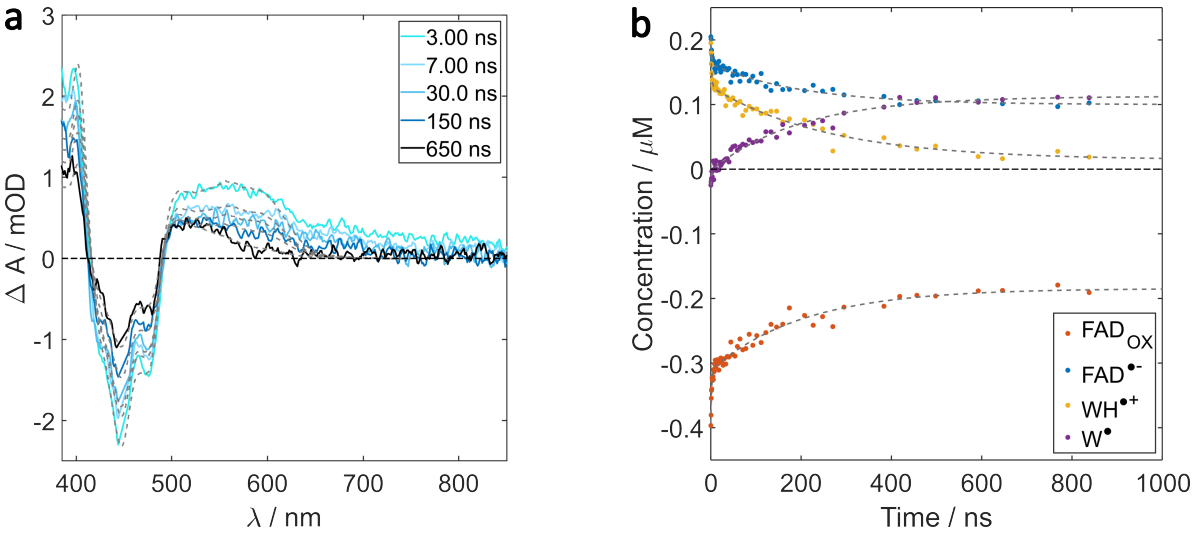

Figure 6.6: a) *Gg*Cry4a W369F global analysis spectral fit results (grey dotted lines) and ΔA spectra (blue lines) at several time points. Global analysis generally fits the data well. b) *Gg*Cry4a W369F global analysis results showing the formation of $W^{\bullet}$ from $WH^{\bullet+}$ and the corresponding partial decay of $FAD^{\bullet-}$ and GSB recovery. Note the matching persistent concentrations of $W^{\bullet}$, $FAD^{\bullet-}$ and FAD_{OX}.

To confirm this interpretation of *Gg*Cry4a W369F, global analysis (*cf.* **Appednix A.3**) was utilised to extract the kinetic evolution of the individual absorbing species. The fitting results are shown in **Fig. 6.6 a** with the extracted species kinetics shown in **Fig. 6.6 b**. In line with the discussion above, the global analysis shows clear formation of $W^{\bullet}$ concurrently with the decay of $WH^{\bullet+}$. Simultaneously, $FAD^{\bullet-}$ decays and plateaus at a concentration approximately equal to that of the formed $W^{\bullet}$. This indicates that $WH^{\bullet+}$ decays *via* recombination with $FAD^{\bullet-}$ and deprotonation to form $W^{\bullet}$. That is, once all of the $WH^{\bullet+}$ has decayed, $FAD^{\bullet-}$ no longer has a recombination partner and persists at a concentration equal to the product of the alternate $WH^{\bullet+}$ decay pathway, $W^{\bullet}$. This is further reflected when fitting the kinetics of each species with a biexponential function, the results of which are shown in **Table 6.3**. Clearly, all species essentially evolve with the same dynamics and rates. FAD_{OX} recovers in line with the decay of $FAD^{\bullet-}$ and $WH^{\bullet+}$, indicating recombination. Likewise, $W^{\bullet}$ grows in on a similar timescale to the $WH^{\bullet+}$ decay, indicating deprotonation of the latter. It thus appears that, in the case of *Gg*Cry4a W369F, singlet recombination of the SCRP and RP2 formation occur on a similar time scale, suggesting efficient competition between k_S and k_T. Due to insufficient time points within the signal-

to-noise, similar analysis was not possible for the other three proteins.[at] However, from their rapid decay and lack of significant $W^{\bullet}$ formation (*cf.* **Fig. 6.4** and **Table 6.2**), it seems that singlet recombination is much more rapid in these systems, despite the greater inter-radical separation (*cf.* **Table 6.1**). This could indicate that back-electron transfer is in the Marcus inverted region, which has been observed in some flavoproteins,[149] however more evidence is required to truly make such a claim.[au]

Species	τ_1 / ns	τ_2 / ns
$FAD^{\bullet-}$	1.9 ± 0.41	201 ± 26.4
FAD_{OX}	1.9 ± 0.32	204 ± 20.8
$WH^{\bullet+}$	2.0 ± 0.33	260 ± 27.9
$W^{\bullet}$	1.9 ± 0.91	198 ± 17.3

Table 6.3: Biexponential fits to the individual species kinetics extracted by global analysis (**Fig. 6.6**). All species evolve on a similar timescale, indicating similar singlet recombination and $WH^{\bullet+}$ deprotonation rate.

TA spectroscopy was further utilised to study the formation and dynamics of any MFEs within the proteins. Similarly to BBCEAS, MFEs are characterised by their $\Delta\Delta A$ which is defined as,

$$\Delta\Delta A(t) \;=\; \Delta A(t, B_0 = 25\text{ mT}) - \Delta A(t, B_0 = 0\text{ mT}). \tag{6.1}$$

As indicated by the EPR results, SCRPs are singlet-born in all four proteins. As such, the application of strong (greater than the RPs effective HFC), 25 mT, magnetic fields will decrease the rate of ST mixing, causing greater recombination and thus a negative MFE on the SCRP concentration and any subsequent photoproducts. As such, TA $\Delta\Delta A$ results are expected to be negative. This is indeed observed as shown in **Fig. 6.7** which shows the time-resolved $\Delta A(t, 25\text{ mT})$ (light blue) and $\Delta A(t, 0\text{ mT})$ (blue) traces for *Gg*Cry4a W369F, averaged between 500 nm and 650 nm. The subtraction, $\Delta\Delta A$ (maroon), is also displayed. As expected, the application of a 25 mT magnetic field lead to a reduction in the radical yield and thus absorption over time. The MFE develops on a similar time scale to that of the individual radical kinetics (*cf.* **Fig. 6.6**) and persists beyond the measurement

[at] For these three proteins the radical signal has almost decayed to zero within 50 ns. Consequently, the fit for the rest of the 1 μs acquisition is to noise and yielded unphysical results for these time points.
[au] This is an ongoing project with some temperature dependent TA experiments underway.

time, thus indicating that the MFE has been inherited by $W^{\bullet}$ following decay of the SCRP. Notably, the MFE does not develop until after the initial sharp (*ca.* 2 ns) drop in the radical absorbance. This is expected since a 25 mT magnetic field (corresponding to a 700 MHz Larmor frequency) does not have sufficient time to significantly effect the spin-mixing on such a short time scale. It is, therefore, unsurprising that TA spectroscopy proved to lack the sensitivity required to reliably discern MFEs in the other three proteins. With this in mind, BBCEAS experiments were employed to study the MFEs within these proteins with far greater sensitivity whilst addressing the radical dynamics on a longer timescale.

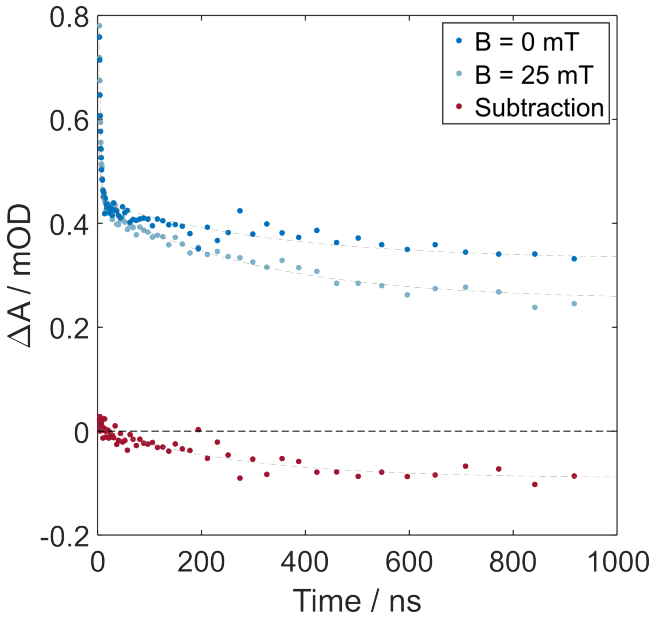

Figure 6.7: *Gg*Cry4a W369F ΔA traces, averaged from 500 nm - 550 nm, obtained in the absence (blue) and presence (grey/blue) of a 25 mT external magnetic field. The subtraction of these traces, $\Delta\Delta A(B_0,t) = \Delta A(B_0 = 25\ mT, t) - \Delta A(B_0 = 0\ mT, t)$, is shown in maroon and characterises a MFE. A gray dashed line is included as a fit to guide the eye.

6.2.2 BBCEAS

Broad Band Cavity Enhanced Absorption Spectroscopy (BBCEAS) has been shown ideally suited to measure magnetic field effects as low as < 1 % (and $\Delta\Delta A$ values of the order of 10^{-6}).[1,76,77] The BBCEAS ΔA results of *Gg*Cry4a WT are shown in **Fig. 6.8**. Under the illumination conditions employed with this technique, the GSB (410 nm - 500 nm) and radical absorbance ($>$ 500 nm) concomitantly decrease and increase, respectively (**Fig. 6.8 a**). Over time, the system is driven ever further towards the long-lived photoproducts, tending to a stationary state which is not achieved within the experiment time. The globally extracted accumulation kinetics of the *Gg*Cry4a WT spectra (*cf.* **Appendix A.3**) indicate

that the dominant absorbing species in the 500 nm -750 nm region are $W^{\bullet}$, $FAD^{\bullet-}$ and $FADH^{\bullet}$ (**Fig. 6.8 b**). This finding is in agreement with the TA results discussed above, where $FAD^{\bullet-}$ and $W^{\bullet}$ were identified as RP2 in *Gg*Cry4a W369F, with $FADH^{\bullet}$ being subsequently generated by (slow) proton transfer beyond the 1 μs time window. As all four proteins exhibited broadly similar ΔA spectra and dynamics (*cf.* **Fig. 5.10 and 5.15**), only the WT is shown here.

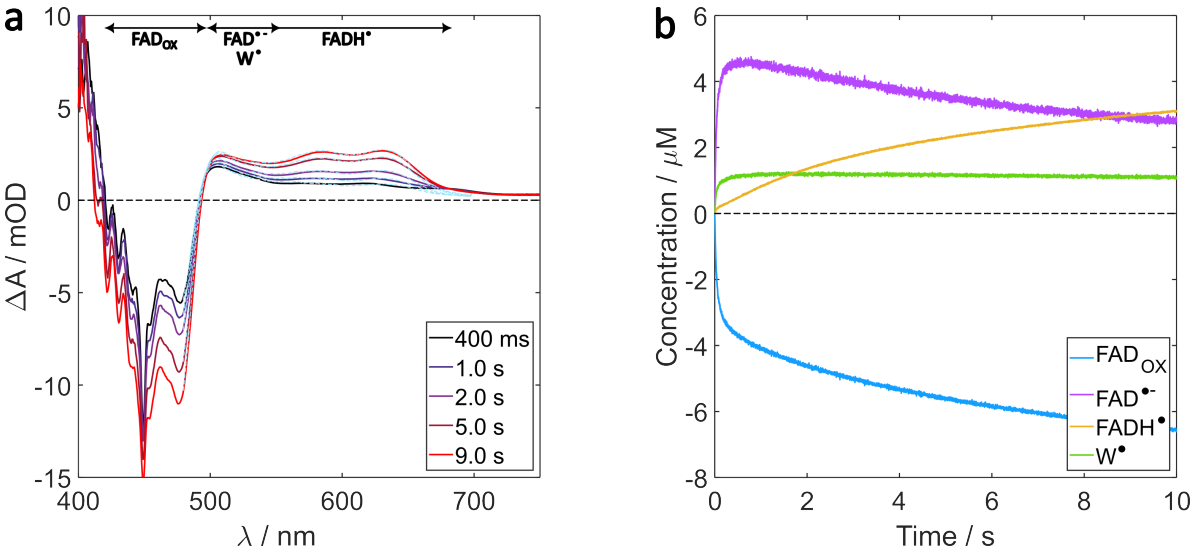

Figure 6.8: a) BBCEAS ΔA results of *Gg*Cry4a WT where each line is a slice through a wavelength by time ΔA surface with 1 ms time and 0.5 nm wavelength resolution. Species contributing to the absorption in different regions of the spectra are indicated at the top of the plot. Dashed lines show the global analysis fit results leading to the the extracted species kinetics in (b). Predicted $WH^{\bullet+}$ contribution was zero.

Based on the BBCEAS ΔA spectra, EPR and TA results, a negative $\Delta\Delta A$ spectrum dominated by an $FADH^{\bullet}$ MFE^{av} is expected for all four proteins. This is indeed the case as observed in **Fig. 6.9 a** which shows the wavelength resolved, time-averaged $\Delta\Delta A$ spectra ($B_0 = 30$ mT) of *Gg*Cry4a WT, R317C, E320K and W369F. All four exhibit purely negative MFEs across the 500 nm – 750 nm wavelength region, confirming that the long-lived, field-sensitive, photoproducts originate from singlet-born SCRPS. In each case the $\Delta\Delta A$ spectrum broadly resembles the absorption spectrum of $FADH^{\bullet}$, generally reflecting their ΔA spectra. On a time scale of seconds, the 30 mT applied magnetic field thus most significantly impacts the concentration of the neutral flavin radical, itself a product of protonation following initial formation of $FAD^{\bullet-}$ *via* electron transfer. Spectral deconvolution of the *Gg*Cry4a WT

[av]Since $FADH^{\bullet}$ has the largest extinction coefficient of all the the species in **Fig. 6.8** above 500 nm (*cf.* **Fig. 2.9**).

time-averaged $\Delta\Delta A$ spectrum (**Fig. 6.9 b**) confirms this assignment, yielding only a minor additional $\Delta\Delta A$ contribution from $W^{\bullet}$. The dominance of $FADH^{\bullet}$ on the $\Delta\Delta A$ spectrum can be further understood by consideration of **Fig. 6.8 b** where $FADH^{\bullet}$ continuously accumulates throughout the measurement period. In contrast, the concentration of $W^{\bullet}$ rises on a sub-second time scale before seemingly reaching a steady state throughout the rest of the measurement period.

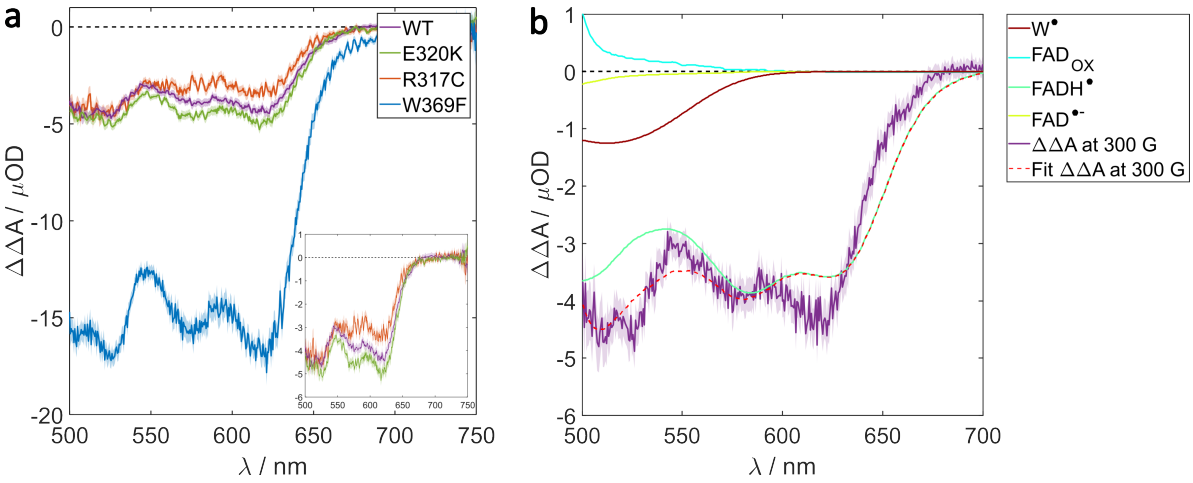

Figure 6.9: a) $\Delta\Delta A$ spectra obtained by BBCEAS on all four proteins, averaged over 10 s, using an applied magnetic field strength of 30 mT and a field switching period of 200 ms. b) Spectral deconvolution of *Gg*Cry4a WT time-averaged $\Delta\Delta A$ spectrum with major contribution from $FADH^{\bullet}$.

Interestingly, *Gg*Cry4a WT, R317C and E320K all exhibit very similar MFE magnitudes ($\Delta\Delta A_{500\,\mathrm{nm}-630\,\mathrm{nm}} \approx -4\ \mu$OD) with any differences arguably within batch-to-batch sample variations. The only sample with any notable difference is *Gg*Cry4a W369F, which exhibits a substantially increased MFE ($\Delta\Delta A_{500\,\mathrm{nm}-630\,\mathrm{nm}} \approx -16\ \mu$OD), in agreement with differences previously observed between *Er*Cry4a WT and *Er*Cry4a W369F by cavity ring-down spectroscopy.[1,aw]

In addition to the $\Delta\Delta A$ spectra, the MFE field dependence of all four protein was studied. **Fig. 6.10 a** shows the normalised wavelength averaged (500 nm - 630 nm) $\Delta\Delta A$ for all four proteins as a function of the applied static magnetic field strength. Each protein exhibits a Lorentzian-like dependence on B_0, characteristic of HFC driven ST mixing of a SCRP. The $B_{1/2}$ values for each protein, estimated by fitting the data with a Lorentzian (equation 4.2), are shown in **Fig. 6.10 b**. As mentioned in previous chapters, this parameter

[aw] MFE experiments using confocal microscopy and continuous illumination exhibited the same MFE relationship between these proteins, demonstrating that this result is consistent across different experimental methods.Confocal microscopy experiments carried out by Jamie Gravell.[117]

reflects the extent of HFC within the SCRP *via* the Weller formula, which predicts a $B_{1/2}$ of approximately 3 mT for an FAD-W SCRP. Thus, complementing the EPR results mentioned above, all four species exhibit a $B_{1/2}$, consistent with an FAD-W SCRP with contributions from spin-relaxation during the RP lifetime.[41,87] While one could argue statistical significance between some of the $B_{1/2}$ values in **Fig. 6.10 b**, batch-to-batch variations in cryptochrome samples can often lead to more significant variations in the measured data. As such, no reasonable comment can be made on any changes to the spin dynamics between the four proteins. Nonetheless, BBCEAS confirms the formation of magnetically sensitive RPs in all four proteins. Furthermore, whilst the mutations near the tryptophan chain seem to have no detectable impact on the field effect size, the removal of the fourth tryptophan lead to a significant boost in the MFE, consistent with the TA data and results found in *Er*Cry4a.[1]

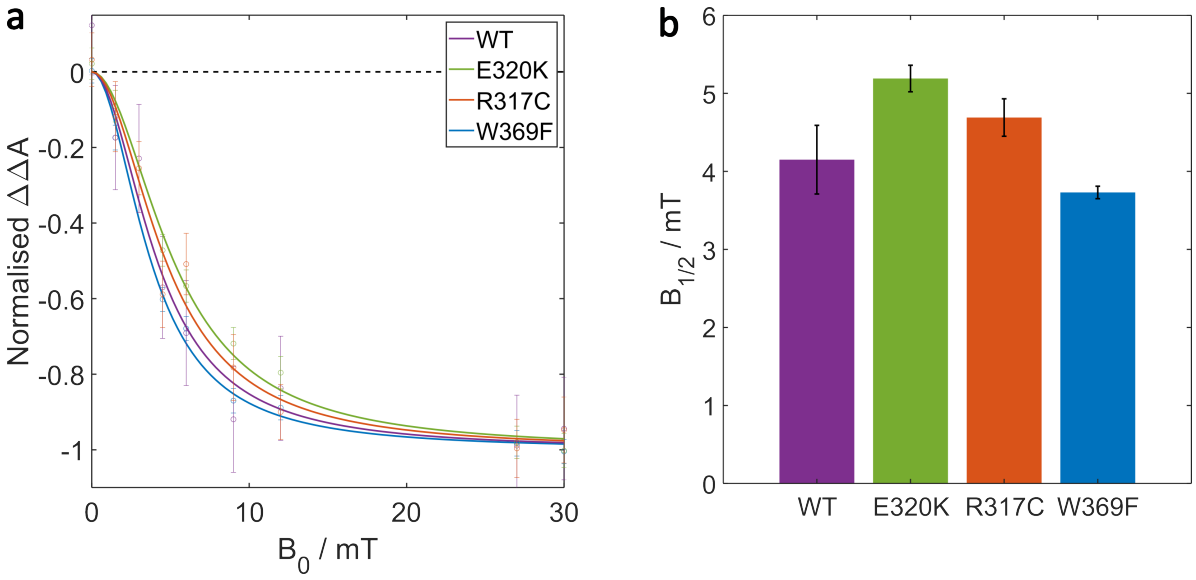

Figure 6.10: a) Normalised MARY curves obtained by applying a modulating magnetic field, with a switching period of 200 ms, at a variety of different field strengths (transparent circles) and calculating the time averaged (over 10 s illumination time) $\Delta\Delta A$ between 500 nm - 550 nm. The data are fit to single Lorentzian curves (solid lines). The data is normalised by $\Delta\Delta A_{sat}$, which is the $\Delta\Delta A$ when it no longer depends on applied field strength (*i.e.*, $B_0 \longrightarrow \infty$), and is obtained from the the Lorentzian fit. b) $B_{1/2}$ values for all four proteins estimated from the Lorentzian fitting in (a). The majority of variation is likely due to batch-batch variations rather than physically meaningful variations.

6.2.3 Continuous Blue Light Irradiation

BBCEAS relies on the efficient cycling of the system to measure MFEs. Without it, the proteins are rapidly bleached and stuck in the long-lived radical state, unable to generate

more SCRPs. Similarly, TA spectroscopy relies on the recovery of the system back to the ground state before re-excitation of the flavin to generate the magnetosensitive RP. Therefore, in order to test the samples recovery behaviour following $FADH^{\bullet}$ formation, and thus cycling capability, the proteins were subjected to one minute continuous exposure to 450 nm light. The purple solid line in **Fig. 6.11 b** show the resulting *Gg*Cry4a WT UV/Vis spectrum immediately after illumination. Like in BBCEAS, the pronounced absorption in the 500 nm - 700 nm region suggests the generation of $FADH^{\bullet}$. The $FADH^{\bullet}$ yield, normalised to their initial ground state absorption, and decay of all four proteins is shown in **Fig. 6.11 a**. The relative proportion of the $FADH^{\bullet}$ radical yield is larger in *Gg*Cry4a WT, R317C and E320K than W369F. This suggests that mutation of the fourth tryptophan for phenylalanine alters the efficiency of $FADH^{\bullet}$ formation. This observation is consistent with similar experiments carried out on *Er*Cry4a WT and *Er*Cry4a W369F by Xu *et al*.[1] Furthermore, these observations are loosely consistent with measurements conducted on single point mutants of *Dm*Cry where mutations to the tryptophan chain, in addition to residues neighbouring the tryptophan chain, were found to decrease both the photoreduction rate and overall yield under continuous illumination conditions.[137,139,150,151] However, these experiments monitored the formation of $FAD^{\bullet-}$, due to differences in redox states stabilised by these proteins, and thus may not reflect observations made herein. Nonetheless, the data does confirm that these systems are efficiently photoreduced, by a neighbouring amino acid, under moderate light intensity.

The reoxidation kinetics of the proteins were examined by fitting the data in **Fig. 6.11 a** with monoexponential functions, including a constant offset. The more rapid recovery of *Gg*Cry4a W369F ($\tau_{rec} = 41$ min) and *Gg*Cry4a E320K ($\tau_{rec} = 23$ min), relative to *Gg*Cry4a WT ($\tau_{rec} = 61$ min), suggest less stable $FADH^{\bullet}$. Conversely, replacement of arginine by a cysteine in *Gg*Cry4a R317C has little effect on the $FADH^{\bullet}$ decay rate ($\tau_{rec} = 64$ min). Global analysis of the spectral evolution after blue-light illumination, assuming a first order recovery involving only two species (*cf.* **Appendix A.3**), yielded decay associated spectra (DAS) consistent with reported $FADH^{\bullet}$ and FAD_{OX} spectra (**Fig. 6.11 b**, yellow and blue spectra respectively), confirming the spectral assignment above.[152] Additionally,

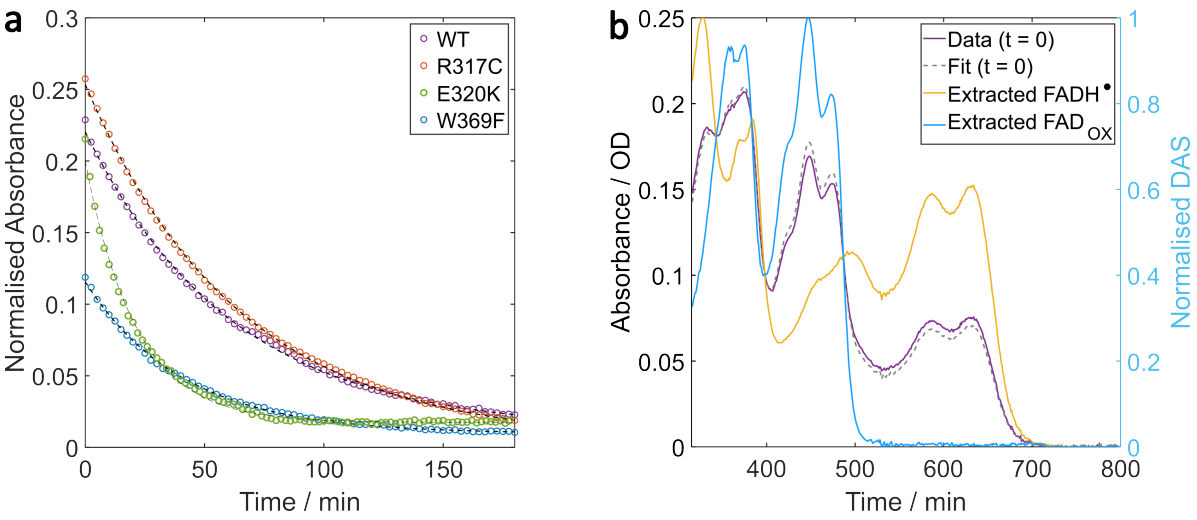

Figure 6.11: a) Kinetic evolution of irradiation data, following illumination, averaged over 605 nm and 615 nm to capture the reoxidation of $FADH^{\bullet}$. Data fitted with monoexponential functions, the results of which are shown in **Table 6.4**. b) Results from global analysis of the irradiation recoveries in (a). Extracted $FADH^{\bullet}$ and FAD_{OX} spectra shown in yellow and blue, respectively. Spectra broadly agree with Müller *et al.*[152]

the lifetimes obtained by this method agree well with the single exponential fits to the data, thus indicating FAD_{OX} recovery directly from $FADH^{\bullet}$. These results are summarised in **Table 6.4**.

Protein	Exponential Fit τ_{rec} / min	Global Analysis τ_{rec} / min
*Gg*Cry4a WT	61.42 ± 0.35	69.85 ± 2.65
*Gg*Cry4a R317C	64.22 ± 0.41	66.87 ± 3.45
*Gg*Cry4a E320K	23.28 ± 0.07	20.38 ± 1.56
*Gg*Cry4a W369F	40.90 ± 0.10	43.12 ± 0.48

Table 6.4: Time constants (τ_{rec}) obtained by monoexponential fitting of the $FADH^{\bullet}$ recovery, generated by continuous blue-light illumination, and global analysis of the spectral evolution. Both methods are in broad agreement and reflect FAD_{OX} recovery directly from $FADH^{\bullet}$.

6.3 Discussion

From the results presented above it is clear that *Gg*Cry4a WT and its mutants herein form a SCRP. Application of an external magnetic field sufficiently perturbed the HFC driven ST mixing in the SCRP to produce MFEs on the concentration of the SCRP and its downstream products. Along with the data presented in **Chapter 5**, these results are the first reported MFEs of any avian Cry protein where molecular oxygen was used to aid efficient photochemical cycling. This is a significant advancement in the study of MFEs in

Cry4a proteins since reoxidation by the more biologically relevant O_2 negates the use of FC.

While the reoxidation mechanism of flavin under oxygen remains unknown, previous studies on a thale cress cryptochrome (*Arabidopsis thaliana*, *At*Cry1) have suggested a mechanism where hydrogen peroxide is formed, *via* superoxide ($O_2^{\bullet-}$), following a reaction between $FADH^{\bullet}$ and O_2.[153] Such a mechanism would be consistent with models proposed for oxidase and mono-oxygenase flavoenzymatic systems.[154,155] In principle, this hypothesis could be tested by adding peroxide scavengers to Cry4a samples and monitoring their consumption as a function of dissolved O_2 concentration and/or illumination condition (intensity/exposure time). In addition to simple sample recovery by O_2, it has been suggested that the reaction of the fully reduced flavin ($FADH^-$) with O_2 could produce an alternative, $FADH^{\bullet}$-$O_2^{\bullet-}$, SCRP.[153] Nevertheless, Player and Hore showed that this SCRP, even if formed, is unlikely to contribute to the spin dynamics of the systems considered here due to rapid spin-relaxation driven by spin-orbit coupling in $O_2^{\bullet-}$.[156]

For the four proteins measured here, it appears that the mutations made to positions 317 and 320 have little impact on the evolution and spin dynamics of the SCRP. This is apparent in several ways. For example, the similarities observed in their BBCEAS MARY plots (**Fig.6.10**) suggest similar spin relaxation dynamics and HFC interactions between the *Gg*Cry4a WT, *Gg*Cry4a E320K and *Gg*Cry4a R317C SCRPs. Additionally, the *Gg*Cry4a WT, *Gg*Cry4a E320K and *Gg*Cry4a R317C SCRP kinetics, determined by TA spectroscopy (**Fig. 6.5**), showed similar lifetimes (τ_2, **Table 6.2**) with little impact from the mutation of residues 317 and 320. It is, therefore, unsurprising that the MFE spectra determined by BBCEAS are so similar in magnitude for these three proteins (**Fig. 6.9**).

Of course, as BBCEAS is a continuous illumination experiment, the asymmetric formation and termination reactions of $FADH^{\bullet}$ and $W^{\bullet}$ also influence the MFE spectra. As such, given the faster recovery of *Gg*Cry4a E320K in the irradiation experiments (**Table 6.4**), one could expect the MFE magnitude and spectral shape to differ in this protein *vs.* *Gg*Cry4a WT and *Gg*Cry4a R317C. Clearly this is not the case, implying a consistent ratio in the concentrations of $FADH^{\bullet}$ and $W^{\bullet}$ between the three proteins. Furthermore, the long-lived

radical yields in BBCEAS were all of a similar magnitude, which suggests comparable long-lived radical dynamics. These differences could arise from the different oxidation conditions employed, with BBCEAS utilising an oxygen atmosphere compared to the standard atmospheric conditions used in the irradiation experiment. The addition of pure molecular oxygen drastically reduces the $FADH^{\bullet}$ lifetime (*cf.* **Table 5.2**), likely overriding alternative recovery mechanisms occurring in the irradiation experiments. Since the local environment around FAD should remain unchanged by the mutations herein, the reduced $FADH^{\bullet}$ lifetime ought to be similar for all four proteins.[157]

It is nonetheless surprising that the E320K mutation appears to influence the lifetime of $FADH^{\bullet}$ under the atmospheric conditions employed in the irradiation experiments. One possible explanation is that the change of charge state adjacent to the fourth tryptophan residue alters its reduction potential in such a way that $W^{\bullet}$ is stabilised. This could promote bimolecular recovery of $FADH^{\bullet}$ and $W^{\bullet}$, through mutual electron and proton transfer. A similar argument could be levied against the shorter *Gg*Cry4a W369F $FADH^{\bullet}$ irradiation-recovery, compared to *Gg*Cry4a WT and R317C. Given that W_C radical is less solvent exposed than W_D,[157] it is logical to expect that any solvent-mediated $W^{\bullet}$ recovery is suppressed in *Gg*Cry4a W369F, thus promoting bimolecular recovery.

As discussed above, the short (*ca.* 2 ns) timescale observed by TA spectroscopy is assigned to $FAD^{\bullet-}/W_BH^{\bullet+}$ back electron transfer while the longer timescale is assigned to direct recombination of the SCRP, $FAD^{\bullet-}$-$W_DH^{\bullet+}$ or $FAD^{\bullet-}$-$W_CH^{\bullet+}$ for *Gg*Cry4a W369F. The much shorter SCRP lifetimes observed in *Gg*Cry4a WT, *Gg*Cry4a E320K and *Gg*Cry4a R317C account for the small ΔA signal after 100 ns ($\approx$ 10 % of the initial signal, *cf.* **Fig. 6.4**). Therefore, only a small fraction of the initially generated RP survives long enough to form the RP2 state probed directly by BBCEAS. Conversely, the much longer *Gg*Cry4a W369F SCRP lifetime lends itself to more effective competition between the fates of the singlet and triplet states and thus efficient RP2 generation. This could partially explain why the *Gg*Cry4a W369F BBCEAS $\Delta\Delta A$ spectrum (**Fig. 6.9**) exhibits a significantly larger MFE than the other three proteins. In addition, the less solvent-exposed W_C may lead to a reduction in random fields type relaxation, due to inhibited solvent interactions. As was shown in

Chapter 5, this type of relaxation reduces the magnitude of MFEs without altering their field dependence (*i.e.*, $B_{1/2}$). Similarly, the more solvent-accessible W_D could promote more rapid $WH^{\bullet+}$ deprotonation (while still slower than recombination) in *Gg*Cry4a WT, R317C and E320K. These effects were explored by both spin-dynamics and kinetic simulations, employing the same methods utilised in **Chapter 5** and kinetic cycle in **Fig. 5.14 a**, the results of which are shown in **Fig. 6.12** where k_r is the singlet recombination rate constant estimated by TA spectroscopy (*cf.* **Table 6.2**).

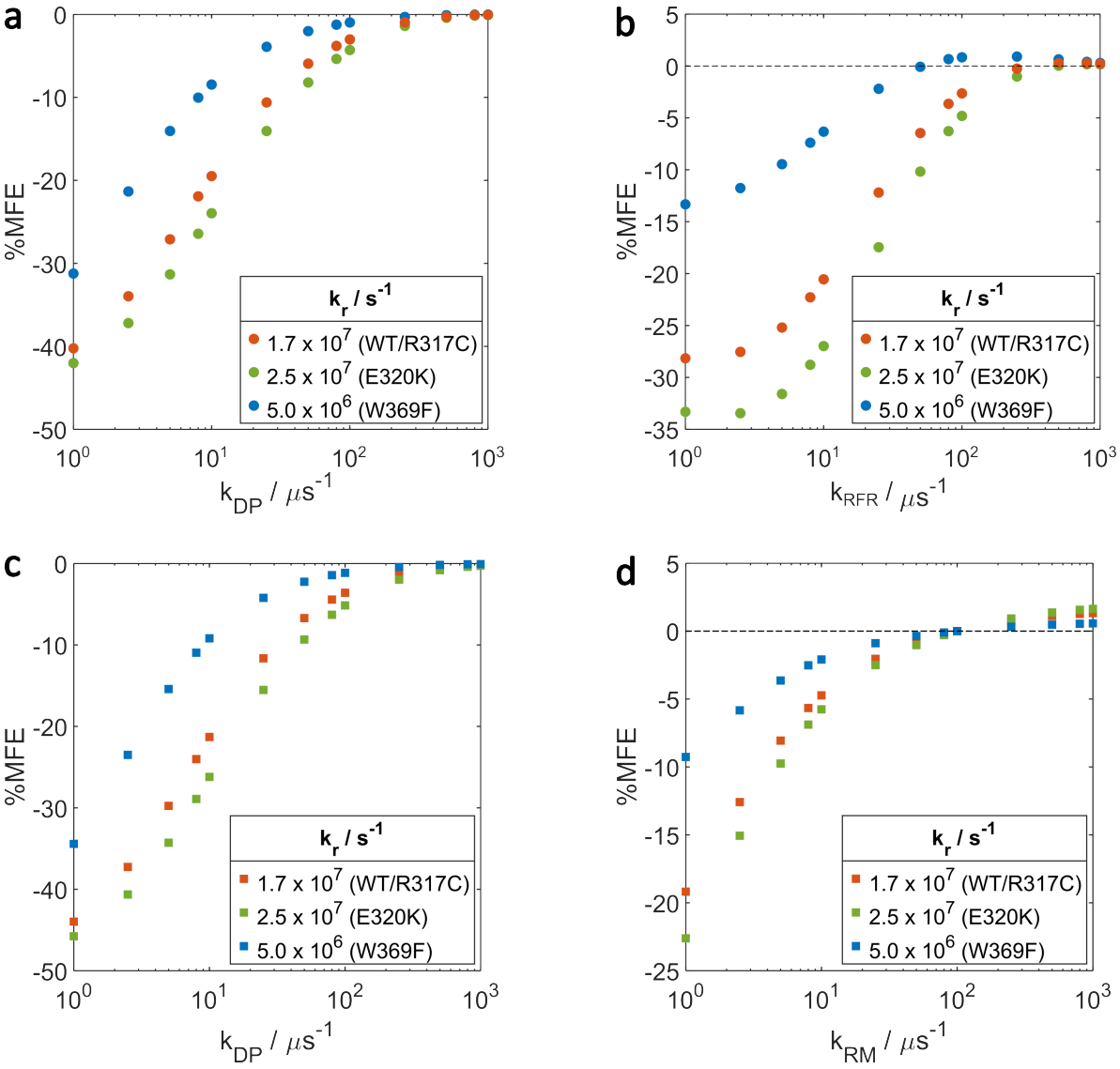

Figure 6.12: Spin-dynamics, (a), and kinetic, (c), simulation results with a varied deprotonation rate constant (k_{DP}). Each line represents a different k_r, taken from **Table 6.2**. No relaxation was included. Spin-dynamics, (b), and kinetic, (d), simulation results with varied relaxation rate constant (k_{RFR} for spin dynamics and k_{RM} for kinetics). Each line represents a different k_r, taken from **Table 6.2**. In all simulations, the rate constant for $FAD^{\bullet-}$ protonation, k_P, was set to 5 s^{-1}.

Interestingly, for any given deprotonation rate (k_{DP}), in the absence of relaxation, the steady state %MFE predicted by spin-dynamics and kinetic simulations (**Fig. 6.12 a** and **c**, respectively) is larger for *Gg*Cry4a E320K, R317C and WT than *Gg*Cry4a W369F, in contrast to the BBCEAS experimental results shown in **Fig. 6.9**. This implies that more rapid singlet recombination is generally favourable, provided it remains significantly slower than the rate of singlet-triplet mixing (recall $k_{HFM} = 1.01 \times 10^8$ s^{-1}, **Chapter 5**). This could be a consequence of more rapid cycling with a greater population of the system passing through the SCRP, experiencing a MFE, at a greater frequency. Furthermore, when $k_r = k_{DP}$ the %MFE is approximately equivalent for each k_r with larger %MFEs observed when $k_r > k_{DP}$. The same trend was also observed in time-dependent spin-dynamics simulations (akin to the TA experiment) where larger maximum MFEs were predicted for systems with faster singlet recombination (**Appendix A.3**). This highlights the important role the ratio between the rate of singlet recombination and product formation plays on the development of MFEs, not just the SCRP lifetime.

A similar trend in the steady state %MFE, with a fixed deprotonation rate ($k_{DP} = 5 \times 10^6$ s^{-1}), was observed for random fields type relaxation (k_{RFR} and k_{RM}, *cf.* **Chapter 5**). That is, the %MFE predicted by spin-dynamics and kinetic simulations (**Fig. 6.12 b** and **d**, respectively) generally decreased with increased relaxation. Once again, for a given relaxation rate constant, the %MFE was larger with larger k_r. It therefore seems that, despite larger MFEs predicted for the systems with shorter lived SCRPs (*Gg*Cry4a WT, R317C and E320K), the impact from alternative processes potentially caused by different W_C and W_D environments, such as rapid deprotonation or random-fields type spin relaxation, outweighs the effect of singlet recombination thus reducing the MFE observed by BBCEAS.

6.4 Conclusion

The results presented in this chapter indicate that, despite the evolutionary conservation of C317 and K320 in night-migratory passerines, they have little impact on either the spin dynamics or RP kinetics when introduced into *Gg*Cry4 WT. Meanwhile, reducing the length of the ETC in *Gg*Cry4 W369F has a significant impact on measured MFEs *in*

vitro, highlighting the importance of these residues in the development of MFEs in Cry4a proteins. This result is in agreement with Xu *et al.*[1] and suggest that while nature has seemingly optimised the avian magnetic compass to use four tryptophan residues, this is at the expense of the candidate magnetoreceptor's sensitivity, at least *in vitro*. However, simulations (**Fig. 6.12**) suggest that, four tryptophans could be optimal *in vivo* provided alternate processes such as deprotonation and spin-relaxation are curtailed. Alternatively, this may point to a role of the solvent-exposed tryptophan residue (W_D, W369) in signalling. As mentioned, it was proposed that Cry4 could stabilise a composite RP where the magnetic sensitivity is optimised through the spin-dependent reactions of W318 and a signalling interaction from W369.[1,135] However, the inter-radical separations obtained by EPR (**Table 6.1**) disabuse this hypothesis with no indication of an equilibrium between an FAD-W_C and FAD-W_D RP. This is further compounded by the large difference in the RP lifetimes observed by TA (**Table 6.2**) which suggest that recombination dominates any potential equilibrium when all four tryptophans are present.

Despite the apparent lack of impact from cysteine and lysine under the conditions employed here, C317 and K320 may play a role *in vivo*. Both are within solvent exposed areas of the protein (**Fig. 6.1**) and could facilitate, either directly or through second order effects, the interaction of Cry4a and binding partners in the cell. The identity of such a binding partner remains unknown, however, several possible candidates are being explored.[158,159] In fact, little is known about the entire signal transduction process in avian magnetoreception and as such any prospective role these residues (and others) may play remain the stuff of speculation for now.[160] With this in mind, experiments in more biologically relevant systems, such as cryptochrome and candidate binding partner composite systems, represent a key area of future research.

Chapter 7

Single Point Mutations of the Electron Transfer Chain in *Gallus gallus* Cryptochrome 4a

The role the electron transfer chain (ETC) plays in the cryptochrome RPM is abundantly clear. Not only does it enable the formation of a spin correlated radical pair but the nature of the ETC influences the RP's lifetime and relaxation processes by dictating the separation of the two radicals and their relative orientation in space. For example, if the separation of the RP is too small then a large electron exchange interaction will inhibit any field sensitivity, even if singlet recombination remains sufficiently slow for MFE development.

The influence the ETC can have on cryptochrome MFEs was demonstrated in the proceeding chapter where removal of the terminal tryptophan (W369) was found to increase chicken cryptochrome MFEs detected by BBCEAS. This naturally prompted questions over Nature's choice of four tryptophans and the length of the ETC in avian cryptochromes. Furthermore, it has been suggested that the ETC may not stop at W369 with some studies suggesting that a tyrosine residue (Y319) in close proximity (*cf.* **Fig. 7.1**) may act as the terminal electron donor.[126,135,157] Despite observation of electron transfer (or proton-coupled electron transfer) from a terminal tyrosine residue in several members of the photolyase-Cry superfamily,[58,104,138,152,161] little evidence of tyrosyl radical ($TyrO^{\bullet}$) formation has been found in avian cryptochromes.[ax] However, recent *Gg*Cry4a W369F OOP-ESEEM experiments (*cf.* **Chapter 6**) by fellow DPhil student Tommy Pitcher picked up a secondary oscillation corresponding to a sub-population of RPs with a 24 Å inter-radical separation. Such a separation matches nicely with the centre-to-centre FAD-Y319 separation, estimated by a *Gg*Cry4a WT homology model (**Fig. 7.1**). Furthermore, replacing Y319 with phenylalanine (F), forming the doubly mutated *Gg*Cry4a W369F Y319F, removed the secondary OOP-ESEEM oscillation leaving only one radical pair population with an

[ax] Otsuka *et al.*[126] claimed detection of the tyrosyl radical in *Gg*Cry4a WT following global analysis of TA data.

inter-radical separation of 17 Å.[ay] Curiously, an FAD-Y319 signature was not observed in the *Gg*Cry4a WT protein.

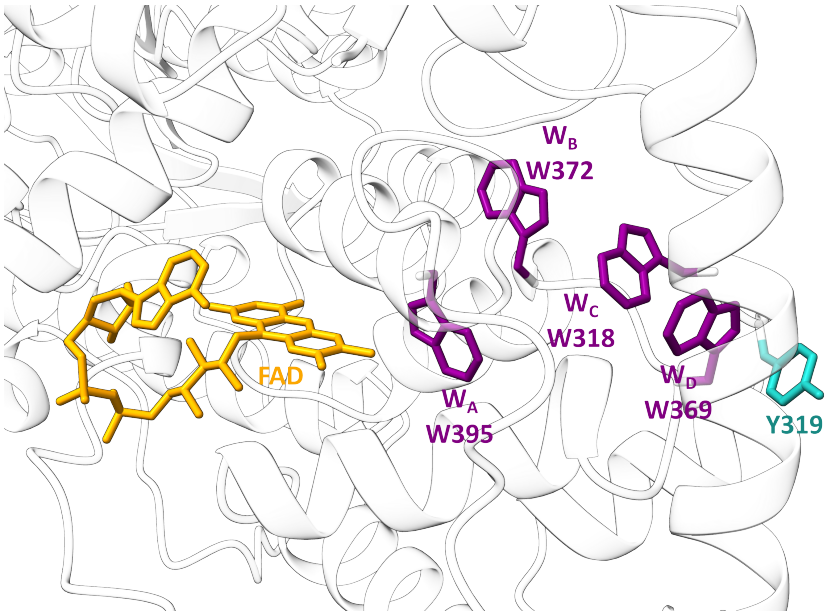

Figure 7.1: Structure of a chicken wild type cryptochrome protein (*Gallus gallus*, *Gg*Cry4a WT). Components implicated in electron transfer chain indicated with the FAD chromophore highlighted in orange, the four tryptophans (W_A/W395, W_B/W372, W_C/W318 and W_D/W369) in purple and the tyrosine (Y319) in blue. Homology model generated using Swiss Model.[118–122]

These intriguing results raise two major questions. Namely, if Y319 is involved in the ETC, how does it influence MFE development? And, if phenylalanine is redox-inactive and blocks electron transfer, how does any of the FAD-Y319 RP form in *Gg*Cry4a W369F? The role of tyrosine was explored by mutating Y319 with a phenylalanine in *Gg*Cry4a W369F and *Gg*Cry4a WT, creating *Gg*Cry4a W369F Y319F and *Gg*Cry4a Y319F. The electron blocking efficiency of phenylalanine was then studied by single-point mutations of the ETC where either W318 (W_C) or W372 (W_B) was replaced with phenylalanine to make *Gg*Cry4a W318F and *Gg*Cry4a W372F.

7.1 Methods

The systems mentioned above were primarily studied using BBCEAS. Some additional TA experiments were carried out on *Gg*Cry4a W369F Y319F by Dr. Kevin Henbest and Holly Hayward (Part II student) with the data analysed by the author. The working principles of BBCEAS and TA were introduced in preceding chapters (see **Chapter 6** and **3**). The

[ay] Research as of yet unpublished.

experimental conditions employed here, for both techniques, were identical to those in **Chapter 6**.

All cryptochrome proteins were expressed and purified by our collaborators in Oldenburg.[1] Dilute spectroscopic samples were prepared in pH 8 tris buffer consisting of 20 mM Tris, 250 mM NaCl and 20% glycerol (V/V).

7.2 Results and Discussion

7.2.1 *Gg*Cry4a W369F Y319F and *Gg*Cry4a Y319F

If a population of FAD-Y319 RPs are forming, *via* electron transfer to W318, in *Gg*Cry4a W369F, then removal of the tyrosine residue could be expected to alter the lifetime and dynamics of photogenerated radicals. To that end, the TA spectroscopy ΔA results of *Gg*Cry4a W369F Y319F are shown in **Fig. 7.2**. The ΔA spectra in **Fig. 7.2 b** are characterised by a negative absorption band between 400 nm and 500 nm, assigned to the FAD_{OX} ground state bleach, and positive absorption bands below 400 nm and above 500 nm, assigned to $FAD^{\bullet-}$ absorption and a combination of $FAD^{\bullet-}$, $WH^{\bullet+}$ and $W^{\bullet}$ absorption, respectively. The kinetic evolution of the ΔA spectra, averaged between 500 nm and 550 nm, is shown in **Fig. 7.2 a** with (orange line) and without (maroon line) a 30 mT applied magnetic field. Both field on and field off traces indicate a fast ($\tau_1 = 7.05 \pm 1.05$ ns) initial decay followed by a slower decay ($\tau_2 = 295 \pm 13.4$ ns).[az] The former is assigned to $FAD^{\bullet-}/W_BH^{\bullet+}$ back electron transfer (BET) while the latter is assigned to a combination of singlet recombination and $WH^{\bullet+}$ deprotonation. The subtraction ($\Delta\Delta A$, grey line) characterises the MFE in this spectral region.

At a glance, these results seem comparable to the results obtained for *Gg*Cry4a W369F (*cf.* **Fig 6.4 and 6.7**) where an $FAD^{\bullet-}$-$WH^{\bullet+}$ RP (RP1) is initially formed before $WH^{\bullet+}$ deprotonates to form $W^{\bullet}$, generating the uncorrelated $FAD^{\bullet-}$-$W^{\bullet}$ RP2. However, there are some marked differences. For example, the *Gg*Cry4a W369F Y319F radical yield is *ca.* four times greater than that of *Gg*Cry4a W369F. Additionally, the initial rapid component in the radical decay is slower and significantly less pronounced than in *Gg*Cry4a W369F.

[az] Decay time constants estimated from a biexponential fit (dashed line) to the field off data in **Fig. 7.2**.

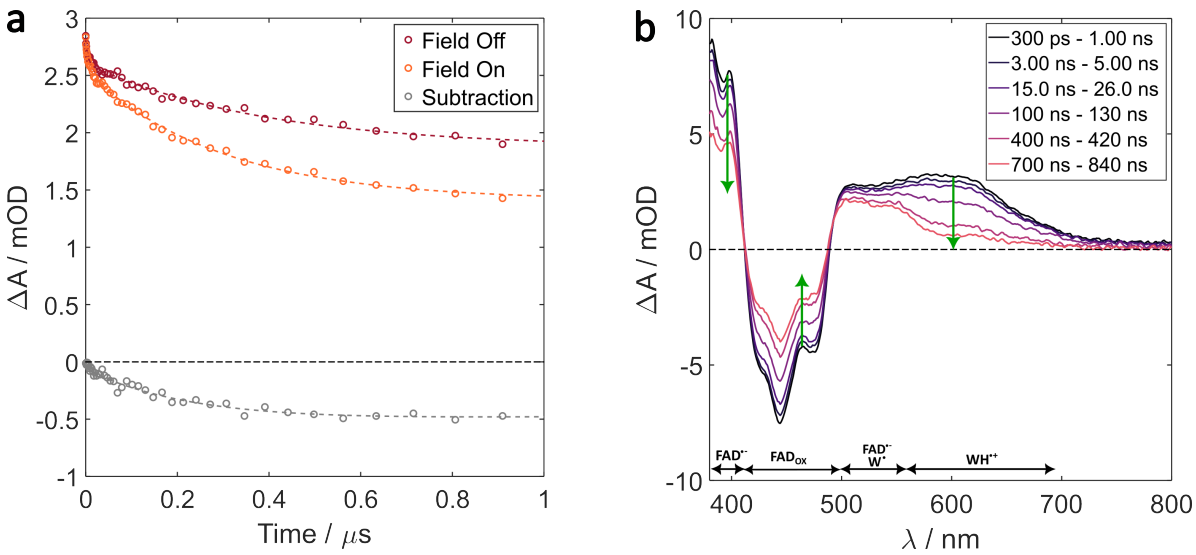

Figure 7.2: ΔA TA results for *Gg*Cry4a W369F Y319F. a) Kinetic evolution of the ΔA signal in (b), averaged between 500 nm and 550 nm, without (maroon line) and with (orange line) 30 mT applied magnetic field. Dashed lines are biexponential fits to the data. The subtraction of field on and field off lines ($\Delta\Delta A$) is shown in grey. b) ΔA spectra averaged over several time windows as indicated by the legend. Evolution shows clear decay of $WH^{\bullet+}$ (550 nm - 650 nm), $FAD^{\bullet-}$ (< 400 nm) and ground state bleach (400 nm - 500 nm). $W^{\bullet}$ (500 nm - 550 nm) initially forms before decaying at later times (> 840 ns). At the bottom of (b), a rough guide indicates which species contribute most to the spectra at a given wavelength.

Consequently, the SCRP and thus RP2 yield is promoted, leading to a substantial MFE (subtraction in **Fig. 7.2**). Furthermore, the $WH^{\bullet+}$ absorption is red-shifted by 30 nm relative to *Gg*Cry4a WT and *Gg*Cry4a W369F, indicating a change in its electronic structure. A similar (25 nm) $WH^{\bullet+}$ red shift was observed by Lacombat *et al.*[58] in an animal-like *Chlamydomonas reinhardtii* (single-cell green alga) cryptochrome which has a tryptophan triad rather than tetrad. These changes could be associated with shifts in the local structure of the protein, thus implicating Y319 as a structurally important residue. However, this would contradict a recent computational study by Frederiksen *et al.*[157] which predicted minimal structural variations upon mutation of Y319. Alternatively, these results could indicate an interaction between Y319 and W318 (in *Gg*Cry4a W369F) where the tyrosine destabilises $W_CH^{\bullet+}$ (W318) making $FAD^{\bullet-}$-$W_CH^{\bullet+}$ less favourable and thus $FAD^{\bullet-}/W_BH^{\bullet+}$ BET more competitive, therefore reducing the overall radical yield.

Once again, global analysis (see **Appendix A.3**) was used to extract individual species kinetics from the TA ΔA spectra, the results of which are shown in **Fig. 7.3**. The extracted species kinetics agree with the spectral evolution assigned above. That is, following minimal $FAD^{\bullet-}/W_BH^{\bullet+}$ BET, $W_CH^{\bullet+}$ decays by a combination of singlet recombination and

deprotonation to form $W^{\bullet}$. Meanwhile, $FAD^{\bullet-}$ decays back to the ground state (FAD_{OX}) until its recombination partner $W_CH^{\bullet+}$ is gone, leaving a persistent longer-lived $FAD^{\bullet-}$ population similar in concentration to the formed $W^{\bullet}$. The cause of the non-zero $W^{\bullet}$ concentration at t = 0 comes from the change in the $WH^{\bullet+}$ absorption profile which is not only red-shifted but broadened as well. Since the reference $WH^{\bullet+}$ spectrum (**Fig. 2.9 b**) was shifted but otherwise unaltered during fitting, a discrepancy in the absorption profile of the data and fit is induced at early times causing the fit to predict a non-zero initial $W^{\bullet}$ population.

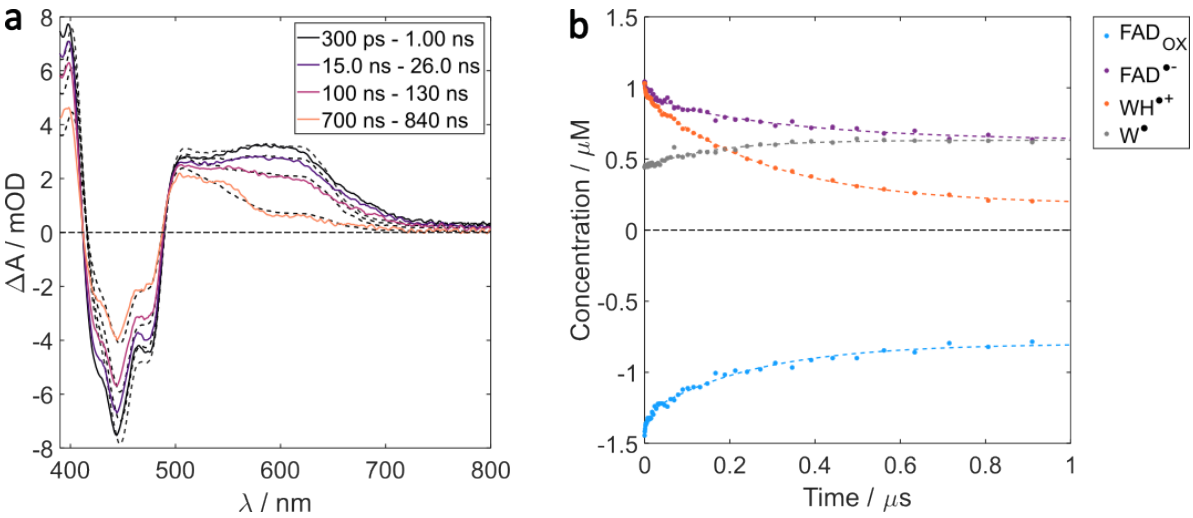

Figure 7.3: a) *Gg*Cry4a W369F Y319F global fitting results of the TA ΔA spectra. Solid coloured lines show the raw data while dashed black lines show the global fit. b) Individual species kinetics extracted from the global fit in (a) where $WH^{\bullet+}$ is shown to decay in conjunction with $FAD^{\bullet-}$, FAD_{OX} recovery and the formation of $W^{\bullet}$. Dashed lines represent fits to the data with the resulting estimated lifetimes shown in **Table 7.1.**

The results of fitting the individual species kinetics in **Fig. 7.3 b** with a biexponential function (except for $W^{\bullet}$ which was mono-exponential) plus a constant offset are summarised in **Table 7.1**. Each species broadly evolves on a similar timescale and predicts comparable SCRP singlet recombination and $WH^{\bullet+}$ deprotonation rates (between 200 ns and 300 ns), similar to *Gg*Cry4a W369F. It could be argued that deprotonation and/or SCRP singlet recombination are slower in *Gg*Cry4a W369F Y319F than *Gg*Cry4a W369F, complementing the altered protein structure and Y319 and W318 interaction arguments made above. However, the extracted lifetime errors are relatively large and thus variations in lifetimes between the two samples may not be significant.

Species	τ_1 / ns	τ_2 / ns
$FAD^{\bullet-}$	22.6 ± 6.74	349 ± 68.6
FAD_{OX}	10.4 ± 3.06	253 ± 23.6
$WH^{\bullet+}$	3.51 ± 0.64	284 ± 7.34
$W^{\bullet}$	167 ± 17.2	

Table 7.1: Biexponential fits to the individual species kinetics extracted by global analysis of the *Gg*Cry4a W369F Y319F TA ΔA results (**Fig. 7.3**). All species evolve on a similar timescale, indicating similar singlet recombination and $WH^{\bullet+}$ deprotonation rates.

It is clear from the TA results that removal of Y319 affects radical formation in *Gg*Cry4a W369F, with less prominent BET, prior to the SCRP, leading to a larger radical yield. This increased radical yield carries through into the MFE, which is also increased in magnitude. However, the %MFE in *Gg*Cry4a W369F and *Gg*Cry4a W369F Y319F are actually consistent (*ca.* 25 % at 1 μs), highlighting the similar SCRP kinetics (*i.e.* $FAD^{\bullet-}/WH^{\bullet+}$ recombination and $WH^{\bullet+}$ deprotonation) and spin-relaxation (such as random-fields) between the two proteins. Additionally, the formation of some FAD-Y319 RP in *Gg*Cry4a W369F does not seem to greatly influence the SCRP lifetime or MFE development.

In spite of the increased RP1 and RP2 yield in TA spectroscopy, the BBCEAS long-lived radical yield is significantly reduced in *Gg*Cry4a W369F Y319F compared to *Gg*Cry4a W369F. This is highlighted in **Fig. 7.4 a** and **b** which directly compares their BBCEAS ΔA spectra. In both cases an $FADH^{\bullet}$ absorption signature (500 nm - 700 nm) accumulates as the sample is photoexcited. However, the dynamics and magnitude of this signal differ significantly with the *Gg*Cry4a W369F photoinduced absorption (PIA) almost an order of magnitude larger than *Gg*Cry4a W369F Y319F, after 9 s of illumination. Furthermore, the *Gg*Cry4a W369F PIA changes spectral shape as it is illuminated while the *Gg*Cry4a W369F Y319F PIA spectral shape changes comparatively little. This is a direct consequence of the differing individual radical species dynamics between the two proteins as demonstrated in **Fig. 7.4 c** and **d** which shows the individual species kinetics for *Gg*Cry4a W369F and *Gg*Cry4a W369F Y319F, respectively. For example, *Gg*Cry4a W369F exhibits a large early (< 1 s) $FAD^{\bullet-}$ signal, causing the prominent peak at *ca.* 510 nm at early times (i.e. 400 ms) in **Fig. 7.4 a**, which decays away as the experiment proceeds. Meanwhile, *Gg*Cry4a W369F

Y319F exhibts essentially zero $FAD^{\bullet-}$ signal. This lack of $FAD^{\bullet-}$ likely accounts for the significantly suppressed $FADH^{\bullet}$ accumulation and indicates a shorter RP2 $FAD^{\bullet-}$ lifetime compared to *Gg*Cry4a W369F. Importantly, it hints at an $FAD^{\bullet-}$ decay mechanism other than protonation or singlet recombination. This will be explored further in **Chapter 8** where a newly developed technique, optical cavity enhanced transient absorption spectroscopy, is used to monitor RP2 decay.

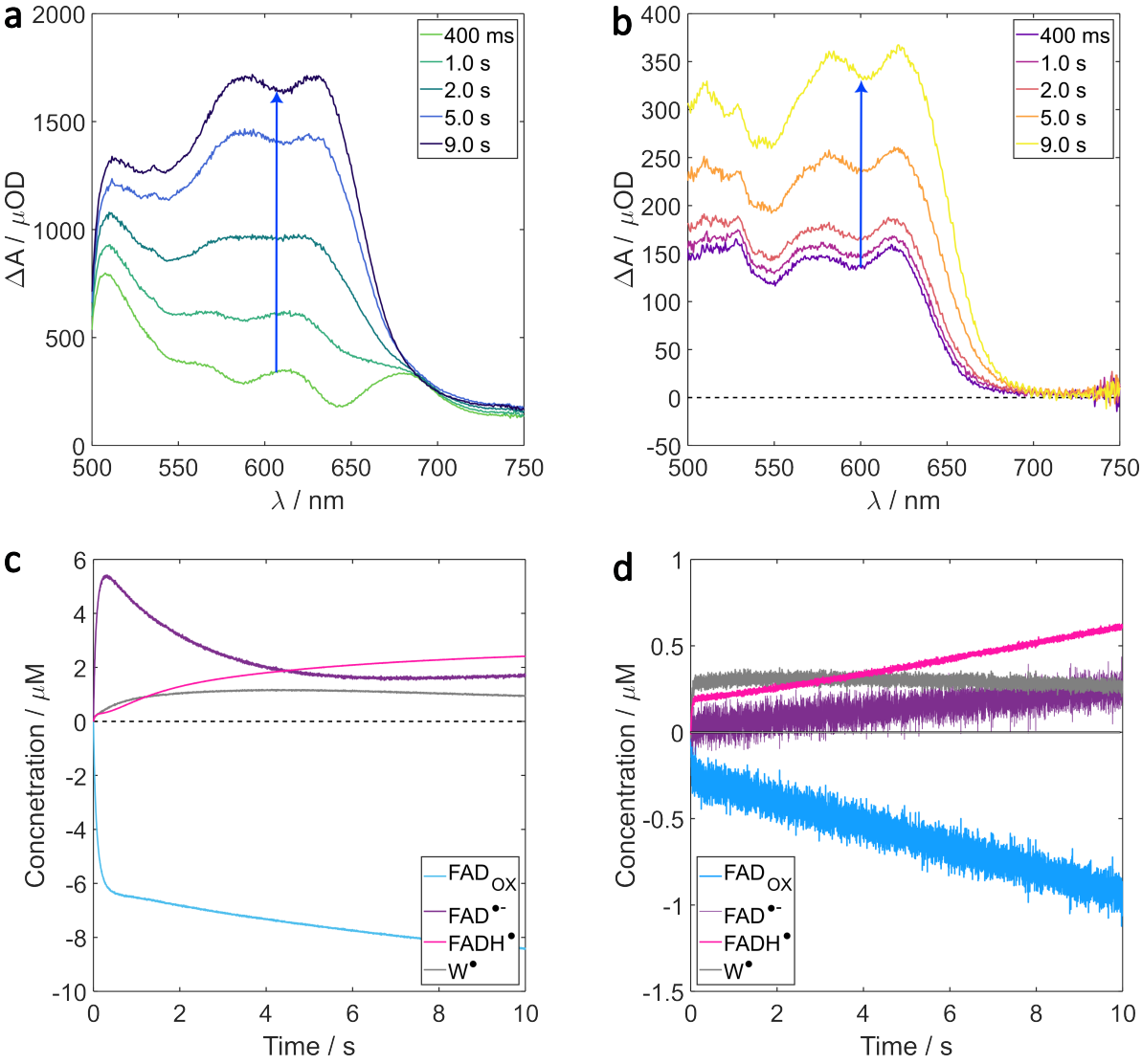

Figure 7.4: BBCEAS ΔA spectra for *Gg*Cry4a W369F (a) and *Gg*Cry4a W369F Y319F (b) where the arrows indicate direction of absorption change as a function of time. Both show formation of $FADH^{\bullet}$ however the long-lived radical yield in *Gg*Cry4a W369F is *ca.* 5 times larger than *Gg*Cry4a W369F Y319F. Extracted individual species kinetics for *Gg*Cry4a W369F (c) and *Gg*Cry4a W369F Y319F (d) obtained from global analysis of the ΔA spectra in (a) and (b) respectively. The lack of $FAD^{\bullet-}$ in *Gg*Cry4a W369F Y319F may account for the suppressed $FADH^{\bullet}$ accumulation.

Applying a 30 mT magnetic field during the BBCEAS illumination cycle yields the *Gg*Cry4a W369F and *Gg*Cry4a W369F Y319F time-averaged $\Delta\Delta A$ spectra displayed in **Fig. 7.5 a** and

b, respectively. In both cases, spectral fitting (*cf.* **Chapter 4**) reveals that their $\Delta\Delta A$ spectra are dominated by a MFE on the accumulation of $FADH^{\bullet}$ with minor contributions from FAD_{OX}, $FAD^{\bullet-}$ and $W^{\bullet}$. Given the significantly reduced *Gg*Cry4a W369F Y319F BBCEAS PIA, it is logical to expect the BBCEAS $\Delta\Delta A$ spectrum to be similarly suppressed. This is not the case as evidenced by **Fig. 7.5 b** which shows the time-averaged *Gg*Cry4a W369F Y319F $\Delta\Delta A$ spectrum to be substantial (*ca.* -45 μOD at 580 nm) and roughly three times greater than the *Gg*Cry4a W369F $\Delta\Delta A$ spectrum (**Fig. 7.5 a**). However, given one would typically expect the percentage change in SCRP yield, upon application of a magnetic field, to carry over to downstream photoproducts, regardless of their subsequent dynamics, this result is actually in line with the %MFE measured by TA. In fact, upon further consideration, the unusual results is the BBCEAS *Gg*Cry4a W369F $\Delta\Delta A$ as it reports a significantly smaller MFE than one would expect from the TA data. The root cause of this is unclear. One possible explanation is that some samples have a significant proportion of misfolded protein which is not magneto-sensitive but can generate $FADH^{\bullet}$. Alternatively, there could be an additional, slow, non (or less) magneto-sensitive mechanism which generates $FADH^{\bullet}$[ba] under continuous illumination that does not occur in *Gg*Cry4a W369F Y319F. Why removal of a far-flung tyrosine residue would effect FAD protonation is not obvious, however, molecular dynamics simulations by Frederiksen *et al.*[157] predicted significant changes in the water exposure of W395, the tryptophan residue immediately adjacent to FAD. This shift in local solvation may well influence FAD protonation, especially if the solvent is the proton source. Furthermore, the change in water exposure may well influence the free energy and reorganization energy thus influencing the initial electron transfer and back electron transfer processes. This could perhaps account for the larger TA radical yield.

Although the magnitude in the BBCEAS $\Delta\Delta A$ spectrum differs between *Gg*Cry4a W369F and *Gg*Cry4a W369F Y319F, their field dependence does not. This is demonstrated by the MARY curves in **Fig. 7.5 c** and **d** which show the time-averaged field dependent $\Delta\Delta A$, between 500 nm and 550 nm, of *Gg*Cry4a W369F and *Gg*Cry4a W369F Y319F, respectively. Lorentzian fits (*cf.* equation 4.2) to the data (solid lines) estimate a $B_{1/2}$ of *ca.* 4 mT in

[ba] For example, electron transfer between the isoalloxazine ring and adenine tail has been shown to generate $FADH^{\bullet}$ and MFEs in aqueous solution.[124,162]

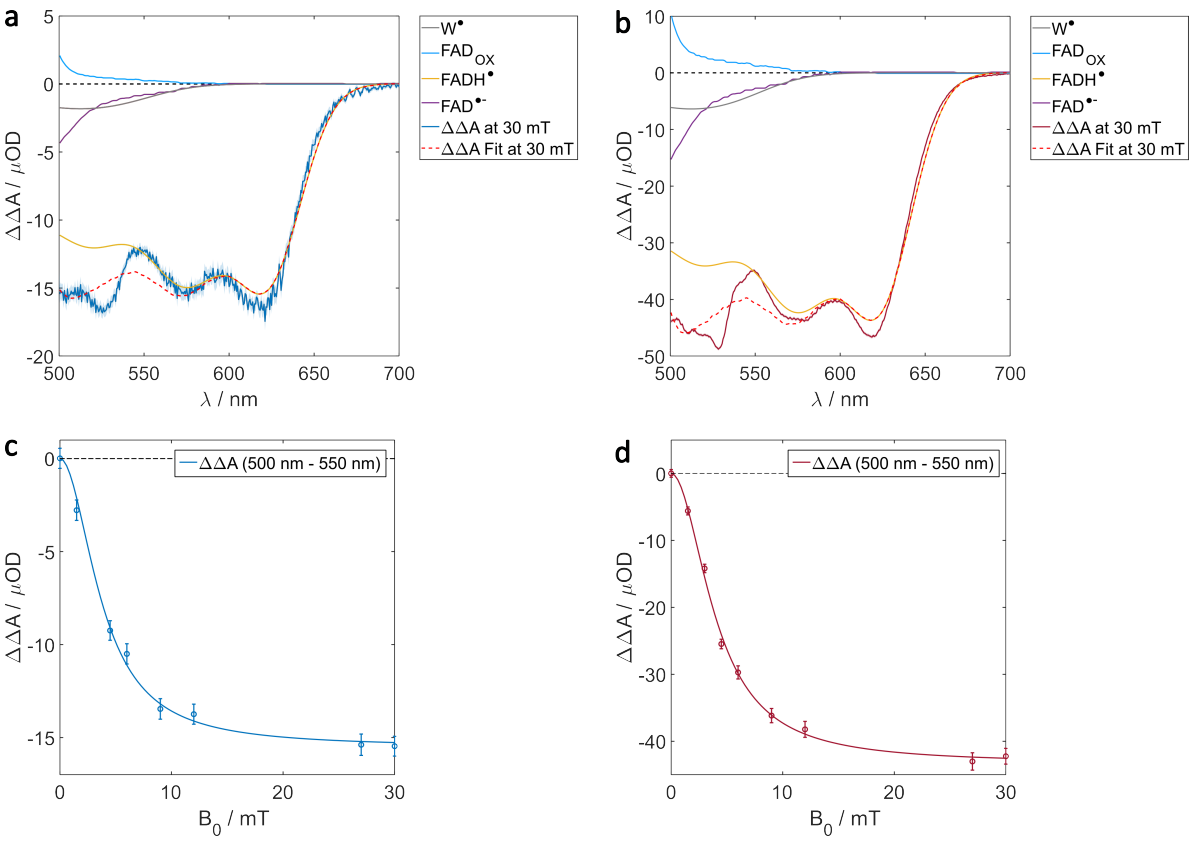

Figure 7.5: Time-averaged BBCEAS $\Delta\Delta A$ spectra, at 30 mT, for *Gg*Cry4a W369F (a) and *Gg*Cry4a W369F Y319F (b), including spectral fits (*cf.* **Chapter 4**). In both cases the $\Delta\Delta A$ spectrum is dominated by a MFE on $FADH^{\bullet}$ with minor contributions from $W^{\bullet}$, $FAD^{\bullet-}$ and FAD_{OX}. c) and d) show the time-averaged magnetically altered reaction yields (MARYs) for *Gg*Cry4a W369F and *Gg*Cry4a W369F Y319F, respectively. MARYs averaged between 500 nm and 550 nm.

both cases.[bb] This further suggests that removal of the Y319 has not greatly altered the SCRP HFC interactions or singlet-triplet dephasing like spin relaxation, at least in *Gg*Cry4a W369F.

While the precise mechanism(s) may remain unknown, Y319 clearly plays a role in the protein photochemistry and MFE development of *Gg*Cry4a W369F. A similar result could therefore be expected when mutating Y319 in *Gg*Cry4a WT, creating a *Gg*Cry4a Y319F mutant cryptochrome. Presented below in **Fig. 7.6** are some preliminary BBCEAS results from *Gg*Cry4a Y319F. Once again, replacement of Y319 with a phenylalanine results in a change in the ΔA spectra. However, unlike *Gg*Cry4a W369F Y319F, mutating the tyrosine does not seem to affect the long-lived radical yield but rather the early time ($\leq$ 2 s) spectral shape. Specifically, *Gg*Cry4a Y319F appears to form large amounts of $W^{\bullet}$ within the first 2 s of illumination before it subsequently decays away as $FADH^{\bullet}$ accumulates.

[bb] *Gg*Cry4a W369F $B_{1/2} = 3.89 \pm 0.15$ mT. *Gg*Cry4a W369F Y319F $B_{1/2} = 4.02 \pm 0.06$ mT.

This thus implies some form of interaction in *Gg*Cry4a WT between W369 and Y319 where the presence of the tyrosine either stabilises $WH^{\bullet+}$ or destabilises $W^{\bullet}$. Once again, molecular dynamics calculations by Frederiksen *et al.* corroborate this observation as a strong hydrogen-bonding interaction between W369 and Y319 was predicted. It is therefore surprising that OOP-ESEEM experiments do not detect any FAD-Y319 RPs in *Gg*Cry4a WT when some manages to form in *Gg*Cry4a W369F. However, this could simply arise from the different SCRP lifetimes observed by TA. Recalling **Chapter 6** and that BET was approximately 5 times faster for *Gg*Cry4a WT than *Gg*Cry4a W369F, it follows that, all other things being equal, FAD-Y319 formation is less competitive in *Gg*Cry4a WT. Alternatively, an interplay between intermolecular interactions and the free energy and reorganisation energy for electron transfer at each site along the ETC could lead to a potential energy surface where the W_C-W_D and W_C-Y319 electron transfers are downhill while the W_D-Y319 electron transfer is uphill.

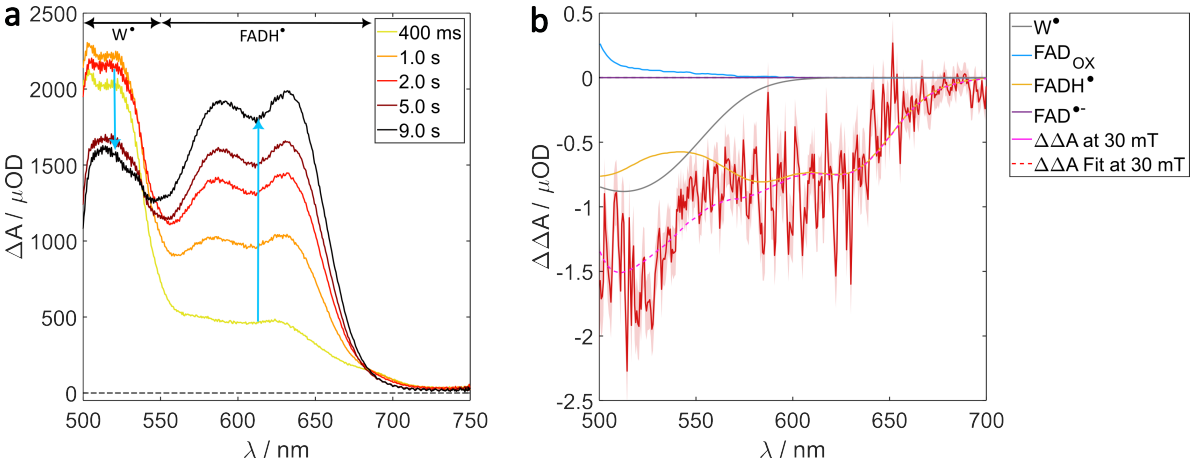

Figure 7.6: a) *Gg*Cry4a Y319F BBCEAS ΔA spectra where $W^{\bullet}$ is initally formed and decays as $FADH^{\bullet}$ begins to accumulate. The predominantly $W^{\bullet}$ and $FADH^{\bullet}$ regions of the spectra are indicated at the top of the plot while the arrows indicate direction of absorption change as a function of time. b) Time-averaged *Gg*Cry4a Y319 $\Delta\Delta A$ spectrum at 30 mT. The spectral fit estimates a more significant relative $W^{\bullet}$ contribution to the MFE than for *Gg*Cry4a W369F and *Gg*Cry4a W369F Y319F, reflecting the ΔA spectra in (a).

Like *Gg*Cry4a W369F Y319F, but in a contrasting fashion, the time-averaged BBCEAS $\Delta\Delta A$ spectrum for *Gg*Cry4a Y319F (**Fig. 7.6 b**) does not reflect the magnitude of its corresponding ΔA signal. In this instance the BBCEAS MFE is small and reduced compared to *Gg*Cry4a WT ($\Delta\Delta A \approx 4\mu$OD). In line with the more prominent $W^{\bullet}$ yield, spectral fitting of the $\Delta\Delta A$ spectrum estimates a comparatively large MFE on $W^{\bullet}$. If, as was mentioned

above, there is an alternative non magneto-sensitive mechanism for $FADH^{\bullet}$ generation then the $\Delta\Delta A$ spectrum may reflect a smaller magneto-sensitive sub population. Indeed, some preliminary TA experiments by Dr. Kevin Henbest and Holly Hayward found that the SCRP lifetime in *Gg*Cry4a Y319F was significantly reduced ($\approx$ 10 ns),[163] however, the GSB recovery was much longer ($\approx$ 80 ns), suggesting that there is a competing FAD_{OX} bleaching process which recovers on a different timescale to SCRP BET. This could arise from changes in the water exposure around FAD (due to the mutation) causing competitive electron transfer between the FAD isoalloxazine ring and adenine tail where strong exchange coupling would impede any subsequent MFEs.[124,162]

While these results may be preliminary, it is evident that Y319 influences the dynamics and MFEs that occur in chicken cryptochrome proteins. Precisely what role it plays remains poorly understood with it having profoundly different, almost opposing, influences on *Gg*Cry4a W369F and *Gg*Cry4a WT. However, given its apparent impact on cryptochrome photochemistry and relative ubiquity throughout the avian cryptochrome family of proteins (such as *Er*Cry4a),[157] more research uncovering its precise role is certainly warranted.

7.2.2 *Gg*Cry4a W318F and *Gg*Cry4a W372F

Phenylalanine is regularly used as an electron blocking substitution for tryptophans and tyrosines[1,56,140,164] since it is comparatively redox-inactive[bc] and structurally similar and thus less likely to significantly alter a protein's structure upon substitution. Importantly, phenylalanine, like tryptophan and tyrosine, is aromatic and should share similar hydrophobicity. However, based on the detection of a potential FAD-Y319 signature in the OOP-ESEEM trace of *Gg*Cry4a W369F, it appears that phenylalanine may not completely block electron transfer. If this is the case then phenylalanine substitutions to the tryptophans W318 and W372 in *Gg*Cry4a WT (*cf.* **Fig. 7.1**) may still form long-lived radicals and develop MFEs.

The BBCEAS ΔA results of *Gg*Cry4a W372F and *Gg*Cry4a W18F are shown in **Fig. 7.7 a** and **b**, respectively. Clearly there is significant $FADH^{\bullet}$ formation in both proteins. However,

[bc] Free in aqueous solution, the phenylalanine redox potential is $\approx$ 0.06 V at pH 7,[165] the tryptophan redox potential is $\approx$ 1.015 V at pH 7 and the tyrosine redox potential is $\approx$ 0.93 V and pH 7.[166]

there is also a lack of any $FAD^{\bullet-}$ signature below 400 nm (*cf.* **Fig. 6.8 a**). Given rapid $FAD^{\bullet-}$-$WH^{\bullet+}$ recombination is expected to dominate in these two proteins, the lack of $FAD^{\bullet-}$ is perhaps expected. Alternatively, a more rapid $FAD^{\bullet-}$ protonation and $FADH^{\bullet}$ recovery could account for the observed ΔA spectra.

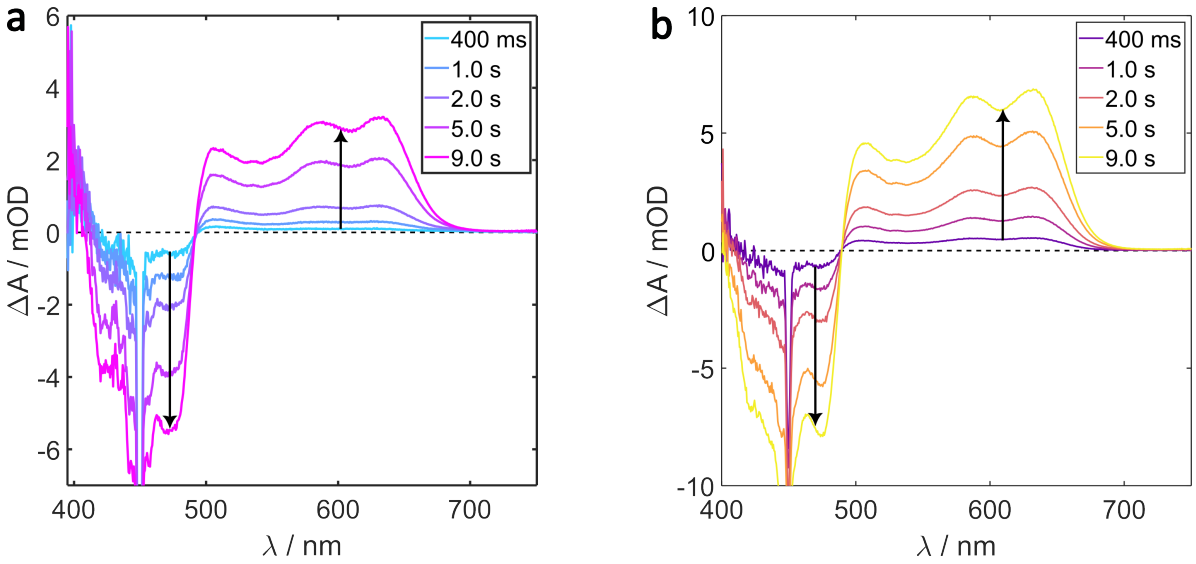

Figure 7.7: BBCEAS ΔA spectra for *Gg*Cry4a W372F (a) and *Gg*Cry4a W318F (b) where arrows indicate absorption change as function of time. In both proteins significant $FADH^{\bullet}$ accumulation is observed (absorption band above 500 nm). However, the lack of absorption at *ca.* 400 nm indicates no $FAD^{\bullet-}$ contribution to the spectra.

While the ΔA results demonstrate that long-lived radical formation is still possible, even when the ETC is hypothetically only one or two tryptophans long, they do not necessarily imply electron hopping past phenylalanine onto W372 in *Gg*Cry4a W318F or W395 in *Gg*Cry4a W372F. However, if some electron transfer does make it past a phenylalanine, one would expect this protein population to form FAD-W369 SCRPs, similarily to *Gg*Cry4a WT, and thus develop MFEs. Accordingly, **Fig. 7.8** shows the time-averaged *Gg*Cry4a W372F (**a**) and *Gg*Cry4a W18F (**b**) $\Delta\Delta A$ spectra due to the application of a 30 mT magnetic field.

While no MFE could be detected (within signal-to-noise) in *Gg*Cry4a W372F, a small MFE was detected in *Gg*Cry4a W318F.[bd] As is usual for all of the cryptochromes measured under an oxygen atmosphere herein, the $\Delta\Delta A$ spectrum for *Gg*Cry4a W318F predominantly arises due to a MFE on the accumulation of $FADH^{\bullet}$. This result suggests that, while most of the generated SCRPs recombine through $FAD^{\bullet-}/W_BH^{\bullet+}$ BET, some fraction manages

[bd] Confocal microscopy experiments by fellow DPhil Jamie Gravell also detected a small MFE from *Gg*Cry4a W318F.

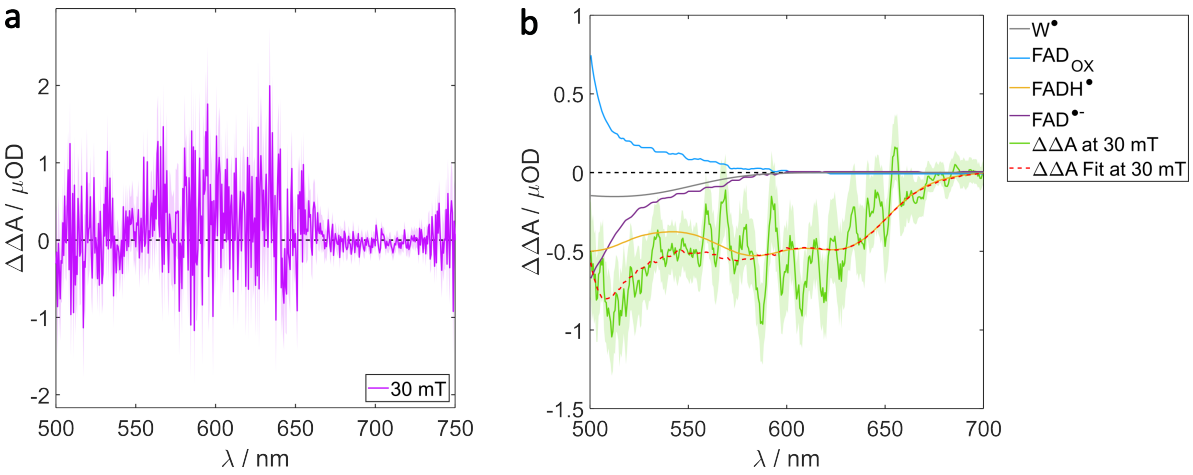

Figure 7.8: 30 mT time-averaged $\Delta\Delta A$ spectrum for *Gg*Cry4a W372F (a) and *Gg*Cry4a W318F (b). No MFE could be detected within signal to noise for *Gg*Cry4a W372F, however, a small MFE is observed in *Gg*Cry4a W318F. Spectral fits indicate a predominantly $FADH^{\bullet}$ contribution to the $\Delta\Delta A$ spectrum.

to make it past the phenylalanine, potentially forming an $FAD^{\bullet-}$-$W_DH^{\bullet+}$ SCRP, capable of developing MFEs. This was later confirmed by OOP-ESEEM measurements by DPhil student Tommy Pitcher which detected a noisy but clear signal corresponding to an inter-radical separation of *ca.* 21 Å, matching the FAD-W_D separation in GgCry4a WT.[117]

The small measurable MFE and OOP-ESEEM result suggest that some degree of electron transfer in *Gg*Cry4a W318F makes it past the phenylalanine and on to W_B.[be] This could happen in a number of ways, for example phenylalanine has been shown to undergo direct electron transfer in peptides where the oxidised phenylalanine is stabilised by a neighbouring primary amide group (not including the peptide backbone).[167] However, given the lack of a nearby glutamine or asparagine residue this mechanism seems unlikely in *Gg*Cry4a. A more commonly invoked mechanism explaining long-range electron transfer in proteins is a tunnelling mechanism known as superexchange tunnelling where electron transfer between a donor (D) and acceptor (A) proceeds *via* a bridge without the electron populating any bridge states (*i.e.* the bridge is never reduced/oxidised).[164,167–169] This is typically described by a modified Marcus theory (*cf.* equation 2.46) where the electronic coupling term between donor and acceptor, H_{DA}, is perturbed by a tunnelling term, T_{DA}, dependent on electronic coupling interactions between the bridging molecule and the

[be]The possibility of some of the protein remaining un-mutated was discarded since there was no MFE or OOP-ESEEM trace for *Gg*Cry4a W372F. Additionally, there is no FAD-W_D signal observed in the OOP-ESEEM of *Gg*Cry4a W369F.

donor or acceptor. That is,

$$H_{DA} = V_{DA} + T_{DA} = V_{DA} + \sum_{ij}^{B} T_{Di} \langle \phi_i | (\epsilon_{tun}\hat{E} - \hat{H}_B)^{-1} | \phi_j \rangle T_{jA} \tag{7.1}$$

where V_{DA} is the direct coupling between D and A, T_{Di} and T_{jA} are the donor-bridge, bridge-acceptor interactions, $|\phi_i\rangle$ and $|\phi_j\rangle$ are bridge atomic orbitals, ϵ_{tun} is the tunnelling energy and $\hat{H}_B$ is the hamiltonian describing the bridge (see provided references for detailed discussion).[164,170–173] The result is a less rapid exponential decay in the electron transfer rate constant as a function of D and A separation due to stronger D and A coupling (essentially lowering the tunnelling barrier).[173]

Recently, Holub *et al.* applied this model to a mutated photolyase protein to explain why photoreduction was still observed when the first amino acid in the ETC was mutated for a phenylalanine.[164] They found that inclusion of superexchange tunnelling, with phenylalanine acting as a bridge, increased the donor (FAD) acceptor (W_B) coupling ten-fold. Such a mechanism could thus explain the observations here where phenylalanine enhances the electronic coupling between the two tryptophan sites, increasing the electron transfer rate constant and making it more competitive with recombination. Thus, in *Gg*Cry4a W319F where the BET is less rapid (*vs.* *Gg*Cry4a W372F) electron transfer from W369 to W372 is sufficiently competitive for a small population of $FAD^{\bullet-}$-$W_DH^{\bullet+}$ to form. Conversely, despite potential superexchange with phenylalanine, the BET in *Gg*Cry4a W372F is too fast for any $FAD^{\bullet-}$-$W_DH^{\bullet+}$ to form. Consequently, no MFE can develop in *Gg*Cry4a W372F due to a combination of the SCRP being too short-lived and a large exchange interaction impeding ST mixing.

Unfortunately, the above argument does not account for the magnitude of the ΔA spectra for both *Gg*Cry4a W372F and *Gg*Cry4a W318F. If in both cases the vast majority of formed SCRPs undergoes rapid recombination then one would expect little, if any, $FADH^{\bullet}$ formation. Again, this hints at an alternative $FADH^{\bullet}$ formation mechanism which is non magneto-sensitive. If this is occurring and $FADH^{\bullet}$ is involved in some form of signalling state then such a mechanism could potentially drown out the magneto-sensitive signal. However,

perhaps this is only a consequence of experimental conditions such as *in vitro* with high laser powers (relative to evening and/or nocturnal irradiance).

7.3 Conclusion

In this chapter, the role of Y319 was explored, and by extension the nature of the ETC. The results presented here show the tyrosine residue to significantly influence the photochemistry of the chicken cryptochrome. In particular, Y319 seems to affect the SCRP yield and the dynamics of long-lived radicals such as $FADH^{\bullet}$. However, the precise mechanism by which it does this remains unclear with more experiments required to better understand the role Y319 plays. Interestingly, despite the OOP-ESEEM measurements providing evidence for an FAD-Y319 RP in *Gg*Cry4a W369F, removal of Y319 did not greatly alter the TA SCRP kinetics. Therefore, it seems any effect the formation of an FAD-Y319 RP may have is outweighed by Y319s influence elsewhere (*i.e.* radical yield etc.). Thus, while ETC adjacent residues C317 and K320 (*cf.* **Chapter 6**) did not seem to alter *in vitro* MFE development, the results for Y319 indicate how amino acid residues in the vicinity of the ETC can influence protein photochemistry and MFE development without necessarily being directly involved in the ETC. For example, removal of the tyrosine residue in *Gg*Cry4a WT to create *Gg*Cry4a Y319F dramatically altered the long-lived radical dynamics and suppressed the development of MFEs in BBCEAS, versus *Gg*Cry4a WT (*cf.* **Chapter 6**). This could suggest that the tyrosine residue is vital for MFE development in WT proteins by indirectly influencing the energetics of electron transfer down the tryptophan tetrad. Furthermore, as the influence of Y319 in *Gg*Cry4a W369F is almost opposite, with its removal boosting MFE formation and impeding long-lived radical accumulation, Y319 may uniquely aid in the magnetic sensitivity of WT proteins. Therefore, since it was shown in **Chapter 6** that four tryptophans may be beneficial *in vivo*, these results indicate that Y319 could be key to the viability of WT Cry4a proteins as a magnetoreceptor.

Naturally, the detection of an FAD-Y319 RP raised questions about phenylalanine's aptitude as an electron transfer blocking mutation. This was thus further explored by mutations to tryptophans W318 and W372, in principle shortening the ETC to two and one residues,

respectively. While no MFE could be detected in *Gg*Cry4a W372F, thus indicating successful blocking of electron transfer by phenylalanine, a small MFE could be measured for *Gg*Cry4a W318F. This was rationalised by invoking a superexchange tunnelling mechanism where phenylalanine acts as a bridge for electron transfer, enhancing the coupling between donor and acceptor and increasing the electron transfer rate for the long range transfer. As such, in *Gg*Cry4a W318F the long-range electron transfer is sufficiently competitive with BET that a small proportion of proteins manage to form a $FAD^{\bullet -}$-$W_DH^{\bullet +}$ SCRP and thus develop a small but measurable MFE. Conversely, in *Gg*Cry4a W372F BET is too rapid for long-range electron transfer to compete, even with superexchange tunnelling. As such, no measurable population of FAD-W369 RPs are formed and thus no MFE is detected. Despite this, large long-lived $FADH^{\bullet}$ concentrations were measured in both proteins, potentially hinting at alternative FAD reduction mechanisms which compete with the desired RPM. This would account for the typically suppressed %MFEs measured by continuous excitation techniques such as BBCEAS and confocal microscopy.[87,102,117,123] Nonetheless, while mutation with phenylalanine may not always entirely block electron transfer, it does significantly suppress it and is thus still a useful mutation. However, it is worth bearing in mind that some electron transfer may occur and thus must be considered when interpreting results from experiments reliant on this mutation.

Chapter 8

Optical Cavity-Enhanced Transient Absorption Spectroscopy

This chapter discusses the development of optical cavity enhanced transient absorption spectroscopy (OCTAS). The working principles and technical aspects of the technique will be introduced before discussing the utility of OCTAS for the study of MFEs in cryptochromes and photoinduced radical pair systems in general. In particular, comparisons to existing techniques will be highlighted where pertinent.

As a means of demonstration, the results from a series of "proof-of-principle" experiments on well characterised model systems are presented with each designed to illustrate the variety of information and data one can obtain for a given system under study. From here, the results from the first OCTAS study of an avian cryptochrome, namely *Gg*Cry4a W369F Y319F, are discussed before finishing the chapter with a few words on the techniques current state of development and some improvements currently being implemented.

8.1 Introduction to OCTAS

As discussed in previous chapters (*e.g.* **Chapter 2**), systems exhibiting the RPM can often involve several orders of magnitude in the timescales of the kinetics with significant spectral overlap of induced photoproducts. This statement is particularly true for cryptochromes and other flavoproteins.[1,4,76,124,149,152,174,175] As such, to truly study these systems, a multi-technique approach is required with each focusing on a different region of the photocycle, either by time scale or detection method (*e.g.*, absorption or fluorescence).

While all time scales are important in constructing a full picture of a RP system there is one of particular importance when studying MFEs therein. By considering the set of conditions required for a MFE to develop (*cf.* **Chapter 2**), it becomes clear that this time scale is in the ns to μs range and largely depends on the HFC interactions within the RP. Take, for



Figure 8.1: Schematic of a 4 level RP system where some ground state (GS) species absorbs a photon to form a SCRP which then undergoes ST mixing and either recombines to the ground state *via* the singlet (S) SCRP state or forms some product (P) *via* the triplet (T) SCRP state.

example, a simple 4-state system where a RP consisting of two electrons and one HFC is formed following photon absorption (*cf.* section 2.4.3). The RP can either recombine from the singlet state or form a long-lived photoproduct from the triplet state (*cf.* **Fig. 8.1**). Assuming the rates of recombination and photoproduct formation are competitive a MFE will develop so long as the rates of recombination and photoproduct formation are not faster than the frequency of ST mixing. That is, the RP must go through one singlet-triplet conversion, in the absence of a magnetic field, before the entanglement is destroyed (radical pair reacts or coherence is lost).[176] This characteristic singlet-triplet conversion time can be estimated in a number of ways[17] but here we will follow Solov'yov *et al.* and calculate it from the Rabi frequency, Ω, between a singlet and triplet state. This is a reasonable approximation since the triplet states are degenerate in the absence of a magnetic field, when electron-electron interactions are negligible.[176]

In the case of a two electron, one spin-$\frac{1}{2}$ nucleus RP, ignoring electron-electron interactions, the spin Hamiltonian is given by

$$\hat{H} = \mu_B B_0(g_A\hat{S}_{zA} + g_B\hat{S}_{zB}) + \mu_B a_{iso}\hat{S}_A \cdot \hat{I}_C \tag{8.1}$$

where B_0 is the applied magnetic field, g_A and g_B are the g-values for the two electrons and a_{iso} is the isotropic HFC between the nucleus with spin $\hat{I}_C$ and the electron with spin $\hat{S}_A$. This Hamiltonian has eight eigenstates with varying degrees of "singlet character" (these are defined in section 2.4.3).[34]

Before estimating any transition rates within the system an appropriate choice of basis states must be made. For the system in question, eight basis states are required (*cf.* **Appendix A.4**) consisting of two singlet and six triplet states. Taking a singlet state

$$|2\rangle \;=\; |S\beta_C\rangle \tag{8.2}$$

and triplet state

$$|4\rangle \;=\; \frac{1}{3}\left(\sqrt{2}\,|T_-\alpha_C\rangle \;-\; |T_0\beta_C\rangle\right) \tag{8.3}$$

where $|AB\rangle = |A\rangle \otimes |B\rangle$, $|\alpha\rangle$ and $|\beta\rangle$ are the two spin states for an $s = 1/2$ nuclear spin and $|S\rangle$, $|T_0\rangle$ and $|T_\pm\rangle$ are the usual two spin-$\frac{1}{2}$ singlet and triplet states (*cf.* equations 2.11 and 2.12), the transition probability between them can be estimated provided[17,176]

$$V_{2\to4} \;=\; \langle 4|\,\hat{H}\,|2\rangle \;\neq\; 0 \tag{8.4}$$

and

$$|V_{2\to4}| \;\geq\; |E_2 - E_4| \;=\; |\Delta E| \tag{8.5}$$

are satisfied. Where, $E_2 = \langle 2|\,\hat{H}\,|2\rangle$ and $E_4 = \langle 4|\,\hat{H}\,|4\rangle$ are the energy expectation values for $|2\rangle$ and $|4\rangle$ respectively. Applying equation 8.4, the matrix element for the transition is given by

$$V_{2\to4} \;=\; \frac{1}{6}\mu_B B_0(g_B \;-\; g_A) \;+\; \frac{1}{4}\mu_B a_{iso} \tag{8.6}$$

Therefore, if the system is initially in $|2\rangle$ then the time dependent probability of finding it in $|4\rangle$ may be determined *via* the Rabi formula as follows[17]

$$P_4(t) = \frac{4V_{2\to4}^2}{4V_{2\to4}^2 + \Delta E^2} \sin^2\left(\frac{\sqrt{(4V_{2\to4}^2 + \Delta E^2)}t}{2\hbar}\right) \tag{8.7}$$

where the characteristic singlet-triplet transition time (neglecting the remaining basis states) is simply the inverse of the rate of oscillation of $P_4(t)$

$$\Omega = \frac{\sqrt{(4V_{2\to4}^2 + \Delta E^2)}}{\hbar} \tag{8.8}$$

Given $E_2 = 0$ and $\Delta E = -E_4$ the energy change upon transition is

$$\Delta E = \frac{1}{9}\mu_B B_0(g_B + g_A) + \frac{1}{6}\mu_B a_{iso} \tag{8.9}$$

Thus, in the absence of an applied magnetic field, the transition matrix element, transition energy and thus characteristic transition time simply depend on the HFC. Therefore, with a HFC of, $a_{iso} = 1.6$ mT, $\Omega = 7.5 \times 10^7$ s^{-1}. Consequently, for a MFE to develop the SCRP must live for approximately 13.3 ns or longer.

With this in mind, techniques targeting the ns to μs time scale are particularly valuable when studying MFEs. In **Chapters 6** and **7** it was demonstrated that TA spectroscopy could effectively monitor the formation and kinetics of photogenerated species on this time scale. However, TA lacks the sensitivity required to reliably monitor the development of the small MFEs inherent in the cryptochrome samples under study. As such, BBCEAS was used to characterise these MFEs due to the technique's significant sensitivity enhancement arising from the implementation of an optical cavity (*cf.* **Chapter 3**). Unfortunately, this gain in sensitivity comes with a drop in time resolution with BBCEAS operating on the ms to s time scale. Additionally, since BBCEAS utilises continuous excitation, it is unable to directly measure any photoproduct lifetimes.

It is perhaps then obvious that some combination of BBCEAS and TA spectroscopy could resolve the drawbacks with each technique whilst lending their respective strengths. Indeed, previous attempts have been made in this vein with the successful development of

condensed phase CRDS[177–180] which employs an optical cavity (á la BBCEAS) and ns pulsed pump and probe lasers (*cf.* **Chapter 3**). However, whilst this technique does maintain a ns time resolution while addressing the lack of sensitivity in TA and providing calibration-free absorbance measurements, it loses significant spectral resolution since the tunable OPO (optical parametric oscillator) probe beam can only monitor one wavelength at any one time. It was thus in an attempt to combine the time resolution and sensitivity of CRDS with the superior spectral resolution of BBCEAS that led to the development of OCTAS, the topic of discussion in this chapter.

8.2 OCTAS Working Principles

In a typical fast pump probe technique, *e.g.* TA and CRDS, a pulsed laser is used to photoexcite a sample before another laser pulse probes the system after some (pump-probe) delay. By then measuring a series of delay points a kinetic profile can be constructed, thus monitoring the lifetimes and dynamics of induced photoproducts. In essence this is exactly how OCTAS functions, the difference being that OCTAS uses "pulsed" (strictly fast-gated) detection rather than probing. This differs from a previous iteration of the OCTAS experiment which utilised continuous time and stepped wavelength acquisition *via* an array of 8 photon multiplier tubes (PMTs) and an oscilloscope.[bf,178]

At its core, OCTAS is simply a modified BBCEAS experiment with both techniques employing a SC source to continuously probe an optical cavity. In each case, the light escaping from the cavity is guided into a spectrograph and dispersed onto a detector, which monitors all wavelengths simultaneously. Where the techniques differ is in the photoexcitation and detection method. That is, where BBCEAS uses a continuous diode laser as its pump source, OCTAS, like CRDS, uses pulsed excitation. Additionally, where BBCEAS uses a conventional, slow, CCD camera, OCTAS uses an intensified CCD camera (iCCD). While these changes are simple they completely change the nature of the information obtained from the experiment and successfully shift the time window from ms to ns/μs.

[bf]Developed by previous group members Dr. Kiminori Maeda, Dr. Dean Sheppard and Dr. Jonathan Storey.

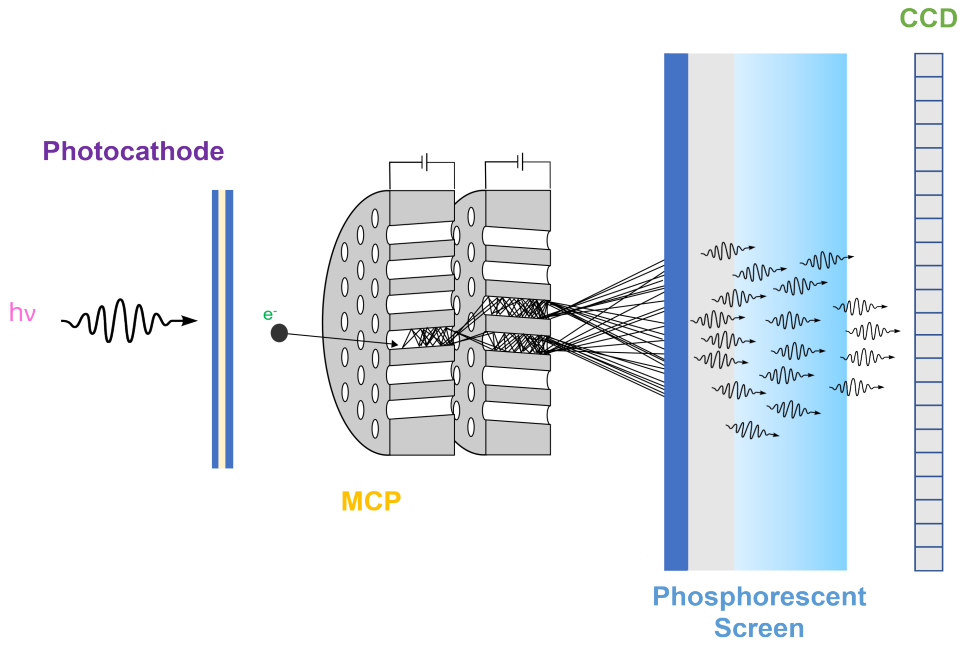

Figure 8.2: Schematic of the major components in an intensified CCD camera.

This significant improvement in temporal resolution largely arises through implementation of the iCCD. As shown in **Fig. 8.2**, photons incident on the iCCD are immediately converted into electrons *via* a photocathode. The number of these electrons is amplified by a microchannel plate (MCP) before impacting a phosphorescent screen, emitting more photons which are subsequently detected by a CCD. By inverting the polarity of the voltage applied to the MCP the flow of electrons to the phosphor screen can be stopped. Since this is an electronic rather than mechanical process, this inversion can be done as fast as 2 ns (with this particular iCCD). Therefore, the light detected by the CCD can be gated (pulsed). Additionally, as this process is done on the photoelectrons from the photocathode, all wavelengths are gated equally and simultaneously, unlike in optical gating (*i.e.* with Pockels or Kerr cells) which is wavelength dependent. Importantly, depending on the desired time scale, the width of the MCP gate and thus acquisition time may be varied to allow more or less light through while kinetic profiles may be constructed by varying the precise timing of the gate pulse relative to photoexcitation.

Due to the optical cavity and short acquisition times, the amount of light reaching the detector is profoundly suppressed. Thus, another important aspect of the iCCD is its amplification of incident light. The majority of this signal gain comes from the MCP

however each of the steps in **Fig. 8.2** has some efficiency which must be taken into account. Therefore, the signal, I, detected by the iCCD may be written as

$$I = N \cdot M \cdot QE(\lambda)_{CCD} \cdot QE(\lambda)_{photocathode} \cdot MCP(V) \cdot Ph_S \tag{8.10}$$

where N is the number of incident photons, M is the electronic gain on the CCD, $QE(\lambda)_{CCD}$ and $QE(\lambda)_{photoacthode}$ are the CCD camera and photocathode quantum efficiencies, $MCP(V)$ is the MCP gain, and Ph_S is the amplification from the phosphor screen given by

$$Ph_S = P_G\left(1-\exp\left(-\frac{t}{\tau}\right)\right) \tag{8.11}$$

where P_G is the maximum phosphorescence gain, t is the CCD exposure time and τ is the emissive lifetime of the phosphor screen.

For an equal number of incident photons, the resulting iCCD signal is several orders of magnitude greater than that of a conventional CCD, depending on the gain voltage applied to the MCP. Therefore, with the appropriate choice of MCP gate width and gain voltage, OCTAS can safely go down to short time windows without loss of sensitivity.

Finally, despite the iCCD's time resolution of a couple of ns, the lower time limit accessible to OCTAS will be dictated by its instrument response function (IRF) which is a measure of the influence an instrument has on a signal measured by it. More specifically, the IRF is the signal acquired from an impulse with an infinitely short lifetime and is defined by the convolution of all of the processes involved in the signal acquisition.[181] Strictly speaking, for spectroscopic measurements, this includes contributions from the lasers, optics, detector and electronics. However, typically some components contribute more than others and the IRF can be approximated to a couple of the most significant. In the case of OCTAS, the instrument response from the detector and electronics is minimal with both significantly faster than the experimental time scale. Consequently, and perhaps

unsurprisingly, the OCTAS IRF is dominated by the optics, due to the optical cavity, and the photoexcitation pulse.[bg]

In **Chapter 3** we saw how an impulse of light decays exponentially as it cycles back and forth in an optical cavity, thus the response of the optical cavity in OCTAS is given by

$$R_C(t) = A\exp\left(-\frac{t}{\tau_{rd}}\right) \tag{8.12}$$

where A is the initial amplitude of light leaving the back cavity mirror, t is time and τ_{rd} is the cavity ring-down time constant, defined by equation 3.11. Meanwhile, the contribution from the excitation pulse reflects its temporal intensity distribution and is given by the following Gaussian

$$G_p(t) = B\exp\left(-\frac{(t-t_0)^2}{\tau_P^2}\right) \tag{8.13}$$

where B is the intensity amplitude, t is time, t_0 is the centre point of the pulse and τ_P determines the pulse width. The IRF is therefore given by

$$\begin{aligned} IRF(t) &\approx \int_{-\infty}^{\infty} G_p(\tau)\, R_C(t-\tau)d\tau \\ &= C\frac{\tau_P\sqrt{\pi}}{2}\exp\left(\frac{\tau_P^2}{4\tau_{rd}^2}-\frac{(t-t_0)}{\tau_{rd}}\right)\left[\mathrm{erf}\left(\frac{(t-t_0)}{\tau_P}-\frac{\tau_P}{2\tau_{rd}}\right)+1\right] \end{aligned} \tag{8.14}$$

where C is some scaling constant and $\mathrm{erf}(z)$ is the error function, with the general definition[182]

$$\mathrm{erf}(z) = \frac{2}{\sqrt{\pi}}\int_0^z e^{-t^2}dt \tag{8.15}$$

[bg]Note, the probe beam need not be considered since it is effectively a constant that scales the contribution from the optical cavity.

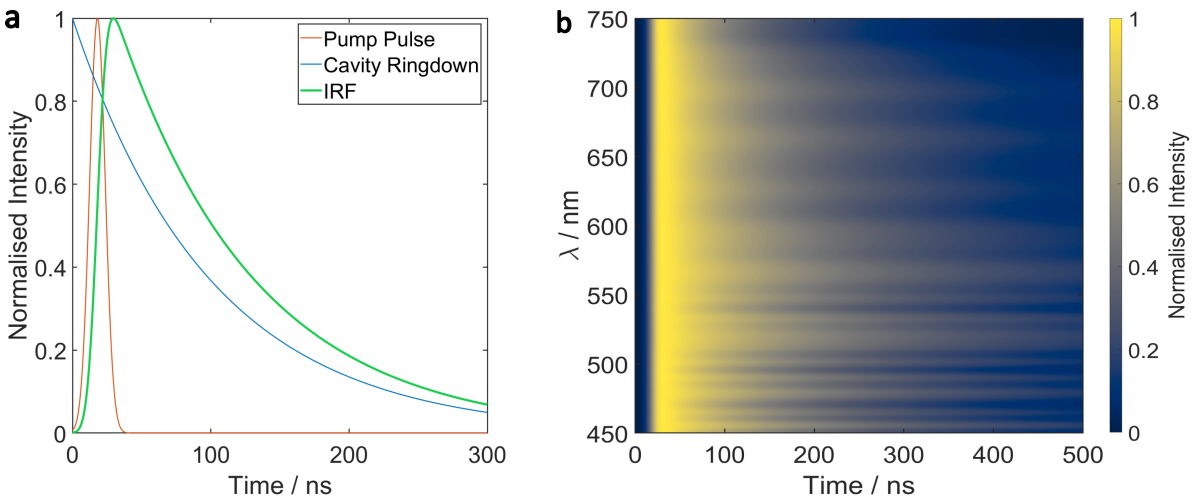

Figure 8.3: a) Shows the analytical form of the IRF (green) along with the individual contribution from the excitation pulse (orange) and cavity ring-down (blue). b) Shows the wavelength dependence of the IRF for a cavity with a water filled sample cell, calculated from a measured R_{eff} spectrum (*cf.* **Chapter 3**).

Fig. 8.3 shows the general profile of the IRF with the major contribution to its overall shape due to τ_{rd}. Since τ_{rd} depends on R_{eff} (effective reflectivity, *cf.* **Chapter 3**) which depends on wavelength, the IRF varies as a function of wavelength. This variation in an empty cavity (water filled sample cell) is displayed in **Fig. 8.3 b** and is calculated from an experimental CEF (cavity enhancement factor, *cf.* **Chapter 3**). To further complicate things, τ_{rd} and thus the IRF depend on the absorption of species within the cavity which in turn varies temporally due to photoproduct formation and dynamics. The IRF is, therefore, clearly sample specific and can vary substantially. Thus, a safe estimate of the lower experimental time limit is that of the empty cavity since sample absorbance works to reduce the IRF by reducing τ_{rd}.

It is, however, possible in some cases to measure the true IRF over some wavelength range by measuring the decay of sample fluorescence within the cavity. If, the fluorescence lifetime is sufficiently shorter than τ_{rd}, and its spectrum is reasonably broad and overlaps with photoproduct formation then the lifetime of the measured cavity signal is essentially τ_{rd}, including the influence of time-dependent absorption from photoproduct formation. Conveniently, this is true in many flavin based systems of interest to the group. An example of this can be found in **Fig. 8.4** which shows a measurement of intracavity fluorescence from 100 μM flavin mononucleotide (FMN), a well characterised highly emissive natural chromophore found in many flavoproteins,[112,175,183–189] in a (50:50, v/v) water/glycerol

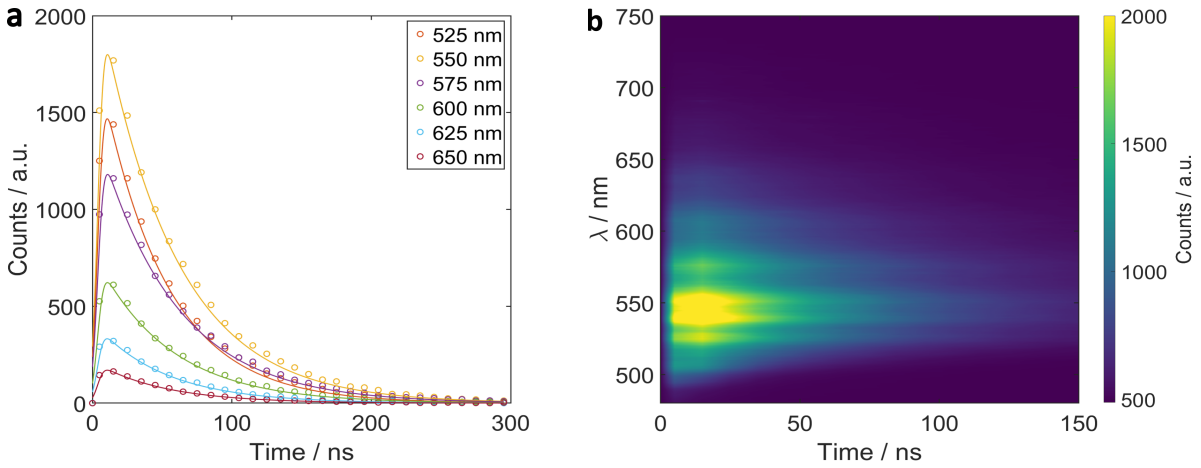

Figure 8.4: a) Individual constant wavelength slices through the fluorescence decay surface, b), of 100 μM FMN following 450 nm pulsed photoexcitation. The solid lines in (a) are fits to the data using the analytical IRF (equation 8.14).

solution. As predicted, the IRF is much shorter than the empty cavity (*cf.* **Fig. 8.3**) due to the rapid formation of the FMN excited triplet state after the laser flash (*cf.* **Fig. 8.7 a**).[bh]

Theoretically, in instances where the IRF is measurable, the lower time limit of the instrument can be further reduced by deconvoluting its influence from the detected signal. This can be done by numerically applying the convolution theorem as follows.[181] Given

$$D(t) = \int_{-\infty}^{\infty} IRF(\tau)\, T_V(t-\tau) d\tau \tag{8.16}$$

where D is the measured value and T_V is the true value.

$$T_V(t) = \mathscr{F}^{-1}\left[\frac{\mathscr{F}\{D(t)\}}{\mathscr{F}\{IRF(t)\}}\right] \tag{8.17}$$

where $\mathscr{F}$ and $\mathscr{F}^{-1}$ are the forward and inverse Fourier transforms respectively and the division is element wise. This, however, remains the subject of future work.

[bh] Of course the IRF will be reduced by the presence of any absorbing species (not just photoinduced). However, in the case of FMN there is good separation between the ground state absorption (main visible peak is at *ca.* 450 nm) and fluorescence spectra. Therefore, any reduction in the IRF above 520 nm is only due to photoinduced absorption changes.

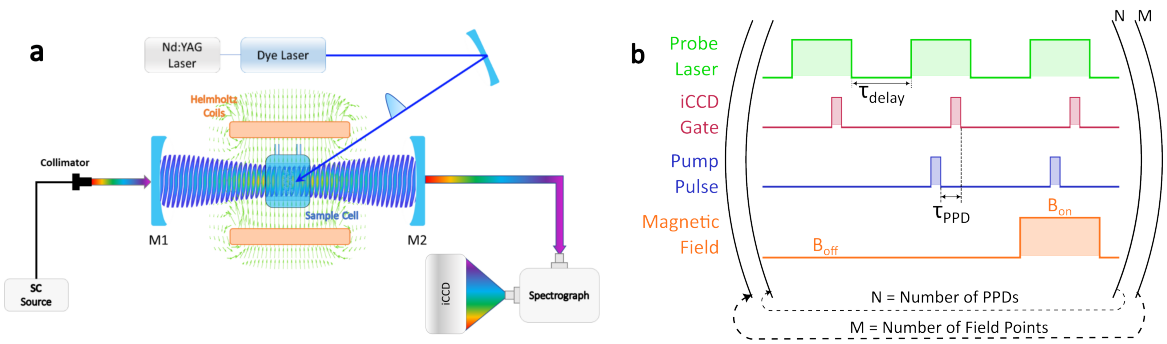

Figure 8.5: Simplified schematic of the OCTAS experimental set-up, a), and triggering sequence, b). τ_{PPD} is the pump-probe delay and is the time delay between laser flash and MCP gate. τ_{delay} is the wait time between individual iCCD acquisitions where the probe laser is shuttered to allow sample recovery. Note the time scales of the individual processes in (b) are not to scale.

8.2.1 Experimental Apparatus

Fig.8.5 shows a simplified schematic of the OCTAS experiment. The optical cavity, SC source, spectrograph and Helmholtz coils employed in the OCTAS experiment are the same as in BBCEAS (*cf.* **Chapter 3**). Photoexcitation is provided by an Nd:YAG (Surelite continuum) pumped dye laser (Sirah Cobra), which produces 8 ns pulses at a variety of wavelengths depending on the dye used. Alternatively, a TTL modulated 450 nm diode laser (Oxxius LBX-450) may be used for longer pulses. In either case, the excitation beam is focused into the sample at a sharp angle relative to the cavity axis such that there is minimal coupling of the pump beam into the cavity. The light escaping from the rear cavity mirror (M2) is dispersed onto the iCCD detector (Andor iStar 320 iCCD) which consists of a Gen3 EVS photocathode (40 % peak efficiency), a P43 phosphor screen (emissive lifetime, τ_P = 2 ms to 10 %) and a 16-bit CCD. The CCD is a 1024×256 array of 26×26 μm pixels providing OCTAS with a spectral resolution up to 0.5 nm per pixel.

All timing and triggering is controlled by a digital delay generator (DDG, Stanford Research Systems DG645) which itself is triggered by the laser flash (either from the Q-switch of the Nd:YAG or TTL signal for the diode). A diagram of the experimental control sequence and acquisition is provided in **Fig.8.5**.

Finally, the whole experiment is controlled *via* a custom written LabView program (National Instruments, 2015 SP1) which allows the user to set experimental parameters (*e.g.* applied

fields, gate delays, MCP gain etc.) and, *via* an AO module (National Instruments, NI-9215), initiates and logs data acquisition.

8.2.2 Experimental Protocol and Data Analysis

Identically to BBCEAS, the fundamental observable detected by OCTAS is the intensity output I_{out} from the optical cavity

$$I_{out} = I_{in}\frac{(1-R)^2T}{1-R^2T^2} \tag{8.18}$$

where I_{in} is the light intensity before the cavity, R is the reflectivity of the cavity mirrors and T is the transmission of light within the cavity. Following the same cavity calibration outlined for BBCEAS in **Chapter 3**, one obtains the effective reflectivity, R_{eff} from which the single pass absorbance is calculated as follows[86,bi]

$$A = -\log_{10}\left[\frac{1}{2{R_{eff}}^2}\left(\sqrt{4{R_{eff}}^2+\left(\frac{I_0}{I_{out}}(1-{R_{eff}}^2)\right)^2}-\frac{I_0}{I_{out}}(1-{R_{eff}}^2)\right)\right] \tag{8.19}$$

where I_{out} is the detected light intensity leaving M2 and I_0 is the intensity of light from an empty reference cavity. As for all pump-probe techniques, we are interested in the change in absorption, ΔA, following photoexcitation. However, for the study of MFEs, we additionally seek to determine the $\Delta\Delta A$. That is, the change in the photoinduced absorption with and without applied magnetic fields. Both ΔA and $\Delta\Delta A$ were defined in **Chapter 3** and are given by equations 3.20 and 3.21 respectively.

The experimental protocol for the measurement of ΔA and $\Delta\Delta A$ is given in **Fig.8.5 b**. For a given data point the instrument takes three measurements, one prior to excitation (I_{GS}), one following photoexcitation (I_{Exc}) and one following photoexcitation with the addition of an applied magnetic field (I_B). Both the pump-probe delay (PPD, delay between excitation pulse and MCP gate) and magnetic field magnitude are randomly selected, to mitigate

[bi] Note, although this differs in form, it is analogous to the single pass absorbance calculated in BBCEAS *cf.* equation 3.19.

systematic noise (*e.g.* laser intensity drift), from a user supplied list with the whole process repeated for every requested PPD and applied magnetic field. This results in a single data set consisting of I_{GS}, I_{Exc} and I_B each with dimensions of wavelength, magnetic field and time. Data sets of many averages are then constructed from multiple repeated acquisitions with the PPDs and applied field vectors re-randomised each time. Finally, a custom Matlab program averages and converts the raw data into ΔA and $\Delta\Delta A$ using equation 8.19. Any additional data processing is not unique to OCTAS and will be demonstrated in the following sections which focus on the results of a variety of "proof-of-principle" experiments.

8.3 Magnetic Field Effects in FMN/HEWL

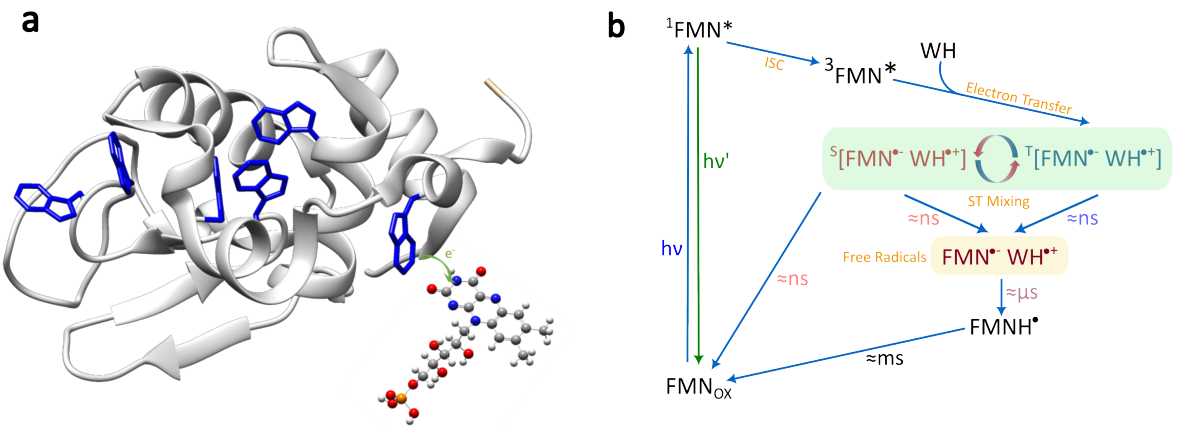

Figure 8.6: a) Crystal structure of the HEWL protein[190] showing the electron transfer from a surface tryptophan to FMN. b) Proposed FMN/HEWL photocycle where a triple born SCRP is formed following electron transfer to the FMN excited triplet state.[175,178]

The first model system explored by OCTAS was FMN and hen egg white lysozyme (HEWL), a classic model system in the study of biologically relevant MFEs.[175,178,191,192] It is thus a very well characterised system and a good standard for testing novel MFE techniques. FMN is a common natural chromophore found throughout biology and plays a vital role in a multitude of processes from photosynthesis to aerobic respiration.[193] HEWL, on the other hand, is a small (14,300 Da) monomeric antibacterial and antifungal enzymatic protein typically used in the food industry.[194,195] However, due to the presence of two surface accessible tryptophan residues,[196] HEWL is an effective electron donor and thus readily forms radical ion pairs with FMN. Thus, thanks to its low cost and availability HEWL has garnered interest as a model for spin chemistry in proteins.

At pH 7 both FMN and HEWL are highly charged in aqueous solution leading to non-specific binding where the FMN molecule freely diffuses around the surface of the HEWL protein.[175] Following absorption of a 450 nm photon, rapid intersystem crossing (ISC) to the excited triplet state precedes electron transfer from a surface tryptophan on HEWL, leading to the formation of a triplet born SCRP. Consequently, any MFEs on photoproducts are expected to be positive by absorption (*cf.* **Chapter 3**). The FMN/HEWL photocycle is summarised in **Fig. 8.6**.

8.3.1 Pulsed Photoexcitation

Fig. 8.7 shows the photoinduced ΔA results of a sample containing 50 μM FMN and 500 μM HEWL in aqueous solution. The FMN $S_0 \rightarrow S_1$ absorption band at 450 nm[183] was excited by a 300 μJ laser pulse over a series of PPDs with the gate width of the iCCD set to 200 ns at early PPD times (up to 1 μs) and 1 μs at later PPDs (after 1 μs).

The initial photoinduced absorption band in **Fig. 8.7 a**, peaking between 650 nm and 700 nm, is attributed to the T_1 triplet absorption of FMN (^{3}FMN*) and decays rapidly, *via* diffusion controlled dynamic quenching, into an FMNH$^\bullet$ absorption band between 500 nm and 650 nm.[175] The kinetic evolution of ^{3}FMN* and FMNH$^\bullet$ are the orange (700 nm) and green (540 nm) traces in **Fig. 8.7 b** respectively. Applying biexponential fits to both yields a lifetime of 1.17 $\pm$ 0.01 μs for the former and 29.7 $\pm$ 18.9 μs for the latter.[bj] More careful analysis of the triplet decay profile allows for the estimation of the rate of ^{3}FMN* quenching by HEWL. Following Miura *et al.*,[175] the decay of ^{3}FMN*, [T], may be modelled by

$$\frac{d[T]}{dt} = -(k_0 + k_q C_{HEWL})[T] - k_{TT}[T]^2 \tag{8.20}$$

where k_q is the quenching rate of [T] by HEWL, C_{HEWL} is the concentration of HEWL, k_{TT} is the rate of triplet-triplet annihilation and k_0 is a first-order rate constant for all other [T]

[bj] Note, the cause of the larger error for the FMNH$^\bullet$ lifetime likely comes from the limited number of data points acquired within its decay.

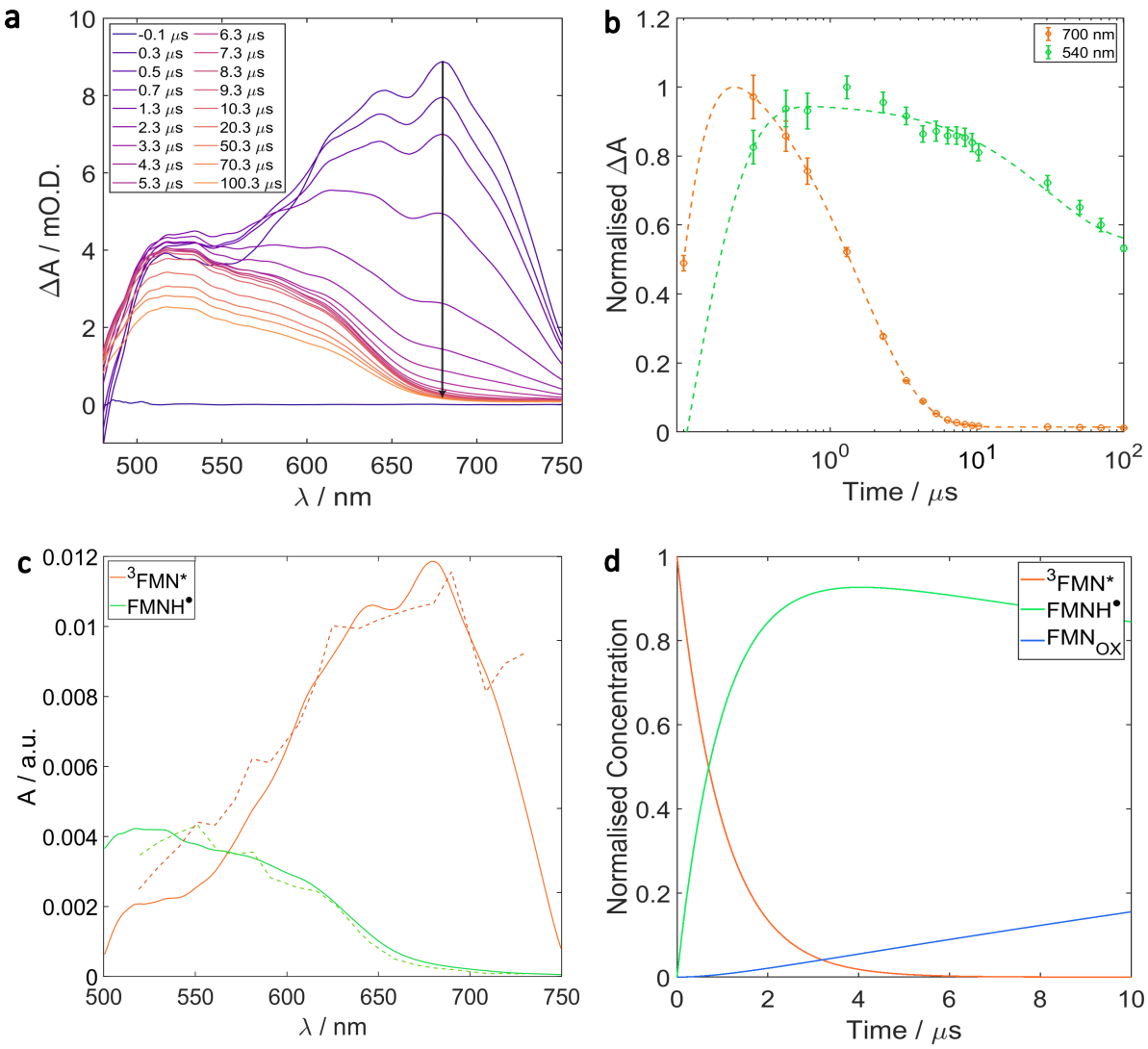

Figure 8.7: a) FMN/HEWL ΔA spectra at individual time points following excitation pulse. b) Kinetic evolution of the ΔA spectra in the $FMNH^{\bullet}$ (green) and $^{3}FMN^{*}$ (orange) absorption regions. The dashed lines are biexponential fits to the data. c) $FMNH^{\bullet}$ (green) and $^{3}FMN^{*}$ (orange) decay associated spectra from global target analysis. The dashed lines are decay associated spectra taken from Dean Sheppard's DPhil thesis.[178] d) $FMNH^{\bullet}$ (green), $^{3}FMN^{*}$ (orange) and FAD_{OX} (blue) kinetic evolution from global target analysis model.

decay processes. Setting $k_0 + k_q C_{HEWL} = k_1$, equation 8.20 can be written as a Bernoulli equation with the general solution[175]

$$[T] = \frac{\exp(-k_1 t)}{\frac{k_{TT}}{k_1}(1-\exp(-k_1 t)) + \frac{1}{[T]_0}} \tag{8.21}$$

where $[T]_0$ is the initial ^{3}FMN* concentration. Setting the triplet-triplet annihilation rate constant, $k_{TTA} = 1.3 \times 10^3$ M^{-1} μs^{-1} (Miura *et al.*)[175] and fitting equation 8.21 to the triplet signal in **Fig. 8.7 b** yields, $k_1 = 0.58 \pm 0.21\ \mu s^{-1}$ and $k_q \approx 710\ M^{-1}\ \mu s^{-1}$.[bk]

The spectral assignments discussed above were confirmed following global target analysis of the ΔA surface assuming a simple A⟶B⟶C kinetic model, where A is ^{3}FMN*, B is FMNH$^\bullet$ and C is the ground state of FMN (see **Appendix A.4** for fit results). The extracted decay associated spectra and their kinetic evolution are shown in **Fig. 8.7 c** and **d** respectively and agree well with previously reported individual species spectra (*cf.* dashed lines in **Fig. 8.7 c**).[124,175,178] These results imply that there is little or no contribution to the ΔA spectra from FMN$^{\bullet-}$, WH$^{\bullet+}$ or W$^\bullet$ [bl] and that FMNH$^\bullet$ forms directly from ^{3}FMN*. This suggests FMNH$^\bullet$ formation actually occurs *via* proton-coupled electron transfer (PCET). Indeed, similar results were observed in TA spectroscopy experiments by Miura *et al.*[175] Moreover, it has been shown that, provided sufficient initial spin polarisation, ST mixing and thus MFEs may occur in neutral radical pairs formed *via* PCET.[197,198]

Photo-CIDNP experiments by Hore and Kaptein showed that RPs in FMN/HEWL were formed with either tryptophan W62 or tryptophan W123 and, given the reference spectra for WH$^{\bullet+}$ and W$^\bullet$ (*cf.* **Fig. 2.9 b**), one would expect to see them in the ΔA spectra above 500 nm. However, if ^{3}FMN* gains both an electron and proton from the tryptophan, forming a [FMNH$^\bullet$ - W$^\bullet$] RP, then WH$^{\bullet+}$ is never present. This is a reasonable suggestion given the proton transfer must be faster than the characteristic singlet-triplet conversion time and is thus unlikely to come quickly enough from the solvent. Thus, the tryptophan is a suitable candidate for proton donation, especially if it's to lose an electron anyway. Additionally, given the solvent accessibility of the tryptophans, W$^\bullet$ is likely rapidly quenched and thus contributes little to the photoinduced absorption. Furthermore, this would remove a recombination partner for FMNH$^\bullet$ potentially leading to it's prolonged lifetime.

[bk] calculated using $k_0 = 2.2 \times 10^5\ s^{-1}$ which was estimated from **Fig. 5** in ref.[175]

[bl] This was further confirmed following a quick analysis of the residual spectra from the fit which was an order of magnitude smaller than the ΔA spectra and exhibited no clear spectral features resembling FMN$^{\bullet-}$, WH$^{\bullet+}$ or W$^\bullet$. A plot of the residuals may be found in **Appendix A.4**

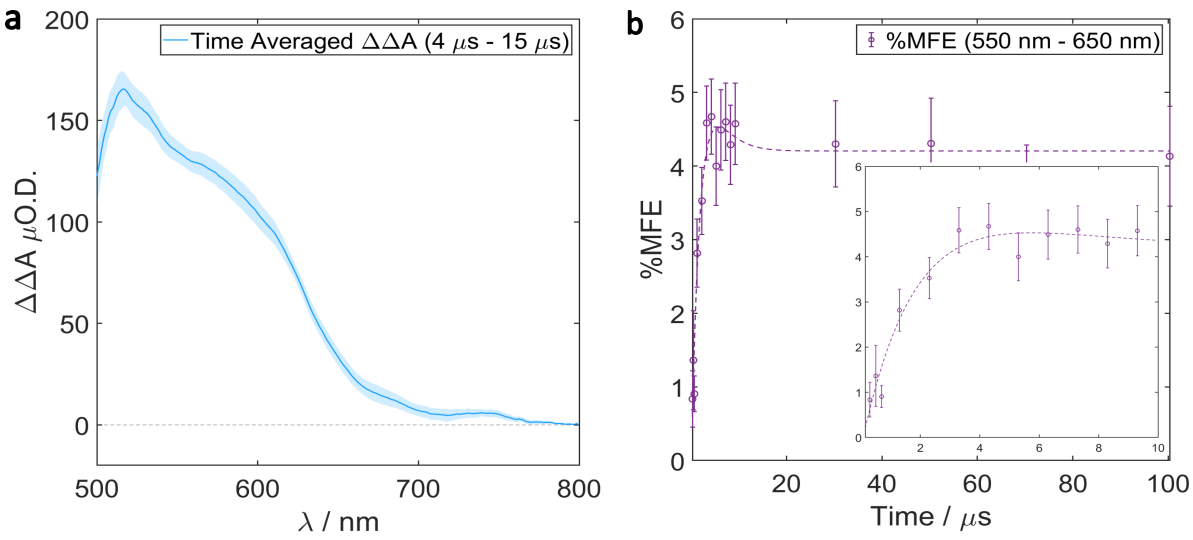

Figure 8.8: a) Time averaged FMN/HEWL $\Delta\Delta A$ spectrum. b) Kinetic evolution of the %MFE averaged over the FMNH$^\bullet$ absorption region (550 nm - 650 nm) where the dashed line is a biexponential fit to the data. The insert shows the %MFE in the first 10 μs following photoexcitation.

The effect of applying a 30 mT magnetic field is shown in **Fig. 8.8** where we observe that the time-averaged $\Delta\Delta A$ spectrum (**Fig. 8.8 a**) consists exclusively of a MFE on the long-lived FMNH$^\bullet$. Consequently, the kinetic evolution of the MFE (**Fig. 8.8 b**) reflects the formation of FMNH$^\bullet$ and peaks at *ca.* 4.7% before plateauing. The MFE grows in as the ^{3}FMN* decays into FMNH$^\bullet$, generating new SCRPS. As the SCRPs stop forming (^{3}FMN* has decayed) and their coherence is lost, *via* relaxation and or quenching of the tryptophan radical, the remaining FMNH$^\bullet$ retains the inherited MFE which persists for as long as FMNH$^\bullet$ does.

The results shown here are in excellent agreement with previous measurements on this system with alternative techniques such as CRDS.[101,178] The advantage here over CRDS is clear, for the same number of averages, and thus laser shots, not only does OCTAS obtain the same kinetic ΔA and MFE data as CRDS, but it also obtains highly resolved ΔA and $\Delta\Delta A$ spectra. Thus providing far more information about the system. This is exemplified by the possibility to identify individual contributing species and spectrally deconvolve them with global target analysis.

8.3.2 Continuous Photoexcitation

We have seen that BBCEAS can accurately monitor the accumulation of long-lived photo-products under constant illumination. However, thanks to the slow CCD detection used,

BBCEAS is blind to the first ms. This potentially limits the dynamic information available if, for example, the formation of the long-lived species is very fast. To circumvent this, OCTAS may be used to map out the first ms (or more) of accumulation under continuous excitation.

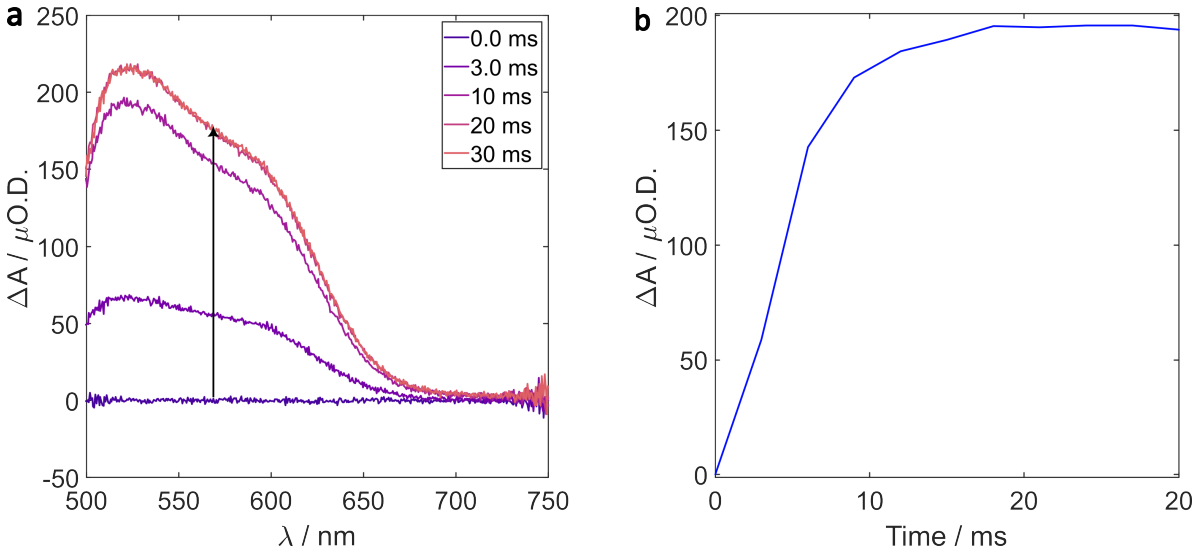

Figure 8.9: BBCEAS ΔA spectra, a), and kinetic evolution, b), of 50 μM FMN and 500 μM HEWL over the first 30 ms. The arrow in a) indicates change in absorption as a function of time which increases as FMNH$^\bullet$ is formed and accumulates.

FMN/HEWL is an example of a system whose long-lived photoproduct (FMNH$^\bullet$) forms rapidly. This is confirmed in **Fig. 8.9 a** and **b** which show the ΔA spectra and kinetics (at 550 nm), respectively, from a BBCEAS experiment on 50 μM FMN and 500 μM HEWL. From the absorption band between 500 nm and 650 nm, it's clear that FMNH$^\bullet$ forms immediately on the BBCEAS timescale and reaches a steady state within 30 ms. As such, the FMNH$^\bullet$ accumulation dynamics are poorly resolved *via* BBCEAS. In the light of this, an OCTAS experiment was carried out on a sample consisting of 50 μM FMN and 500 μM HEWL, continuously excited at 450 nm with a diode laser at 70 mW. The gate width of the iCCD was set to 1 μs

Fig. 8.10 a shows the ΔA spectra over the first ms of illumination. As expected, there is clear formation and accumulation of the long-lived FMNH$^\bullet$ which is characterised by the absorption band between 500 nm and 650 nm. The kinetics of this accumulation can be seen in **Fig. 8.10 b** which exhibits a single wavelength slice at 540 nm. The monoexponential fit, indicates an accumulation time constant of 446 $\pm$ 15.5 μs and

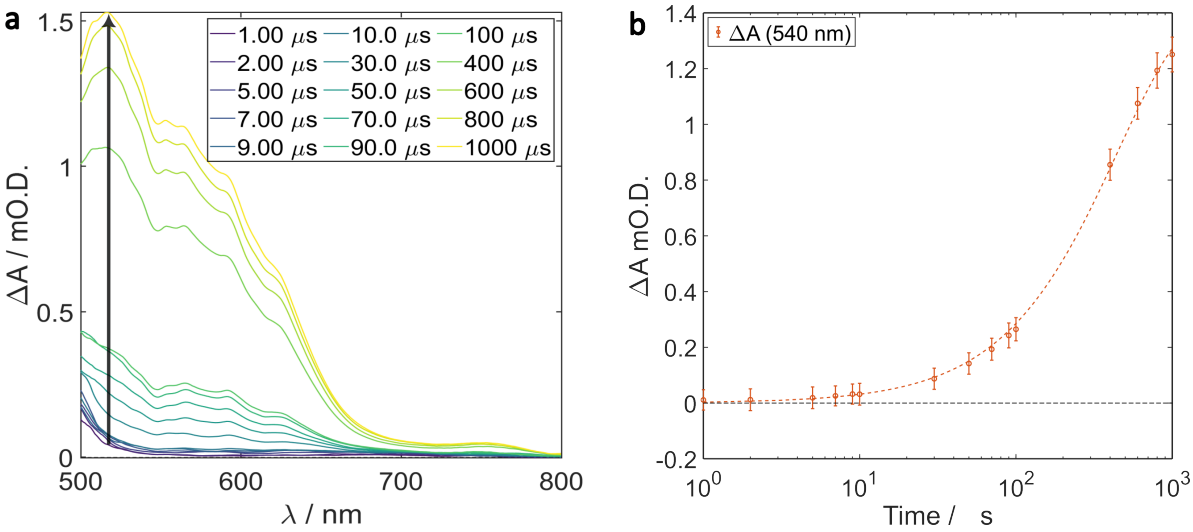

Figure 8.10: ΔA spectra, a), and kinetic evolution, b), of FMN/HEWL under continuous illumination. The dashed line in b) is a monoexponential fit to the data. The arrow in a) indicates the change in absorption as a function of time which increases as $FMNH^{\bullet}$ is formed and accumulates.

suggests the presence of only one significantly accumulating species within that spectral region. This aligns well with the analysis discussed above for pulsed excitation.

The time-averaged $\Delta\Delta A$ spectrum in **Fig. 8.11 a**, once again indicates an MFE exclusively on the formation of $FMNH^{\bullet}$. Consequently, the evolution of the MFE under continuous illumination should simply reflect the accumulation kinetics of $FMNH^{\bullet}$. This is indeed the case as indicated by the $\Delta\Delta A$ kinetics shown in **Fig. 8.11 b**.

The combination of OCTAS and BBCEAS promises to be a fruitful partnership in elucidating the accumulation and MFE dynamics of systems under continuous illumination. This is particularly relevant in the study of magnetoreception and photosensitive biological systems in general since natural forms of light (*e.g.* sun, moon, stars *etc.*) are rarely pulsed, especially on a ns timescale. Thus, while pulsed techniques are important in the study of photosensitive processes, continuous illumination techniques offer an arguably more representative characterisation of such systems. Therefore, the ability to observe both early and late system dynamics under such conditions holds great value. This is never truer than in the study of cryptochromes where the early stages following continuous excitation have yet to be observed. Although BBCEAS has been used extensively to monitor cryptochrome photochemistry over long time scales, it potentially misses much of the kinetic behaviour

of $FAD^{\bullet-}$ and $W^{\bullet}$. With OCTAS, this initial behaviour may finally be measured, however, this is the subject of future work.

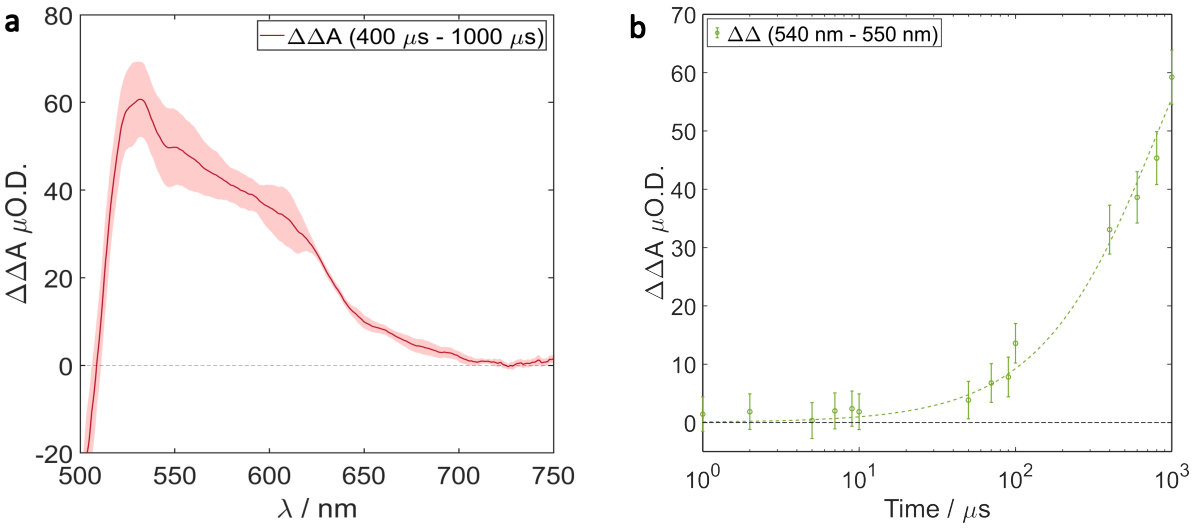

Figure 8.11: Time-averaged (400 μs - 1 ms) $\Delta\Delta A$ spectrum, a), and $\Delta\Delta A$ kinetic evolution, b), of FMN/HEWL under continuous illumination. The dashed line in b) is a monoexponential fit to the data.

8.4 Magnetic Field Effects in FAD

Like FMN, flavin adenine dinucleotide (FAD) is a common natural chromophore found throughout biology and famously acts as the chromophore in the cryptochrome proteins potentially responsible for avian magnetoreception. The spin chemistry of FAD in aqueous solutions is very well established and has been the subject of a multitude of research articles.[124,162,189,199–201] It is, therefore, an ideal model system to benchmark any new technique seeking to monitor MFEs arising from RPs.

Following photon absorption, the excited triplet state is formed *via* ISC before FAD reversibly accepts an electron from the adenine moiety at the end of it's N5 tail (*cf.* **Fig. A.9**). Therefore, unlike FMN/HEWL, FAD forms an intramolcular SCRP. As usual, the SCRP undergoes ST mixing and can either recombine to the ground state *via* the singlet or recombine back to the excited triplet state of FAD. Thus, the SCRP is in equilibrium with the FAD T_1 state. This photochemistry is summarised in **Fig. 8.12**.

It should be noted that the system is strongly pH dependent. In particular, the identity of the SCRP varies depending on the native protonation states of the adenine (A) and isoalloxazine ring which thus alter the HFC interactions within the RP. Additionally, the

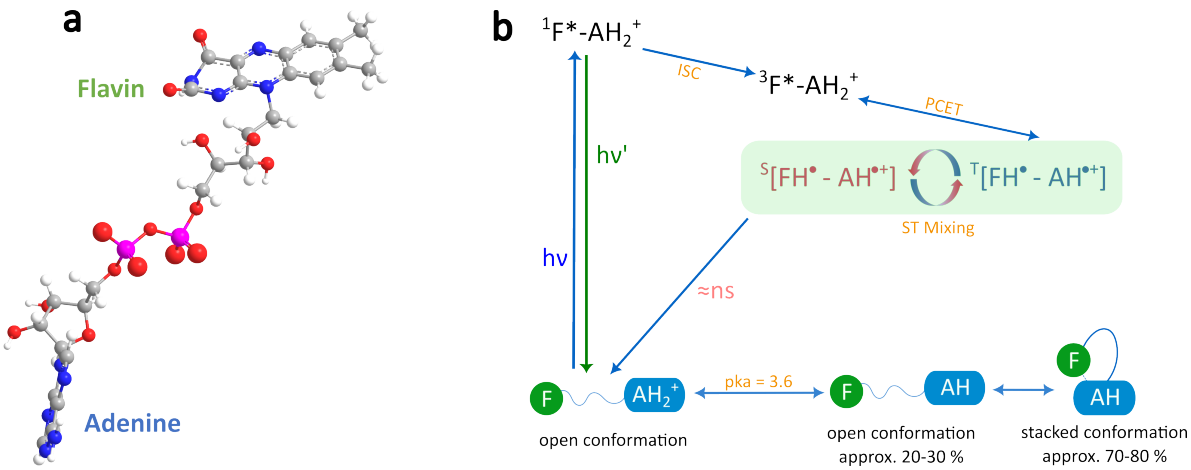

Figure 8.12: a) Structure of FAD. Grey atoms = carbon, white atoms = hydrogen, blue atoms = nitrogen, red atoms = oxygen and pink atoms = phosphorus. b) Proposed photoscheme for intramolecular MFEs in FAD under acidic conditions.

recombination rate increases, decreasing the RP lifetime, steadily from acidic to neutral pH due to the formation of a stacked conformation (*cf.* **Fig. 8.12**). On top of this, the close proximity of the adenine and isoalloxazine ring in the stacked confirmation leads to a large exchange interaction between the radicals, impeding any spin coherent effects.[124,162,175] With this in mind, a 50 μM FAD sample was prepared in a citric buffer solution (4 mM Na_2HPO_4, 98 mM citric acid monohydrate in distilled water) at pH 2.3. The pulsed dye laser was used to excite the sample at 450 nm with 300 μJ pulses while the iCCD gate width was set to 1 μs.

The ΔA results are displayed in **Fig. 8.13**. Immediately after excitation, formation of the $^3F^*$ state is observed and characterised by the large absorption band centred at *ca.* 660 nm in **Fig. 8.13 a**. The $^3F^*$ state decays rapidly, with a lifetime of 852 ± 24.4 *ns* (*cf.* **Fig. 8.13 b**), into some long-lived state whose absorption spectrum significantly overlaps with that of the triplet state. However, the absorption band between 500 nm and 550 nm indicates immediate (1.5 μs) formation from the FAD triplet state. The precise identity of this state is unclear. Several authors have suggested it could be FH$^\bullet$ owing to the formation of an FH$^\bullet$ - AH$^{\bullet+}$ RP.[124,162,175,178,199,200] However, for the FH$^\bullet$ - AH$^{\bullet+}$ RP to develop MFEs, it must retain the spin polarisation obtained from the electron transfer during the protonation/deprotonation process. Therefore, given protonation and deprotonation is not spin-selective, the F$^{\bullet-}$ - AH$_2^{\bullet 2+}$ to FH$^\bullet$ - AH$^{\bullet+}$ conversion must be faster or similar to the singlet-triplet conversion time.[202] Indeed, CIDNP experiments by Stob *et al.* suggested that

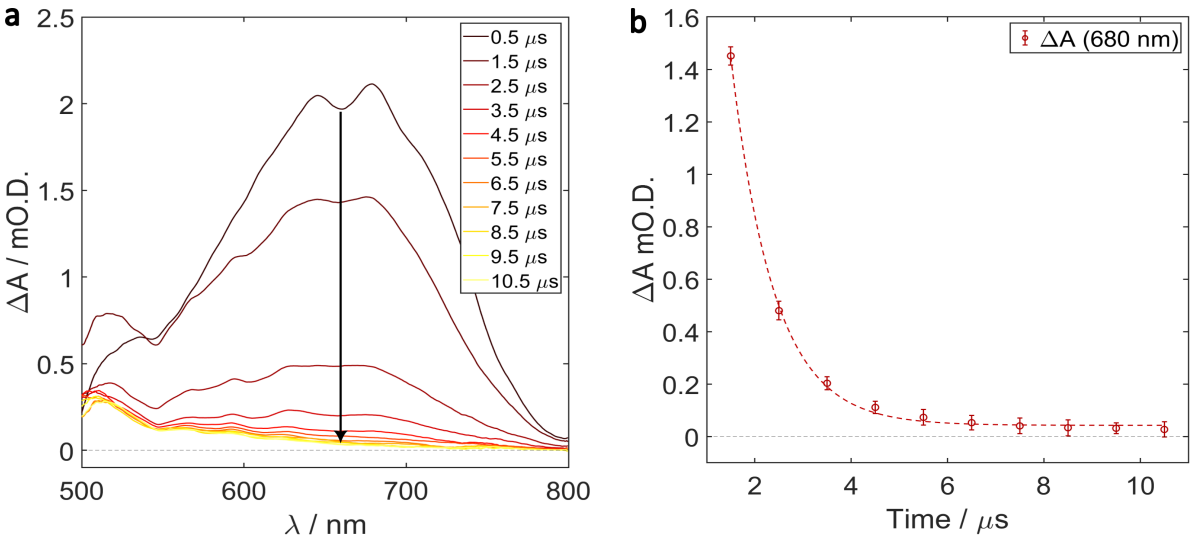

Figure 8.13: a) Time dependent ΔA spectra of FAD and kinetic evolution at 680 nm, b). The ΔA spectra primarily shows the formation and decay of the FAD triplet state. The dotted line in (b) is a mono-exponential fit to the data with a constant offset.

rapid intramolecular proton transfer between the adenine and isoalloxazine[199] is likely, at least within their experiment time scale. Thus it seems plausible that, like FMN/HEWL, the reaction scheme essentially follows PCET between $^3F^*$ and AH_2^+. Nonetheless, the spectral profile of $FH^\bullet$ has been well characterised[1,149] and is at odds with the observed spectra here. If anything, by eye, this long-lived species more closely resembles known spectra for $F^{\bullet-}$ which would imply a $F^{\bullet-}$ - $AH^{\bullet+}$ RP. However, for this to be true the (de)protonation reactions must occur with the solvent/buffer and must be relatively slow.

The effect of applying a 30 mT magnetic field to the system is shown in **Fig. 8.14**. The $\Delta\Delta A$ spectra in **Fig. 8.14 a** closely resembles the ΔA spectra and shows a large positive MFE primarily on the FAD triplet state, confirming the existence of the triplet/RP equilibrium. As with the ΔA spectra, the shoulder present between 500 nm and 550 nm suggests a contribution to the MFE from this long-lived species. The positive sign of the $\Delta\Delta A$ spectra confirms the formation of a SCRP from a net triplet state. Interestingly, the $\Delta\Delta A$ spectra appears to decay to zero within a few μs, with no long lived component resembling that observed in the ΔA spectra. This implies that the process leading to its formation in the ΔA spectra may not proceed *via* a SCRP. Alternatively, it could indicate the presence of some stacked conformation, even at pH 2.3. This is because the mechanism for the stacked conformation leads to a, potentially long-lived, $FH^\bullet$ - $A^\bullet$ biradical while the large exchange interaction would destroy any MFEs.[124,162,202]

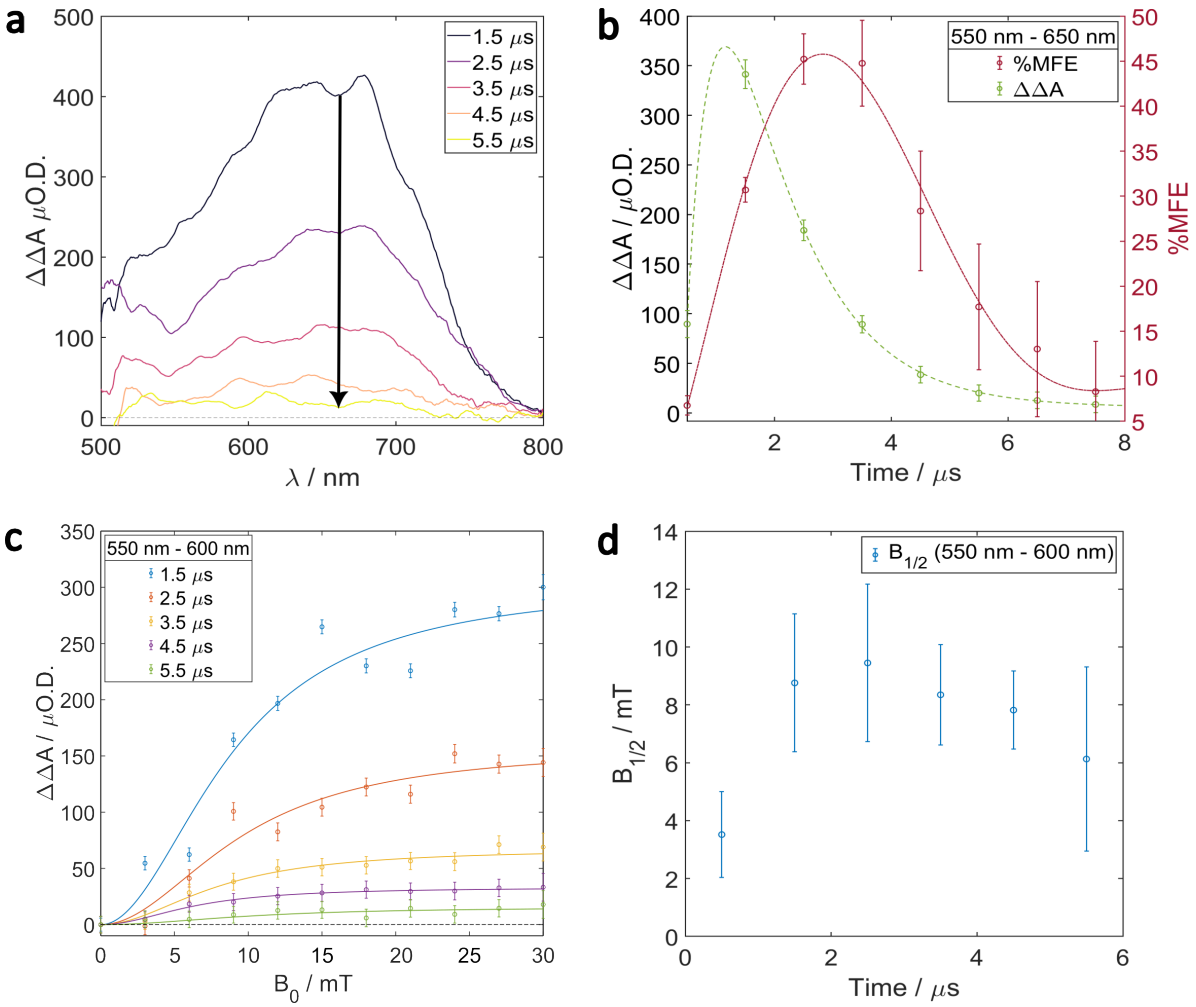

Figure 8.14: a) Time dependent $\Delta\Delta A$ spectra and MFE evolution following photoexcitation, b). MARY spectra, c), and the corresponding $B_{1/2}$ time dependence, d). The green dashed line in b) is a biexponential fit to the data while the solid line is a spline interpolation and is there to guide the eye.

The green data points in **Fig. 8.14 b** show the kinetics of the $\Delta\Delta A$ spectra averaged from 550 nm to 650 nm. The kinetic evolution of the $\Delta\Delta A$, unsurprisingly, closely resembles that of the ΔA kinetics and has a lifetime of $1.04 \pm 0.18\,\mu s$. Converting to a percentage MFE yields slightly different dynamics due to the varying timescales involved in the evolution of the ΔA and $\Delta\Delta A$ spectra. The percentage MFE peaks at a very respectable 45 % and is in good agreement with CRDS measurements on the same system.[178] However, while the evolution of the MFE is in good agreement with Murakami *et al.*,[124] the magnitude differs from some reported values (*e.g.* Antill *et al.* $\%MFE \approx 16\,\%$).[162] This is likely a result of the higher FAD concentration ($200\,\mu M$) used in those publications leading to greater competing triplet-triplet annihilation processes which work to reduce the formation of SCRPs (*cf.* equation 8.20).[123,124]

Magnetically altered reaction yields (MARYs) were measured and the results are shown in **Fig. 8.14 c** and **d**. The saturation point of the MARY profiles obviously decays in correspondence with the $\Delta\Delta A$, however, interestingly, the $B_{1/2}$ appears to grow in, peaking at 9.45 mT after 2.5 μs, before gradually decreasing to 6.13 mT after 5.5 μs. The initial increase from 3.52 mT is expected since spin relaxation on the SCRP lifetime causes time dependent broadening, depending on the relaxation mechanism (*cf.* **Chapter 2**). Given the Weller formula, which may only be empirical and approximate, predicts a $B_{1/2}$ of 2.6 mT for a flavin-adenine RP, it seems clear that there is extensive spin relaxation with some broadening already present in the first time point measured. This relaxation likely occurs due to modulation of the electron exchange and dipolar coupling interactions as the adenine and isoalloxazine are free to move around relative to one another.[162]

The subsequent decline of the $B_{1/2}$ is more unusual as typically one would expect relaxation induced broadening to converge to some constant value after some time specific to a given system.[180,203] However, it is worth recalling that the majority of the observed MFE is on the FAD triplet state which is in equilibrium with the SCRP. As such, the MFE is inherited, and due to the constant repopulating of the SCRP, contains contributions from varying "sets" of SCRPs at varying time points which have relaxed to different extents. All of this further complicates the observed behaviour and could work to average out much of the minutiae. In spite of this, some preliminary simulations of the SCRP, including the equilibrium, failed to reproduce the $B_{1/2}$ decay. In any case, the $B_{1/2}$ behaviour must be independently reproduced before any conclusions can be drawn. Nonetheless, the MARY plots obtained with OCTAS are in good agreement with those in the literature and successfully demonstrate the instrument's capabilities in both time and field dependent experiments.

8.5 Magnetic Field Effects in a CPF Triad

The third, and final model system explored with OCTAS is that of the carotenoid-porphyrin-fullerene (CPF) triad which is shown, along with its photocycle, in **Fig. 8.15**. Originally developed as a mimetic for photosynthetic reaction centres, the CPF triad garnered interest

in the spin chemistry community due to its rapid formation of, relatively, long-lived RPs in high yield (*ca.* 95 %).[13,34,204–207] Additionally, unlike the FAD and FMN/HEWL model systems previously discussed, the CPF triad forms singlet born RPs, similarly to cryptochrome proteins. As such, one would typically expect negative MFEs in the photoinduced absorption.

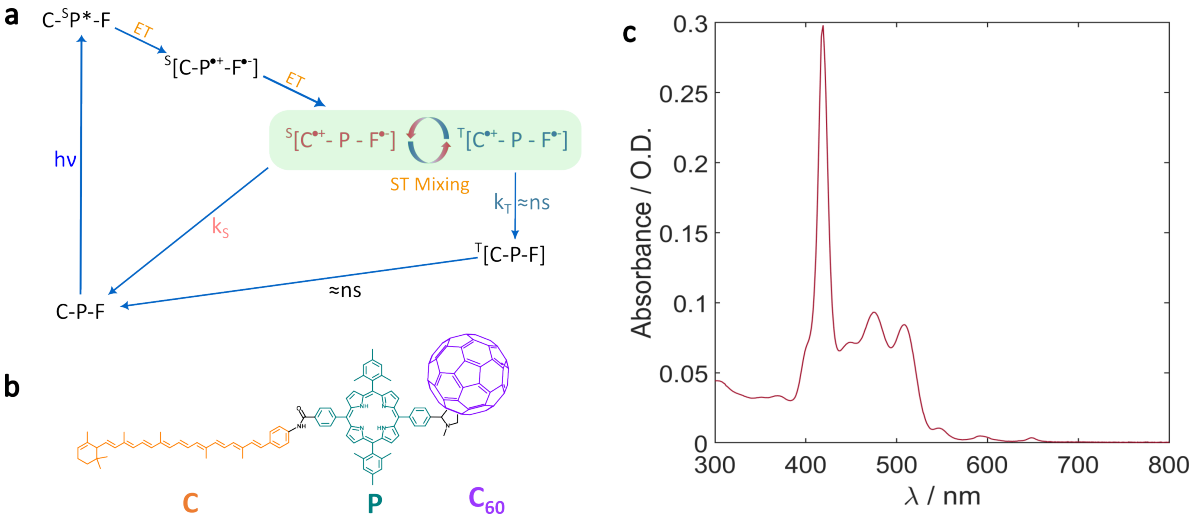

Figure 8.15: CPF photocycle a) and structure, b), where the fullerene, C_{60}, is shown in purple, the porphyrin, P, in green and the carotenoid, C, in orange. ET = electron transfer, k_S = singlet recombination rate constant and k_T = triplet recombination rate constant. c) shows the ground state absorption spectrum of a CPF sample and is simply the sum of the absorption spectra from individual triad components.

Photoexcitation of the porphyrin into its S_1 or S_2 state (Q-band or Soret-band) leads to rapid ($\tau \approx 32$ ps)[204] electron transfer to the fullerene, creating a ^{S}[C-P$^{\bullet+}$-F$^{\bullet-}$] RP. Charge separation is achieved following a second rapid electron transfer ($\tau \approx 125$ ps)[204] from the carotenoid moiety to the porphyrin, generating the long-lived ($\tau \approx 56$ ns)[204] [C$^{\bullet+}$-P-F$^{\bullet-}$] RP. As usual, the RP can then undergo ST mixing before either recombining, *via* the singlet, to the ground state or, *via* the triplet, to the triplet state of the carotenoid, ^{3}C-P-F. At room temperature in 2-methyltetrahydrofuran (2-MeTHF), recombination to the ground state is believed to be in the Marcus inverted region while recombination to the carotenoid triplet state is in the Marcus normal region. Hence, the formation of ^{3}C-P-F over the ground state is favourable and occurs with a *ca.* 95 % yield.[204] The implication here is that $k_T >> k_S$ such that k_S is approximately zero, relatively speaking. This relationship is, however, solvent and temperature dependent. More specifically, the electron transfer reactions are

largely driven by thermodynamic considerations rather than electronic coupling and as such depend strongly on the relative permittivity, ϵ_r, of the solvent.[204]

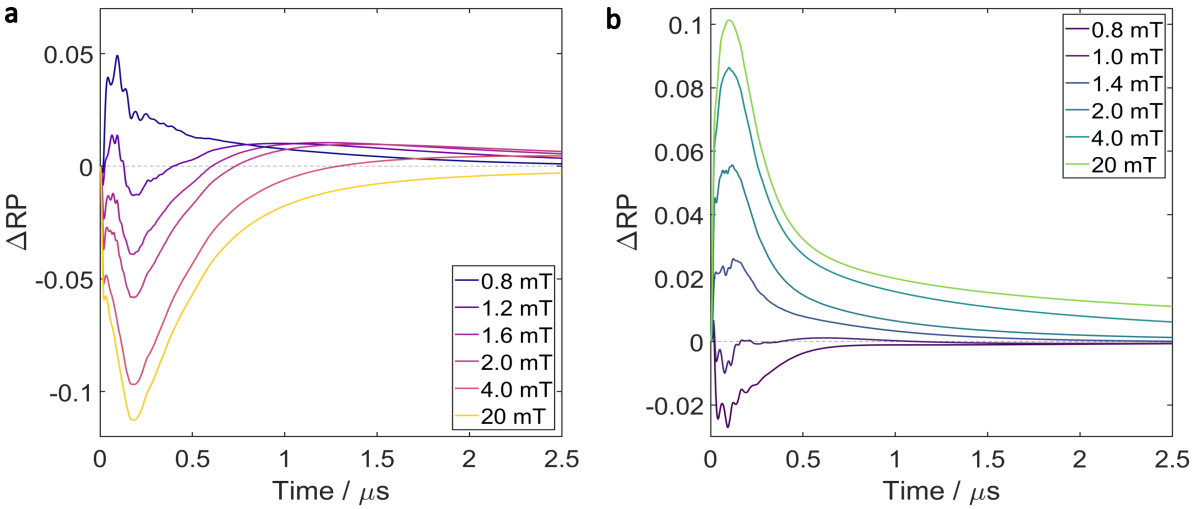

Figure 8.16: Spin dynamics simulations of the CPF triad where $\Delta RP = P_{RP}(B) - P_{RP}(B=0)$ is the change in the total RP probability when a magnetic field is applied. In a), $k_S > k_T$ and in b), $k_T > k_S$. All simulations were done using the trace sampling method developed by Lewis *et al.*[208] and Fay *et al.*[209] (*cf.* **Appendix A.3**). Calculations included the largest 15 isotropic HFC constants on the carotenoid and 0 HFC constants on the C_{60}, exchange coupling and relxation were ignored. The HFC constants were obtained from Lewis *et al.*[207]

In 2-MeTHF, ϵ_r is particularly temperature dependent and steadily increases as the temperature is lowered from 298 K to 110 K at which point it freezes causing a sharp drop.[205] As ϵ_r increases little happens to ^{3}C-P-F, however it does cause an increase in the reorganisation energy, λ, and stabilises ^{S}[C$^{\bullet+}$-P-F$^{\bullet-}$] resulting in a decrease in the driving force, ΔG^o. Consequently, due to the singlet and triplet recombinations existing in the Marcus inverted and Marcus normal regions respectively, k_S increases while k_T decreases such that $k_S >> k_T$ at low temperatures (*e.g. ca.* 120 K, $\epsilon_r = 18$) and $k_T >> k_S$ at higher temperatures (*e.g.* 298 K, $\epsilon_r = 6.5$). Accordingly, the kinetic evolution and MFEs of the CPF triad vary profoundly with temperature in 2-MeTHF.[205,210] For example, at 120 K, when $k_S >> k_T$, the MFE on [C$^{\bullet+}$-P-F$^{\bullet-}$] exhibits magnetic field dependent multiphasic behaviour at low magnetic fields strengths (< 2 mT). Conversely, at stronger magnetic fields, the high magnetic field effect dominates and the MFE is monophasic and negative.[210] A theoretical study by Lewis *et al.* suggested that this complex behaviour arises from the different time-dependent probabilities of the T_+, T_- and T_0 states at different magnetic field strengths.[34] Furthermore, at 298 K, the [C$^{\bullet+}$-P-F$^{\bullet-}$] MFE is all monophasic and positive, apart from a low field effect below 1.0 mT.[210] Despite this complex behaviour in [C$^{\bullet+}$-P-F$^{\bullet-}$],

the MFEs in ^{3}C-P-F should remain negative, regardless of the k_S/k_T relationship, since the application of a constant magnetic field always works to reduce the triplet recombination fraction. These behaviours are summarised in **Fig. 8.16** which shows the results of a series of theoretical calculations at different external field strengths for $k_S >> k_T$ and $k_T >> k_S$.

Given the minimum time scale available to OCTAS (equation 8.14), the primary species of interest here is the formation and evolution of ^{3}C-P-F and any inherited MFEs it may have. In this regard, a sample of *ca.* 0.3 OD at 419 nm (*cf.* **Fig. 8.15**) CPF was prepared in 2-MeTHF.[bm] The system was photoexcited with 600 μJ laser pulses at 420 nm (Soret band) and the iCCD gate width was set to 100 ns. Due to cooling limitations with the current experimental setup, experiments were run at 280 K.

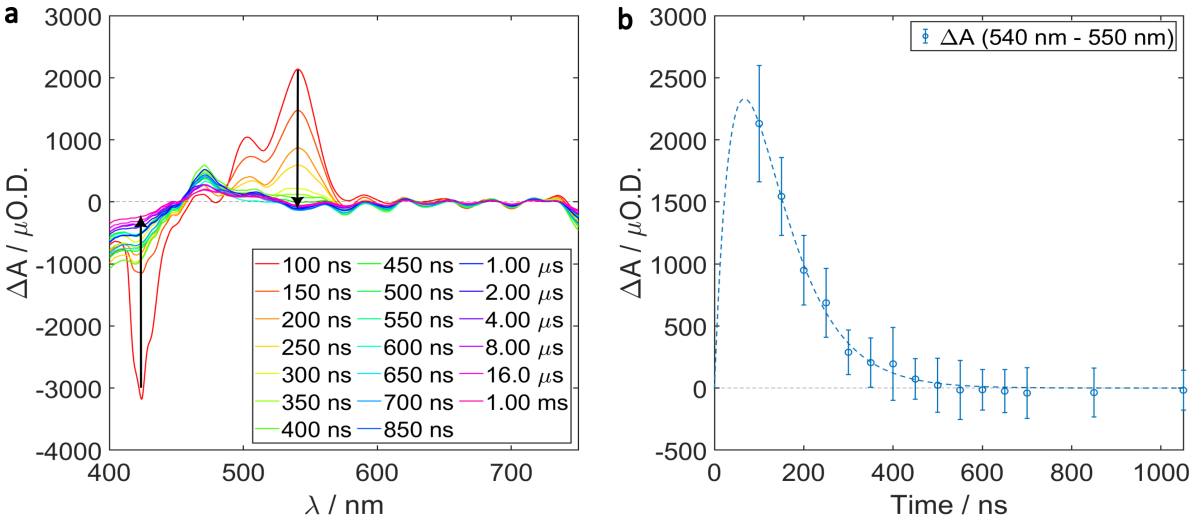

Figure 8.17: a) CPF ΔA spectra at varying PPDs following excitation. b) shows the ΔA kinetic evolution of ^{3}C-P-F (540 nm - 550 nm). The arrows in a) indicate the change in absorption as a function of time while the dashed line in b) is a fit to the data using equation 8.22.

Fig. 8.17 a shows the ΔA spectra at several PPDs after excitation. The ^{3}C-P-F absorption band is characterised by the peak centred at 540 nm which decays rapidly after photoexcitation. The kinetic evolution of ^{3}C-P-F is shown in **Fig. 8.17 b** where the trace is fitted to

$$\Delta A_{540nm-550nm} = \frac{A\,k_f}{k_d - k_f}\left(e^{-k_f t} - e^{-k_d t}\right) \tag{8.22}$$

[bm] Concentration not reported here due to the wildly varying published extinction coefficients for tetraphenylporphyrins. However, the concentration will be as low as a few hundred nM.[211]

which is the general solution for the intermediate species in an A⟶B⟶C kinetic system. Here, k_f is the rate of formation of ^{3}C-P-F from [C$^{\bullet+}$-P-F$^{\bullet-}$], k_d is the rate of decay of ^{3}C-P-F and A is a scaling constant.[36] The fit provides an estimated ^{3}C-P-F lifetime of 86 ± 15 *ns* and [C$^{\bullet+}$-P-F$^{\bullet-}$] lifetime of 53 ± 13 *ns*. While the [C$^{\bullet+}$-P-F$^{\bullet-}$] lifetime is in excellent agreement with Gust *et al.* the lifetime of ^{3}C-P-F is much shorter than previous estimates due to the dissolved oxygen concentration in solution.[204,210] Typically when measuring CPF, the solvent is degassed to prevent quenching of the carotenoid triplet state by O_2. This was not possible in this case as the solvent and sample had to be exposed to air upon transfer into the sample cell which itself is not perfectly air tight. This largely arises as a bi-product of the experiment being primarily designed to study proteins in aqueous solution.

The influence of a 30 mT applied magnetic field is shown in **Fig. 8.18** where the $\Delta\Delta A$ spectrum in **Fig. 8.18 a** (time averaged from 100 ns - 200 ns) indicates a ^{3}C-P-F MFE through the negative absorption band centred at 540 nm. As predicted above, this observed MFE on the carotenoid triplet state is negative with a measured magnitude of 142 $\mu O.D.$ (*ca.* 6.66 %) and evolves on a similar time scale to the ΔA kinetics (*cf.* **Fig. 8.18 b** and **Fig. 8.17 b**). Once again, the presence of dissolved oxygen works to quench ^{3}C-P-F, reducing the magnitude and lifetime of the MFE. Nonetheless, the magnitude of the MFE agrees reasonably well with previously reported results under similar conditions.[210]

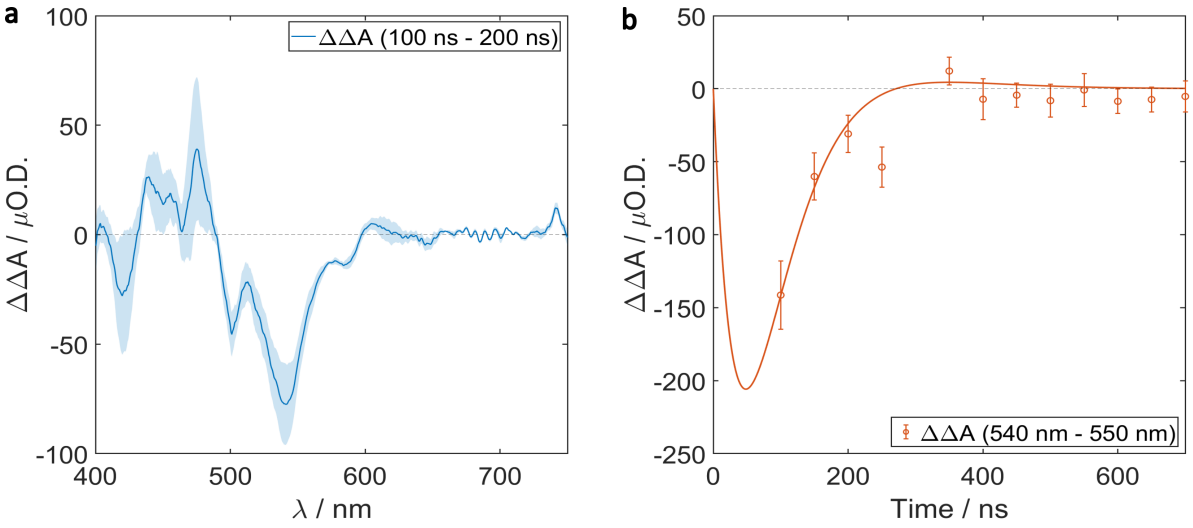

Figure 8.18: a) $\Delta\Delta A$ spectra averaged from 100 ns to 200 ns and, b), $\Delta\Delta A$ kinetics of ^{3}C-P-F. The solid line in b) indicates the subtraction of fits to the ΔA data with and without applied magnetic fields using equation 8.22.

The line through the data points in **Fig. 8.18 b** is the result of subtracting a fit to the ΔA kinetics with an applied magnetic field, using equation 8.21, from the fit in **Fig. 8.17 b**. Given the lifetime of ^{3}C-P-F ought to be unaffected by the application of a magnetic field, k_d was kept the same for the field-on fit thus only allowing the ^{3}C-P-F formation rate constant, k_f, to vary. This is to be expected despite the fact that applying a magnetic field will not effect k_S or k_T and can be understood by considering the limit where $k_S = 0$. Under this condition all of [C$^{\bullet+}$-P-F$^{\bullet-}$] goes on to form ^{3}C-P-F thus, its formation dynamics is simply [^{3}C-P-F] $= A(1 - RP_{tot})$ where RP_{tot} is the total [C$^{\bullet+}$-P-F$^{\bullet-}$] probability and A scales the dynamics to absorption. As the application of a magnetic field reduces the rate of ST mixing and isolates the T_+ and T_- states, the overall probability of the triplet states is reduced meaning less of the [C$^{\bullet+}$-P-F$^{\bullet-}$] can go onto form ^{3}C-P-F at any one time. This results in a reduction in the measurable reaction rate constant, k_f, and causes a time dependent MFE, even though the magnetic field has no effect on the overall ^{3}C-P-F yield.

Interestingly, the fit in **Fig. 8.18 b** also predicts a slight positive MFE after *ca.* 300 ns. This is a result of the slower formation of the carotenoid triplet shifting it's maximum concentration to a later time. Unfortunately this time region lacks the data points required to back up the predicted biphasic MFE with more experiments required to adequately test this behaviour. However, if true, it would demonstrate the influence the relationship between the evolution of the SCRP and the lifetime of downstream products has on the evolution of inherited MFEs. In this instance, for example, a monophasic MFE on the SCRP may correspond to a more complex biphasic MFE in a downstream species.

8.6 Magnetic Field Effects in *Gg*Cry4a W369F Y319F

Following the above demonstration of OCTAS' capabilities in the study of MFEs, some preliminary experiments on an avian cryptochrome were performed. For this endeavour, *Gg*Cry4a W369F Y319F was chosen due to its high stability, high radical yield and rapid reoxidation. *Gg*Cry4a W369F Y319F was originally expressed to study the role of the tyrosine (Y319) adjacent to the terminal tryptophan and then subsequently phenylalanine as an electron blocker. This particular protein has already been studied with several

techniques and was discussed extensively in **Chapter 7**. For the following experiment, a 30μM (0.3 OD at 450 nm) sample was prepared in pH 8 Tris buffer (10 mM Tris, 250 mM NaCl and 20 % glycerol in water v/v). The system was then excited at 450 nm with 300 μJ, 8 ns, laser pulses while the iCCD gate width was set to 1 μs.[bn]

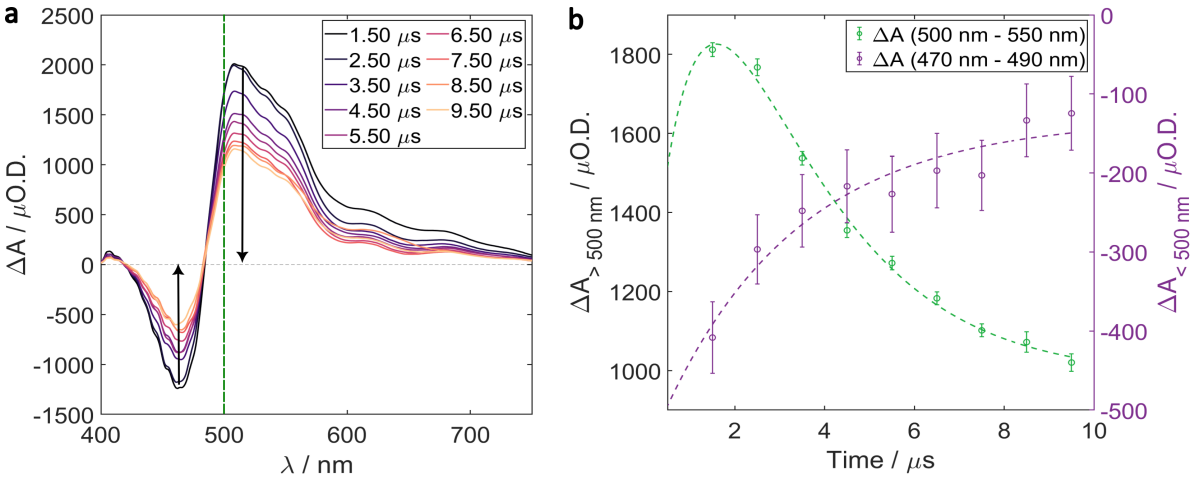

Figure 8.19: *Gg*Cry4a W369F Y319F ΔA spectra and kinetic evolution following photoexcitation are shown in a) and b) respectively. The green trace in b) reflects the kinetic evolution in the radical ($W^{\bullet}$, 500 nm - 550 nm) region while the purple trace reflects the ground state recovery (470 nm - 490 nm). The vertical green line in a) indicates the cut-off where anything below it (*i.e.* $<$ 500 nm) becomes spectrally distorted due to low light levels escaping the optical cavity. As such, any spectral shapes and ΔA magnitudes below 500 nm cannot be quantitative.

The ΔA spectra over a period of 10 μs is shown in **Fig. 8.19 a**. The oxidised FAD ground state bleach (GSB) is characterised by the negative absorption band between 400 nm and 500 nm. Note that the GSB spectra is significantly distorted due to the low blue light generation of the SC source and high absorption from the sample causing some distortion from the CEF. This behaviour is also a problem with conventional BBCEAS and has been mentioned above (*cf.* **Chapter 6**). Nonetheless, the GSB recovery can be estimated from the peak's kinetic evolution which is shown as the purple trace in **Fig. 8.19 b**. Fitting with a monoexponential function yields a recovery of $\tau_{GS} = 3.00 \pm 0.94\,\mu s$. After an isosbestic point at *ca.* 500 nm, the absorption of photoinduced radicals can be seen between 500 nm and 600 nm. The kinetics of this region are plotted as the green line in **Fig. 8.19 b** and give an estimate of the lifetime of $\tau_{500-550\,nm} = 2.27 \pm 0.81\,\mu s$, following a fit to equation 8.22. While the photoinduced absorption spectra above 500 nm appear to be mainly $W^{\bullet}$, due to the overlapping absorption spectra of the majority of the photoinduced

[bn]These experiments were done in collaboration with DPhil student Carl Olavesen.

radicals in cryptochromes, the spectra and thus measured lifetime are likely a combination of several competing processes. However, due to the high quality of the ΔA spectra, it was possible to perform global analysis and extract the contributing species and their evolution. The results of this analysis are shown **Fig. 8.20** where **Fig. 8.20 a** shows the raw data (solid lines) and fit respectively (dashed lines). Note that the fit is from 500 nm to 700 nm due to aforementioned issues with laser light and cavity artefacts below 500 nm.

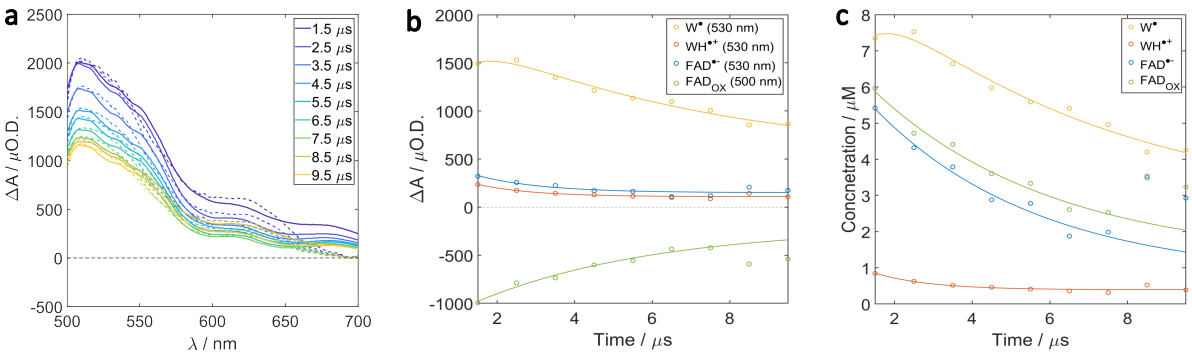

Figure 8.20: a) Global analysis fit results of the *Gg*Cry4a W369F Y319F ΔA data. The fit is good between 500 nm and 600 nm. The poorer fit at higher wavelengths is due to the offset above 650 nm which is likely an artefact. c) and d) show the individual species kinetics extracted from the global target analysis in ΔA and concentration respectively.

The extracted individual species kinetics are shown in **Fig. 8.20 b** and indicates, as expected, the major absorbing species between 500 nm and 600 nm is $W^{\bullet}$, however, with additional contributions from $FAD^{\bullet-}$ and $WH^{\bullet+}$. While these contributions are minor by absorption, upon conversion to concentration (**Fig. 8.20 c**), the contribution from $FAD^{\bullet-}$ becomes more significant such that the initial concentrations of $W^{\bullet}$ and $FAD^{\bullet-}$ are more comparable with fractional yields of *ca.* 0.25 and 0.18 respectively. Unsurprisingly, the contribution from $WH^{\bullet+}$ is low, both by absorption and concentration, due to singlet recombination with $FAD^{\bullet-}$ and rapid deprotonation to form $W^{\bullet}$. More unusual is the $FAD^{\bullet-}$ yield. Provided the major decay route for $FAD^{\bullet-}$ is through singlet recombination with $WH^{\bullet+}$, if all of the $WH^{\bullet+}$ has been consumed by recombination and deprotonation, one would expect the $FAD^{\bullet-}$ yield to match that of $W^{\bullet}$. The cause of this reduced $FAD^{\bullet-}$ yield, relative to $W^{\bullet}$, seems to come from its more rapid decay, assuming that at some earlier time the yields were 1:1. The natural assumption for this additional decay route is by protonation to form $FADH^{\bullet}$. However, this does not appear to be forming within the experiment time. In fact, when included in the global analysis its extracted contribution to

the spectra was zero. Additionally, the $FAD^{\bullet-}$ decay clearly matches the recovery of FAD_{OX}. The implication is that there must be another mechanism, which does not involve $FADH^{\bullet}$ formation or singlet recombination, by which the $FAD^{\bullet-}$ recovers back to the ground state. Unfortunately, at this stage, the precise mechanism is unknown and could occur in several ways. For example, a change in the protein folding could allow the protonated arginine in position 356 (< 5 Å away) to rapidly oxidise $FAD^{\bullet-}$.[212] In any case, assuming that the protonation rate of $FAD^{\bullet-}$ is unaffected by the mutation and remains *ca.* 200 ms,[126] this additional rapid decay of $FAD^{\bullet-}$ does explain the suppressed $FADH^{\bullet}$ accumulation observed in BBCEAS (*cf.* **Chapter 7**).

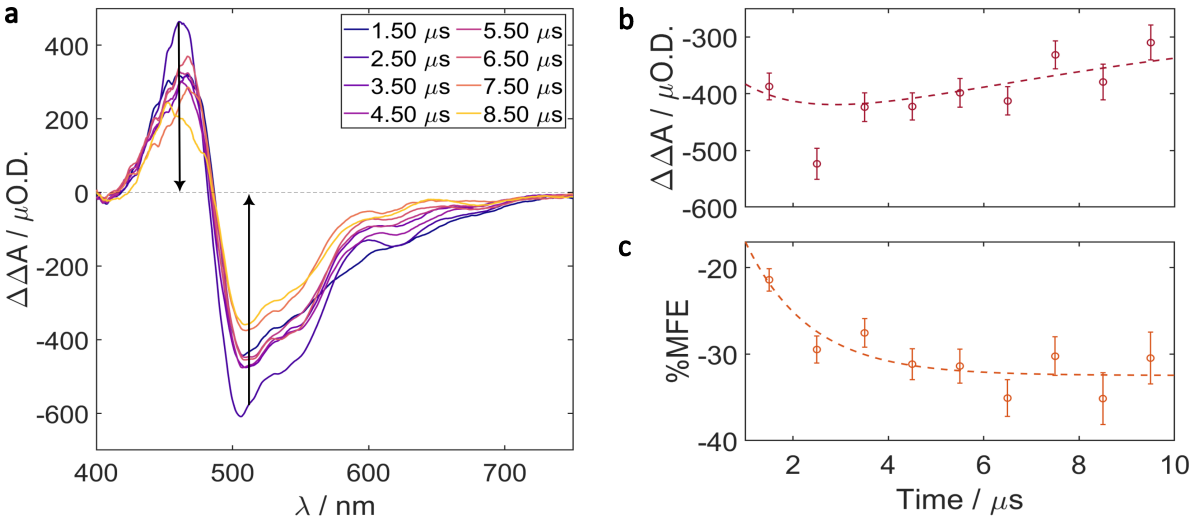

Figure 8.21: *Gg*Cry4a W369F Y319F MFE $\Delta\Delta A$ spectra, a), and kinetic evolution at 530 nm, b). The %MFE at 530 nm is shown in c). The dashed lines in b) and c) are biexponential fits to the data.

Applying a 30 mT magnetic field to the system causes the expected reduction in radical yield due to the reduction in the efficiency of ST mixing. This can be seen in the $\Delta\Delta A$ spectra in **Fig. 8.21 a** where the positive absorption band below 500 nm is the MFE on the GSB and the negative absorption band between 500 nm and 600 nm is the MFE on the photoinduced radicals discussed above. Analogously to the ΔA spectra, the $\Delta\Delta A$ spectrum above 500 nm is dominated by a MFE on the $W^{\bullet}$ yield. The $\Delta\Delta A$ and $\%MFE$ dynamics (averaged from 500 nm to 550 nm) are shown in **Fig. 8.21 b and c** respectively where the $\Delta\Delta A$ peaks at around 2.5 μs with a magnitude of *ca.* 400 μO.D. On the other hand, the $\%MFE$ does not peak within the time points measured but rather plateaus after around 5 μs at approximately 32.5 %.

The results presented here are in excellent agreement with MFEs measured by TA (*cf.* **Chapter** 7). Furthermore, unlike TA, OCTAS additionally acquired high resolution $\Delta\Delta A$ spectra. In future experiments on the system, more early time points on the ns timescale would enable detection of $WH^{\bullet+}$ while more late time points would better characterise the evolution of the MFE. Additionally, OCTAS would be well suited to study the time-dependent evolution of the MARYs which is thought to exist in *Gg*Cry4a W369F Y319F. Nonetheless, OCTAS is clearly well suited for the study of cryptochromes and their MFEs.

8.7 Conclusions and Outlook

In this Chapter OCTAS has been introduced and its efficacy in the study of MFEs in radical pair based systems demonstrated in model systems and a *Gg*Cry4a W369F Y319F protein. The key results from these model systems are summarised and compared to published results from similar techniques in **Table 8.1**. Clearly OCTAS successfully reproduced well established results whilst improving on the sensitivity, spectral resolution and or time resolution of alternative absorption experiments. This allowed for the measurement of high spectral resolution, time-resolved, $\Delta\Delta A$ spectra typically difficult to observe, providing a deeper understanding of these systems. The technique has, therefore, proved effective in monitoring MFEs as a function of time and field and was shown to be capable of monitoring both small molecule and biological systems under either pulsed or continuous illumination. These results prove that the concept works and show how OCTAS can become a vital new tool in the pursuit of understanding avian magnetoreception and radical pair spin chemistry in general. The technique is, however, still in its infancy and can be improved in a number of ways.

System	OCTAS Main Results	Results From Other Techniques	Comments
FMN/HEWL	$\lvert MFE \rvert = 4.5$ % (>4 us)	$\lvert MFE \rvert = 4.5$ % (>4 us) - CRDS[101]	Improved spectral resolution with $\Delta\Delta A$ spectra measured.
FAD	$\lvert MFE \rvert = 45$ % $B_{1/2} \sim 8$ mT	$\lvert MFE \rvert = 42$ % - CRDS[178] $B_{1/2} \sim 8$ mT - TA microscopy[162]	Improved spectral resolution with $\Delta\Delta A$ spectra measured.
CPF	$\lvert MFE \rvert = 6.7$ % (sample not degassed)	$\lvert MFE \rvert \sim 10$ % - TA[210] (sample degassed)	Improved spectral resolution, sensitivity and signal-to-noise with $\Delta\Delta A$ spectra measured for the first time.

Table 8.1: Summary of the key OCTAS results from model systems in comparison to published results from alternative techniques. A few comments on the benefits of OCTAS in comparison to those techniques are included.

One fair way of evaluating a technique's usefulness is to consider how much information may be acquired with a single measurement. In this case, that would be a single field and PPD measurement which yields ΔA and $\Delta\Delta A$ spectra, each with 0.5 nm wavelength resolution over a 400 nm to 800 nm spectral region. The most obvious restriction here is that one such measurement only produces one time point. As such, many experiments are required to build up a kinetic profile of the system. This means that the sample must be hit more times with the pump laser, thus causing more degradation and prolonging the time it takes to acquire a full data set. This is an inherent drawback of any pulsed probing technique, be it with a pulsed laser or, in this case, detector. Clearly, a way around this would be to use continuous acquisition. This was the route taken with the previous generation of OCTAS which used a PMT array as the detector. The drawback there was, instead of discretised time, that the wavelength acquisition had to be discretised, significantly reducing the spectral resolution. Therefore, a detector that yields both continuous time and full spectral resolution would be perfect. Indeed the initial detector proposed for this new version of OCTAS was a streak camera. These work much like the iCCD and retain the full spectral resolution that it enjoys. However, rather than just a gate pulse to measure snapshots, streak cameras apply a time-varying electric field as the photogenerated electrons from the MCP are accelerated to the phosphor screen. This causes electrons arriving at different times to be deflected at different angles thus causing a "streak" on the phosphor screen. A streak camera, therefore, acquires a 2-dimensional data set consisting of time and wavelength with every measurement. This differs from the iCCD which only obtains a 1-dimensional wavelength data set at a single set time. Unfortunately the cost of a streak camera proved prohibitive and we settled on the iCCD as an alternative, prioritising wavelength resolution. However, the data from a streak camera may be approximated by coupling the iCCD with a small array of PMTs. This upgrade is currently being implemented and will work as follows.

The light leaving the rear cavity mirror (M2) will be passed through an 80/20 beam splitter with 80 % of the light passed onto the spectrograph and iCCD as usual. The other 20 % will be split again, this time with a 50/50 beam splitter with each beam passed through a

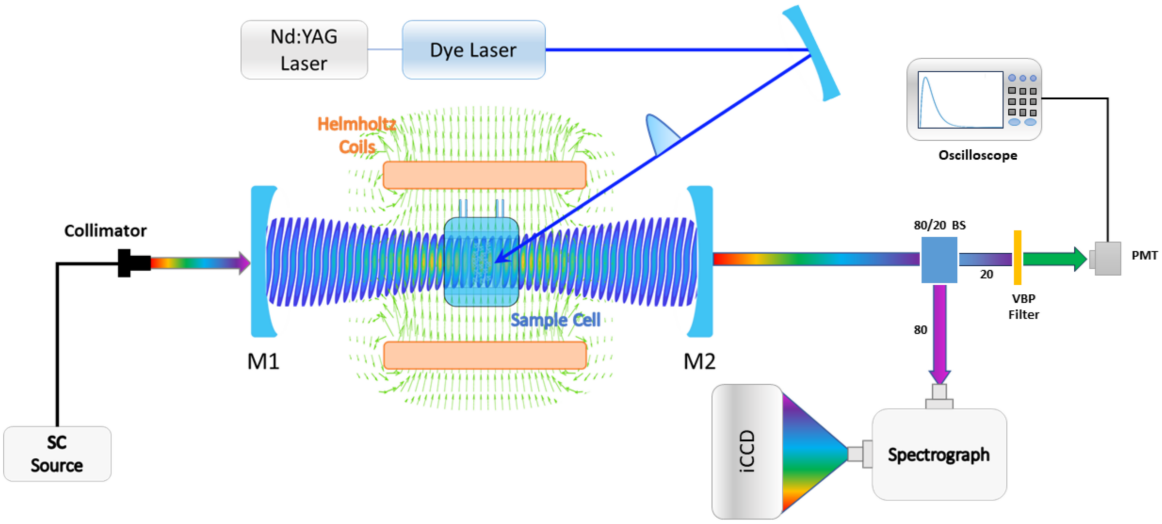

Figure 8.22: Schematic of OCTAS with the proposed further developments. BS = beam splitter and VBP = variable band-pass

variable band pass filter before coupling into an optical fibre connected to a PMT. The PMT signals are then recorded by an oscilloscope providing continuous time resolution over each of the selected spectral regions with every pump laser shot. This clearly drastically increases the amount of information obtainable from each laser shot. The new set-up is summarised in the schematic shown in **Fig. 8.22**.

Another way the technique can be improved is by reducing the errors in both ΔA and $\Delta\Delta A$ measurements by taking into account fluctuations in the energy of the pump pulse. While the Sirah Cobra dye laser is reasonably stable, its root mean square stability is still over 7 %. This becomes a problem with some of the systems under study (*e.g.* *Er*Cry4a WT) whose MFEs are much smaller than the fluctuation in the laser pulse. Clearly, the relationship between the uncertainty in the measured MFEs and the laser stability are not one to one such that an MFE of less than 7 % is immeasurable. For example, the total laser power and the power dependence of the photoproduct yield must be considered. That is, if the laser power is in the saturation region of the ΔA *vs.* power relationship, then minor fluctuations in that power will not correlate with fluctuations in the ΔA. Nonetheless, experiments are rarely run in this power region and thus accounting for pump fluctuations should reduce uncertainties in both the ΔA and $\Delta\Delta A$ measurements. To do this one simply needs to monitor the laser power every time a measurement is taken. This can be done by inserting a glass slide into the pump beam path. Most of the light will transmit through to the sample,

however, a small proportion will be reflected and can be measured with a photodiode and oscilloscope. Collecting all of the acquired signals over a full measurement should result in a normal distribution of laser powers that corresponds to the ΔA signals. From here, all measured signals can be normalised to the centre of the laser power distribution thus accounting for systematic fluctuations in the pump pulses.[bo]

[bo] The laser power normal distribution may not necessarily match the distribution in the ΔA which is likely more complex due to other sources of error such as the gate pulse, MCP gain, probe beam fluctuations etc.

Chapter 9

Development of a New Instrument for Microdroplet Fluorescence Magnetic Field Effects

Due to the difficulty and cost involved in the expression of cryptochrome proteins, means of reducing the amount of sample required for MFE measurements is valuable. Additionally, due to the instability of many of the cryptochromes, methods which do not degrade the sample significantly during data acquisition are highly sought after. In an attempt to address these factors, Microdroplet Fluorescence MARY (μDF-MARY) was conceived and seeks to take advantage of microfluidic droplet formation to generate a constant stream of thousands of tiny fresh "samples" encapsulated within microdroplets. By illuminating these droplets with a laser and measuring their fluorescence with and without applied magnetic fields, MFEs may be detected and averaged over many acquisitions with minimal sample consumption. For example, for a typical microdroplet diameter of *ca.* 80 μm, the droplet ("sample") volume is approximately 268 pL. Therefore, a 20 μL sample of precious cryptochrome yields over 74000 potential individual measurements. Additionally, since every measurement is on a new droplet, the influence of sample degradation and the need for multiple reoxidation steps is mitigated.

With this in mind, the forthcoming chapter will briefly introduce the core concepts of microfluidic mechanics before discussing μDF-MARY development, implementation and methods of data processing. Following on from here, the results from a series of preliminary experiments[bp] will be presented before finishing the chapter with a discussion of the technique's current state of development and any future improvements that can be made.

[bp] Experiments on model systems were done in collaboration with MChem student Madeline Buffet and MRes student Laurynas Paskevicius.

9.1 Microfluidics - A Brief Introduction

Emerging in the early 1980s[213] the field of microfluidics is vast and of great interest to both scientists and mathematicians. Fundamentally, microfludics involves the flow and manipulation of fluids through μm channels (*cf.* **Fig. 9.1**) where the small length scales drastically alters the relationship and influence of governing forces. For example, surface effects become increasingly important while the influence of gravity can be neglected.

Naturally, microfluidics has practical applications in any system that processes tiny volumes such as inkjet printing, high-throughput screening and haemoglobin meters.[bq] In particular, the field of lab-on-a-chip systems has seen significant development in recent years due to its applications in synthetic chemistry, bio-chemistry, molecular diagnostics and the medicinal sciences.[213–217]

A Lab-on-a-chip is a miniaturised device which performs one or more laboratory functions in a single integrated microfluidic circuit or chip. For example, lab-on-a-chip systems have been used to generate microreactors, in the form of microdroplets, with highly controlled and predictable outcomes.[215,218] More recently, lab-on-a-chip devices, known as organ-on-a-chip, have been used to model biological processes such as blood flow, cell migration, biofilm formation and tissue formation.[214,219,220] Although the application proposed here may differ from typical lab-on-a-chip experiments, the underlying microfluidic principles remain the same and will be discussed below.

9.1.1 Fluid Particles and Fields

Fluid mechanics is a branch of continuum mechanics and treats fluids,[br] liquid or gas, macroscopically ($\gtrsim$ 10 μm), describing their physical properties as fields. More specifically, it assumes that the macroscopic properties of a perfectly continuous fluid are identical to one consisting of individual molecules. Consequently, rather than the motion of molecules within the fluid, the motion of finite volumes, known as fluid particles, is considered. Importantly, a fluid particle is mesoscopic ($\gtrsim$ 0.3 *nm* and $\lesssim$ 10 μm) in size and is just

[bq] A finger-prick test which measures haemoglobin levels to check for anaemia.

[br] A fluid is a substance defined by the property that it has no preferred shape and will deform continuously under the influence of external forces.

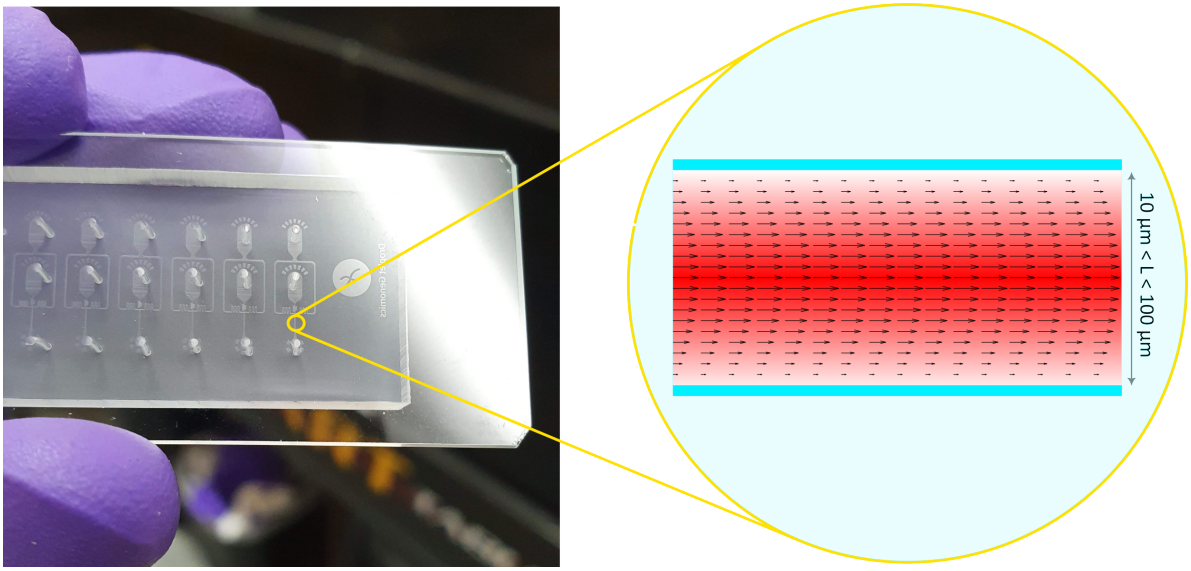

Figure 9.1: A flow focusing droplet generating microfluidic chip (left) with a simulation of the fluid flow within the microchannel shown on the right .

large enough such that it contains sufficient molecules with which well-defined average values may be obtained, with little statistical fluctuation. Additionally, a fluid particle must be small enough such that it sufficiently captures spatial variations in the physical properties of the fluid.[221]

With the concept of fluid particles it is possible to define fluid properties in terms of fields. This may be done by considering how a relevant field evolves in time over fixed points, $\mathbf{r}$, in space. This is know as the Eulerian description[bs] where the field, $F(\mathbf{r}, t)$, of some variable is defined as the average of all of the corresponding molecular values, $F_{mol}(\mathbf{r}', t)$, of molecules contained within a single fluid particle with volume, $\Delta V(\mathbf{r})$, at any given position, $\mathbf{r}$, and time, t.[221]

$$F(\mathbf{r}, t) = \langle F_{mol}(\mathbf{r}', t) \rangle_{\mathbf{r}' \epsilon \Delta V(\mathbf{r})} \tag{9.1}$$

This field value may correspond to any property of a fluid such as, density, viscosity, temperature, velocity, pressure gradient or velocity gradient to name a few.

[bs]This differs from the Lagrangian description which follows the motion of individual fluid particles. Thus, the coordinate of a given fluid particle depends on time.

9.1.2 The Continuity Equation

A key concept in non-relativistic classical mechanics is that of the conservation of mass, *i.e.* mass cannot appear or disappear spontaneously. In the context of fluid mechanics that means that the change of mass within an arbitrary, fixed, region of space, Ω, must correlate with the flow of matter in or out.

The mass, $M(\Omega, t)$, inside Ω is defined by the volume integral of the density of the fluid within it

$$M(\Omega, t) = \int_{\Omega} \rho(\mathbf{r}, t)\, d\mathbf{r} \tag{9.2}$$

where $\rho(\mathbf{r}, t)$ is the density of the fluid and $d\mathbf{r}$ denotes the integral over x, y and z. As indicated above, the mass may fluctuate only if there is flow into or out of Ω through its surface, $\partial\Omega$. This flow is characterised by the mass current density $\mathbf{J}$ which is given by

$$\mathbf{J}(\mathbf{r}, t) = \rho(\mathbf{r}, t)\mathbf{u}(\mathbf{r}, t) \tag{9.3}$$

where $\mathbf{u}(\mathbf{r}, t)$ is the velocity field. Since Ω is fixed, the fluctuations in $M(\Omega, t)$ are given by its time derivative

$$\frac{\partial}{\partial t} M(\Omega, t) = \int_{\Omega} \frac{\partial}{\partial t} \rho(\mathbf{r}, t)\, d\mathbf{r} \tag{9.4}$$

Alternatively, the change in mass per unit time may be defined by considering the flux of matter through $\partial\Omega$

$$\frac{\partial}{\partial t} M(\Omega, t) = -\int_{\partial\Omega} (\rho(\mathbf{r}, t)\mathbf{u}(\mathbf{r}, t)) \cdot \mathbf{n}\, da = -\int_{\Omega} \nabla \cdot (\rho(\mathbf{r}, t)\mathbf{u}(\mathbf{r}, t))\, d\mathbf{r} \tag{9.5}$$

where da is an infinitesimal unit of area on the surface $\partial\Omega$ and $\mathbf{n}$ is the unit normal to da. The second equality in equation 9.5 is obtained by applying Gauss' theorem while

the negative sign before the integral ensures that the mass decreases when the net flow is outwards.[221]

Upon comparison of equations 9.4 and 9.5, it follows that

$$\int_{\Omega}\left(\frac{\partial}{\partial t}\rho(\mathbf{r},t) + \nabla\cdot(\rho(\mathbf{r},t)\mathbf{u}(\mathbf{r},t))\right)d\mathbf{r} = 0 \tag{9.6}$$

and, therefore,

$$\frac{\partial}{\partial t}\rho(\mathbf{r},t) + \nabla\cdot\mathbf{J}(\mathbf{r},t) = 0 \tag{9.7}$$

which formally states that a temporal change in density is proportional to the divergence of the current density ($\nabla\cdot\mathbf{J}$, flow in or out), *i.e.* a change in mass correlates to a flow of matter. This result is known as the continuity equation and arises in any situation where some quantity is locally conserved (*e.g.* $\mathbf{J}$ could equally be charge current density with charge the conserved quantity).[26,221]

Equation 9.7 is generally true for any compressible fluid (its density may vary as a function of space and time). However, in many microfluidic systems the fluid may be considered as incompressible such that its density is constant in space and time. Therefore, equation 9.7 simplifies to

$$\nabla\cdot\mathbf{u}(\mathbf{r},t) = 0 \tag{9.8}$$

9.1.3 The Navier-Stokes Equation

The Navier-Stokes equation is the principal equation in fluid mechanics and, in theory, accurately describes the behaviour of any fluid. Fundamentally, it is the extension of Newtons second law to the motion of fluid particles where the mass is replaced by the fluid particle density, ρ, and the external forces by force densities, $\mathbf{f}$. In this form, Newton's second law reads

$$\rho D_t \mathbf{u} = \sum_i \mathbf{f_i} \tag{9.9}$$

where $\mathbf{u}$ is the fluid velocity field. D_t is known as the material time derivative (as opposed to the time derivative) and accounts for the fact that $\mathbf{u}$ is not the velocity of a specific fluid particle, as it should be in Newton's second law. An explicit expression for D_t may be derived by considering the total derivative of $\mathbf{u}$ with respect to time

$$\begin{aligned} \frac{d}{dt}\mathbf{u}(\mathbf{r},t) &= \frac{\partial \mathbf{u}}{\partial t} + \left(\frac{\partial \mathbf{u}}{\partial x}\right)\left(\frac{\partial x}{\partial t}\right) + \left(\frac{\partial \mathbf{u}}{\partial y}\right)\left(\frac{\partial y}{\partial t}\right) + \left(\frac{\partial \mathbf{u}}{\partial z}\right)\left(\frac{\partial z}{\partial t}\right) \\ &= \frac{\partial \mathbf{u}}{\partial t} + \frac{d\mathbf{r}}{dt}\cdot\nabla\mathbf{u} \end{aligned} \tag{9.10}$$

where $\frac{d\mathbf{r}}{dt}$ describes the path taken by some object through the fluid. Since we wish to describe a fluid particle, that path taken is equal to the fluid velocity field, $\mathbf{u}$. Therefore

$$D_t = \frac{\partial \mathbf{u}}{\partial t} + (\mathbf{u}\cdot\nabla)\mathbf{u} \tag{9.11}$$

and equation 9.9 becomes

$$\rho\left(\frac{\partial \mathbf{u}}{\partial t} + (\mathbf{u}\cdot\nabla)\mathbf{u}\right) = \sum_i \mathbf{f_i} \tag{9.12}$$

which is the Navier-Stokes equation in its most basic form. For a more complete form, expressions for the various force densities, $\mathbf{f_i}$, must be found. However, in the interest of time the most relevant will be simply stated while complete derivations can be found in any fluid mechanics text book (*e.g.* Theoretical Microfluidics by Henrik Bruus).[221]

All of the forces considered here are body forces which are external forces that act throughout the entire body of fluid (*e.g.* gravity). Of particular importance here are the forces associated with pressure, p, and fluid viscosity, η.

The force density for pressure is defined by the pressure gradient

$$\mathbf{f}_{\text{pres}} = -\nabla p \tag{9.13}$$

while the force density for viscosity is given by

$$\mathbf{f}_{\text{visc}} = \eta\nabla^2\mathbf{u} + \left(\frac{\eta}{3} + \zeta\right)\nabla(\nabla\cdot\mathbf{u}) \tag{9.14}$$

where η is the shear viscosity and ζ is the bulk viscosity.[bt] In essence, equation 9.14 describes the influence of frictional forces within the fluid itself.[221]

Inserting equations 9.13 and 9.14 into equation 9.12 yields the Navier-Stokes equation for compressible fluids

$$\rho\left(\frac{\partial\mathbf{u}}{\partial t} + (\mathbf{u}\cdot\nabla)\mathbf{u}\right) = -\nabla p + \eta\nabla^2\mathbf{u} + \left(\frac{\eta}{3} + \zeta\right)\nabla(\nabla\cdot\mathbf{u}) + \mathbf{f} \tag{9.15}$$

where $\mathbf{f}$ includes any and all other influencing forces. Furthermore, recalling equation 9.8, the Navier-Stokes equation for an incompressible fluid is

$$\rho\left(\frac{\partial\mathbf{u}}{\partial t} + (\mathbf{u}\cdot\nabla)\mathbf{u}\right) = -\nabla p + \eta\nabla^2\mathbf{u} + \mathbf{f} \tag{9.16}$$

and is the fundamental equation in the fluid mechanics of most microfluidic systems.[221]

9.1.4 Microdroplet formation

The specific subset of microfluidics μDF-MARY aims to take advantage of is microfluidic droplet formation where microdroplets of one fluid (disperse phase) are formed in the flow of another (carrier phase). This is achieved by flowing two immiscible fluids together such that the respective flows of each fluid induce deformations and instabilities in the interface between them.[215] To do this, microfluidic chips are fabricated such that the two phases are driven separately to a point where they encounter each other, forming droplets.

[bt] The shear viscosity describes a fluid's resistance to deformation at a given rate under shear forces while the bulk viscosity is a fluid's resistance to compression or expansion under shearless forces.

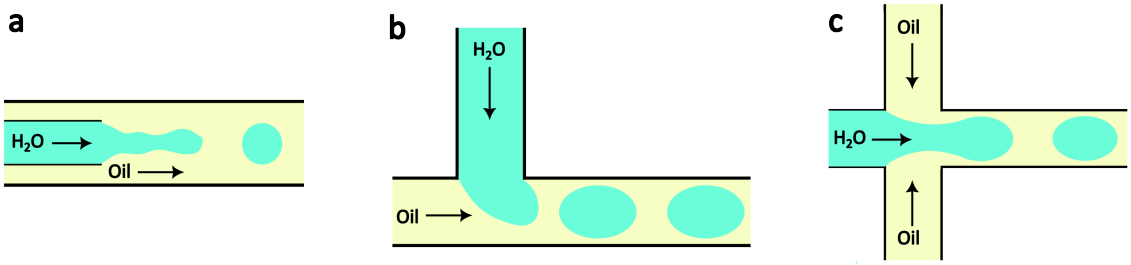

Figure 9.2: a), b) and c) show schematics of co-flow, cross flow and elongational strained flow microfluidic chips.

The precise geometry of this meeting point determines the manner in which the droplets are formed and can be broken down into three main approaches, co-flowing, cross flowing and elongational strained flows (*cf.* **Fig. 9.2 a, b** and **c** respectively).

In co-flowing systems, the disperse phase is introduced into the carrier phase in a parallel stream with the disperse phase typically inserted into the carrier phase channel such that the disperse phase stream breaks up into droplets as it enters the carrier phase flow. In cross-flowing systems, the flows of the two phases are orthogonal such that the flow of the carrier phase breaks up the disperse phase where they meet. Finally, in flow-focusing devices (elongational strained flows) droplets are formed when the disperse phase is squeezed by two counter-flowing carrier phase channels which pinch a, typically, orthogonal disperse phase flow. In all three cases, the size and shape of the formed droplet is due to the interplay between pressure (due to external flow), viscous shear stresses and capillary pressure.[215,218]

In the process of droplet formation, the flow of each phase is well described by equation 9.16 with the addition of suitable boundary conditions that account for the liquid-liquid interface and liquid-chip interface. The latter is known as the no-slip boundary condition and states that the velocity field at a solid wall interface, $\partial\Omega$, is zero, *i.e.*[221]

$$\mathbf{u}(\mathbf{r}) = 0 \tag{9.17}$$

for $r \epsilon \partial\Omega$.[bu]

The first of the liquid-liquid interfacial boundary-conditions is an extension of the no-slip condition and comes from the fact that at any given point on the interface the velocities of the two fluids must be equal[222]

$$\mathbf{u}_d(\mathbf{r},t)\cdot\mathbf{n} = \mathbf{u}_c(\mathbf{r},t)\cdot\mathbf{n} \tag{9.18}$$

where **n** is the unit normal vector to the phase boundary and the subscripts c and d refer to the carrier and disperse phases respectively. From here, the remaining boundary condition arises from balancing the stress each phase exerts on the interface. This is defined by[222]

$$\mathbf{n}\cdot\mathbf{T}_d - \mathbf{n}\cdot\mathbf{T}_c = \gamma\mathbf{n}(\nabla\cdot\mathbf{n}) - \nabla\gamma \tag{9.19}$$

where γ is the interfacial tension and $\mathbf{T} = -p\mathbf{I} + \eta(\nabla\mathbf{u} + \mathbf{u}^T)$ is the stress tensor which contains the pressure, p, viscosity, η, and fluid velocity **u** with **I** the indentity matrix. $\nabla\cdot\mathbf{n}$ describes the local curvature of the interface thus the first term on the right hand side of equation 9.19 describes the variation in the interfacial tension due to the interfacial geometry. On the other hand, the second term on the right hand side describes the tangential stress due to gradients in the interfacial tension.

Equation 9.19 can be further broken down into its normal and tangential components with the normal stress balance equation given by

$$\mathbf{n}\cdot\mathbf{T}_d\cdot\mathbf{n} - \mathbf{n}\cdot\mathbf{T}_c\cdot\mathbf{n} = \gamma(\nabla\cdot\mathbf{n}) \tag{9.20}$$

and the tangential stress balance equation given by

$$\mathbf{n}\cdot\mathbf{T}_d\cdot\mathbf{t} - \mathbf{n}\cdot\mathbf{T}_c\cdot\mathbf{t} = \nabla\gamma\cdot\mathbf{t} \tag{9.21}$$

[bu] The no-slip boundary condition is the assumption that there is complete momentum relaxation between the stationary molecules of the wall and the molecules that collide with it.[221]

where **t** is the unit tangent vector.

The interface itself is not infinitely thin but rather has a small, but finite, defined thickness which must be explicitly considered during the process of droplet formation. The thickness of the interface depends on the range of molecular interactions (*e.g.* Lennard-Jones potential) and is typically a few nanometers wide.[223–226] Additionally, thermodynamic properties such as density, chemical potential and stress vary continuously over the boundary between the two fluids. These characteristics of the interface are determined by the (Helmholtz) free energy of the system which depends both on the local composition and immediate environment. More specifically, the free energy, $\mathscr{E}$, of a fluid particle in an inhomogeneous solution can be expressed as the sum of the free energy that fluid particle would have in a homogeneous solution and a perturbative energy gradient due to the local composition[227]

$$\mathscr{E} = \int_V \left(f_0 + \frac{1}{2}\kappa(\nabla c)^2 \right) d\mathbf{r} \tag{9.22}$$

where f_0 is the homogeneous free energy per molecule,[bv] $\kappa(\nabla c)^2$ is the energy gradient due to inhomogeneity, c is the concentration of one of the fluids and κ is the so-called energy gradient parameter and is related to the width of the interface.[224,227]

Taking the functional derivative of equation 9.22 with respect to concentration yields the chemical potential, μ[36,224]

$$\mu = \beta c^3 - \alpha c - \kappa \nabla^2 c \tag{9.23}$$

where α and β are positive constants.[224] By considering the system at equilibrium, $\mu = 0$, the concentration of a fluid across the interface may be determined by

$$c(z) = c_B \tanh\left(\frac{z}{\sqrt{2\zeta}} \right) \tag{9.24}$$

[bv] $f_0 = \frac{1}{4}\beta c^4 - \frac{1}{2}\alpha c^2$ and is known as the Ginzburg-Landau free energy.

where $c_B = \pm\sqrt{\frac{\alpha}{\beta}}$ is the concentration of the bulk solutions and $\zeta = \sqrt{\frac{\kappa}{\alpha}}$ is the width of the interface.[224,225] With this, the interfacial tension may be calculated as follows[224]

$$\gamma = \kappa \int_{-\infty}^{\infty} \left(\frac{dc}{dz}\right)^2 dz = \frac{2\sqrt{2}}{3}\frac{\kappa c_B^2}{\zeta} \tag{9.25}$$

In general, however, the process of droplet formation is one far from equilibrium thus, given diffusion is always down chemical potential gradients, the flux of the interface may be written as[36]

$$\mathbf{J} = -M\nabla\mu + \mathbf{u}c \tag{9.26}$$

where M is the mobility. The first term in equation 9.26 describes diffusive flux while the second term describes advective flux (movement due to fluid flow).

Recalling the continuity equation (equation 9.7) and changing the conserved quantity from density to concentration yields a differential equation that describes the dynamics and motion of the interface. This is known as the Cahn-Hilliard equation and is given by

$$\frac{\partial c}{\partial t} + \mathbf{u}\cdot\nabla c = M\nabla^2\mu \tag{9.27}$$

Since the purpose of the following is not to explore the mathematical intricacies of fluid mechanics, a substantial amount of mathematics was skipped or glossed over in the process of deriving equation 9.27 however, full mathematical proofs can be found in the referenced literature.[221–225,227–229] Nonetheless, by inspection of equations 9.27 and 9.16 and the various boundary conditions involved, the major contributing factors to droplet formation appear to be the viscosity of the phases, the interfacial tension, the pressure gradient and the fluid velocity of each phase. Together they indicate three major governing forces (excluding gravity). Namely the inertial force, viscous force and capillary force. The ratio of any two of these forces defines an important dimensionless number in fluid mechanics.[215,218]

The Reynolds number, *Re*, characterises the relative influence of the inertial and viscous forces

$$Re_s = \frac{\rho_s u_s L}{\eta_s} \tag{9.28}$$

where the subscript s represents either the carrier or disperse phase and L is the width (or diameter) of the channel through which the fluid flows. In microfluidic applications *Re* is typically between 10^{-6} and 10 and thus the viscous force dominates leading to laminar flow. That is, smooth even flow without any complex behaviour (*i.e.* turbulence).[215]

Of particular relevance to droplet formation is the capillary number, Ca, which represents the relative importance of viscous stress and interfacial tension

$$Ca_s = \frac{\eta_s u_s}{\gamma} \tag{9.29}$$

and, in microdroplet generating applications, is usually between 10^{-3} and 10.[215] At low capillary numbers, when the interfacial tension dominates, spherical droplets are formed while at high capillary numbers, when viscous forces dominate, droplets are formed in long plugs.[215] The length scale, L, does not appear in Ca because the magnitude of the viscous stress and interfacial tension both depend on it. For example, reducing L enhances both. In fact, on the micron scale of microfluidic chips the viscous stress and interfacial tension significantly dominate the inertial and gravitational forces such that they can be safely ignored.[215] Nonetheless, for the sake of completeness, the third dimensionless number is the Weber number, given by the ratio of the inertial and capillary forces

$$We_s = \frac{\rho_s u_s^2 L}{\gamma} \tag{9.30}$$

and is typically < 1 in microfluidics.

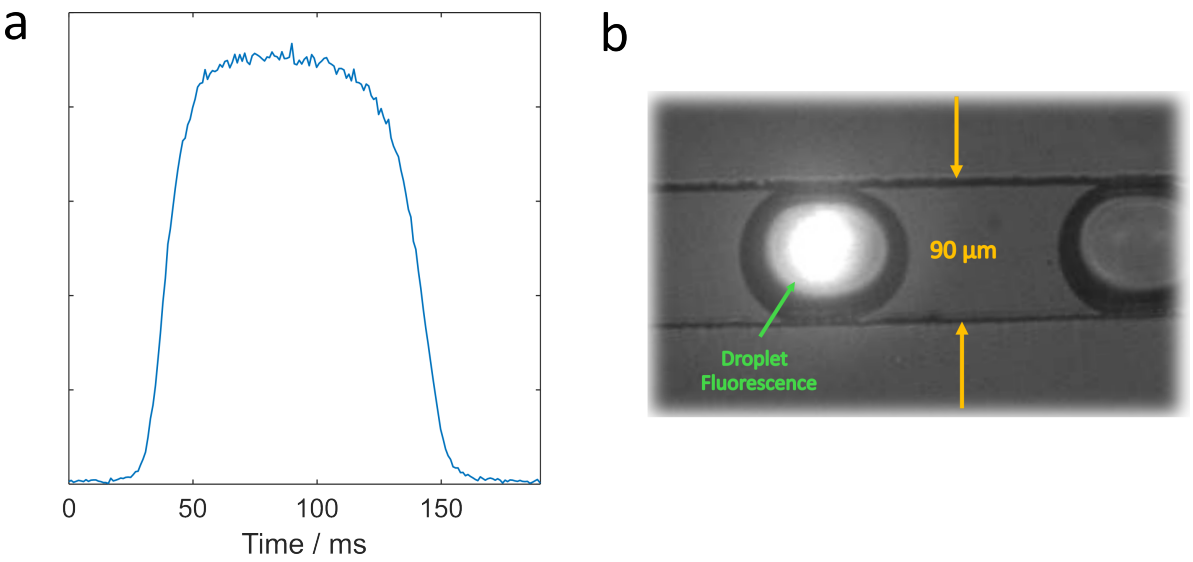

Figure 9.3: a) PMT signal of fluroescence (and/or scattering) from a single FMN/HEWL microdroplet. b) Image of microdroplet emission as it passes through the laser beam.

9.2 μDF-MARY Working Principles

The core concept behind μDF-MARY is that samples are delivered into the system in the form of microdroplets. This is achieved with the use of a microfluidic chip, specifically flow focusing chips (*cf.* **Fig. 9.2**), where careful control of the flow rate of the two phases produces a stable and consistent stream of microdroplets with a typical production rate of 2 - 10 Hz. Encapsulated within these droplets is a sample of interest which is studied by flowing the droplets through the path of a laser beam, exciting the system inside. The subsequent luminescence from the sample is then collected and detected by a PMT or spectrograph thus allowing characterisation of the system within the droplet.

μDF-MARY relies on luminescence (usually fluorescence) which occurs when an excited electronic state decays to the ground state, releasing the excess energy as a photon. As such, the magnitude of the fluorescent signal depends on the excited state population, and thus ground state absorption, minus any non-radiative losses (*i.e.* electron transfer, heat dissipation, intersystem crossing). Consequently, measuring the fluorescence of a system under continuous illumination provides an indirect measurement of the ground state concentration. Thus, for a system undergoing the RPM, the application of a magnetic field alters the fluorescence intensity by modulating the ground state concentration. For example, applying a large magnetic field to a singlet born RP system will increase the fluorescence

signal by decreasing the ST mixing efficiency and promoting singlet recombination to the ground state (*cf.* **Chapter 2**). Therefore, μDF-MARY characterises MFEs in the ground state population by detecting changes in microdroplet fluorescence upon the application of magnetic fields. This means that the system must go through the SCRP and back to the ground state (several times) within the time it takes the droplet to pass through the laser beam for a MFE to be measurable. Given the production rate mentioned above, the typical residence time of a droplet within the excitation volume is a few hundred ms. Thus, MFEs measured by μDF-MARY arise mainly from direct singlet recombination of the SCRP and will have little contribution from the recovery of long-lived photoproducts (*e.g.* $FADH^{\bullet}$ in cryptochromes).

Detection *via* the spectrograph allows characterisation of the emission spectrum and thus helps to determine the emissive species. However, due to the fact that the microdroplets are small, the pathlength of the laser through the sample, and thus the excitation volume, is also small. The emission from a single droplet is thus very low and it is necessary to average over the emission of several droplets to obtain good emission spectra. Additionally, the CCD in the spectrograph has limited time resolution making it impossible to detect any dynamic information from the droplets, even if the emission intensity was such that averaging multiple droplets was not necessary. This makes the spectrograph a poor choice for attempting to study any MFEs occurring within the droplets. As such, once the emission spectrum has been characterised the method of detection is switched to a PMT which sacrifices wavelength resolution for sensitivity and time resolution.

The signal from the PMT represents the total emission from the droplet (integrated over wavelength) at any given time and enables full characterisation of the emission dynamics from a single droplet passing through the laser beam. A typical PMT signal from a single droplet is shown in **Fig. 9.3** where the signal grows in as the droplet and laser beam begin to overlap until the full beam spot is inside the droplet. The signal then decays again once the rear edge of the droplet starts to exit the excitation volume.

9.2.1 Experimental Apparatus and Protocol

Given the size of the microdroplets, the laser beam used to measure them must be tightly focused such that the beam spot at the droplet is substantially smaller than the width of the droplet. μDF-MARY uses a custom-built inverted confocal microscope where the excitation beam from a 450 nm diode laser (Oxxius LBX-450-70) is directed, by way of a long-pass dichroic mirror, through an oil immersion objective lens (Leica HC PL APO 40×/1,30 OIL CS2) which tightly focuses the beam (*ca.* 10 μm) into a sample causing it to fluoresce. The proportion of emitted light incident on the objective is collimated[bw] as it passes back through the objective, directed through the dichroic mirror and refocused through a pinhole onto an optical fibre. The signal is detected and measured by a spectrometer (Avantes AvaSpec-ULS2048x64TEC) or PMT (Hamamatsu R928) in conjunction with an oscilloscope (LeCroy HDO8058).[bx]

Refocusing of the emitted light through a pinhole gives confocal microscopy its name and is done to remove light from outside of the focal plane.[by] This is achieved since the pinhole is placed precisely at the refocus point where only light from the focal plane is diffraction limited and small enough to pass through.

Microdroplets are generated in flow-focusing chips mounted on an xy translation stage. The droplets produced can be aqueous in an oil carrier phase or vice versa depending on the material of the microfluidic chip (*i.e.* hydrophobic polydimethylsiloxane for aqueous droplets). Since aqueous droplets are required for studying cryptochromes, as well as the model systems studied below, hydrophobic TOPAS®COC (COC = cyclic olefin copolymer) chips (Microfluidic ChipShop, Fluidic 440) were used with channel, and thus droplet, widths ranging from 80 μ*m* down to 10 μm. Silicone oils were used as the carrier phase for all systems due to the solubility of COC polymers in mineral oils. Disperse and carrier phase flow rates are controlled by applying gas pressure to their respective reservoirs external to the microfluidic chip. The precise pressure applied to each phase is controlled

[bw] This is called infinity corrected since it "focuses" the light at a point infinitely far away.

[bx] The instrumentation is very general and as such capable of essentially any fixed beam fluorescence measurement. That is, bulk solutions, thin films, crystals *etc.* can all be characterised by continuous or pulsed excitation. What it cannot yet do is raster the laser beam or sample.

[by] The focal plane is the plane at the focal point of the objective perpendicular to the optical axis.

with a piezoelectric pressure controller (Elveflow OB1), accurate to 12 μbar, which itself is controlled by Elveflow's ESI software.

Magnetic fields are applied to the system *via* a set of Helmholtz coils manufactured by the University of Oxford Physical and Theoretical Chemistry Electronic and Mechanical Workshops and are identical to those employed by OCTAS and BBCEAS (*cf.* **Chapter 8** and **3**).

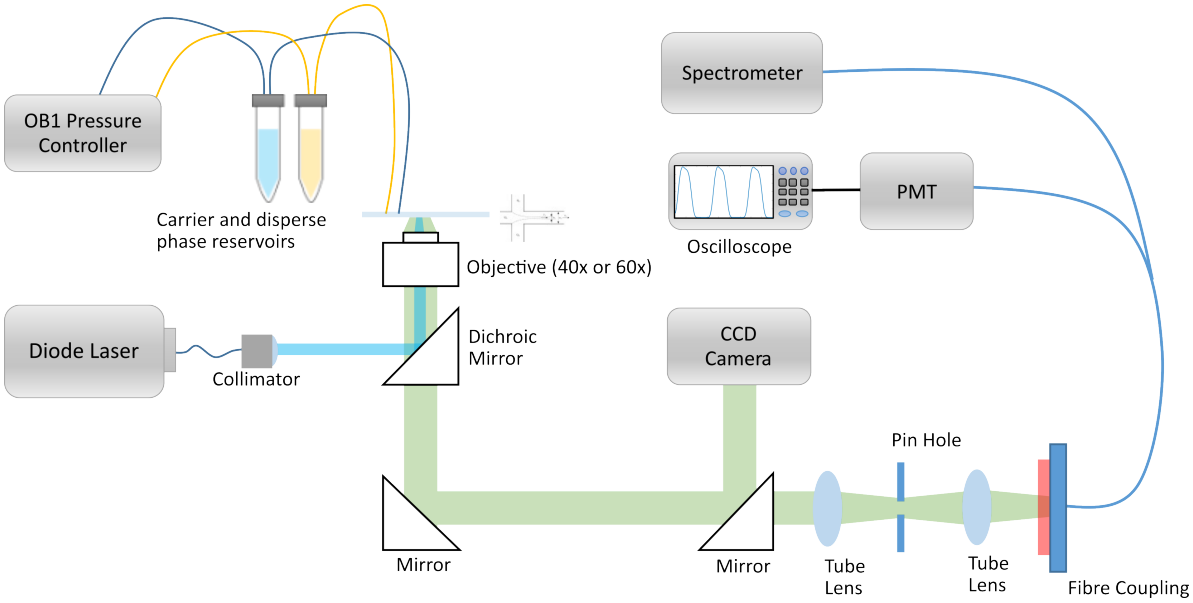

Figure 9.4: Schematic of the custom built confocal fluorescence microscope experiment used to study microdroplet MFEs. The dichroic mirror is a 490 nm cut-on long-pass dichroic mirror, however, any scattered light from the 450 nm diode laser which makes it to the fibre coupling is filtered out by a 450 nm long-pass filter.

The experimental set-up is summarised in **Fig. 9.4** where the additional CCD camera (Thorlabs 340M, discontinued) is used to align and focus the microfluidic channel with the excitation laser and to help calibrate the pressures of the disperse-phase and carrier-phase reservoirs and thus droplet generation. Live camera images are obtained using Thorlabs ThorCam software.

A typical microdroplet MFE experiment is run as follows. First, the CCD camera is used to image the microfluidic chip and focus on the junction where droplets are generated. Droplet generation is then calibrated by modifying the disperse and carrier phase pressures until a stable and consistent stream of droplets, at a desired production rate, is observed on the camera. Once achieved, the excitation beam spot and generated droplets are aligned (*cf.* **Fig. 9.3**). From here, the mirror diverting light to the CCD is removed allowing the

signal to pass through the pinhole and couple into the optical fibre. The droplet emission spectra are then measured with the spectrograph and processed with AvaSoft software. Finally, the detection method is switched to the PMT and oscilloscope.

The MFE experiment is controlled by a custom written LabView software package which controls the oscilloscope, laser and Helmholtz coils. The experiment measures both the laser power and magnetic field dependence where, for each single MFE measurement, the oscilloscope acquires two time traces, one without an applied magnetic field and one with an applied magnetic field, over a user specified acquisition time (typically 1 or 2 seconds due to slow data transfer speeds from the oscilloscope). Due to the aforementioned droplet production rate, each signal usually consists of 2 to 20 droplets. To acquire a whole data set, a laser power is randomly selected from a user supplied list before MFE measurements are done for every user supplied magnetic field strength, in a randomised order. This whole process is then repeated for every requested laser power and number of averages. This sequence is summarised in **Fig. 9.5**.

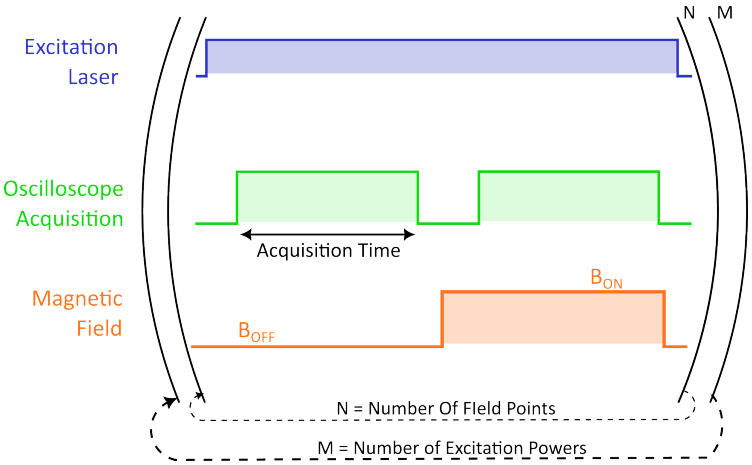

Figure 9.5: Experimental procedure implemented by a LabView program. The sequence represents a single average consisting of N field points and M excitation powers.

9.2.2 Data Analysis

The raw data acquired by the oscilloscope are analysed by a custom written MatLab program which extracts the individual droplet signals within a time trace and averages them together into a single characteristic droplet signal. This is achieved by implementing a droplet detection algorithm which numerically takes the second derivative of the raw data. This enables determination of the start and end points of each individual droplet in

the trace since the maxima in the resulting function represent points of maximum curvature in the raw data signal.

The second derivative is obtained by taking the numerical convolution of the normalised raw data with the analytical second derivative of a Gaussian

$$\frac{d^2F_t(V,t)}{dt^2} \approx \int_{-\infty}^{\infty} F_t(V,\tau)G''(t-\tau)\,d\tau = \mathscr{F}^{-1}[\mathscr{F}\{F_t(V,t)\}\cdot\mathscr{F}\{G''(t)\}] \tag{9.31}$$

where $\mathscr{F}$ and $\mathscr{F}^{-1}$ are the forward and inverse Fourier transforms respectively, $F_t(V,t)$ is the raw fluorescence trace and

$$G''(t) = \frac{1}{\sqrt{2\pi}\sigma^5}\left(\left(t-\frac{t_{aq}}{2}\right)-\sigma^2\right)\exp\left(-\frac{\left(t-\frac{t_{aq}}{2}\right)^2}{2\sigma^2}\right) \tag{9.32}$$

where σ is related to the width of the signal from a single droplet (estimated from the raw data) and t_{aq} is the acquisition time of each trace (the length of each trace's time axis). Both σ and t_{aq} are specific to a given experiment and are required as inputs when analysing the data.

Once the second derivative has been calculated and normalised, the algorithm finds all positive maxima. Since these points correspond to the beginnings and ends of droplet signals, the gradient of the raw data at these points is calculated and used to determine whether each point is the start or end of a signal. These points are subsequently sorted into pairs and used to slice the raw data thus extracting individual droplet signals which are then averaged. This process can be seen in **Fig. 9.6**.

The second derivative is calculated in this way as the process of convolution with a noise free analytical function additionally smooths the result, thus avoiding large artefacts from signal noise. Additionally, this smoothing of the second order derivative data allows reliable droplet detection, even in noisy data, without smoothing or altering the raw data before averaging. Furthermore, by calculating the start and end points of droplets in this way, the detection algorithm is robust to partial, clipped, droplet signals (since these don't have

a start and end point pair), fluctuations in droplet width and variations in droplet signal magnitude.

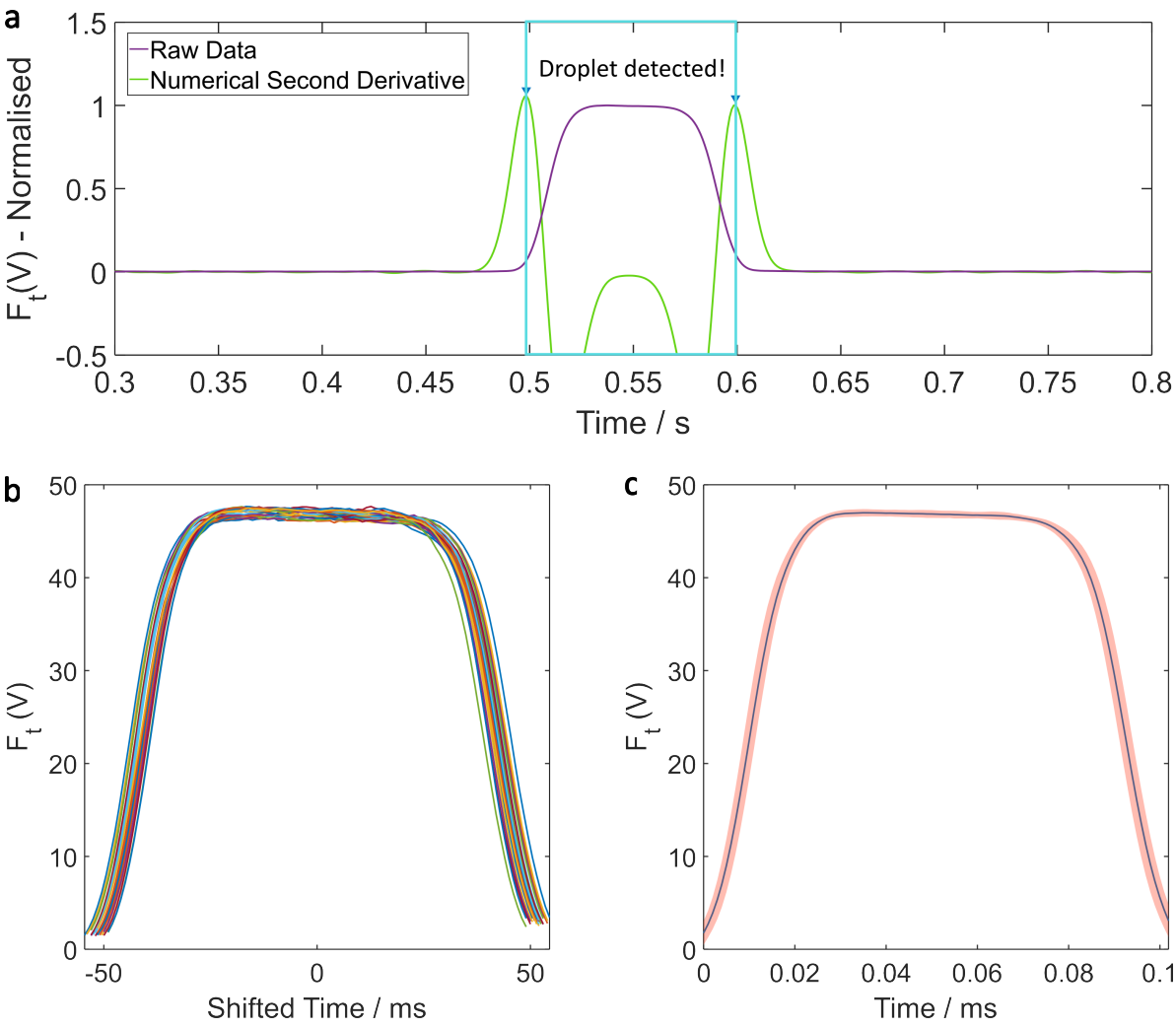

Figure 9.6: a) Shows a droplet detected by the algorithm which implements equations 9.31 and 9.32. The blue box highlights the region of raw data extracted from the trace by the detection algorithm. b) Shows the collection of detected droplet signals for a set of acquired oscilloscope traces which together yield the averaged droplet signal shown in c).

The specific shape and magnitude of the averaged droplet PMT signal depends on many factors such as droplet velocity, droplet shape, beam spot size, laser power and the chemical kinetics of the sample. In general this is captured by the convolution of a droplet passing through the beam, integrated over the axis perpendicular to droplet flow

$$F_t(V) = \int_{y_1}^{y_2} \int_{-\infty}^{\infty} G(y,\tau) D(y, t-\tau)\, d\tau dy \tag{9.33}$$

where the integral with respect to y is over the width, L, of the channel and $G(y,t)$ and $D(y,t)$ are the Gaussian profile of the laser spot and the droplet emission respectively. For the sake of simplicity, the laser is assumed to have a perfectly Gaussian beam profile with no higher order transverse modes, thus the beam is given by[59]

$$G(y,t) = I_0 \exp\left(-2\frac{(tu_D)^2 + y^2}{w^2}\right) \tag{9.34}$$

where I_0 is the intensity, t is time, u_D is the droplet velocity and w determines the spot size. The emission from the droplet is given by,

$$D(y,t) = OI_0\Phi\varepsilon cl(y,t) \tag{9.35}$$

where O is a scaling constant which accounts for signal losses during detection (*i.e.* scattering of emission, collection efficiency *etc.*), I_0 is the incident light intensity, Φ is the emission quantum yield, ε is the extinction coefficient of the absorbing species, c is the concentration of the absorbing species and finally, $l(y,t)$ is the pathlength of light through the droplet, *i.e.* the droplet width. Clearly, $l(y,t)$ depends on the shape of the droplet which is determined by solving the Navier-Stokes and Cahn-Hilliard equations. However, to a good approximation, the droplets shape may be described by the capsule geometry (hemisphere capped cylinder *cf.* **Fig. 9.7 a**)

$$r^2 = (z-r)^2 + y^2 + \frac{1}{4}(|x-a| + |x+a| - 2a)^2 \tag{9.36}$$

where r is the droplet radius, if spherical, or the radius of curvature of the end of the droplet, if a plug, and a is related to the length of the plug ($a = 0$ for a spherical droplet). Since we have taken y to be perpendicular to the direction of excitation, the pathlength of light through the droplet is determined by the z coordinates. These are found by simply solving the quadratic formula for z,

$$\begin{aligned} z_{\pm} &= r \pm \frac{1}{2}\sqrt{4r^2-4y^2-(|x-a| + |x+a| - 2a)^2} \\ &= r \pm \frac{1}{2}\sqrt{4r^2-4y^2-(|u_d t-a| + |u_d t+a| - 2a)^2} \end{aligned} \tag{9.37}$$

where, once again, the x dimension has been converted into time. The pathlength of light through the sample is thus the difference in the roots $z_{\pm}$

$$l(y,t) = z_+ - z_- = \sqrt{4r^2-4y^2-(|u_D t-a|+|u_D t+a|-2a)^2} \tag{9.38}$$

The resulting droplet signal detected by the PMT, assuming the length of the confocal parameter[bz] is larger than the droplet width, is now,

$$F_t(V) = OI_0\Phi\varepsilon c \int_{y_1}^{y_2}\int_{-\infty}^{\infty} \exp\left(-2\frac{(\tau u_D)^2+y^2}{w^2}\right) l(y,t-\tau)\, d\tau dy \tag{9.39}$$

Unfortunately, equation 9.39 has no analytical solution. However it can be solved numerically and thus used to fit and analyse droplet PMT signals (*cf.* **Fig. 9.7 b**). Alternatively, the droplet signal may be approximated to an empirical function consisting of the difference between two sigmoidal functions

$$F_t(V) = A\left(\frac{1}{1+e^{-k_1(t-b_1)}} - \frac{1}{1+e^{-k_2(t-b_2)}}\right) \tag{9.40}$$

where A is the amplitude of the signal, k_i (i=1 or 2) determines the growth or decay of the droplet signal and b_i determines the grow in and decay time (and therefore width) of the droplet. Typically, equation 9.40 is used in analysis due to the large amount of information required to solve or fit equation 9.39.

In all cases, A can be time dependent if there is significant bleaching of the system within the resident time of the droplet within the excitation volume. Nonetheless, following characterisation of droplet emission, MFEs are determined by subtracting the averaged

[bz] The confocal parameter is the length over which the beam diameter of a focused laser is less than or equal to twice the beam waist.

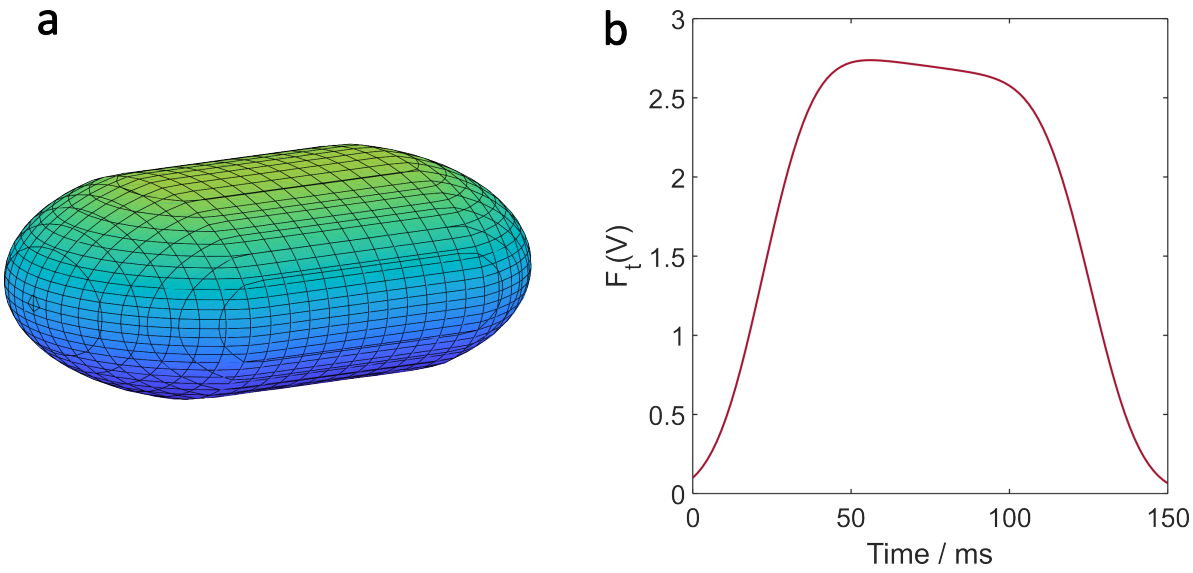

Figure 9.7: a) Capsule geometry for a plug type droplet. b) result from solving equation 9.39 numerically.

droplet signal without a magnetic field, $F_t(V)_{B=off}$ from the averaged droplet signal with a magnetic field, $F_t(V)_{B=on}$. With the $\%MFE$ determined by

$$\%MFE = \frac{F_t(V)_{B=on} - F_t(V)_{B=off}}{F_t(V)_{B=off}} \cdot 100 \tag{9.41}$$

9.3 Microfluidic Magnetic Field Effects in FAD

The first model system explored by μDF-MARY was FAD under acidic conditions since it has a high fluorescence quantum yield and is known to exhibit magnetic field dependent emission under continuous excitation.[230] The photochemistry of this system has already been discussed extensively in **Chapter 8**. Here it is sufficient to recall that FAD forms a triplet born [$FH^{\bullet}$-$AH^{\bullet+}$] RP. As such, strong magnetic fields reduce the amount of singlet recombination from the RP, thus reducing the GS concentration. Therefore, MFEs measured by fluorescence are negative.

Measurements were made on microdroplets containing 30 μM FAD in pH 2.3 citric buffer (4 mM Na_2HPO_4, 98 mM citric acid monohydrate in deionised water). A high viscosity silicone oil carrier phase was used in conjunction with a flow-focusing microfluidic chip with 80μm channels. The resulting droplets were approximately 380 pL in volume with a

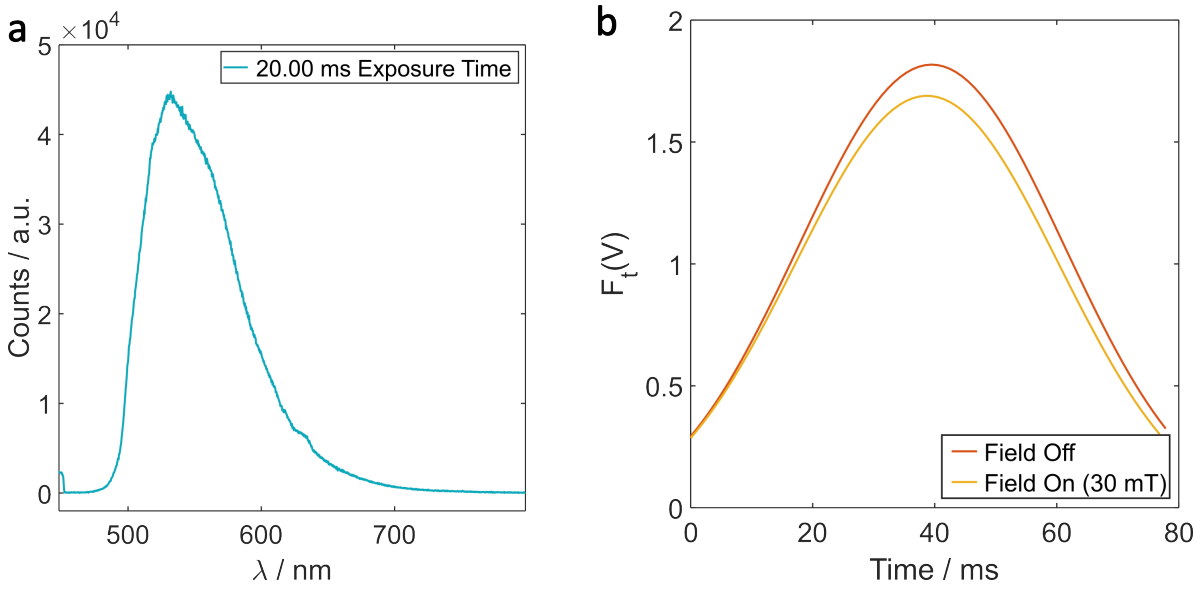

Figure 9.8: a) Emission spectrum from FAD-containing microdroplets illuminated at 450nm. The spectra represents the average over 2 - 3 microdroplets. b) Averaged droplet PMT signals with (30 mT) and without an applied magnetic field. Droplets were illuminated with 4 mW of power.

production rate of 6 Hz. The system was photoexcited at 450 nm and MFEs were measured at a variety of different laser powers and magnetic field strengths.

Fig. 9.8 a shows the emission spectrum from the microdroplets and consists of a single emission band peaking at around 530 nm. This is in agreement with the known FAD emission spectrum and corresponds to the $S_1 \rightarrow S_0$ transition.[162] The spectral shape is moderately distorted due to a sharp water Raman scattering signal at 532 nm and a back reflection/scattering signal from the objective. Nonetheless, the signal detected from the microdroplets is confirmed to be FAD emission. The corresponding averaged droplet signal detected by the PMT, with (30 mT) and without a magnetic field, is shown in **Fig. 9.8 b** and exhibits an average droplet illumination time of *ca.* 80 ms and clear MFE.[ca]

Despite the short excitation time experienced by each droplet, clear MFEs were observed upon the application of a 30 mT magnetic field and can be seen in **Fig. 9.9 a** which shows the MFE (time-averaged percentage difference between the field-on and field-off signals) as a function of excitation power. The magnitude of the MFE increases with increasing laser power and appears to plateau, beyond the excitation powers measured, at *ca.* −6.5%. This increase in MFE corresponds to an increase in the overall fluorescence as

[ca]The lack of a plateau in the droplet signal when the full beam spot is within the droplet is likely due to bleaching of the FAD on a comparable timescale to the droplet residence time within the excitation volume.

the power increases and can be understood by considering the rate processes involved in the photocycle (*cf.* **Fig. 9.9 b**).

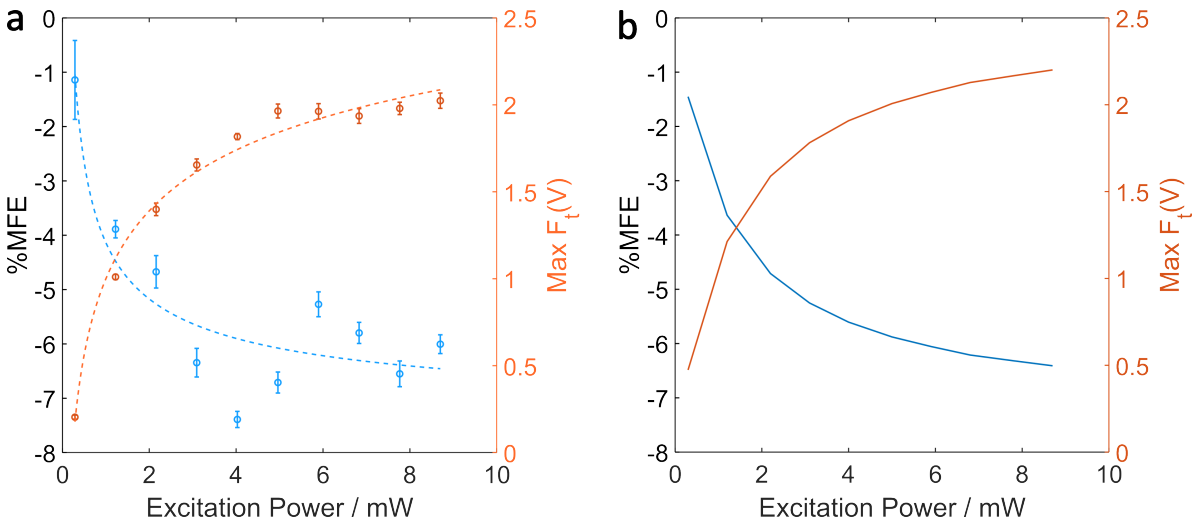

Figure 9.9: a) Experimental data from microdroplets where the blue data points represent the MFE power dependence from a 30 mT applied magnetic field. The orange data points are the corresponding droplet emission intensities as a function of power. For both data sets, the lines are fits to a power series and are there to guide the eye. b) Shows kinetic simulations of the experimental data in a). Similarly, the blue line shows the MFE and the orange line shows the emission intensity. The simulations are illustrative rather than quantitative.

That is, as the power is increased, the ground state becomes more depleted leading to greater populations of photoinduced states. The emission intensity thus increases due to a higher excited state population relaxing and emitting photons. Similarly, the MFE increases in magnitude due to the greater SCRP population inducing larger MFEs in the ground state and, consequently, the rest of the photocycle. This can be seen in *cf.* **Fig. 9.9 b** which displays the results from a kinetic model and shows the effect of increasing power on the excited singlet state population (orange line) and the corresponding MFEs (blue line) induced in this state following application of a magnetic field. Both the simulated data and the experimental results begin to plateau at higher powers since, eventually, the rate at which the ground state is depleted is greater than the rate in which it is replenished. The kinetic model used to generate **Fig. 9.9 b** may be found in **Appendix** A.5.

The field dependence of the MFE at each excitation power was measured and the resulting MARY plots are displayed in **Fig. 9.10 a**. As expected, the saturation point of the MARY plots follow the power dependence in the MFEs shown in **Fig. 9.9 a**. The $B_{1/2}$ values extracted from the MARYs exhibit no obvious power dependence and can be seen in **Fig.**

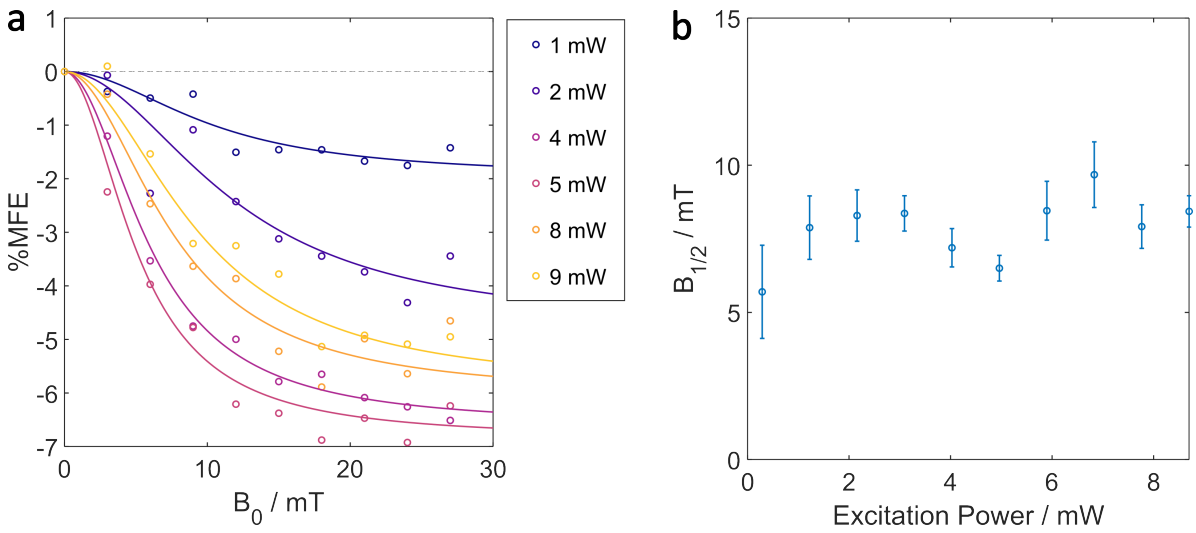

Figure 9.10: a) FAD microdroplet MARY plots at various excitation powers. For clarity, errorbars have been omitted and not all acquired MARYs shown. b) Shows the $B_{1/2}$ extracted for all acquired MARYs.

9.10 b. This is expected since increasing the power only works to change the relative populations of species within the photocycle and should not interfere with any of the spin dynamics (*i.e.* HFCs or relaxation). Nonetheless the average $B_{1/2}$ is 7.84 ± 0.86 mT and agrees reasonably well with those measured by OCTAS in **Chapter 8** and Antill *et al.*[162]

9.4 Magnetic Field Effect on FMN/Ascorbic Acid

To test the sensitivity of μDF-MARY to small MFEs, experiments were carried out on the FMN/Ascorbic acid RP system since it is known to exhibit small high field effects and even smaller low field effects.[231] Ascorbic acid ($AscH_2$), more commonly known as vitamin C, is a vital biological nutrient which plays a key role in the mechanisms of tissue repair, collagen formation, the immune system and neurotransmitter production.[232] Importantly, ascorbic acid functions as a reductant, acting as a cofactor in metalloenzyme reactions and as an antioxidant.[232] Due to these properties, $AscH_2$ readily reduces photoexcited flavins to form RPs. Its structure can be found in **Fig. 9.11**.

Initially, interest in the flavin/$AscH_2$ RP system arose due to the near negligible HFC interactions present in $AscH_2$.[231,233,234] This is because theoretical calculations indicated that a RP between FAD and some species with no HFCs would be two orders of magnitude more sensitive to magnetic field inclination than an FAD-W RP. As such, flavin/$AscH_2$ appeared to be a promising model for the hypothetical flavin/Z RP, where Z is a radical

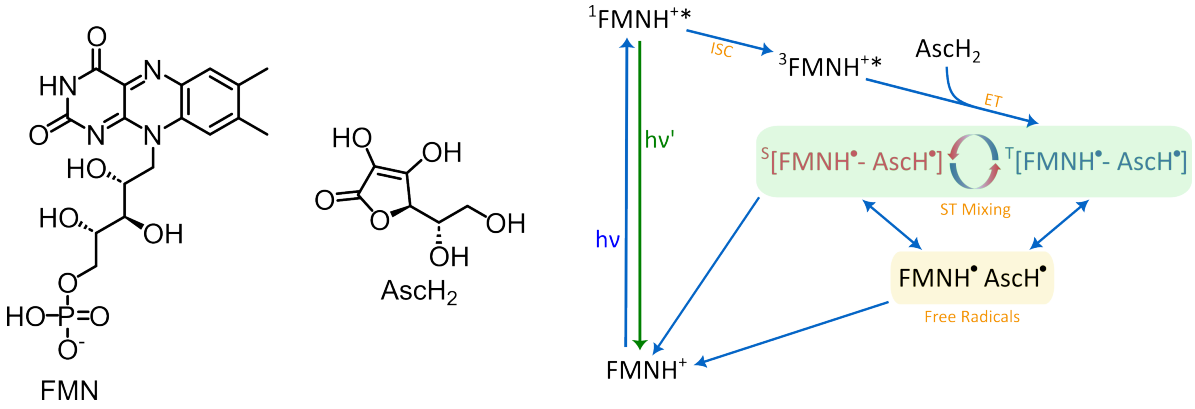

Figure 9.11: Chemical structures of FMN and ascorbic acid. Photocycle (at low pH) for FMN/$AscH_2$ shown on the right.[231]

with zero HFCs.[231,233] In any case, the small magnitude of the MFEs observed in this system make it a suitable model system to probe μDF-MARYs current sensitivity.

The FMN/Ascorbic acid photochemical reaction scheme, at pH 3, is shown in **Fig. 9.11** and is very similar to that of FMN/HEWL. That is, [$FMNH^{\bullet}$ $AscH^{\bullet}$] RPs are formed in the triplet state following photon absorption by $FMNH^{+}$ and electron transfer from $AscH_2$ to $^{s}FMNH^{+}*$.[cb] Consequently, fluorescence detected MFEs in the high field regime are negative while MFEs in the low field regime are positive.[231,234]

With this in mind, experiments were done on microdroplets containing 10 μM FMN and 2 mM $AscH_2$ in formate buffer (pH 3 or pH 7, ionic strength $I_c = 0.1$ M, in deionised water). The microdroplets were formed in a flow-focusing chip with 80 μm channels and a high viscosity silicone oil carrier phase. Droplets were produced at a rate of 2 Hz with a typical droplet illumination time of 120 ms. The back reflection from the objective was filtered out by a 550 nm long pass filter to remove its influence on the MFE measurements due to the very low fluorescence observed in this system. The system was illuminated with an excitation power of 1.6 mW.

The MARY results are shown in **Fig. 9.12** with both high and low field effects successfully detected. The amplitude of the LFEs were 26 % and 7.9 % of the magnitude of the HFEs at pH 3 and pH 7 respectively. Both curves were fit to a sum of two Lorentzians[235]

[cb] It ought to be noted that, for sufficiently high ascorbic acid concentrations, radical pairs can be formed in the singlet state. Naturally, the ratio of singlet born vs triplet born RPs depends on the diffusion controlled electron transfer from ascorbic acid to FMN and thus on the relative concentrations of donor and acceptor.

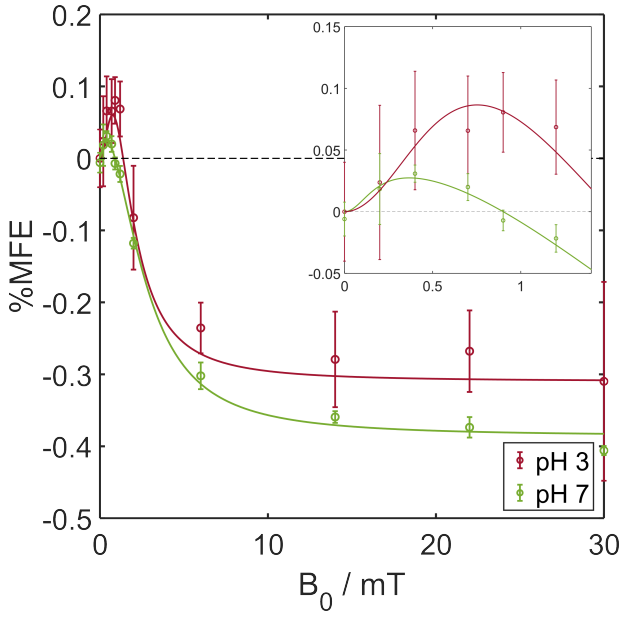

Figure 9.12: MARY plots for FMN/ascorbic acid at pH 3 and pH 7. The insert is a zoom in on the LFE region.

$$\mathscr{L} = A_1\left(\frac{\Gamma_1}{B^2+\Gamma_1}-1\right)-A_2\left(\frac{\Gamma_2}{B^2+\Gamma_2}-1\right) \tag{9.42}$$

where A and B scale the saturation of the HFE ($\%MFE_{sat}$), Γ_1 determines the width of the MARY curve, and is thus related to the $B_{1/2}$, and Γ_2 determines the depth of the LFE ($\%MFE_{LFE}$). The results are summarised in **Table 9.1** where B_{LFE} and B_{zero} are the field values at the LFE maxima and where the $\%MFE$ is zero respectively. The results agree well with previously reported results.[231,235]

Sample	$B_{1/2}$/mT	$\%MFE_{sat}$	$\%MFE_{LFE}$	B_{LFE}/mT	B_{zero}/mT
pH 3	2.71 ± 0.1	-0.29 ± 0.14	0.08 ± 0.03	0.9 ± 0.03	1.4 ± 0.05
pH 7	2.98 ± 0.04	-0.38 ± 0.01	0.03 ± 0.01	0.4 ± 0.01	0.9 ± 0.02

Table 9.1: Summary of MARY results.

The larger errors in the pH 3 results in **Fig. 9.12** arise due to the fewer averages acquired, 300 traces for each field point, compared to the 2000 traces, for each field point, measured for the pH 7 data. In the pH 7 case, each trace had an acquisition time of 2 s and thus between 3 and 4 droplets yielding a total of 6000 to 8000 averages for each field point. Despite this, the total consumed volume of sample was still only *ca* 45 μL. In any case, with this level of sampling there is sufficient data present to characterise the influence the number of acquisitions has on the signal-to-noise ratio. This is achieved by taking the

Allan deviation (*cf.* **Appendix A.5**) which estimates the noise as a function of the number of averages.

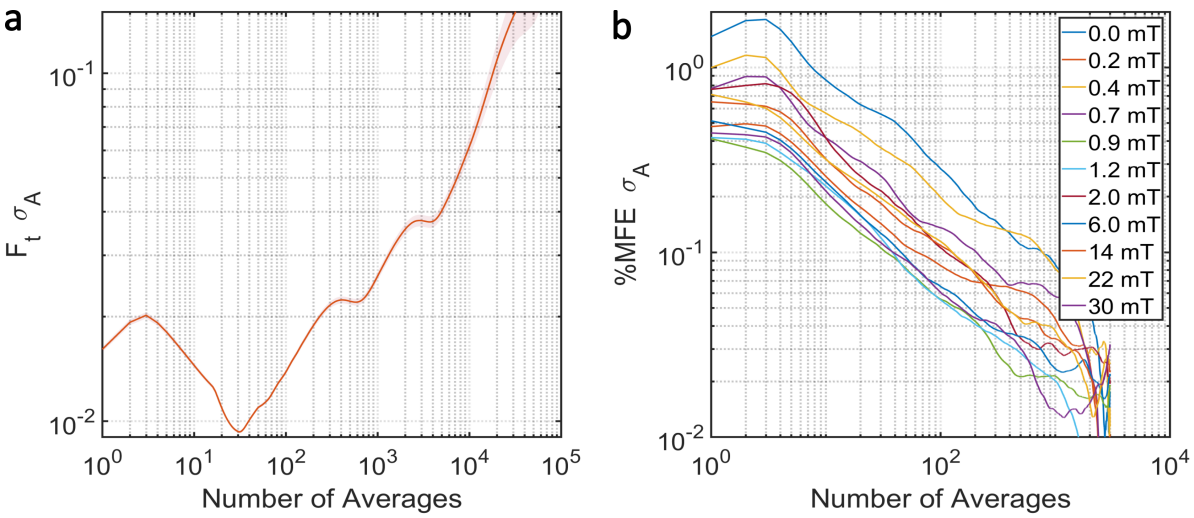

Figure 9.13: a) Allan deviation for the fluorescence amplitude of all measured droplets, without the magnetic field, detected *via* the PMT. Shaded area represents the estimated error in the Allan deviation, $\sigma_{err} = \frac{\sigma_A}{\sqrt{\frac{k}{N}+1}}$ where k is the average number and N is the total number of averages acquired. b) Allan deviation of the %MFE for each field point.

When it comes to the uncertainty in the averaged droplet signal, the minimum in the Allan deviation shown in **Fig. 9.13 a** indicates the signal-to-noise improves over the first 32 droplets before systematic drift worsens the uncertainty.[178] This was found to be due to instability in the PMT leading to long term drift in the magnitude of the droplet signals. Despite this, the uncertainty in the MFE continuously improves with greater averaging, at least within the number of measurements made here (*cf.* **Fig. 9.13 b**). By calculating the %MFE for each on-off trace, the uncertainty due to the PMT drift is mitigated since the %MFE is independent of the magnitude of the PMT signal.[cc] In any case, it is clear that a new detector would drastically improve the signal-to-noise of the experiment. As such, a single photon counting avalanche photodiode (SPAD) has been ordered and is set to be implemented. Not only will this improve the long term stability of measurements but it will also significantly reduce the dark counts (signal without light) and thus background noise inherent to the system.

[cc]Of course, this would not be the case for the change in fluorescence ΔI which would be influenced by the drift in the PMT signal.

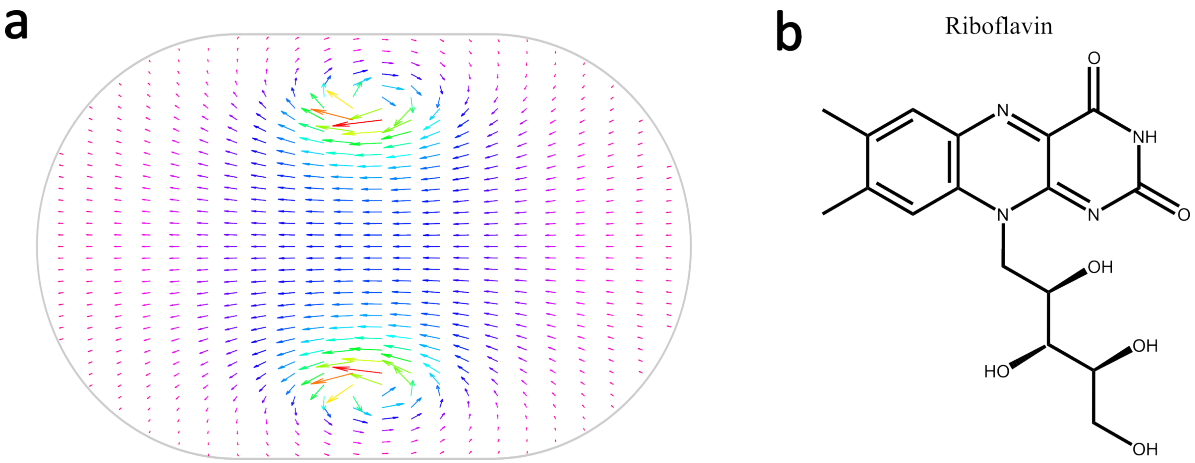

Figure 9.14: a) Illustrative example of flow topology inside a moving microdroplet. Inspired by results by Ma *et al.*,[237] it is in no way quantitative. b) Structure of riboflavin.

9.5 Microdroplet Size and Magnetic Field Effects

Due to the different dominant forces, such as surface tension, on the micron scale versus conventional bulk experiments, properties such as diffusion can differ significantly. This is particularly true for microdroplets since the high surface area to volume ratio can lead to pseudo ordering within droplets due to the varying degrees of interfacial affinity experienced by different constituents within the fluid.[236] Additionally, the process of droplet formation and subsequent flow causes specific mixing currents within the droplet itself (*cf.* **Fig. 9.14 a**), something that is taken advantage of in the design of microdroplet reactors where the mixing efficiency is optimised to improve reaction rates etc.[237–240] It thus follows that the size, and shape, of a microdroplet will influence the diffusion dynamics of solutes and thus any diffusion dependent process such as intermolecular electron transfer. In turn, this could effect MFEs in bi-molecular radical pair systems.[241]

To test the influence the droplet size has on the MFE, a sample consisting of 10 μM riboflavin (Rbf, *cf.* **Fig. 9.14 b**) and 500 μM tryptophan was prepared in deionised water. This intermolecular radical pair system was chosen since it is both well characterised and has already demonstrated MFEs dependent on spatial restriction in micelles.[192] Its photochemical scheme is much the same as FMN and ascorbic acid (*cf.* **Fig. 9.11**) where SCRPs, $[Rbf^{\bullet-}\ WH^{\bullet+}]$, are formed in the triplet state following absorption of a photon by Rbf. Application of magnetic fields leads to negative MFEs in the ground state concentration and thus fluorescence.

Microdroplets where generated in TOPAS®COC flow focusing chips with channel diameters of 20 μm, 50 μm, 60 μm, 70 μm, 80 μm. Droplet production rates ranged from 2-4 Hz. In each case the droplet residence times were between 100 ms and 200 ms. The Rbf was excited at 450 nm with an excitation power of 2 mW. The resulting MFEs at 30 mT are shown below in **Fig. 9.15** where the droplet diameter, $\emptyset_D$, refers to the cross section of a plug shaped droplet whose width is constrained and determined by the width of the microfluidic channel it moves through.

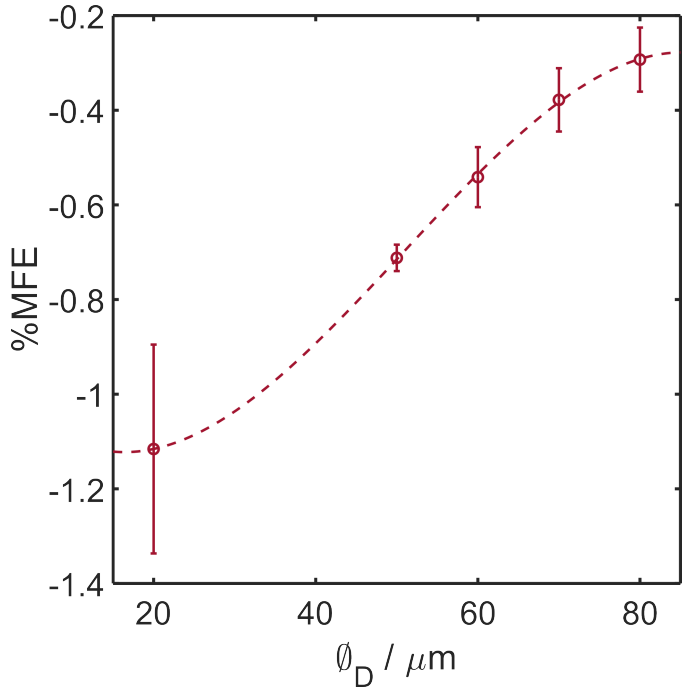

Figure 9.15: Droplet diameter, $\emptyset_D$, dependent %MFEs. Fitted line is only there to guide the eye.

Clearly the MFE increases in magnitude as the droplet size decreases. This implies that either the radical yield is enhanced or the lifetime of the SCRP is prolonged or a combination of both. Due to the significant advection component in the solute motion, it follows that an increased SCRP yield is to be expected due to an increase in the collision frequency leading to more efficient electron transfer from the tryptophan to the Rbf.

Werner *et al.* predicted that smaller relative radical diffusion rates enhance the MFEs in an intermolecular radical pair system undergoing Brownian diffusion due to a prolonging of the geminate recombination rate.[192,231,241] Something similar could explain the enhanced MFEs observed here. Since the smaller droplets have a higher surface area to volume ratio, a greater repulsive influence from the droplet interface could limit the stochastic

diffusion. Additionally, mixing currents induced by the droplets' flow will be influenced by the channel width due to a greater influence from the channel walls (which leads to inner droplet fluid motion) relative to the droplet diameter. In any case, if the SCRP lifetime is indeed longer then the $B_{1/2}$ extracted from field dependent MFEs should increase since the effects of spin relaxation have more time to develop during the RP lifetime.[234] This is indeed observed as indicated in **Fig. 9.16**.

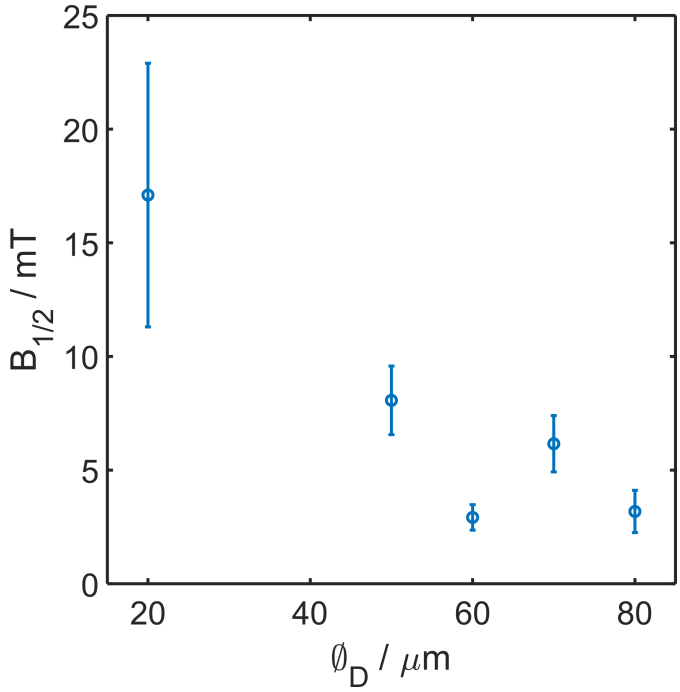

Figure 9.16: Droplet diameter, $\emptyset_D$, dependent $B_{1/2}$, extracted from Rbf-W droplet MARY plots.

Clearly, the above discussion is simple conjecture. To really understand the influence droplet size, and by extension diffusion, has on the development of MFEs in intermolecular systems, more rigorous calculations and experiments are required. For example one could employ the Smoluchowski convection-diffusion equation (which accounts for fluid motion)

$$\mathscr{L}\rho(\mathbf{r},t) = \nabla\cdot(D\nabla\rho(\mathbf{r},t)) - \nabla\cdot(M\mathbf{F}\rho(\mathbf{r},t)) - \nabla\cdot(\mathbf{u}(\mathbf{r},t)\rho(\mathbf{r},t)) \tag{9.43}$$

where $\rho(\mathbf{r},t)$ is the RP density matrix, D is the diffusion coefficient, M is the mobility, $\mathbf{F}$ describes the interparticle interaction force and $\mathbf{u}(\mathbf{r},t)$ is the velocity field which could be obtained experimentally[237] or from numerically solving equations 9.16 and 9.27. Naturally, equation 9.43 would be combined with spin Hamiltonian, recombination and relaxation terms to form a complete equation of motion for $\rho(\mathbf{r},t)$, thus adequately capturing the

spin dynamics within the microdroplet. This is, however, the product of future work and represents a way in which microdroplets could be used to study the effect of system dynamics on the spin dynamics without altering the components of the system itself.

Since this is an ongoing project, unfortunately, some of the data presented in this section are somewhat noisy with repeats ongoing.[cd] Furthermore, the data set is incomplete as the 10μm, 30μm and 40μm channels are yet to be measured. Nonetheless, the data above clearly indicate a pronounced effect on the development of MFEs due to the size of the microdroplet and show how the dynamic (rather than chemical) properties of a system can play an important role in the development of MFEs.

9.6 Conclusion and Outlook

μDF-MARY proves to be a promising new technique in the study of MFEs with minimal sample consumption coupled to high sampling and averaging. It has been shown to effectively measure MFEs in several flavin based model systems and able to detect MFEs down to 0.007% (*cf.* **Fig. 9.12**). The key results from these model systems are summarised in **Table 9.2** and compared to published results from alternative fluorescence techniques where possible. Clearly, μDF-MARY can reliably measure small MFEs and can thus be readily utilised in the study of cryptochromes and magnetoreception. Furthermore, since the technique is still in the early stages of development, significant improvements to its sensitivity can be made.

The implementation of a more sensitive and stable detector (SPAD) has been mentioned already and is soon to be implemented. In addition to this, the overall mechanical stability can be improved with a more rigid microscope body and xy translation stage. Moreover, the accuracy and consistency of alignment and set up can be improved with the implementation of piezo electric controls for the objective and xy translation stage. These improvements are underway and ought to significantly improve the consistency and sensitivity of the technique.

[cd] Ongoing experiments are being carried out by MRes student Laurynas Paskevicius.

System	Main Results	Results From Other Techniques
FAD	|MFE| = 6 % $B_{1/2}$ = 7.84 mT	|MFE| = 6 % - confocal microscopy, unpublished $B_{1/2}$ ~8 mT - TA microscopy[162]
FMN/$AscH_2$	LFE/HFE = 28 % (pH 3) $B_{1/2}$ = 2.71 mT LFE/HFE = 8 % (pH 7) $B_{1/2}$ = 2.98 mT	LFE/HFE = 27 % (pH 3) - prompt fluorescence[231] $B_{1/2}$ = 2.55 mT LFE/HFE = 9 % (pH 7) $B_{1/2}$ = 2.20 mT
Rbf/W	|MFE| = 1.2 % (20 μm droplet) |MFE| = 0.3 % (80 μm droplet) $B_{1/2}$ = 17 mT (20 μm droplet) $B_{1/2}$ = 3.18 mT (80 μm droplet)	n.a. |MFE| = 0.2 % (bulk solution)[234] n.a. $B_{1/2}$ = 3.5 mT (bulk solution)[234]

Table 9.2: Summary of the key μDF-MARY results from model systems in comparison to published results, where possible, from alternative fluorescence or microscopy techniques. In the FMN/$AscH_2$ system, LFE/HFE refers to the percentage ratio between the maximum of the LFE and saturation point of the HFE. Refer to Evans *et al.*[242] for a description of the prompt fluorescence MFE experiment. n.a. indicates that there is no relevant published data to compare to.

With improved sensitivity and consistency more challenging systems can be studied such as cryptochromes and cryptochrome containing cells. The latter representing a primary initial motivation for the development of μDF-MARY. As mentioned, the short laser exposure time experienced by each droplet significantly reduces sample degradation and thus its influence on the measured data. This is particularly important for the study of cells which are readily and rapidly destroyed by laser irradiation.

To measure MFEs on cells encapsulated within microdroplets, the distribution of the number of encapsulated cells must be accounted for and will depend on the type of cell, and thus its size, and the droplet size. Thankfully this should simply follow a Gaussian distribution which will correspond to a distribution in the emission intensity from the droplets. An example of the data and MFE produced by such an experiment is shown in **Fig. 9.17** where the distribution is from FMN/HEWL droplet emission intensity and reflects the variation in droplet size rather than encapsulated cells. Nonetheless, the logic carries through to future experiments containing cells.

Other potential experiments possible with the microdroplets are pump-probe experiments. For example, the droplet passes through an excitation beam and then a measurement beam with the pump-probe delay controlled by the laser separation, the droplet velocity and/or pump-probe delay from pulsed lasers. This could allow for some of the system dynamics to be monitored, overcoming one of the technique's current major drawbacks. Additionally, the probe wavelength could be altered to map out more of the system and could be done

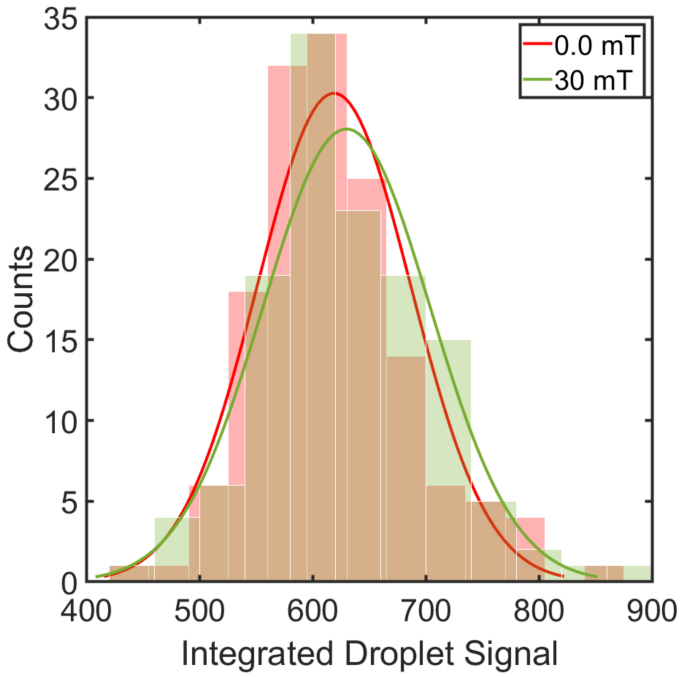

Figure 9.17: Example of analysis method to be applied to experiments involving encapsulated cells.

via emission or even transmission, providing time dependent excitation and absorption spectra. Alternatively, fluorescence lifetime measurements could be probed with pulsed photoexcitation. In any case, with the basic experimental concept of microdroplet based MFEs demonstrated, there is scope for the development of a variety of exotic microdroplet based experiments.

Chapter 10

Summary and Outlook

In this thesis the results from a series of studies on the photochemistry and magnetic sensitivity of avian Cry4a proteins, in particular *Gg*Cry4a WT and its mutants, were presented. Together, these studies sought to determine, whether avian Cry4a proteins exhibited *in vitro* MFEs and if so whether proteins from migrating birds known to have a magnetic sense were more field sensitive (**Chapter 4**), how the presence of the artificial reoxidant FC influences the photochemistry and MFE development in Cry4a proteins (**Chapter 5**), the role played by evolutionarily conserved amino acid residues adjacent to the tryptophan tetrad and the influence of the electron transfer chain length on the development of MFEs (**Chapters 6 and 7**). In addition, the development of two novel sensitive spectroscopic techniques for the study of MFEs and spin chemistry, OCTAS and μDF-MARY, were reported on (**Chapters 8** and **9**) with their capabilities demonstrated through measurements of well-studied radical pair forming systems.

In **Chapter 4** BBCEAS was used to measure and compare the MFEs from several avian Cry4a proteins, namely the European robin, common quail, common pigeon and domestic chicken. These results confirmed that avian Cry4a proteins *in vitro* can sense weak magnetic fields, lending credence to the Cry4a RPM hypothesis of magnetoreception. Interestingly, the magnetic sensitivity of proteins from migrating birds (*e.g. Er*Cry4a) were not observed to be more magnetically sensitive. This suggests that the magnetic sense in night-migratory passerines may arise from evolutionary optimisation of processes such as signal transduction rather than the magneto sensitive Cry4a protein.

Up until now all spectroscopic MFE studies on cryptochrome proteins utilised FC to aid in sample recovery following photoreduction. However, valid concerns over the biological relevance of FC and the influence it may have on the proteins prompted a close look at its photochemistry and impact on MFE measurements. This was explored in **Chapter 5** through

a combination of continuous irradiation and BBCEAS in conjunction with DFT, kinetic and spin dynamics simulations. From UV/Vis and IR continuous irradiation experiments it was found that FC undergoes significant photochemistry when excited at 450 nm, forming stable photoproducts, *via* solvent-ligand exchange, whose absorption overlaps with that of Cry4a proteins. Furthermore, following a BBCEAS FC concentration dependence study on MFEs in *Gg*Cry4a W369F, FC was found to play an active role in the RPM, influencing rate processes of photoinduced radical species and the spin dynamics of the SCRP. These results demonstrated that FC is an unsuitable reoxidant when studying MFEs in Cry4a proteins. However, the BBCEAS results also showed, for the first time, that MFEs could be measured with pure molecular oxygen as a reoxidant. This marks a major step forward in the study of MFEs in cryptochrome proteins, providing a far more biologically relevant reoxidant which does not influence the absorption spectra in spectroscopic MFE measurements.

The role played by amino acid residues, C317 and K320, in close spatial proximity to the tryptophan tetrad and evolutionarily conserved in night-migratory passerines was explored by TA spectroscopy, BBCEAS and continuous irradiation experiments in **Chapter 6**. In line with the results in **Chapter 4**, these residues were shown to have little to no impact on the photochemistry and MFEs of *Gg*Cry4a proteins where these residues had been substituted in (*Gg*Cry4a R317C and E320K). However, removal of the fourth tryptophan in the tetrad (*Gg*Cry4a W369F) was shown to increase the SCRP lifetime and significantly enhance the MFE, hinting that the SCRP recombination may be in the Marcus inverted region. Furthermore, simulations showed that the shorter SCRP lifetime of the WT type protein may lead to larger MFEs if the tryptophan deprotonation rate or relaxation rate is suppressed. Thus suggesting that the WT protein may be a more suitable magnetoreceptor *in vivo*.

Further mutations to the tryptophan chain in **Chapter 7** showed the use of phenylalanine as a tryptophan substitution for blocking electron transfer may not always be effective with MFEs still measurable in *Gg*Cry4a W318F where electron transfer is expected to stop on the second tryptophan such that SCRP recombination is too fast for MFE development. Therefore, caution must be used when analysing data and drawing conclusions from the

kinetics and MFEs measured on proteins with this amino acid substitution. Additionally, a tyrosine residue (Y319) located after the final tryptophan in the tetrad was shown to significantly influence the photochemistry of *Gg*Cry4a in an as yet unclear manner. Nonetheless, these results did demonstrate that amino acid residues adjacent to the electron transfer chain can influence protein photochemistry and may be vital for *in vivo* MFE development.

Together these results mark major progress in the study of cryptochrome MFEs and offer insight into future directions of research. The lack of impact from the cysteine and lysine mutations suggest that these residues may play a role elsewhere in the magnetic sensing process, perhaps in binding to a signalling protein. Additionally, despite enhanced *in vitro* MFEs, it was predicted that the prolonged SCRP lifetime in *Gg*Cry4a W369F may negatively impact MFE development *in vivo*. These results together with the observation that MFEs in Cry4a proteins from migratory birds were not superior to those from non-migratory birds *in vitro*, suggest that future studies must be done in more biologically relevant conditions. For example MFE studies of cryptochromes with candidate binding partners may produce significantly different photochemical and magnetic sensitivity behaviour, inducing measurable differences between proteins from migratory and non-migratory species or inverting the relationship between WT and W369F MFEs. Such experiments could shed light on the origin of the evolutionary conservation of amino acids such as C317 and K320, not directly involved in the RPM photochemistry and help understand whether the WT proteins are better suited as magnetoreceptors *in vivo*. In, addition, as shown in **Chapter 5**, the dynamics of long-lived radical recovery ($FADH^{\bullet}$ and $W^{\bullet}$) can drastically influence the formation and behaviour of MFEs. Despite this, their mechanism(s) of recovery are still unknown. It is thus vitally important to understand this process and determine the mechanism of protein recovery *in vitro* and *in vivo*.

Due to the weak MFEs observed in cryptochrome proteins, OCTAS was developed to improve on the sensitivity of TA spectroscopy, the wavelength resolution of CRDS and the time resolution of BBCEAS, thus producing a technique capable of measuring the majority of time scales (150 ns and up) present in the Cry4a RPM with full spectral resolution

over the primary region of interest (400 nm - 800 nm) with a sensitivity 3 orders of magnitude greater than TA. The development of OCTAS was presented in **Chapter 8** with the new technique's capabilities demonstrated in several model systems, reproducing results measured by other techniques whilst improving on the signal-to-noise, sensitivity or depth of information obtained. In addition to OCTAS, μDF-MARY was developed where a flow of sample containing microfluidic droplets are used to minimise sample consumption and degradation during measurement. Its development was presented in **Chapter 9** where, once again, model systems were used to demonstrate the technique's capabilities, reproducing results from alternative fluorescence experiments whilst drastically minimising sample consumption.

Now that both techniques have been shown to sensitively measure MFEs in radical pair based systems they can be applied to the study of Cry4a MFEs, replacing existing techniques currently in use. In particular, OCTAS can be used to study MFEs of Cry4a plus binding partner systems by both pulsed excitation, to observe SCRP formation and dynamics, and continuous excitation to map out early time long-lived radical accumulation, bridging the gap between BBCEAS and TA/CRDS. In addition to transitioning to new systems of interest, the single shot depth of information will be improved by implementing a small PMT array to acquire full time traces at select wavelengths with every single laser flash. This is currently under implementation and represents a significant upgrade to the technique. Meanwhile, once μDF-MARY is shown to be capable of measuring cryptochrome MFEs it can be used to study MFEs in cryptochrome containing cells, perhaps by implementing a pump-probe fluorescence technique that detects the emission from magnetically sensitive photoinduced species whose absorption can be separated from other intracellular chromophores. To achieve this the techniques reproducibility must first be improved. This can be done by implementation of a new SPAD detector and rebuilding the microscope and translation stage on a more rigid frame with piezoelectric motors to control objective focus and the translation stage position.

Bibliography

1. Xu, J. *et al.*; en; *Nature* **594,** 535–540;ISSN: 0028-0836, 1476-4687; https://www.nature.com/articles/s41586-021-03618-9 (2023) (June 2021)
2. Johnsen, S. *et al.*; en; *Physics Today* **61,** 29–35;ISSN: 0031-9228, 1945-0699; http://physicstoday.scitation.org/doi/10.1063/1.2897947 (2023) (Mar. 2008)
3. Homer *et al.*; en; ISBN: 978-0-14-044504-6; (A.S. Barnes & Co, New York, 1848)
4. Hore, P. J. *et al.*; en; *Annual Review of Biophysics* **45,** 299–344;ISSN: 1936-122X, 1936-1238; https://www.annualreviews.org/doi/10.1146/annurev-biophys-032116-094545 (2023) (July 2016)
5. Richardson, W. J.; en; in *Bird Migration*; (ed Gwinner, E.) ; (Springer, Berlin, Heidelberg, 1990), 78–101; ISBN: 978-3-642-74542-3
6. Wiltschko, W. *et al.*; en; *Science* **176,** 62–64;ISSN: 0036-8075, 1095-9203; https://www.science.org/doi/10.1126/science.176.4030.62 (2023) (Apr. 1972)
7. Wiltschko, W. *et al.*; eng; *The Journal of Experimental Biology* **204,** 3295–3302;ISSN: 0022-0949 (Oct. 2001)
8. Zapka, M. *et al.*; en; *Nature* **461**;Number: 7268 Publisher: Nature Publishing Group, 1274–1277;ISSN: 1476-4687; https://www.nature.com/articles/nature08528 (2024) (Oct. 2009)
9. Ritz, T. *et al.*; en; *Biophysical Journal* **78,** 707–718;ISSN: 00063495; https://linkinghub.elsevier.com/retrieve/pii/S000634950076629X (2023) (Feb. 2000)
10. Günther, A. *et al.*; en; *Current Biology* **28,** 211–223.e4;ISSN: 09609822; https://linkinghub.elsevier.com/retrieve/pii/S0960982217316056 (2023) (Jan. 2018)
11. Schulten, K. *et al.*; en; *Zeitschrift für Physikalische Chemie* **111,** 1–5;ISSN: 2196-7156, 0942-9352; https://www.degruyter.com/document/doi/10.1524/zpch.1978.111.1.001/html (2023) (Jan. 1978)
12. Schulten, K. *et al.*; en; *The Journal of Chemical Physics* **68,** 3292–3297;ISSN: 0021-9606, 1089-7690;

https://pubs.aip.org/aip/jcp/article/68/7/3292-3297/533127 (2023) (Apr. 1978)

13. KERPAL, C. *et al.*; en; *Nature Communications* **10,** 3707;ISSN: 2041-1723; https://www.nature.com/articles/s41467-019-11655-2 (2023) (Aug. 2019)
14. HORE, P. J. *et al.*; *The Journal of Chemical Physics* **152,** 120401;ISSN: 0021-9606; https://doi.org/10.1063/5.0006547 (2023) (Mar. 2020)
15. FESSENDEN, R. W. *et al.*; *The Journal of Chemical Physics* **39,** 2147–2195;ISSN: 0021-9606; https://doi.org/10.1063/1.1701415 (2023) (June 2004)
16. KAPTEIN, R. *et al.*; *Chemical Physics Letters* **4,** 195–197;ISSN: 0009-2614; https://www.sciencedirect.com/science/article/pii/0009261469800989 (2023) (Nov. 1969)
17. ATKINS, P. W. *et al.* 5th ed; ISBN: 978-0-19-954142-3; (Oxford University Press, Oxford ; New York, 2011)
18. BECKER, A.; en; Sept. 2023; https://www.scientificamerican.com/article/quantum-particles-arent-spinning-so-where-does-their-spin-come-from/ (2023)
19. OHANIAN, H. C.; en; *American Journal of Physics* **54,** 500–505;ISSN: 0002-9505, 1943-2909; https://pubs.aip.org/ajp/article/54/6/500/1052743/What-is-spin (2023) (June 1986)
20. PAULI, W.; de; *Zeitschrift für Physik* **43,** 601–623;ISSN: 0044-3328; https://doi.org/10.1007/BF01397326 (2023) (Sept. 1927)
21. MANDL, F. First Edition; en; ISBN: 978-0-471-93155-3 978-0-471-92971-0; (Wiley, 2001)
22. TONG, D. Lecute Notes; en; https://www.damtp.cam.ac.uk/user/tong/qft.html; (Department of Applied Mathematics et al., Cambridge, 2015)
23. KUPROV, I.; en; ISBN: 978-3-031-05606-2 978-3-031-05607-9; https://link.springer.com/10.1007/978-3-031-05607-9 (2023); (Springer International Publishing, Cham, 2023)
24. KUPROV, I. *et al.* Lecture Notes; https://spindynamics.org/group/?page_id=18; (University of Southampton)
25. CHECHIK, V. *et al.*; ISBN: 978-0-19-872760-6; (Oxford University Press, Oxford, 2016)
26. TONG, D. Lecture Notes; en; https://www.damtp.cam.ac.uk/user/tong/em.html; (Department of Applied Mathematics et al., Cambridge, 2015)

27. MOSTAFANEJAD, M.; en; *International Journal of Quantum Chemistry* **114,** 1495–1512;ISSN: 00207608; https://onlinelibrary.wiley.com/doi/10.1002/qua.24721 (2023) (Nov. 2014)
28. ANDERSON, P. W.; en; *Physical Review* **79,** 350–356;ISSN: 0031-899X; https://link.aps.org/doi/10.1103/PhysRev.79.350 (2023) (July 1950)
29. ANDERSON, P. W.; en; *Physical Review* **115,** 2–13;ISSN: 0031-899X; https://link.aps.org/doi/10.1103/PhysRev.115.2 (2023) (July 1959)
30. MANZANO, D.; en; *AIP Advances* **10,** 025106;ISSN: 2158-3226; https://pubs.aip.org/aip/adv/article/1021638 (2023) (Feb. 2020)
31. BREUER, H.-P. *et al.* Repr; eng; ISBN: 978-0-19-921390-0; (Clarendon Press, Oxford, 2010)
32. HABER, H. Lecture Notes; https://scipp.ucsc.edu/~haber/ph215/; (University of California Santa Cruz, 2018)
33. TIMMEL, C. *et al.*; en; *Molecular Physics* **95,** 71–89;ISSN: 0026-8976, 1362-3028; http://www.tandfonline.com/doi/abs/10.1080/00268979809483134 (2023) (Sept. 1998)
34. LEWIS, A. M. *et al.*; en; *The Journal of Chemical Physics* **149,** 034103;ISSN: 0021-9606, 1089-7690; https://pubs.aip.org/jcp/article/149/3/034103/196957/On-the-low-magnetic-field-effect-in-radical-pair (2023) (July 2018)
35. KRISHTALIK, L. I.; en; *Biochimica et Biophysica Acta (BBA) - Bioenergetics* **1458,** 6–27;ISSN: 00052728; https://linkinghub.elsevier.com/retrieve/pii/S0005272800000578 (2023) (May 2000)
36. ATKINS, P. W. *et al.* Eleventh edition; ISBN: 978-0-19-876986-6; (Oxford University Press, Oxford, United Kingdom ; New York, NY, 2018)
37. HABERKORN, R.; en; *Molecular Physics* **32,** 1491–1493;ISSN: 0026-8976, 1362-3028; https://www.tandfonline.com/doi/full/10.1080/00268977600102851 (2023) (Nov. 1976)
38. FAY, T. P. *et al.*; en; *The Journal of Chemical Physics* **149,** 064107;ISSN: 0021-9606, 1089-7690; https://pubs.aip.org/jcp/article/149/6/064107/363343/Spin-selective-electron-transfer-reactions-of (2023) (Aug. 2018)
39. WELLER, A. *et al.*; *Chemical Physics Letters* **96,** 24–27;ISSN: 0009-2614; https://www.sciencedirect.com/science/article/pii/0009261483801092 (2024) (Mar. 1983)

40. WONG, S. Y. *et al.*; en; *Physical Chemistry Chemical Physics* **25**;Publisher: The Royal Society of Chemistry, 975–982;ISSN: 1463-9084; https://pubs.rsc.org/en/content/articlelanding/2023/cp/d2cp03793a (2023) (Jan. 2023)
41. GOLESWORTHY, M. J. *et al.*; en; *The Journal of Chemical Physics* **159,** 105102;ISSN: 0021-9606, 1089-7690; https://pubs.aip.org/jcp/article/159/10/105102/2910503/Singlet-triplet-dephasing-in-radical-pairs-in (2023) (Sept. 2023)
42. FAY, T. P. *et al.*; en; *Faraday Discussions* **221,** 77–91;ISSN: 1359-6640, 1364-5498; http://xlink.rsc.org/?DOI=C9FD00049F (2023) (2020)
43. HOGBEN, H. J.; en; DPhil Thesis;(University of Oxford, 2011)
44. BRASIL, C. A. *et al.*; en; *Revista Brasileira de Ensino de Física* **35,** 01–09;ISSN: 1806-9126, 1806-1117; http://arxiv.org/abs/1110.2122 (2023) (Mar. 2013)
45. WILTSCHKO, W. *et al.*; en; *Nature* **364**;Number: 6437 Publisher: Nature Publishing Group, 525–527;ISSN: 1476-4687; https://www.nature.com/articles/364525a0 (2023) (Aug. 1993)
46. WILTSCHKO, R. *et al.*; *The Journal of Experimental Biology* **217,** 4225–4228;ISSN: 0022-0949; https://www.ncbi.nlm.nih.gov/pmc/articles/PMC4254397/ (2023) (Dec. 2014)
47. LIEDVOGEL, M. *et al.*; en; *European Journal of Neuroscience* **25**;_eprint: https://onlinelibrary.wiley.com/doi/pdf/10.1111/j.1460-9568.2007.05350.x, 1166–1173;ISSN: 1460-9568; https://onlinelibrary.wiley.com/doi/abs/10.1111/j.1460-9568.2007.05350.x (2023) (2007)
48. HEIN, C. M. *et al.*; en; *Nature* **471**;Number: 7340 Publisher: Nature Publishing Group, E1–E1;ISSN: 1476-4687; https://www.nature.com/articles/nature09875 (2023) (Mar. 2011)
49. CHETVERIKOVA, R. *et al.*; *Journal of The Royal Society Interface* **19**;Publisher: Royal Society, 20210877; https://royalsocietypublishing.org/doi/full/10.1098/rsif.2021.0877 (2023) (Apr. 2022)
50. MOURITSEN, H. *et al.*; *Proceedings of the National Academy of Sciences* **101**;Publisher: Proceedings of the National Academy of Sciences, 14294–14299; https://www.pnas.org/doi/10.1073/pnas.0405968101 (2023) (Sept. 2004)
51. LIN, C. *et al.*; *Genome Biology* **6,** 220;ISSN: 1474-760X; https://doi.org/10.1186/gb-2005-6-5-220 (2023) (Apr. 2005)

52. LAMBERT, N. *et al.*; en; *Nature Physics* **9**;Number: 1 Publisher: Nature Publishing Group, 10–18;ISSN: 1745-2481; https://www.nature.com/articles/nphys2474 (2023) (Jan. 2013)
53. ZOLTOWSKI, B. D. *et al.*; *Proceedings of the National Academy of Sciences* **116**;Publisher: Proceedings of the National Academy of Sciences, 19449–19457; https://www.pnas.org/doi/full/10.1073/pnas.1907875116 (2023) (Sept. 2019)
54. BISCONTIN, A. *et al.*; en; *Scientific Reports* **7**;Number: 1 Publisher: Nature Publishing Group, 17742;ISSN: 2045-2322; https://www.nature.com/articles/s41598-017-18009-2 (2023) (Dec. 2017)
55. EINWICH, A. *et al.*; en; *Scientific Reports* **10**;Number: 1 Publisher: Nature Publishing Group, 15794;ISSN: 2045-2322; https://www.nature.com/articles/s41598-020-72579-2 (2023) (Sept. 2020)
56. TIMMER, D. *et al.*; en; *Journal of the American Chemical Society,* jacs.3c00442;ISSN: 0002-7863, 1520-5126; https://pubs.acs.org/doi/10.1021/jacs.3c00442 (2023) (May 2023)
57. HISCOCK, H. G. *et al.*; *Proceedings of the National Academy of Sciences* **113**;Publisher: Proceedings of the National Academy of Sciences, 4634–4639; https://www.pnas.org/doi/abs/10.1073/pnas.1600341113 (2023) (Apr. 2016)
58. LACOMBAT, F. *et al.*; en; *Journal of the American Chemical Society* **141,** 13394–13409;ISSN: 0002-7863, 1520-5126; https://pubs.acs.org/doi/10.1021/jacs.9b03680 (2023) (Aug. 2019)
59. HOOKER, S. *et al.*; *Oxford master series in physics. Atomic, optical, and laser physics* **9**; ISBN: 978-0-19-850692-8 978-0-19-850691-1; (Oxford University Press, Oxford ; New York, 2010)
60. JESTÄDT, R. *et al.*; en; *Advances in Physics* **68,** 225–333;ISSN: 0001-8732, 1460-6976; https://www.tandfonline.com/doi/full/10.1080/00018732.2019.1695875 (2023) (Oct. 2019)
61. HOLLAS, J. M. 4th ed; ISBN: 978-0-470-84415-1 978-0-470-84416-8; (J. Wiley, Chichester ; Hoboken, NJ, 2004)
62. GAGLIARDI, G. *et al.*; en; *Springer series in optical sciences* **179**; ISBN: 978-3-642-40002-5; (Springer, Berlin Heidelberg, 2014)
63. LIU, X. *et al.*; en; *Nature Photonics* **9**;Number: 1 Publisher: Nature Publishing Group, 30–34;ISSN: 1749-4893; https://www.nature.com/articles/nphoton.2014.304 (2023) (Jan. 2015)

64. FISCHER, E. W. *et al.*; en; *Physical Chemistry Chemical Physics* **25**;Publisher: The Royal Society of Chemistry, 11771–11779;ISSN: 1463-9084; https://pubs.rsc.org/en/content/articlelanding/2023/cp/d3cp00175j (2023) (Apr. 2023)
65. DUTRA, S. M. *et al.*; en; *Journal of Optics B: Quantum and Semiclassical Optics* **2,** 584;ISSN: 1464-4266; https://dx.doi.org/10.1088/1464-4266/2/5/305 (2023) (Oct. 2000)
66. PANDYA, R. *et al.*; en; *Nature Communications* **12**;Number: 1 Publisher: Nature Publishing Group, 6519;ISSN: 2041-1723; https://www.nature.com/articles/s41467-021-26617-w (2023) (Nov. 2021)
67. CUEVAS, *et al.*; *Science Advances* **4**;Publisher: American Association for the Advancement of Science, eaao6814; https://www.science.org/doi/10.1126/sciadv.aao6814 (2023) (Apr. 2018)
68. COLLABORATION, T. L. S. *et al.*; *Physical Review Letters* **116**;arXiv:1602.03841 [gr-qc], 221101;ISSN: 0031-9007, 1079-7114; http://arxiv.org/abs/1602.03841 (2023) (May 2016)
69. LIGO SCIENTIFIC COLLABORATION AND VIRGO COLLABORATION *et al.*; *Physical Review Letters* **116**;Publisher: American Physical Society, 061102; https://link.aps.org/doi/10.1103/PhysRevLett.116.061102 (2023) (Feb. 2016)
70. LIGO; https://www.ligo.caltech.edu/ (2023)
71. O'KEEFE, A. *et al.*; *Review of Scientific Instruments* **59,** 2544–2551;ISSN: 0034-6748; https://doi.org/10.1063/1.1139895 (2023) (Dec. 1988)
72. O'KEEFE, A.; en; *Chemical Physics Letters* **293,** 331–336;ISSN: 00092614; https://linkinghub.elsevier.com/retrieve/pii/S0009261498007854 (2023) (Sept. 1998)
73. WANG, M. *et al.*; *Analytical Chemistry* **94**;Publisher: American Chemical Society, 4286–4293;ISSN: 0003-2700; https://doi.org/10.1021/acs.analchem.1c04940 (2023) (Mar. 2022)
74. TRICHET, A. A. P. *et al.*; en; *Lab Chip* **14,** 4244–4249;ISSN: 1473-0197, 1473-0189; http://xlink.rsc.org/?DOI=C4LC00817K (2023) (2014)
75. TRAN, D.-B.-A. *et al.*; *Analytical Chemistry* **93**;Publisher: American Chemical Society, 5403–5411;ISSN: 0003-2700; https://doi.org/10.1021/acs.analchem.0c04651 (2023) (Apr. 2021)
76. SHEPPARD, D. M. W. *et al.*; en; *Scientific Reports* **7,** 42228;ISSN: 2045-2322; https://www.nature.com/articles/srep42228 (2023) (Feb. 2017)
77. NEIL, S. R. T. *et al.*; en; *Lab on a Chip* **11,** 3953;ISSN: 1473-0197, 1473-0189; http://xlink.rsc.org/?DOI=c1lc20854c (2023) (2011)

78. VAHALA, K. J.; en; *Nature* **424**;Number: 6950 Publisher: Nature Publishing Group, 839–846;ISSN: 1476-4687; https://www.nature.com/articles/nature01939 (2023) (Aug. 2003)
79. REBER, M. A. R. *et al.*; en; *Optica* **3**;arXiv:1511.02973 [physics], 311;ISSN: 2334-2536; http://arxiv.org/abs/1511.02973 (2023) (Mar. 2016)
80. SCHAWLOW, A. L. *et al.*; *Physical Review* **112**;Publisher: American Physical Society, 1940–1949; https://link.aps.org/doi/10.1103/PhysRev.112.1940 (2024) (Dec. 1958)
81. BARLOW, T. M. *et al.*; en; *Journal of Modern Optics* **62,** S11–S20;ISSN: 0950-0340, 1362-3044; http://www.tandfonline.com/doi/full/10.1080/09500340.2014.992992 (2023) (Dec. 2015)
82. PHILBIN, T. G.; en; *New Journal of Physics* **12,** 123008;ISSN: 1367-2630; https://dx.doi.org/10.1088/1367-2630/12/12/123008 (2023) (Dec. 2010)
83. WELZEL, S. *et al.*; *Journal of Applied Physics* **104,** 093115;ISSN: 0021-8979; https://doi.org/10.1063/1.3008014 (2023) (Nov. 2008)
84. PAUL, J. B. *et al.*; EN; *Applied Optics* **40**;Publisher: Optica Publishing Group, 4904–4910;ISSN: 2155-3165; https://opg.optica.org/ao/abstract.cfm?uri=ao-40-27-4904 (2023) (Sept. 2001)
85. SCHERER, J. J. *et al.*; *Chemical Reviews* **97**;Publisher: American Chemical Society, 25–52;ISSN: 0009-2665; https://doi.org/10.1021/cr930048d (2023) (Feb. 1997)
86. FIEDLER, S. E. *et al.*; en; *Chemical Physics Letters* **371,** 284–294;ISSN: 00092614; https://linkinghub.elsevier.com/retrieve/pii/S000926140300263X (2023) (Apr. 2003)
87. MAEDA, K. *et al.*; en; *Proceedings of the National Academy of Sciences* **109,** 4774–4779;ISSN: 0027-8424, 1091-6490; https://pnas.org/doi/full/10.1073/pnas.1118959109 (2023) (Mar. 2012)
88. HENBEST, K. B. *et al.*; *Proceedings of the National Academy of Sciences* **105**;Publisher: Proceedings of the National Academy of Sciences, 14395–14399; https://www.pnas.org/doi/10.1073/pnas.0803620105 (2023) (Sept. 2008)
89. JEAN-CHARLES GUYOMARC'H *et al.*; en; Publisher: European Communities; http://rgdoi.net/10.13140/RG.2.2.10912.69125 (2023) (2009)
90. ZUCKERBROT, Y. *et al.*; *Ibis* **122,** 1–14 (Apr. 2008)
91. BAIRLEIN, F.; en; *Science* **354,** 547–548;ISSN: 0036-8075, 1095-9203; https://www.science.org/doi/10.1126/science.aah6647 (2023) (Nov. 2016)

92. NADAL, J. *et al.*; en; *Science of The Total Environment* **808,** 152173;ISSN: 00489697; https://linkinghub.elsevier.com/retrieve/pii/S0048969721072491 (2023) (Feb. 2022)
93. DEL PRIORE, L. *et al.*; en; *PLOS ONE* **15**;(ed FUNG, J. C.) e0240245;ISSN: 1932-6203; https://dx.plos.org/10.1371/journal.pone.0240245 (2023) (Oct. 2020)
94. PRUM, R. O. *et al.*; en; *Nature* **526,** 569–573;ISSN: 1476-4687; https://www.nature.com/articles/nature15697 (2023) (Oct. 2015)
95. LANGEBRAKE, C. *et al.*; en; *bioRxiv*; http://biorxiv.org/lookup/doi/10.1101/2023.03.25.534197 (2023) (Mar. 2023)
96. WILTSCHKO, R. *et al.*; en; *Behavioral Ecology and Sociobiology* **24,** 163–173;ISSN: 1432-0762; https://doi.org/10.1007/BF00292099 (2023) (Mar. 1989)
97. WALCOTT, C.; en; *Integrative and Comparative Biology* **45,** 574–581;ISSN: 1540-7063, 1557-7023; https://academic.oup.com/icb/article-lookup/doi/10.1093/icb/45.3.574 (2023) (June 2005)
98. HANIĆ, M. *et al.*; en; *The European Physical Journal D* **76,** 198;ISSN: 1434-6079; https://doi.org/10.1140/epjd/s10053-022-00520-5 (2023) (Oct. 2022)
99. WILTSCHKO, R. *et al.*; en; *Science* **214,** 343–345;ISSN: 0036-8075, 1095-9203; https://www.science.org/doi/10.1126/science.7280697 (2023) (Oct. 1981)
100. LI, S. *et al.*; *RSC Advances* **8,** 25941–25948;ISSN: 2046-2069; https://www.ncbi.nlm.nih.gov/pmc/articles/PMC9082899/ (2023)
101. MAEDA, K. *et al.*; en; *Journal of the American Chemical Society* **133,** 17807–17815;ISSN: 0002-7863, 1520-5126; https://pubs.acs.org/doi/10.1021/ja206783t (2023) (Nov. 2011)
102. DÉJEAN, V. *et al.*; en; *Chemical Science* **11,** 7772–7781;ISSN: 2041-6520, 2041-6539; http://xlink.rsc.org/?DOI=D0SC01986K (2023) (2020)
103. BERNTSSON, O. *et al.*; *Science Advances* **5,** eaaw1531;ISSN: 2375-2548; https://www.ncbi.nlm.nih.gov/pmc/articles/PMC6636987/ (2023) (July 2019)
104. NOHR, D. *et al.*; *Biophysical Journal* **111,** 301–311;ISSN: 0006-3495; https://www.ncbi.nlm.nih.gov/pmc/articles/PMC4968396/ (2023) (July 2016)
105. ENGEL, N. *et al.*; en; *Physical Chemistry Chemical Physics* **19,** 14248–14255;ISSN: 1463-9076, 1463-9084; http://xlink.rsc.org/?DOI=C7CP01288H (2023) (2017)

106. ATANASOV, M. *et al.*; en;
The Journal of Physical Chemistry A **111,** 9145–9163;ISSN: 1089-5639, 1520-5215;
https://pubs.acs.org/doi/10.1021/jp0731912 (2023) (Sept. 2007)
107. REINHARD, M. *et al.*; en; *Nature Communications* **14,** 2443;ISSN: 2041-1723;
https://www.nature.com/articles/s41467-023-37922-x (2023) (May 2023)
108. REINHARD, M. *et al.*; en; *Journal of the American Chemical Society* **139,**
7335–7347;ISSN: 0002-7863, 1520-5126;
https://pubs.acs.org/doi/10.1021/jacs.7b02769 (2023) (May 2017)
109. OJEDA, J. *et al.*; en; *Physical Chemistry Chemical Physics* **19,** 17052–17062;ISSN:
1463-9076, 1463-9084; http://xlink.rsc.org/?DOI=C7CP03337K (2023)
(2017)
110. ZHANG, W. *et al.*; en; *Journal of the American Chemical Society* **134,**
2581–2588;ISSN: 0002-7863, 1520-5126;
https://pubs.acs.org/doi/10.1021/ja207306t (2023) (Feb. 2012)
111. O'REILLY, J. E.;
Biochimica et Biophysica Acta (BBA) - Bioenergetics **292,** 509–515;ISSN: 0005-2728;
https://www.sciencedirect.com/science/article/pii/0005272873900017
(2023) (Apr. 1973)
112. OPRIAN, D. D. *et al.*; en;
Journal of Biological Chemistry **257,** 8935–8944;ISSN: 00219258;
https://linkinghub.elsevier.com/retrieve/pii/S0021925818342236
(2023) (Aug. 1982)
113. ROSS, M. *et al.*; en;
The Journal of Physical Chemistry B **122,** 5075–5086;ISSN: 1520-6106, 1520-5207;
https://pubs.acs.org/doi/10.1021/acs.jpcb.7b12532 (2023) (May 2018)
114. REINHARD, M. *et al.*; en; *Structural Dynamics* **1,** 024901;ISSN: 2329-7778;
https://pubs.aip.org/sdy/article/1/2/024901/365339/Photooxidation-
and-photoaquation-of-iron (2023) (Mar. 2014)
115. VAZ DA CRUZ, V. *et al.*; en; *Physical Chemistry Chemical Physics* **24,**
27819–27826;ISSN: 1463-9076, 1463-9084;
http://xlink.rsc.org/?DOI=D2CP04084K (2023) (2022)
116. SMITH, D. A. *et al.*; en; *Journal of the American Chemical Society* **106,**
3053–3054;ISSN: 0002-7863, 1520-5126;
https://pubs.acs.org/doi/abs/10.1021/ja00322a062 (2023) (May 1984)
117. MURTON, P. D. F. *et al.*; *In Preperation* (July 2022)
118. WATERHOUSE, A. *et al.*; en;
Nucleic Acids Research **46,** W296–W303;ISSN: 0305-1048, 1362-4962;
https://academic.oup.com/nar/article/46/W1/W296/5000024 (2023)
(July 2018)

119. BIENERT, S. *et al.*; en; *Nucleic Acids Research* **45,** D313–D319;ISSN: 0305-1048, 1362-4962; https://academic.oup.com/nar/article-lookup/doi/10.1093/nar/gkw1132 (2023) (Jan. 2017)
120. GUEX, N. *et al.*; en; *ELECTROPHORESIS* **30**;ISSN: 0173-0835, 1522-2683; https://analyticalsciencejournals.onlinelibrary.wiley.com/doi/10.1002/elps.200900140 (2023) (June 2009)
121. STUDER, G. *et al.*; en; *Bioinformatics* **36**;(ed ELOFSSON, A.) 1765–1771;ISSN: 1367-4803, 1367-4811; https://academic.oup.com/bioinformatics/article/36/6/1765/5614424 (2023) (Mar. 2020)
122. BERTONI, M. *et al.*; en; *Scientific Reports* **7,** 10480;ISSN: 2045-2322; https://www.nature.com/articles/s41598-017-09654-8 (2023) (Sept. 2017)
123. KATTNIG, D. R. *et al.*; en; *Nature Chemistry* **8,** 384–391;ISSN: 1755-4330, 1755-4349; https://www.nature.com/articles/nchem.2447 (2023) (Apr. 2016)
124. MURAKAMI, M. *et al.*; en; *The Journal of Physical Chemistry A* **109,** 5793–5800;ISSN: 1089-5639, 1520-5215; https://pubs.acs.org/doi/10.1021/jp0519722 (2023) (July 2005)
125. STEINER, U. E. *et al.*; en; *Chemical Reviews* **89,** 51–147;ISSN: 0009-2665, 1520-6890; https://pubs.acs.org/doi/abs/10.1021/cr00091a003 (2023) (Jan. 1989)
126. OTSUKA, H. *et al.*; en; *Biochemistry* **59,** 3615–3625;ISSN: 0006-2960, 1520-4995; https://pubs.acs.org/doi/10.1021/acs.biochem.0c00495 (2023) (Sept. 2020)
127. YAKUNIN, I. N. *et al.*; en; *Russian Journal of Physical Chemistry B* **4,** 210–216;ISSN: 1990-7931, 1990-7923; http://link.springer.com/10.1134/S1990793110020053 (2023) (Apr. 2010)
128. LETUTA, A. S. *et al.*; en; *Doklady Physical Chemistry* **463,** 179–181;ISSN: 0012-5016, 1608-3121; http://link.springer.com/10.1134/S0012501615080059 (2023) (Aug. 2015)
129. KATTNIG, D. R. *et al.*; en; *Scientific Reports* **7,** 11640;ISSN: 2045-2322; https://www.nature.com/articles/s41598-017-09914-7 (2023) (Sept. 2017)
130. LUIS, A.; en; *Physical Review A* **67,** 062113;ISSN: 1050-2947, 1094-1622; https://link.aps.org/doi/10.1103/PhysRevA.67.062113 (2023) (June 2003)
131. BABCOCK, N. S. *et al.*; en; *JACS Au* **1,** 2033–2046;ISSN: 2691-3704, 2691-3704; https://pubs.acs.org/doi/10.1021/jacsau.1c00332 (2023) (Nov. 2021)

132. PLAYER, T. C. *et al.*; en; *Scientific Reports* **11,** 9615;ISSN: 2045-2322; https://www.nature.com/articles/s41598-021-88871-8 (2023) (May 2021)
133. KATTNIG, D. R. *et al.*; en; *New Journal of Physics* **18,** 063007;ISSN: 1367-2630; https://iopscience.iop.org/article/10.1088/1367-2630/18/6/063007 (2023) (June 2016)
134. BERDNIKOV, V. M. *et al.*; en; *Journal of Structural Chemistry* **19,** 319–321;ISSN: 0022-4766, 1573-8779; http://link.springer.com/10.1007/BF00746977 (2023) (1978)
135. WONG, S. Y. *et al.*; *Journal of The Royal Society Interface* **18**;Publisher: Royal Society, 20210601; https://royalsocietypublishing.org/doi/10.1098/rsif.2021.0601 (2023) (Nov. 2021)
136. WANG, M. *et al.*; en; *Angewandte Chemie International Edition* **48**;_eprint: https://onlinelibrary.wiley.com/doi/pdf/10.1002/anie.200900827, 4232–4234;ISSN: 1521-3773; https://onlinelibrary.wiley.com/doi/abs/10.1002/anie.200900827 (2023) (2009)
137. EINHOLZ, C. *et al.*; *Archives of Biochemistry and Biophysics* **700,** 108787;ISSN: 0003-9861; https://www.sciencedirect.com/science/article/pii/S0003986121000370 (2023) (Mar. 2021)
138. OLDEMEYER, S. *et al.*; en; *Biophysical Journal* **117,** 490–499;ISSN: 00063495; https://linkinghub.elsevier.com/retrieve/pii/S0006349519305351 (2023) (Aug. 2019)
139. CZARNA, A. *et al.*; en; *Cell* **153,** 1394–1405;ISSN: 00928674; https://linkinghub.elsevier.com/retrieve/pii/S009286741300576X (2023) (June 2013)
140. PAULUS, B. *et al.*; en; *The FEBS Journal* **282**;_eprint: https://onlinelibrary.wiley.com/doi/pdf/10.1111/febs.13299, 3175–3189;ISSN: 1742-4658; https://onlinelibrary.wiley.com/doi/abs/10.1111/febs.13299 (2023) (2015)
141. BISKUP, T. *et al.*; *Angewandte Chemie International Edition* **48**;_eprint: https://onlinelibrary.wiley.com/doi/pdf/10.1002/anie.200803102, 404–407;ISSN: 1521-3773; https://onlinelibrary.wiley.com/doi/abs/10.1002/anie.200803102 (2023) (2009)
142. BISKUP, T. *et al.*; English; *Journal of Biological Chemistry* **288**;Publisher: Elsevier, 9249–9260;ISSN: 0021-9258, 1083-351X;

https://www.jbc.org/article/S0021-9258(19)35084-7/abstract (2023) (Mar. 2013)

143. NOHR, D. *et al.*; en; *Angewandte Chemie International Edition* **56**;_eprint: https://onlinelibrary.wiley.com/doi/pdf/10.1002/anie.201700389, 8550–8554;ISSN: 1521-3773; https://onlinelibrary.wiley.com/doi/abs/10.1002/anie.201700389 (2023) (2017)
144. THURNAUER, M. *et al.*; *Chemical Physics Letters* **76,** 557–561;ISSN: 0009-2614; https://www.sciencedirect.com/science/article/pii/0009261480806671 (2024) (Dec. 1980)
145. THURNAUER, M. *et al.*; en; *FEBS Letters* **100,** 309–312;ISSN: 0014-5793, 1873-3468; https://febs.onlinelibrary.wiley.com/doi/10.1016/0014-5793%2879%2980358-0 (2023) (Apr. 1979)
146. TAN, J. *et al.*; *Chemical Physics Letters* **219,** 283–290;ISSN: 0009-2614; https://www.sciencedirect.com/science/article/pii/0009261494870594 (2023) (Mar. 1994)
147. BITTL, R. *et al.*; en; *Biochimica et Biophysica Acta (BBA) - Bioenergetics* **1507,** 194–211;ISSN: 00052728; https://linkinghub.elsevier.com/retrieve/pii/S0005272801002109 (2023) (Oct. 2001)
148. HUNTER, D. A. *et al.*; en; in *Techniques and New Developments in Photosynthesis Research*; (eds BARBER, J. *et al.*) 297–300; (Springer US, Boston, MA, 1989); ISBN: 978-1-4684-8571-4; https://doi.org/10.1007/978-1-4684-8571-4_41 (2023)
149. LIU, Z. *et al.*; *Proceedings of the National Academy of Sciences* **110**;Publisher: Proceedings of the National Academy of Sciences, 12966–12971; https://www.pnas.org/doi/full/10.1073/pnas.1311073110 (2023) (Aug. 2013)
150. OZTURK, N. *et al.*; en-US; *Journal of Biological Chemistry* **283**;Publisher: Elsevier, 3256–3263;ISSN: 0021-9258; https://www.sciencedirect.com/science/article/pii/S0021925820697885 (2023) (Feb. 2008)
151. BERNDT, A. *et al.*; en; *Journal of Biological Chemistry* **282,** 13011–13021;ISSN: 00219258; https://linkinghub.elsevier.com/retrieve/pii/S0021925818950751 (2023) (Apr. 2007)
152. MÜLLER, P. *et al.*; en; *Chemical Science* **9,** 1200–1212;ISSN: 2041-6520, 2041-6539; http://xlink.rsc.org/?DOI=C7SC03969G (2023) (2018)

153. MÜLLER, P. *et al.*; en; *Journal of Biological Chemistry* **286,** 21033–21040;ISSN: 00219258; https://linkinghub.elsevier.com/retrieve/pii/S0021925819489850 (2023) (June 2011)
154. ROMERO, E. *et al.*; *Chemical Reviews* **118**;Publisher: American Chemical Society, 1742–1769;ISSN: 0009-2665; https://doi.org/10.1021/acs.chemrev.7b00650 (2023) (Feb. 2018)
155. CHAIYEN, P. *et al.*; eng; *Trends in Biochemical Sciences* **37,** 373–380;ISSN: 0968-0004 (Sept. 2012)
156. PLAYER, T. C. *et al.*; en; *The Journal of Chemical Physics* **151,** 225101;ISSN: 0021-9606, 1089-7690; https://pubs.aip.org/jcp/article/151/22/225101/198329/Viability-of-superoxide-containing-radical-pairs (2023) (Dec. 2019)
157. FREDERIKSEN, A. *et al.*; *ACS Omega* **8,** 26425–26436;ISSN: 2470-1343; https://www.ncbi.nlm.nih.gov/pmc/articles/PMC10373462/ (2023) (July 2023)
158. GÖRTEMAKER, K. *et al.*; eng; *Cells* **11,** 2043;ISSN: 2073-4409 (June 2022)
159. YEE, C. *et al.*; *Frontiers in Molecular Neuroscience* **16**;ISSN: 1662-5099; https://www.frontiersin.org/articles/10.3389/fnmol.2023.1107025 (2023) (2023)
160. WILTSCHKO, R. *et al.*; *Journal of The Royal Society Interface* **16**;Publisher: Royal Society, 20190295; https://royalsocietypublishing.org/doi/10.1098/rsif.2019.0295 (2023) (Sept. 2019)
161. LACOMBAT, F. *et al.*; en; *Physical Chemistry Chemical Physics* **20**;Publisher: The Royal Society of Chemistry, 25446–25457;ISSN: 1463-9084; https://pubs.rsc.org/en/content/articlelanding/2018/cp/c8cp04548h (2023) (Oct. 2018)
162. ANTILL, L. M. *et al.*; en; *The Journal of Physical Chemistry Letters* **9,** 2691–2696;ISSN: 1948-7185, 1948-7185; https://pubs.acs.org/doi/10.1021/acs.jpclett.8b01088 (2023) (May 2018)
163. HAYWARD, H.; Part II Thesis;(University of Oxford, June 2023)
164. HOLUB, D. *et al.*; en; *Chemical Science* **9,** 1259–1272;ISSN: 2041-6520, 2041-6539; http://xlink.rsc.org/?DOI=C7SC03386A (2023) (2018)
165. SAHA, M. *et al.*; en; *Journal of Nanostructure in Chemistry* **4,** 102;ISSN: 2193-8865; https://doi.org/10.1007/s40097-014-0102-5 (2023) (Apr. 2014)

166. HARRIMAN, A.; *The Journal of Physical Chemistry* **91**;Publisher: American Chemical Society, 6102–6104;ISSN: 0022-3654; https://doi.org/10.1021/j100308a011 (2023) (Nov. 1987)
167. NATHANAEL, J. G. *et al.*; en; *ChemBioChem* **19**;_eprint: https://onlinelibrary.wiley.com/doi/pdf/10.1002/cbic.201800098, 922–926;ISSN: 1439-7633; https://onlinelibrary.wiley.com/doi/abs/10.1002/cbic.201800098 (2023) (2018)
168. SAXENA, C. *et al.*; *The Journal of Physical Chemistry B* **108**;Publisher: American Chemical Society, 18026–18033;ISSN: 1520-6106; https://doi.org/10.1021/jp048376c (2023) (Nov. 2004)
169. ING, N. L. *et al.*; *The Journal of Physical Chemistry B* **122**;Publisher: American Chemical Society, 10403–10423;ISSN: 1520-6106; https://doi.org/10.1021/acs.jpcb.8b07431 (2023) (Nov. 2018)
170. KURNIKOV, I. V. *et al.*; en; *The Journal of Chemical Physics* **105,** 9561–9573;ISSN: 0021-9606, 1089-7690; https://pubs.aip.org/jcp/article/105/21/9561/478438/Ab-initio-based-effective-Hamiltonians-for-long (2023) (Dec. 1996)
171. HECK, A. *et al.*; *The Journal of Physical Chemistry B* **118**;Publisher: American Chemical Society, 4261–4272;ISSN: 1520-6106; https://doi.org/10.1021/jp408907g (2023) (Apr. 2014)
172. GILLET, N. *et al.*; *Journal of Chemical Theory and Computation* **12**;Publisher: American Chemical Society, 4793–4805;ISSN: 1549-9618; https://doi.org/10.1021/acs.jctc.6b00564 (2023) (Oct. 2016)
173. BLUMBERGER, J.; *Chemical Reviews* **115**;Publisher: American Chemical Society, 11191–11238;ISSN: 0009-2665; https://doi.org/10.1021/acs.chemrev.5b00298 (2023) (Oct. 2015)
174. LANGENBACHER, T. *et al.*; en; *Journal of the American Chemical Society* **131,** 14274–14280;ISSN: 0002-7863, 1520-5126; https://pubs.acs.org/doi/10.1021/ja901628y (2023) (Oct. 2009)
175. MIURA, T. *et al.*; en; *The Journal of Physical Chemistry B* **107,** 6474–6478;ISSN: 1520-6106, 1520-5207; https://pubs.acs.org/doi/10.1021/jp034068n (2023) (July 2003)
176. SOLOV'YOV, I. A. *et al.*; en; *Biophysical Journal* **92,** 2711–2726;ISSN: 00063495; https://linkinghub.elsevier.com/retrieve/pii/S0006349507710779 (2023) (Apr. 2007)
177. NIEL, S.; DPhil Thesis;(University of Oxford, Oxford, 2013)
178. SHEPPARD, D.; DPhil Thesis;(University of Oxford, Oxford, 2016)
179. ZOLLITSCH, T.; DPhil Thesis;(University of Oxford, Oxford, 2018)

180. GOLESWORTHY, M.; DPhil Thesis;(University of Oxford, Oxford, 2021)
181. VAN STOKKUM, I. H. *et al.*; en;
Biochimica et Biophysica Acta (BBA) - Bioenergetics **1657,** 82–104;ISSN: 00052728;
https://linkinghub.elsevier.com/retrieve/pii/S0005272804001094
(2023) (July 2004)
182. WEISSTEIN, E.; https://mathworld.wolfram.com/Erf.html
183. GRAJEK, H. *et al.*; en; *Biochimica et Biophysica Acta (BBA) - General Subjects* **801,**
456–460;ISSN: 03044165;
https://linkinghub.elsevier.com/retrieve/pii/0304416584901521 (2023)
(Oct. 1984)
184. GRAJEK, H. *et al.*; en;
Photochemistry and Photobiology **55,** 381–387;ISSN: 0031-8655, 1751-1097;
https://onlinelibrary.wiley.com/doi/10.1111/j.1751-1097.1992.tb04251.x (2023) (Mar. 1992)
185. GRAJEK, H. *et al.*; en; *Biochimica et Biophysica Acta (BBA) - General Subjects* **881,**
241–247;ISSN: 03044165;
https://linkinghub.elsevier.com/retrieve/pii/0304416586900103 (2023)
(Apr. 1986)
186. NEIL, S. R. T. *et al.*; *The Journal of Physical Chemistry B* **118**;Publisher: American Chemical Society, 4177–4184;ISSN: 1520-6106;
https://doi.org/10.1021/jp500732u (2024) (Apr. 2014)
187. PIMENTA, F. M. *et al.*; en;
Photochemistry and Photobiology **89,** 1116–1126;ISSN: 00318655;
https://onlinelibrary.wiley.com/doi/10.1111/php.12111 (2023)
(Sept. 2013)
188. SAKAI, M. *et al.*; en; *Journal of Molecular Structure* **379,** 9–18;ISSN: 00222860;
https://linkinghub.elsevier.com/retrieve/pii/0022286095091769 (2023)
(June 1996)
189. SENGUPTA, A. *et al.*; en; *Journal of Photochemistry and Photobiology A: Chemistry* **221,** 105–112;ISSN: 10106030;
https://linkinghub.elsevier.com/retrieve/pii/S1010603011001894
(2023) (June 2011)
190. SERAJ, Z. *et al.*;
International Journal of Biological Macromolecules **146,** 705–715;ISSN: 0141-8130;
https://www.sciencedirect.com/science/article/pii/S0141813019370229
(2024) (Mar. 2020)
191. KONOWALCZYK, M.; DPhil Thesis;(University of Oxford, Oxford, 2020)

192. EVANS, E. W. *et al.*; en; *Interface Focus* **3,** 20130037;ISSN: 2042-8898, 2042-8901; https://royalsocietypublishing.org/doi/10.1098/rsfs.2013.0037 (2023) (Oct. 2013)
193. MANSOORABADI, S. O. *et al.*; en; *The Journal of Organic Chemistry* **72,** 6329–6342;ISSN: 0022-3263, 1520-6904; https://pubs.acs.org/doi/10.1021/jo0703092 (2023) (Aug. 2007)
194. SILVETTI, T. *et al.*; en; in *Egg Innovations and Strategies for Improvements* 233–242; (Elsevier, 2017); ISBN: 978-0-12-800879-9; https://linkinghub.elsevier.com/retrieve/pii/B9780128008799000226 (2024)
195. THEIS, K. *et al.*; https://proteopedia.org/wiki/index.php/Hen_Egg-White_(HEW)_Lysozyme
196. HORE, P. J. *et al.*; en; *Biochemistry* **22,** 1906–1911;ISSN: 0006-2960, 1520-4995; https://pubs.acs.org/doi/abs/10.1021/bi00277a026 (2023) (Apr. 1983)
197. BRUGH, A. M. *et al.*; en; *Chemical Science* **11,** 6268–6274;ISSN: 2041-6520, 2041-6539; http://xlink.rsc.org/?DOI=D0SC02691C (2023) (2020)
198. MOROZOVA, O. B. *et al.*; en; *Molecular Physics* **100,** 1187–1195;ISSN: 0026-8976, 1362-3028; http://www.tandfonline.com/doi/abs/10.1080/00268970110109970 (2023) (Apr. 2002)
199. STOB, S. *et al.*; en; *Journal of the American Chemical Society* **111,** 7036–7042;ISSN: 0002-7863, 1520-5126; https://pubs.acs.org/doi/abs/10.1021/ja00200a021 (2023) (Aug. 1989)
200. VAN SCHAGEN, C. G. *et al.*; en; *Biochemistry* **21,** 402–407;ISSN: 0006-2960, 1520-4995; https://pubs.acs.org/doi/abs/10.1021/bi00531a030 (2023) (Jan. 1982)
201. ZHUKOV, I. V. *et al.*; English; *Magnetic Resonance* **2**;Publisher: Copernicus GmbH, 139–148; https://mr.copernicus.org/articles/2/139/2021/ (2023) (Apr. 2021)
202. ZHANG, Y. *et al.*; en; *International Journal of Quantum Chemistry* **115,** 1327–1341;ISSN: 00207608; https://onlinelibrary.wiley.com/doi/10.1002/qua.24943 (2023) (Oct. 2015)
203. MAEDA, K. *et al.*; en; *Molecular Physics* **104,** 1779–1788;ISSN: 0026-8976, 1362-3028; http://www.tandfonline.com/doi/abs/10.1080/14767050600588106 (2023) (May 2006)

204. KODIS, G. *et al.*; en;
Journal of Physical Organic Chemistry **17,** 724–734;ISSN: 0894-3230, 1099-1395;
https://onlinelibrary.wiley.com/doi/10.1002/poc.787 (2023)
(Sept. 2004)
205. MAEDA, K. *et al.*; en;
Chemical Communications **47,** 6563;ISSN: 1359-7345, 1364-548X;
http://xlink.rsc.org/?DOI=c1cc11625h (2023) (2011)
206. MAEDA, K. *et al.*; en;
The Journal of Chemical Physics **139,** 234309;ISSN: 0021-9606, 1089-7690;
https://pubs.aip.org/jcp/article/139/23/234309/152440/Spin-selective-recombination-reactions-of-radical (2023) (Dec. 2013)
207. LEWIS, A. M. *et al.*; *The Journal of Chemical Physics* **141,** 044111;ISSN: 0021-9606;
https://doi.org/10.1063/1.4890659 (2023) (July 2014)
208. LEWIS, A. M. *et al.*; *The Journal of Chemical Physics* **145,** 244101;ISSN: 0021-9606;
https://doi.org/10.1063/1.4972277 (2023) (Dec. 2016)
209. FAY, T. P. *et al.*; en;
The Journal of Chemical Physics **154,** 084121;ISSN: 0021-9606, 1089-7690;
https://pubs.aip.org/jcp/article/154/8/084121/76322/Spin-relaxation-in-radical-pairs-from-the (2023) (Feb. 2021)
210. REDMAN, A. *et al.*; *In Preperation*
211. TANIGUCHI, M. *et al.*; en; *Journal of Photochemistry and Photobiology C: Photochemistry Reviews* **46,** 100401;ISSN: 13895567;
https://linkinghub.elsevier.com/retrieve/pii/S1389556720300691 (2023) (Mar. 2021)
212. ZHUANG, B. *et al.*; en; *Proceedings of the National Academy of Sciences* **119,** e2118924119;ISSN: 0027-8424, 1091-6490;
https://pnas.org/doi/full/10.1073/pnas.2118924119 (2023) (Feb. 2022)
213. NICULESCU, A.-G. *et al.*; en;
International Journal of Molecular Sciences **22,** 2011;ISSN: 1422-0067;
https://www.mdpi.com/1422-0067/22/4/2011 (2023) (Feb. 2021)
214. BHATIA, S. N. *et al.*; en; *Nature Biotechnology* **32**;Number: 8 Publisher: Nature Publishing Group, 760–772;ISSN: 1546-1696;
https://www.nature.com/articles/nbt.2989 (2023) (Aug. 2014)
215. ZHU, P. *et al.*; en; *Lab on a Chip* **17,** 34–75;ISSN: 1473-0197, 1473-0189;
http://xlink.rsc.org/?DOI=C6LC01018K (2023) (2017)
216. SANFILIPPO, J. E. *et al.*; en; *Nature Microbiology* **4,** 1274–1281;ISSN: 2058-5276;
https://www.nature.com/articles/s41564-019-0455-0 (2023) (May 2019)

217. DITTRICH, P. S. *et al.*; en; *Nature Reviews Drug Discovery* **5,** 210–218;ISSN: 1474-1776, 1474-1784; https://www.nature.com/articles/nrd1985 (2023) (Mar. 2006)
218. BAROUD, C. N. *et al.*; en; *Lab on a Chip* **10,** 2032;ISSN: 1473-0197, 1473-0189; http://xlink.rsc.org/?DOI=c001191f (2023) (2010)
219. LEUNG, C. M. *et al.*; en; *Nature Reviews Methods Primers* **2**;Number: 1 Publisher: Nature Publishing Group, 1–29;ISSN: 2662-8449; https://www.nature.com/articles/s43586-022-00118-6 (2023) (May 2022)
220. NELSON, C. M. *et al.*; en; *Development,* dev.154823;ISSN: 1477-9129, 0950-1991; https://journals.biologists.com/dev/article/doi/10.1242/dev.154823/264427/Microfluidic-chest-cavities-reveal-that-transmural (2023) (Jan. 2017)
221. BRUUS, H.; *Oxford master series in physics* **18**; OCLC: ocn156817008; ISBN: 978-0-19-923508-7 978-0-19-923509-4; (Oxford University Press, Oxford ; New York, 2008)
222. BUSH, J. Lecture Notes; (MIT, 2013)
223. VAN DER WAALS, J. D.; en; *Journal of Statistical Physics* **20,** 200–244;ISSN: 0022-4715, 1572-9613; http://link.springer.com/10.1007/BF01011514 (2023) (Feb. 1979)
224. KHATAVKAR, V. *et al.*; en; *Chemical Engineering Science* **61,** 2364–2378;ISSN: 00092509; https://linkinghub.elsevier.com/retrieve/pii/S0009250905008043 (2023) (Apr. 2006)
225. QIAN, T. *et al.*; en; *Physical Review E* **68,** 016306;ISSN: 1063-651X, 1095-3787; https://link.aps.org/doi/10.1103/PhysRevE.68.016306 (2023) (July 2003)
226. DAS, A. *et al.*; en; *Journal of Molecular Liquids* **277,** 217–232;ISSN: 01677322; https://linkinghub.elsevier.com/retrieve/pii/S0167732218357428 (2023) (Mar. 2019)
227. CAHN, J. W. *et al.*; *The Journal of Chemical Physics* **28,** 258–267;ISSN: 0021-9606; https://doi.org/10.1063/1.1744102 (2023) (Aug. 2004)
228. WU, H.; en; *Electronic Research Archive* **30**;Cc_license_type: cc_by Number: era-30-08-143 Primary_atype: Electronic Research Archive Subject_term: Review Subject_term_id: Review, 2788–2832;ISSN: 2688-1594; http://www.aimspress.com/rticle/doi/10.3934/era.2022143 (2023) (2022)
229. ANDERSON, D. M. *et al.*; *Annual Review of Fluid Mechanics* **30**;_eprint: https://doi.org/10.1146/annurev.fluid.30.1.139, 139–165; https://doi.org/10.1146/annurev.fluid.30.1.139 (2023) (1998)
230. LI, J.; DPhil Thesis;(Oxford, 2013)

231. Evans, E. W. *et al.*; en;
The Journal of Chemical Physics **145,** 085101;ISSN: 0021-9606, 1089-7690;
https://pubs.aip.org/jcp/article/145/8/085101/561871/Sub-millitesla-magnetic-field-effects-on-the (2023) (Aug. 2016)
232. (ed of Medicine (U.S.), I.) ; ISBN: 978-0-309-06949-6 978-0-309-06935-9;
(National Academy Press, Washington, D.C, 2000)
233. Lee, A. A. *et al.*;
Journal of The Royal Society Interface **11**;Publisher: Royal Society, 20131063;
https://royalsocietypublishing.org/doi/10.1098/rsif.2013.1063 (2023) (June 2014)
234. Evans, E. W.; en; DPhil Thesis;(University of Oxford, 2016)
235. Déjean, V.; DPhil Thesis;(University of Oxford, 2021)
236. Chamberlayne, C. F. *et al.*; en;
The Journal of Chemical Physics **152,** 184702;ISSN: 0021-9606, 1089-7690;
https://pubs.aip.org/aip/jcp/article/1061917 (2023) (May 2020)
237. Ma, S. *et al.*; en; *Lab Chip* **14,** 3611–3620;ISSN: 1473-0197, 1473-0189;
http://xlink.rsc.org/?DOI=C4LC00671B (2023) (2014)
238. Chen, C. *et al.*; en; *Micromachines* **9**;Number: 4 Publisher: Multidisciplinary Digital Publishing Institute, 160;ISSN: 2072-666X;
https://www.mdpi.com/2072-666X/9/4/160 (2023) (Apr. 2018)
239. Grigoriev, R. O. *et al.*; en; *Lab on a Chip* **6,** 1369;ISSN: 1473-0197, 1473-0189;
http://xlink.rsc.org/?DOI=b607003e (2023) (2006)
240. Belousov, K. I. *et al.*; en; *Scientific Reports* **11,** 8797;ISSN: 2045-2322;
https://www.nature.com/articles/s41598-021-88174-y (2023) (Apr. 2021)
241. Werner, H.-J. *et al.*; en;
The Journal of Chemical Physics **67,** 646–663;ISSN: 0021-9606, 1089-7690;
https://pubs.aip.org/jcp/article/67/2/646/217031/Theory-of-the-magnetic-field-modulated-geminate (2023) (July 1977)
242. Evans, E. W. *et al.*; en; *Physical Chemistry Chemical Physics* **17,** 18456–18463;ISSN: 1463-9076, 1463-9084; http://xlink.rsc.org/?DOI=C5CP00723B (2023) (2015)
243. Larkin, M. *et al.*; *Bioinformatics* **23,** 2947–2948;ISSN: 1367-4803;
https://doi.org/10.1093/bioinformatics/btm404 (2023) (Nov. 2007)
244. Rose, R. *et al.*; *Bioinformatics* **35,** 1963–1965;ISSN: 1367-4803;
https://doi.org/10.1093/bioinformatics/bty901 (2023) (June 2019)
245. Braver, Y. *et al.*; en; *Chemical Physics* **525,** 110403;ISSN: 03010104;
https://linkinghub.elsevier.com/retrieve/pii/S030101041930271X (2023) (Sept. 2019)

246. HISCOCK, H. G. *et al.*; en;
Quarterly Reviews of Biophysics **52,** e9;ISSN: 0033-5835, 1469-8994;
https://www.cambridge.org/core/product/identifier/S0033583519000076/type/journal_article (2023) (2019)
247. ANTILL, L. M.; https://radicalpy.readthedocs.io/en/latest/ (2024)
248. SOLOV'YOV, I. A. *et al.*; en;
The Journal of Physical Chemistry B **116,** 1089–1099;ISSN: 1520-6106, 1520-5207;
https://pubs.acs.org/doi/10.1021/jp209508y (2023) (Jan. 2012)

Appendix A

Appendices

A.1 Appendix 1

Chapter 4 supplementary material.

A.1.1 *Er*Cry4a, *Cc*Cry4a, *Cl*Cry4a and *Gg*Cry4a BBCEAS ΔA Spectra

Fig. A.1 shows the BBCEAS ΔA spectra of *Er*Cry4a, *Cc*Cry4a, *Cl*Cry4a and *Gg*Cry4a. The spectra largely arises from potassium ferricyanide photochemistry (see **Chapter 5**). The shoulder peaking at 520 nm in 400 ms spectra indicates $W^{\bullet}$ formation.

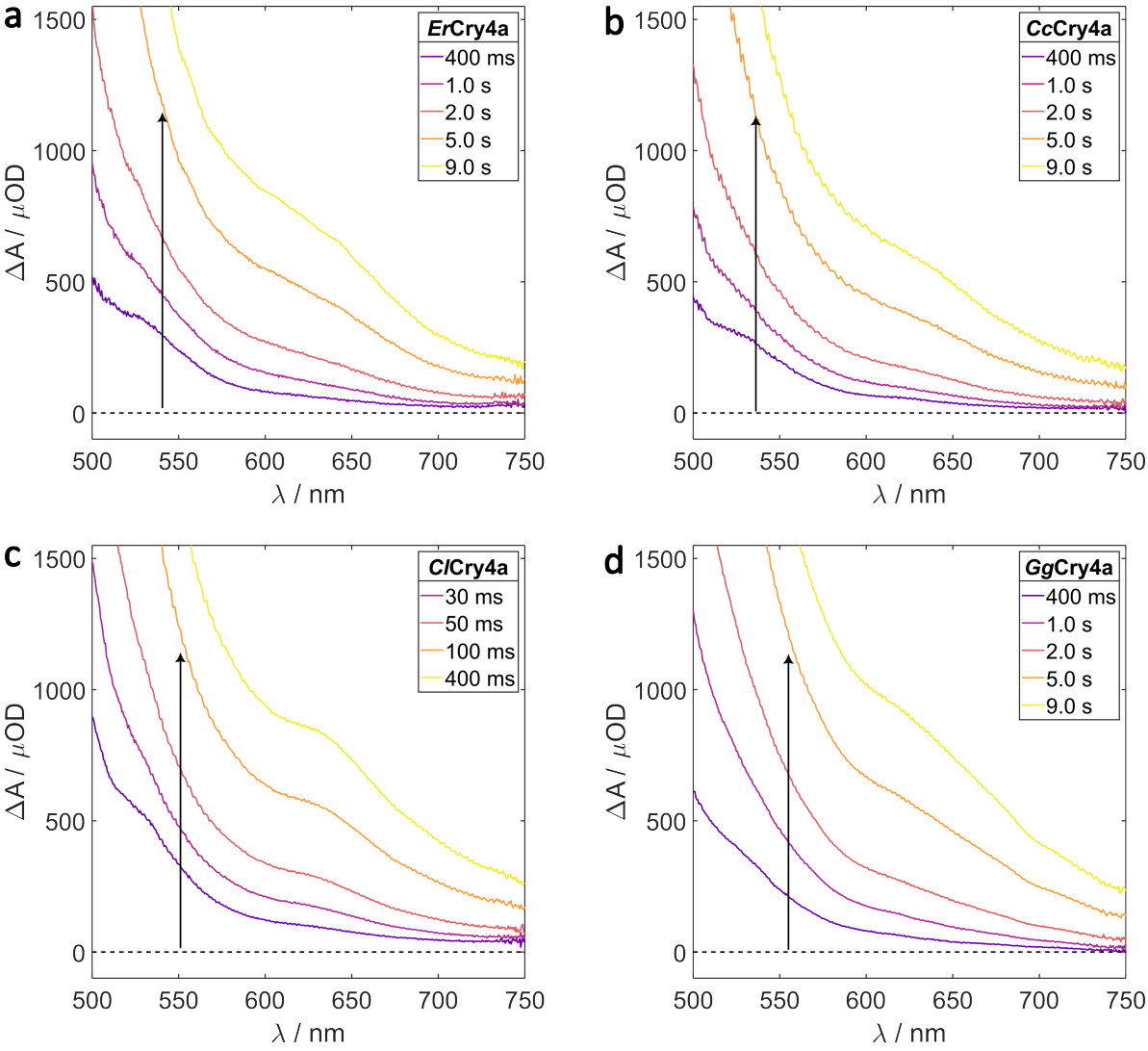

Figure A.1: ΔA spectra of *Er*Cry4a (a), *Cc*Cry4a (b), *Cl*Cry4a (c) and *Gg*Cry4a (d). Arrows indicate growth of ΔA in time. Shoulder peaking at 520 nm in 400 ms spectra indicates $W^{\bullet}$ formation. Subsequent spectra after 400 ms arise from ferricyanide photochemistry as discussed in **Chapter 5**.

A.1.2 Potassium Ferricyanide $\Delta\Delta A$ Spectrum

Potassium ferricyanide (FC) $\Delta\Delta A$ spectrum, acquired with a 30 mT applied magnetic field, is shown in **Fig. A.2**. Potassium ferricyanide exhibited no MFE. The data was acquired from a sample consisting of 5 mM FC in pH 8 tris buffer (20 mM Tris, 250 mM NaCl and 20% glycerol (V/V)) and was measured by BBCEAS under the same conditions as the cryptochrome samples discussed in the main text (*i.e.* continuous 450 nm, 3.82 kW m^{-2}, photoexcitation over a period of 10 s with a simultaneous 200 ms on-off modulated applied external magnetic field).

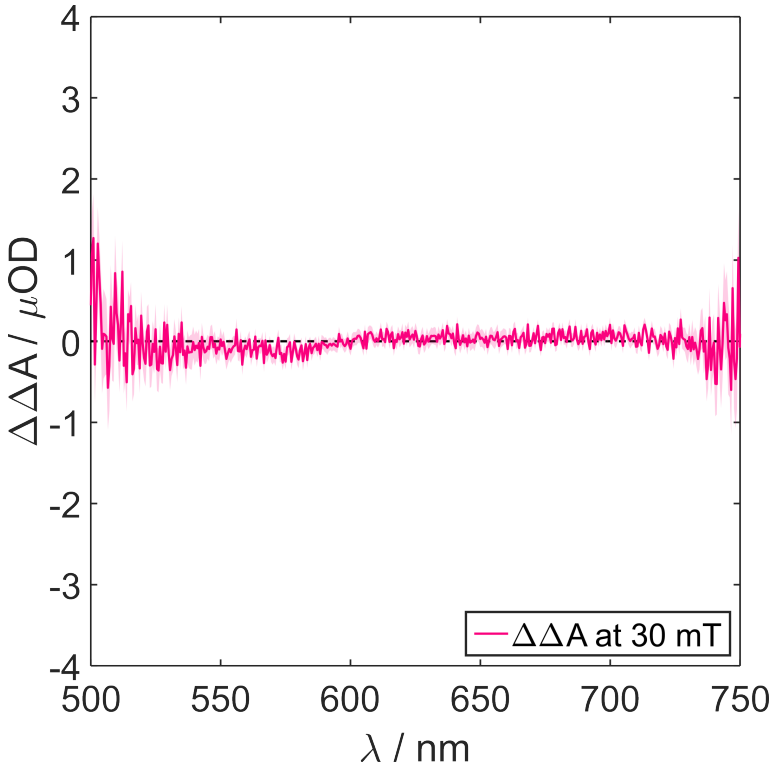

Figure A.2: 30 mT BBCEAS $\Delta\Delta A$ spectrum of 5 mM potassium ferricyanide in tris buffer (20 mM Tris, 250 mM NaCl and 20% glycerol (V/V)). No MFE detected. Noise around 500 nm and 750 nm is due to low probe light intensity.

A.1.3 *Er*Cry4a, *Cc*Cry4a, *Cl*Cry4a and *Gg*Cry4a BBCEAS $\Delta\Delta A$ Spectral Fits

BBCEAS $\Delta\Delta A$ spectral fits. Fitting procedure outlined in the main text.

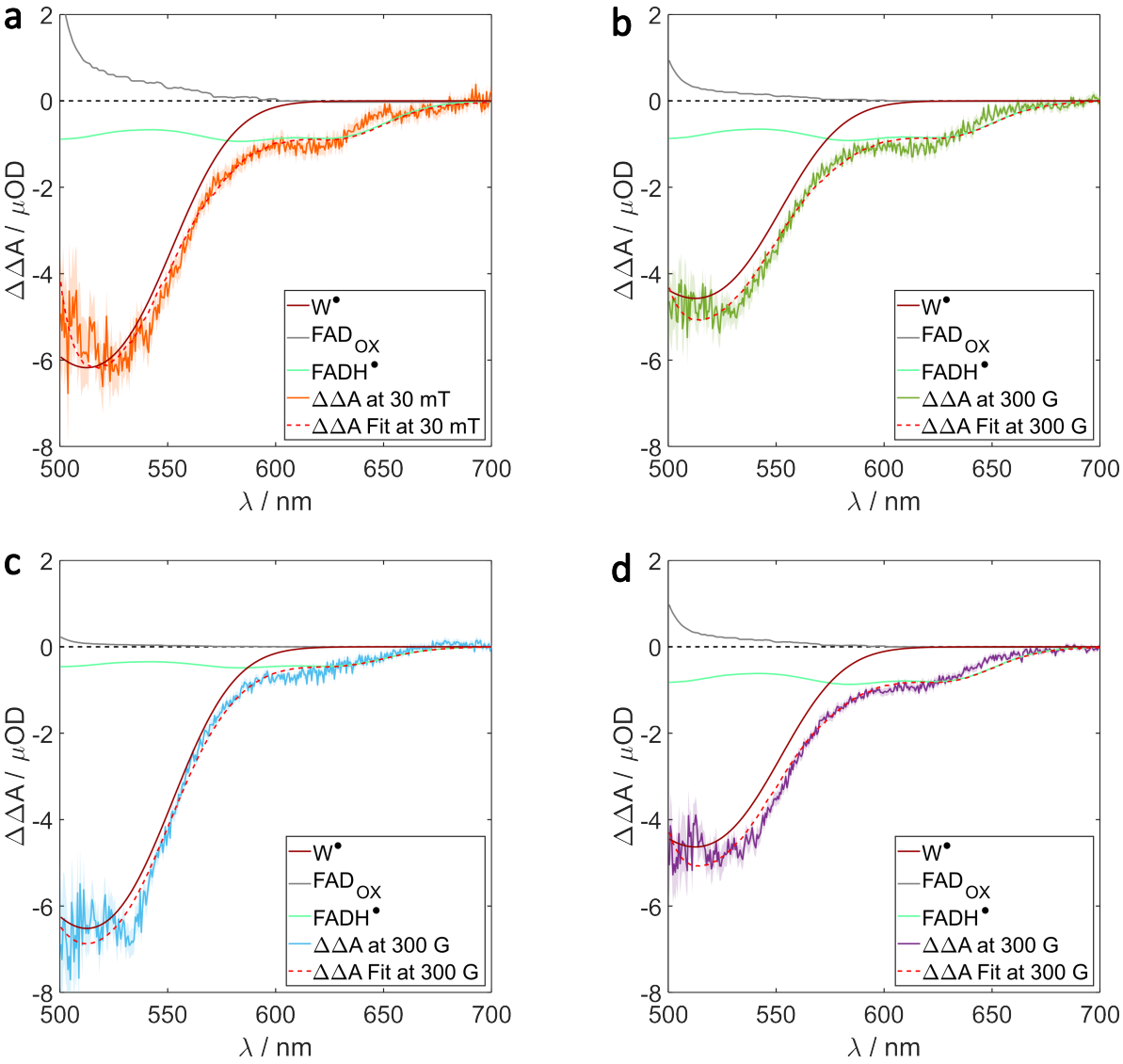

Figure A.3: $\Delta\Delta A$ spectral fits for *Er*Cry4a (a), *Cc*Cry4a (b), *Cl*Cry4a (c) and *Gg*Cry4a (d). All consist of a large negative $W^{\bullet}$ MFE with smaller negative $FADH^{\bullet}$ and positive FAD_{OX} contributions.

A.1.4 *Er*Cry4a, *Cc*Cry4a, *Cl*Cry4a and *Gg*Cry4a Sequence Alignments

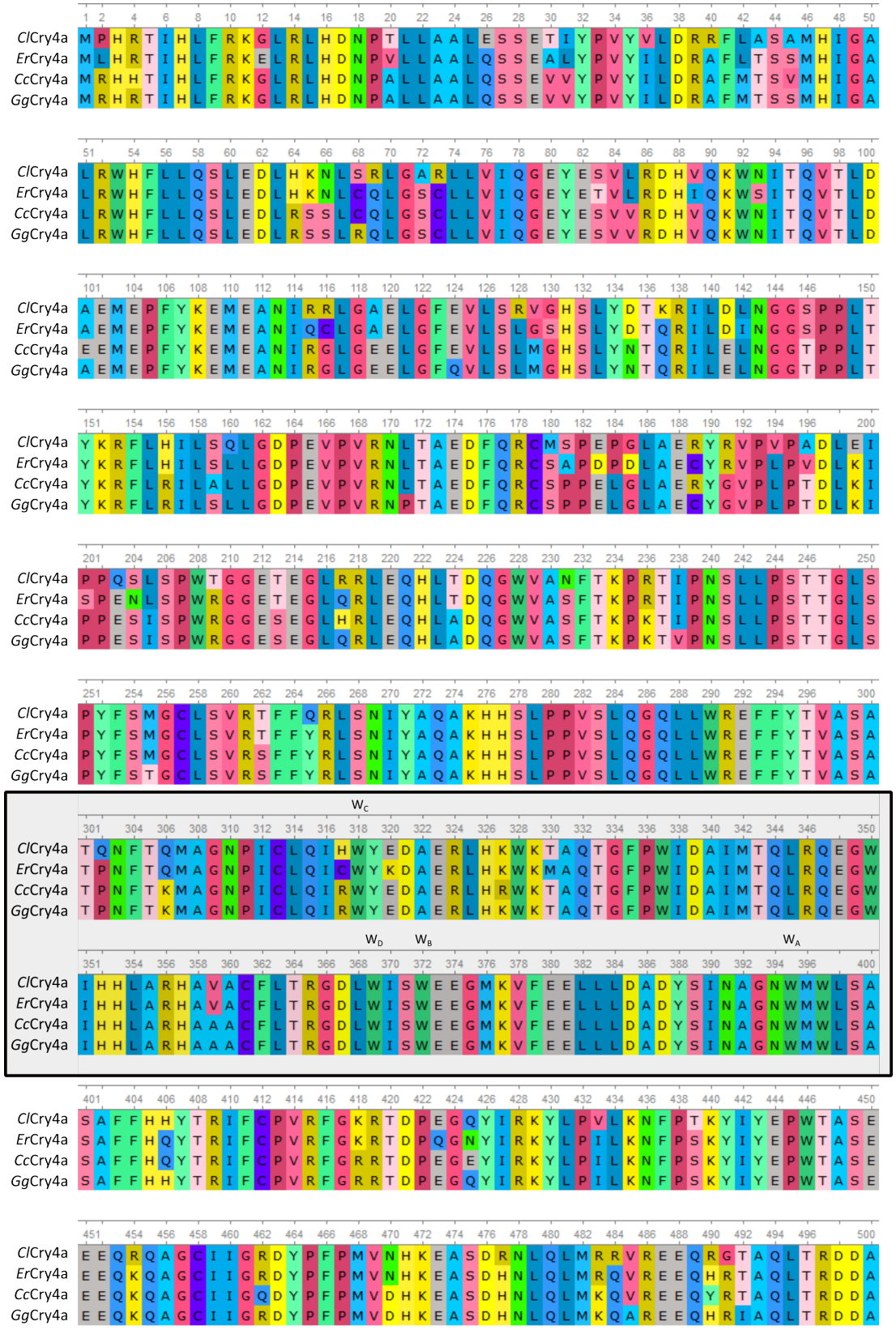

Figure A.4: Amino acid sequence alignment of *Er*Cry4a, *Cc*Cry4a, *Cl*Cry4a and *Gg*Cry4a. The sequences were aligned using ClustalW and visualised with UGENE.[243,244] Box around residues 301-400 marks the radical pair mechanism region of the proteins.

A.2 Appendix 2

Additional figures and material for **Chapter 5**.

A.2.1 Glycerol and Tris Structures

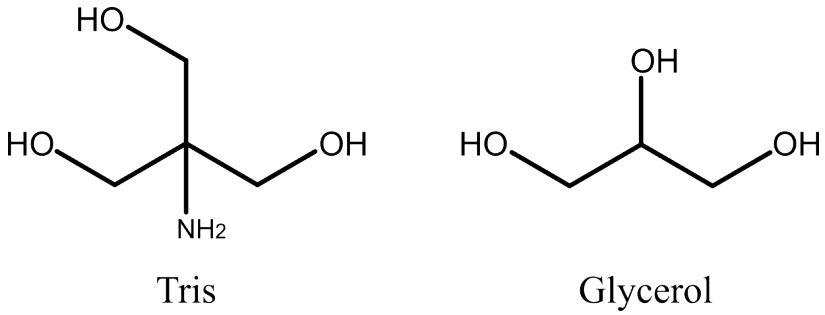

Figure A.5: Molecular structures of tris and glycerol.

A.2.2 Potential Potassium Ferricyanide Degradation Product Calculated IR Spectra

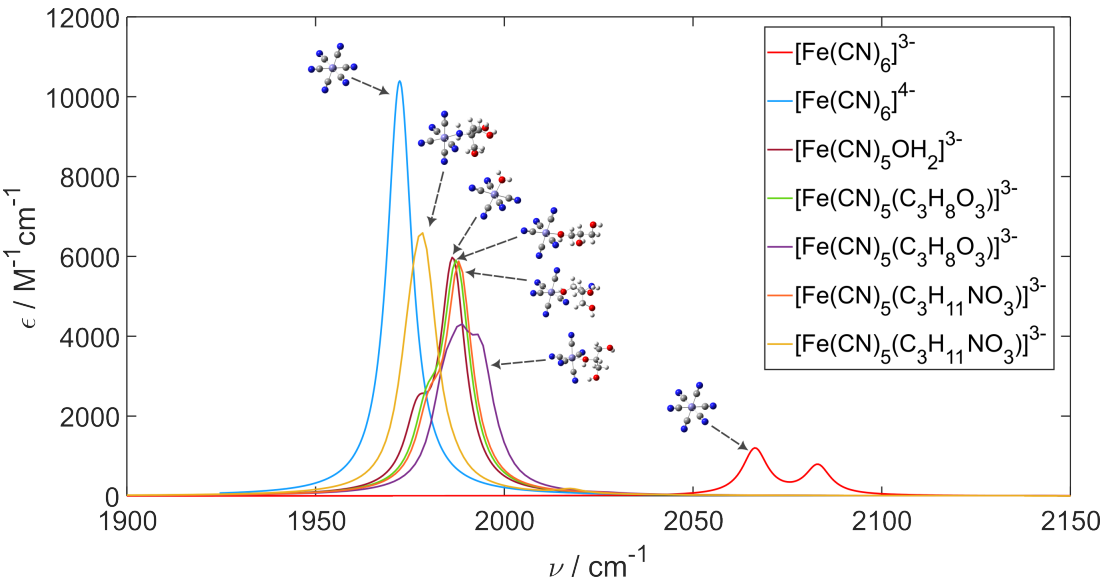

Figure A.6: DFT simulated IR spectra for potassium ferrocyanide, potassium ferricyanide and its potential photodegradation products. All IR peaks arise due to CN stretches with some species exhibiting shoulders or split peaks due to structural shifts away from a fully symmetric octahedral geometry. Note that potassium ferricyanide exhibits two peaks due to the DFT method predicting a Jahn-Teller distortion, leading to a D_{4h} point group. All peaks are red-shifted relative to the experimental IR peaks (*cf.* **Chapter 5**), however the general trend is consistent. That is, Fe(II) species exhibit a lower wavenumber than Fe(III).

A.2.3 Kinetic Modelling Details

Below are the details of the kinetic modelling simulations presented in **Chapter 5** (and **Chapter 6**). All kinetic models use Matlab's ODE15s differential equation solver to solve a system of equations of the form

$$\frac{d\boldsymbol{c}}{dt} = \boldsymbol{K}\boldsymbol{c} \tag{A.1}$$

where $\boldsymbol{c}$ is a vector of photocycle state concentrations and $\boldsymbol{K}$ is a matrix of rate constants.

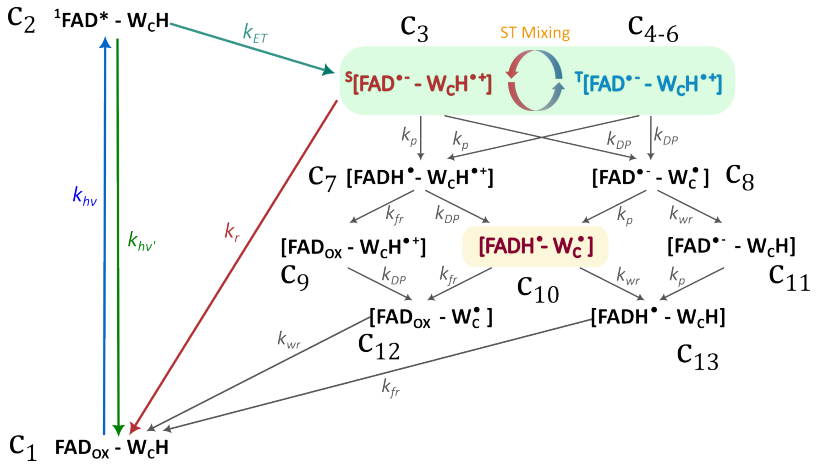

Figure A.7: *Gg*Cry4 W369F under an oxygen atmosphere photocycle used to simulate the BBCEAS kinetics in **Chapter 5**. All states in the photocycle are labelled in reference to the rate equations A.2 with the SCRP triplet state split into the three separate triplet states $|T_0\rangle$ ($\boldsymbol{c}_4$) and $|T_\pm\rangle$ ($\boldsymbol{c}_{5/6}$).

For the simulation of *Gg*Cry4a W369F under continuous illumination and an oxygen atmosphere, the concentration vector $\boldsymbol{c}$ consisted of 13 (see **Fig. A.7**) states with the initial ground state concentration 30 μM and all other state concentrations 0 μM. The corresponding rate equations in the absence of a magnetic field are,

$$\frac{d\boldsymbol{c}}{dt} = \begin{pmatrix} -k_{h\nu}\boldsymbol{c}_1 + k_{h\nu'}\boldsymbol{c}_2 + k_{wr}\boldsymbol{c}_{12} + k_{fr}\boldsymbol{c}_{13} \\ k_{h\nu}\boldsymbol{c}_1 - (k_{h\nu'} + k_{ET})\boldsymbol{c}_2 \\ k_{ET}\boldsymbol{c}_2 - (k_r + k_P + k_{DP} + 3k_{HFM})\boldsymbol{c}_3 + k_{HFM}\boldsymbol{c}_4 + k_{HFM}\boldsymbol{c}_5 + k_{HFM}\boldsymbol{c}_6 \\ k_{HFM}\boldsymbol{c}_3 - (k_r + k_P + k_{DP} + 3k_{HFM})\boldsymbol{c}_4 + k_{HFM}\boldsymbol{c}_5 + k_{HFM}\boldsymbol{c}_6 \\ k_{HFM}\boldsymbol{c}_3 + k_{HFM}\boldsymbol{c}_4 - (k_r + k_P + k_{DP} + 2k_{HFM})\boldsymbol{c}_5 \\ k_{HFM}\boldsymbol{c}_3 + k_{HFM}\boldsymbol{c}_4 - (k_r + k_P + k_{DP} + 2k_{HFM})\boldsymbol{c}_6 \\ k_P(\boldsymbol{c}_3 + \boldsymbol{c}_4 + \boldsymbol{c}_5 + \boldsymbol{c}_6) - (k_{DP} + k_{fr})\boldsymbol{c}_7 \\ k_{DP}(\boldsymbol{c}_3 + \boldsymbol{c}_4 + \boldsymbol{c}_5 + \boldsymbol{c}_6) - (k_P + k_{wr})\boldsymbol{c}_8 \\ k_{fr}\boldsymbol{c}_7 - k_{DP}\boldsymbol{c}_9 \\ k_{DP}\boldsymbol{c}_7 + k_P\boldsymbol{c}_8 - (k_{fr} + k_{wr})\boldsymbol{c}_{10} \\ k_{wr}\boldsymbol{c}_8 - k_P\boldsymbol{c}_{11} \\ k_{DP}\boldsymbol{c}_9 + k_{fr}\boldsymbol{c}_{10} - k_{wr}\boldsymbol{c}_{12} \\ k_{wr}\boldsymbol{c}_{10} + k_p\boldsymbol{c}_{11} - k_{fr}\boldsymbol{c}_{13} \end{pmatrix} \tag{A.2}$$

where the numeric subscripts indicate a state in $\boldsymbol{c}$ (*cf.* **Fig. A.7**) and the numerical values for all of the rate constants are discussed in the main text.

In the presence of a strong external magnetic field the only states altered are the SCRP singlet ($\boldsymbol{c}_3$) and triplet ($\boldsymbol{c}_{4-6}$) states which become

$$\begin{aligned}
\frac{d\boldsymbol{c}_3}{dt} &= k_{ET}\boldsymbol{c}_2 - (k_r + k_P + k_{DP} + k_{HFM} + 2k_{RM})\boldsymbol{c}_3 + k_{HFM}\boldsymbol{c}_4 + k_{RM}\boldsymbol{c}_5 + k_{RM}\boldsymbol{c}_6 \\
\frac{d\boldsymbol{c}_4}{dt} &= k_{HFM}\boldsymbol{c}_3 - (k_r + k_P + k_{DP} + k_{HFM} + 2k_{RM})\boldsymbol{c}_4 + k_{RM}\boldsymbol{c}_5 + k_{RM}\boldsymbol{c}_6 \\
\frac{d\boldsymbol{c}_{5/6}}{dt} &= k_{RM}\boldsymbol{c}_3 + k_{RM}\boldsymbol{c}_4 - (k_r + k_P + k_{DP} + 2k_{RM})\boldsymbol{c}_{5/6}
\end{aligned} \tag{A.3}$$

where k_{HFM} now only mixes the $|S\rangle$ ($\boldsymbol{c}_3$) and $|T_0\rangle$ ($\boldsymbol{c}_4$) states since the $|T_\pm\rangle$ ($\boldsymbol{c}_{5/6}$) are energetically isolated due to the Zeeman interaction. Some mixing still occurs between $|S\rangle$ and $|T_\pm\rangle$ and $|T_0\rangle$ and $|T_\pm\rangle$ due to an incoherent mechanism characterised by the rate constant k_{RM}. This typically just scales the magnitude of the MFE and was set to 1×10^7 s^{-1}.

For the simulation of *Gg*Cry4a W369F under continuous illumination and in the presence of FC (see **Fig. A.8**), the concentration vector $\boldsymbol{c}$ consisted of 16 states with the initial ground state concentration 30 μM and all other state concentrations 0 μM. The new states (*vs.* **Fig. A.7**) arise from splitting the $FADH^\bullet$ recovery into a two step process.

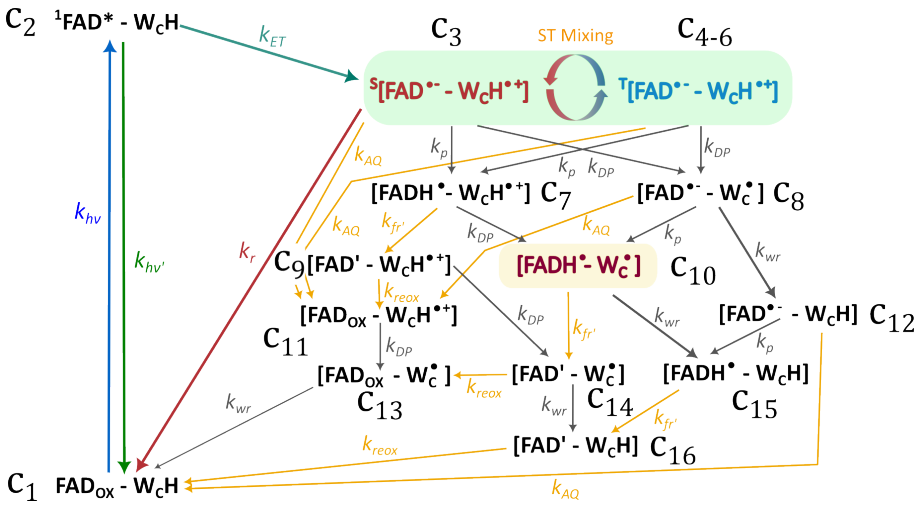

Figure A.8: The photocycle for *Gg*Cry4 W369F in the presence of potassium ferricyanide used to simulate the BBCEAS kinetics in **Chapter 5**. All states in the photocycle are labelled in reference to the rate equations A.4 with the SCRP triplet state split into the three separate triplet states $|T_0\rangle$ and $|T_\pm\rangle$ ($\boldsymbol{c}_{4-6}$).

The rate equations describing *Gg*Cry4 W369F in the presence of potassium ferricyanide and in the absence of an applied external magnetic field are

$$\frac{d\boldsymbol{c}}{dt} = \begin{pmatrix} -k_{h\nu}\boldsymbol{c}_1 + k_{h\nu'}\boldsymbol{c}_2 + k_r\boldsymbol{c}_3 + k_{AQ}\boldsymbol{c}_{12} + k_{wr}\boldsymbol{c}_{13} + k_{reox}\boldsymbol{c}_{16} \\ k_{h\nu}\boldsymbol{c}_1 - (k_{h\nu'} + k_{ET})\boldsymbol{c}_2 \\ k_{ET}\boldsymbol{c}_2 - (k_r + k_P + k_{DP} + k_{AQ} + 3k_{HFM})\boldsymbol{c}_3 + k_{HFM}\boldsymbol{c}_4 + k_{HFM}\boldsymbol{c}_5 + k_{HFM}\boldsymbol{c}_6 \\ k_{HFM}\boldsymbol{c}_3 - (k_r + k_P + k_{DP} + k_{AQ} + 3k_{HFM})\boldsymbol{c}_4 + k_{HFM}\boldsymbol{c}_5 + k_{HFM}\boldsymbol{c}_6 \\ k_{HFM}\boldsymbol{c}_3 + k_{HFM}\boldsymbol{c}_4 - (k_r + k_P + k_{DP} + k_{AQ} + 2k_{HFM})\boldsymbol{c}_5 \\ k_{HFM}\boldsymbol{c}_3 + k_{HFM}\boldsymbol{c}_4 - (k_r + k_P + k_{DP} + k_{AQ} + 2k_{HFM})\boldsymbol{c}_6 \\ k_P(\boldsymbol{c}_3 + \boldsymbol{c}_4 + \boldsymbol{c}_5 + \boldsymbol{c}_6) - (k_{DP} + k_{fr'})\boldsymbol{c}_7 \\ k_{DP}(\boldsymbol{c}_3 + \boldsymbol{c}_4 + \boldsymbol{c}_5 + \boldsymbol{c}_6) - (k_P + k_{AQ} + k_{wr})\boldsymbol{c}_8 \\ k_{fr'}\boldsymbol{c}_7 - (k_{DP} + k_{reox})\boldsymbol{c}_9 \\ k_{DP}\boldsymbol{c}_7 + k_P\boldsymbol{c}_8 - (k_{fr'} + k_{wr})\boldsymbol{c}_{10} \\ k_{AQ}(\boldsymbol{c}_3 + \boldsymbol{c}_4 + \boldsymbol{c}_5 + \boldsymbol{c}_6 + \boldsymbol{c}_8) + k_{reox}\boldsymbol{c}_9 - k_{DP}\boldsymbol{c}_{11} \\ k_{wr}\boldsymbol{c}_8 + k_{fr}\boldsymbol{c}_{10} - (k_P + k_{AQ})\boldsymbol{c}_{12} \\ k_{DP}\boldsymbol{c}_{11} + k_{reox}\boldsymbol{c}_{14} - k_{wr}\boldsymbol{c}_{13} \\ k_{DP}\boldsymbol{c}_9 + k_{fr'}\boldsymbol{c}_{10} - (k_{reox} + k_{wr})\boldsymbol{c}_{14} \\ k_{wr}\boldsymbol{c}_{10} + k_p\boldsymbol{c}_{12} - k_{fr'}\boldsymbol{c}_{15} \\ k_{wr}\boldsymbol{c}_{14} + k_{fr'}\boldsymbol{c}_{15} - k_{reox}\boldsymbol{c}_{16} \end{pmatrix} \tag{A.4}$$

where the numeric subscripts indicate a state in $\boldsymbol{c}$ (*cf.* **Fig. A.8**) and the numerical values for all bar one rate constant are discussed in the main text. The only constant not defined or discussed in detail was the $FAD^{\bullet-}$ quenching rate by Fe(III), k_{AQ}. This was estimated to be $k_{AQ} = 26.6\ s^{-1}$, following fitting to the radical species as discussed in the main text.

Once again, applying an external magnetic field to the system only affects the rate equations for the SCRP singlet ($\boldsymbol{c}_3$) and triplet ($\boldsymbol{c}_{4-6}$) states. The rate equations describing these states in the presence of an external magnetic field are

$$\begin{aligned} \frac{d\boldsymbol{c}_3}{dt} &= k_{ET}\boldsymbol{c}_2 - (k_r + k_P + k_{DP} + k_{AQ} + k_{HFM} + 2k_{RM})\boldsymbol{c}_3 + k_{HFM}\boldsymbol{c}_4 + k_{RM}\boldsymbol{c}_5 + k_{RM}\boldsymbol{c}_6 \\ \frac{d\boldsymbol{c}_4}{dt} &= k_{HFM}\boldsymbol{c}_3 - (k_r + k_P + k_{DP} + k_{AQ} + k_{HFM} + 2k_{RM})\boldsymbol{c}_4 + k_{RM}\boldsymbol{c}_5 + k_{RM}\boldsymbol{c}_6 \\ \frac{d\boldsymbol{c}_{5/6}}{dt} &= k_{RM}\boldsymbol{c}_3 + k_{RM}\boldsymbol{c}_4 - (k_r + k_P + k_{DP} + k_{AQ} + 2k_{RM})\boldsymbol{c}_{5/6} \end{aligned} \tag{A.5}$$

where k_{RM} is defined as above and was set to $7 \times 10^6\ s^{-1}$.

A.2.4 FAD and Tryptophan HFC Atom Labels

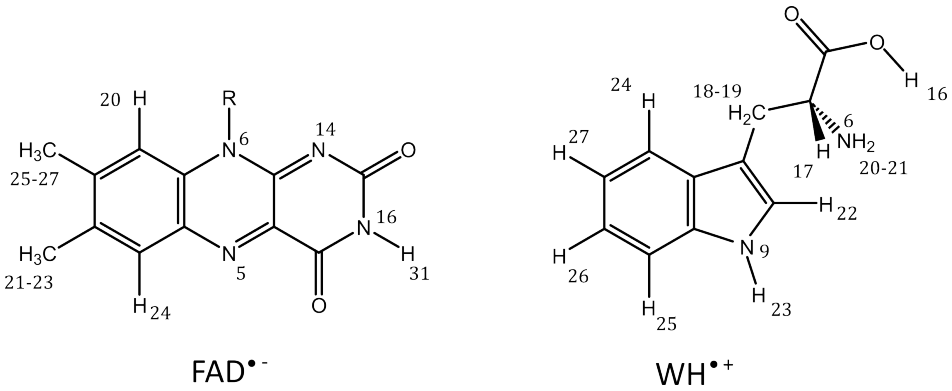

Figure A.9: Atom labels for all HFC constants present in the $FAD^{\bullet-}$ and $WH^{\bullet+}$ radicals. Adapted from Maeda *et al.*[87]

A.2.5 Kinetic Parameters for Spin Dynamics Simulations

Rate constants for the singlet and triplet SCRP state reactions in the Haberkorn recombination operator used in the simulations presented in **Fig. 5.19**. For each state the rate constant is defined by a sum of multiple reaction processes

$$\begin{aligned} k_S &= k_r + k_{DP} + k_P \\ k_T &= k_{DP} + k_P \end{aligned} \tag{A.6}$$

where k_r is the rate constant for singlet recombination, k_{DP} is the rate constant for $WH^{\bullet+}$ deprotonation and k_P is the rate constant for $FAD^{\bullet-}$ protonation. All of these rate constants are defined in **Table A.1**

Rate Constant	Units / s^{-1}
k_{DP}	5×10^6
k_P	5
k_r	5×10^6

Table A.1: Rate constants for the SCRP reactions used in the simulations presented in **Fig. 5.19**.

A.2.6 Electron Hopping Spin Dynamics

The electron hopping mechanism is simulated in much the same way as the other mechanisms discussed in the main text except that there are now two coupled systems which only vary in the strength of their exchange interactions (*i.e.* HFC interactions are the same). For simplicity, SCRP singlet recombination or (de)protonation was assumed to only occur from one of the two possible sites, site 1 (W_C). Therefore, the coupled Liouvillians describing the system were

$$\begin{aligned} \hat{\hat{L}}_1 &= i\hat{\hat{H}}_1 + \hat{\hat{K}} \\ \hat{\hat{L}}_2 &= i\hat{\hat{H}}_2 - k_{hop'}\hat{\hat{E}} \end{aligned} \tag{A.7}$$

where the subscripts indicate site 1 (W_C) or site 2 (W_B), $k_{hop'}$ is the rate constant for the electron transfer from site 2 to site 1 (fixed at $k_{hop'} = 1 \times 10^{10}$ s^{-1}) and $\hat{K}$ is a modified Haberkorn recombination operator (*cf.* equation 2.47),

$$\hat{K} = \frac{k_S}{2}\hat{P}_S + \frac{k_T}{2}\hat{P}_T + k_{hop}\hat{E} \tag{A.8}$$

where k_{hop} is the rate constant for the electron transfer from site 1 to site 2 and is varied in the simulations presented in the main text (*cf.* **Fig. 5.19**). $\hat{\hat{H}}_i$ is the Hamiltonian (given by equation 5.9) for site 1 or site 2 in Liouville space. The exchange interaction at site 1 was set to 0.3 MHz while the exchange interaction at site 2 was set to 0.6 GHz. All other parameters where kept the same as in the STD and RFR mechanisms.

Applying the steady state approximation to both site 1 and site 2 produces the following row-wise flattened density matrix for the SCRP at site 1

$$|\rho_1\rangle = \left(\hat{\hat{L}}_1 - k_{hop}k_{hop'}\hat{\hat{L}}_2^{-1}\right)^{-1}\frac{k_0}{Z}|\hat{P}_S\rangle \tag{A.9}$$

Observables, such as singlet probability, are calculated from equation A.9 in the usual way (*cf.* equation 2.41).

A.3 Appendix 3

Presented here is the supplementary material largely, but not exclusively, relevant to **Chapter 6**.

A.3.1 Global Analysis Methods

Global target analysis was utilised in the analysis of the TA (**Fig. 6.6**), BBCEAS (**Fig. 6.8**) and continuous illumination data (**Fig. 6.11**). In general, a 2D absorption (or ΔA) data array, **D**, with dimensions of wavelength, Dim(λ), by time, Dim(t), can be factorised such that

$$\mathbf{D}(\lambda, t) \;=\; \mathbf{C}(t)\mathbf{S}^{\mathrm{T}}(\lambda) \;=\; \sum_{i=1}^{n} c(t)_i s(\lambda)_i \tag{A.10}$$

where $\mathbf{C}(t)$ is a Dim(t) $\times$ n matrix of coefficients proportional to concentration, $\mathbf{S}(\lambda)$ is a Dim(λ) $\times$ n matrix of individual species' absorption spectra and n is the number of absorbing species within the data signal.[181,245] Given the acquired data are known, if either the kinetic evolution, determined by $\mathbf{C}(t)$, or absorbing species, $\mathbf{S}(\lambda)$, are known (or a suitable model assumed) then the unknown factor can be calculated by solving equation A.10 with numerical methods. Here Matlab's backslash function was employed (least square solution).

For the construction of **Fig. 6.11 b** an $A \longrightarrow B$ kinetic model was assumed for $\mathbf{C}(t)$ such that

$$\mathbf{C}(t)^{\mathrm{T}} \;=\; \begin{pmatrix} \zeta e^{-t/\tau} \\ 1-\zeta e^{-t/\tau} \end{pmatrix} \tag{A.11}$$

where τ is the time constant for the formation of B from A, and ζ determines the relative amount of A at t = 0. Solutions of equation A.10 with respect to $\mathbf{S}(\lambda)$ were used to obtain estimates for τ and ζ and thus more accurate solutions for $\mathbf{S}(\lambda)$ by minimising the least square error (Err) in the fitted data array $\mathbf{D}_{fit}(\lambda, t)$ with respect to the measurement data, $\mathbf{D}(\lambda, t)$. That is

$$Err \;=\; \big(\mathbf{D}(\lambda, t) - \mathbf{D}_{fit}(\lambda, t)\big)^2 \tag{A.12}$$

Conversely, to extract individual species kinetics from the BBCEAS ΔA data (**Fig. 6.8**), for example, the absorbing species' spectra were assumed and taken from **Fig. 2.9 b**.[152] Specifically, due to the BBCEAS time scale and known cryptochrome photoinduced radical lifetimes, four contributing species were assumed, namely: FAD_{OX}, $FAD^{\bullet -}$, $FADH^{\bullet}$ and $W^{\bullet}$. With the assumed $\mathbf{S}(\lambda)$ matrix, equation A.10 was solved for $\mathbf{C}(t)$ iteratively over each time point such that equation A.10 was reduced to a series of calculations of the form

$$\mathbf{d}_j(\lambda, t) = \mathbf{S}(\lambda)\mathrm{c}_j \tag{A.13}$$

where $\mathbf{d}_j(\lambda, t)$ is a column of $\mathbf{D}(\lambda, t)$ at the jth time point and c_j is a row of $\mathbf{C}(t)$ at the jth time point. This same method, with absorbing species appropriate for the given time scale, was employed in the analysis of the TA data in (**Fig. 6.6**) and in **Chapters** 5, 8 and 7.

A.3.2 Time Dependent Spin Dynamics Simulations

Time dependent spin dynamics were carried out using the trace sampling method developed by Lewis *et al.*[208], and later Fay *et al.*[209] where ensemble-averaged observables, $\langle O(t)\rangle$, are determined from the stochastic Schrödinger equation by,

$$\langle O(t)\rangle = \left\langle \int d\zeta p(\zeta) \langle \Psi_{S,\zeta}(t)| \hat{O} |\Psi_{S,\zeta}(t)\rangle \right\rangle \tag{A.14}$$

where $|\Psi_{S,\zeta}(0)\rangle = |S\rangle \otimes |\Psi_\zeta\rangle$, $|S\rangle$ is the singlet state, $|\Psi_\zeta\rangle$ is a set of normalised nuclear spin-states characterised by real variables ζ, and $|\Psi_{S,\zeta}(t)\rangle$ obeys the stochastic Schrödinger equation,

$$\frac{d}{dt}|\Psi_{S,\zeta}(t)\rangle = \left(-\frac{i}{\hbar}\hat{H}(X(t)) - \hat{K}\right)|\Psi_{S,\zeta}(t)\rangle \tag{A.15}$$

Here, $\hat{K}$ is the spin-selective recombination operator (defined by equation 2.47) and $\hat{H}(X(t))$ is the Hamiltonian which fluctuates in time as a function of stochastically fluctuating variable $X(t)$. A full derivation and implementation of equation A.14 can be found in Lewis *et al.*[208] and Fay *et al.*[209] In any case, thanks to the computational efficiency of this method, several HFC interactions could be included in the Hamiltonian (defined by equation 5.9 with $J = 0.3$ MHz).[117] These are listed in **Table A.2**.

$FAD^{\bullet-}$	HFC / mT	$WH^{\bullet+}$	HFC / mT
N5	0.523	N1	0.322
N10	0.187	Hβ1	1.605
H8	0.440	H1	−0.598
H6	−0.387	H4	−0.488

Table A.2: HFC interactions used in all simulations were taken from Hiscock *et al.*[246] Refer to **Fig. A.9** for atom labels.

No relaxation mechanisms were included. Rate constants for recombination and product formation depended on the system simulated and will be discussed below. However, in general the singlet state decay is defined as $k_S = k_r + k_{DP} + k_P$ and the triplet state decay is defined as $k_T = k_{DP} + k_P$ where k_r charecterises singlet recombination back to the ground state, k_{DP} is the rate constant for $WH^{\bullet+}$ deprotontation and k_P is the rate constant for $FAD^{\bullet-}$ protonation.

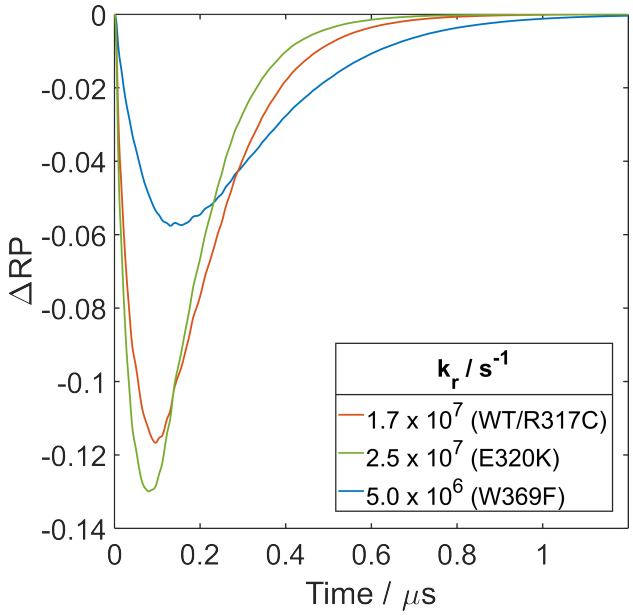

Figure A.10: Time dependent MFEs, ΔRP, at several singlet recombination rate constants. Generally faster recombination leads to larger, but shorter lived, MFEs. ΔRP is the change in the total SCRP probability upon application of a 30 mT magnetic field. Plotted lines represent the result from 5 SU(Z) initial nuclear spin states.

Modelling a system with $k_{DP} = 5 \times 10^6$ s^{-1}, $k_P = 5$ s^{-1} and taking k_r from **Table 6.2** allowed evaluation of the effect k_r has on MFE development. These results are shown in **Fig. A.10** which demonstrate how a faster recombination rate can lead to a shorter lived MFE, ΔRP (*cf.* **Chapter 5**), with a larger maximum magnitude.

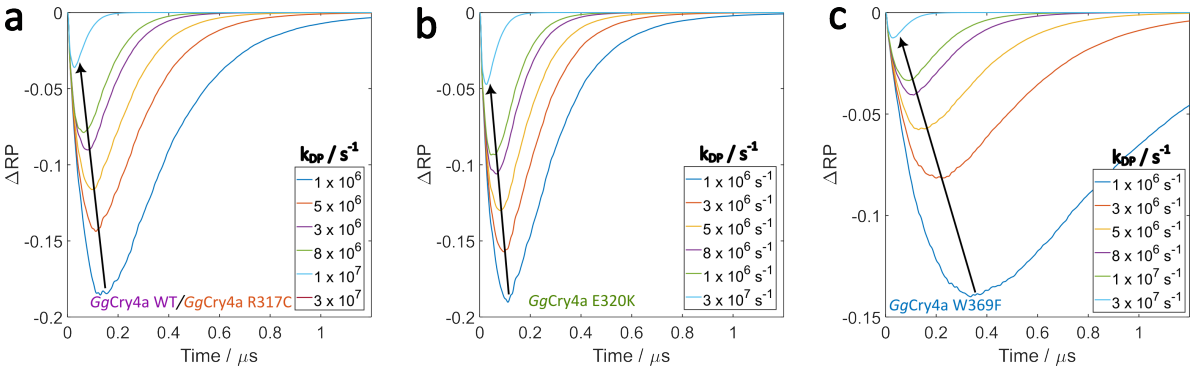

Figure A.11: Results from varying $WH^{\bullet+}$ deprotonation rate constant. a) Simulation results with $k_r = 1.7 \times 10^7$ s^{-1}, akin to the *Gg*Cry4a WT and R317C proteins. b) Simulation results with $k_r = 2.5 \times 10^7$ s^{-1}, akin to the *Gg*Cry4a E320K protein. c) Simulation results with $k_r = 5 \times 10^6$ s^{-1}, akin to the *Gg*Cry4a W369F protein. In all cases, $k_P = 5$ s^{-1}. Generally, larger k_{DP} leads to smaller, shorter-lived MFEs, ΔRP. ΔRP is the change in the total SCRP probability upon application of a 30 mT magnetic field. Arrows indicate direction of ΔRP as k_{DP} is increased. Plotted lines represent the result from 5 SU(Z) initial nuclear spin states.

In line with the steady state simulations in the main text (*cf.* **Fig. 6.12**), calculations where the rate constant of deprotonation was varied for each value of k_r in **Fig. A.10** showed a decrease in the magnitude, and lifetime, of the MFE. These results are summarised in **Fig. A.11**.

A.4 Appendix 4

Additional material for **Chapter** 8.

A.4.1 Basis States for Characteristic ST Mixing Rate Estimation

Below are the eight basis states from which $|2\rangle$ and $|4\rangle$ were used to calculate the characteristic ST mixing time in **Chapter** 8 section 8.1.

$$
\begin{aligned}
|1\rangle &= |S\alpha_C\rangle \\
|2\rangle &= |S\beta_C\rangle \\
|3\rangle &= \frac{1}{3}\left(\sqrt{2}|T_+\beta_C\rangle - |T_0\alpha_C\rangle\right) \\
|4\rangle &= \frac{1}{3}\left(\sqrt{2}|T_-\alpha_C\rangle - |T_0\beta_C\rangle\right) \\
|5\rangle &= |T_+\alpha_C\rangle \\
|6\rangle &= \frac{1}{3}\left(|T_+\beta_C\rangle + \sqrt{2}|T_0\alpha_C\rangle\right) \\
|7\rangle &= \frac{1}{3}\left(|T_-\alpha_C\rangle + \sqrt{2}|T_0\beta_C\rangle\right) \\
|8\rangle &= |T_-\beta_C\rangle
\end{aligned}
\tag{A.16}
$$

A.4.2 FMN HEWL Global Fit Results

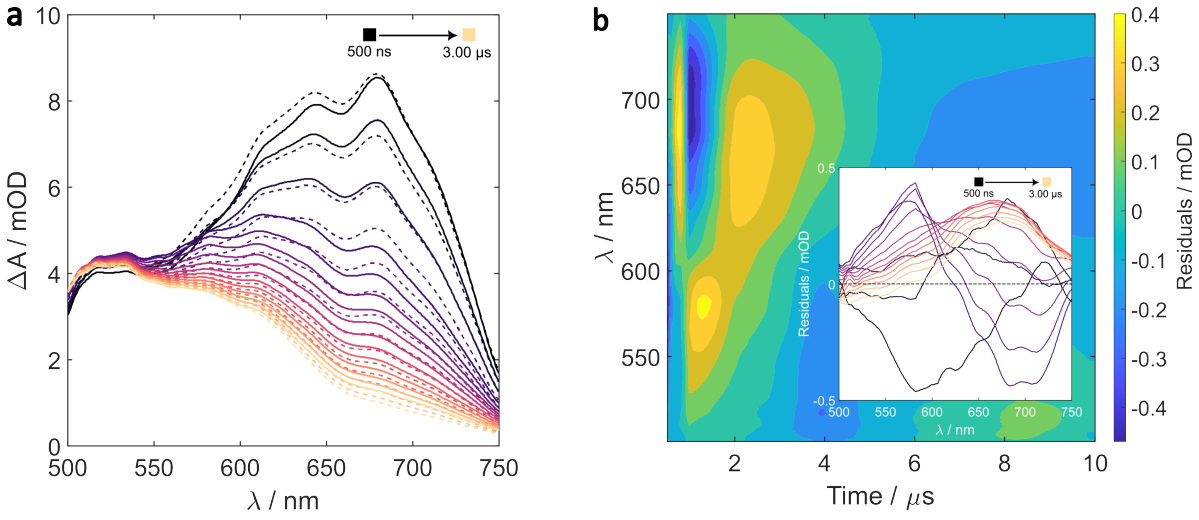

Figure A.12: a) ΔA spectra (solid lines) and the global fit result (dashed lines) at a series of time points going from 500 ns to 3 μs in even steps. Fit is broadly in good agreement with the data. b) Residuals from the fitting procedure (data-fit). The magnitude of the residuals is over an order of magnitude less than the data with no clear spectral features from potential absorbing species. This is more clearly seen in the inset which shows wavelength slices through the residual surface at a series of time points going from 500 ns to 3 μs in even steps.

A.5 Appendix 5

Additional material for **Chapter** 9.

A.5.1 FAD Kinetic Model Used In Simulation

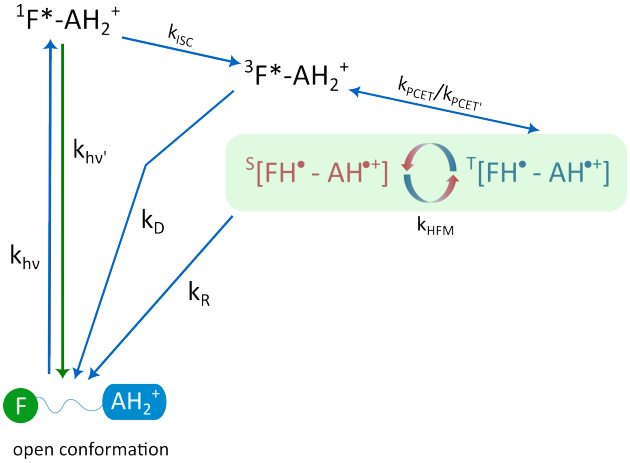

Figure A.13: Kinetic cycle employed in the kinetic simulations of FAD under acidic conditions.

Simulations were performed in python using the RadicalPy toolbox.[247] The rate equations used to model the photocycle shown in **Fig. A.13** are as follows

$$\begin{aligned}
\frac{d[GS]}{dt} &= -(k_{hv})[GS] + k_D[^3F^*_\pm] + k_D[^3F^*_0] + k_R[S] + k_{hv'} + k_{IC}[S_1] \\
\frac{d[^1F^*]}{dt} &= -(k_{hv'} + k_{IC} + 3k_{ISC})[^1F^*] + k_{hv}[GS] \\
\frac{d[^3F^*_\pm]}{dt} &= -(k_D + k_{PCET})[^3F^*_\pm] + [H^+]k_{PCET'}[T_\pm] + 2k_{ISC}[^1F^*] \\
\frac{d[^3F^*_0]}{dt} &= -(k_D + k_{PCET})[^3F^*_0] + [H^+]k_{PCET'}[T_0] + k_{ISC}[^1F^*]
\end{aligned} \tag{A.17}$$

with the SCRP singlet and triplet states in the absence of a magnetic field

$$\begin{aligned}
\frac{d[S]}{dt} &= -(3k_{HFM} + k_R)[S] + k_{HFM}[T_\pm] + k_{HFM}[T_0] \\
\frac{d[T_\pm]}{dt} &= -(2k_{HFM} + [H^+]k_{PCET'})[T_\pm] + 2k_{HFM}[S] + 2k_{HFM}[T_0] + k_{PCET}[^3F^*_\pm] \\
\frac{d[T_0]}{dt} &= -(3k_{HFM} + [H^+]k_{PCET'})[T_0] + k_{HFM}[S] + k_{HFM}[T_\pm] + k_{PCET}[^3F^*_0]
\end{aligned} \tag{A.18}$$

and in the presence of a high magnetic field

$$\begin{aligned}
\frac{d[S]}{dt} &= -(2k_{RM} + k_{HFM} + k_R)[S] + k_{RM}[T_\pm] + k_{HFM}[T_0] \\
\frac{d[T_\pm]}{dt} &= -(2k_{RM} + [H^+]k_{PCET'})[T_\pm] + 2k_{RM}[S] + 2k_{RM}[T_0] + k_{PCET}[^3F^*_\pm] \\
\frac{d[T_0]}{dt} &= -(2k_{RM} + k_{HFM} + [H^+]k_{PCET'})[T_0] + k_{HFM}[S] + k_{RM}[T_\pm] + k_{PCET}[^3F^*_0]
\end{aligned} \tag{A.19}$$

where $[GS]$ is the ground state concentration and refers to the open confirmation of FAD shown in **Fig. A.13** and the flavin excited triplet state, $[^3F^*]$, has been split into its three separate triplet states. The proton concentration $[H^+]$ was assumed to be constant (5 mM) and determined by the pH (2.3).

MFEs were calculated from the ground state concentration after a steady state was reached. Similarly, the fluorescence signal was calculated from the steady state flavin excited singlet state, $[^1F^*]$, concentration. Of course, this does not account for the fluorescence quantum yield, the collection efficiency in the microscope nor the PMT gain. Therefore, the resulting $[^1F^*]$ concentration was scaled appropriately to reflect the experimental data.

The rate constant for absorption $k_{h\nu}$ was calculate from the photoexcitation power assuming a first order process.[123,248] The following ten excitation powers were used: 0.3, 1.2, 2.2, 3.1, 4.0, 5.0, 5.9, 6.8, 7.8 and 8.7 mW, matching the experimental laser powers applied at the sample. The remaining rate constants are provided in **Table A.3**

Rate Constant	Units / s^{-1}	Process
$k_{h\nu'}$	3.55×10^8	fluorescence rate
k_{IC}	2.58×10^9	internal conversion rate (non-radiative decay)
k_{ISC}	3.64×10^8	intersystem crossing rate
k_{HFM}	8×10^7	HFC driven ST mixing rate
k_D	3×10^5	flavin triplet back to the ground state rate
k_{PCET}	7×10^6	rate of PCET to form SCRP
$k_{PCET'}$	2.7×10^9	rate of reverse PCET form SCRP to flavin triplet
k_R	1.1×10^7	SCRP singlet recombination
k_{RM}	1×10^7	Incoherent ST mixing rate

Table A.3: Rate constants for the FAD fluorescence kinetic modelling done in **Chapter 9**. All values were taken from Antill *et al.*[162,247] or Kattnig *et al.*[123]

A.5.2 Allan Deviation

The Allan deviation is a measure of the balance between random and systematic noise (specifically frequency stability) in a series of measurements.[178] That is, it characterises how much repeated measurement improves signal-to-noise before there is either no more gain or systematic noise comes into play and continued averaging worsens the signal-to-noise. This could be due to a drop in laser power over time or the heating of a detector beyond its operational temperature (common problem in liquid nitrogen cooled detectors) for example. If an experiment takes N measurements which can be split into M subgroups containing k separate measurements ($M = N/k$), then the Allan deviation for the subgroups of size k is defined as[178]

$$\sigma_A = \sqrt{\frac{1}{2(M-1)} \sum_{i=1}^{M-1} (x_{i+1} - x_i)^2} \tag{A.20}$$

Abbreviations

$AscH_2$	Ascorbic acid
At	*Arabidopsis thaliana* (Thale cress)
BBCEAS	Broad-band cavity enhanced absorption spectroscopy
BET	Back electron transfer
C	Cysteine
Cc	*Coturnix coturnix* (Quail)
CIDNP	Chemically induced dynamic nuclear polarisation
Cl	*Columba livia* (Pigeon)
CPF	Carotenoid-porphyrin-fullerene
Cry	Cryptochrome
CZE	Chemical Zeno effect
Dm	*Drosophila melanogaster* (Fruit fly)
E	Glutamic acid
Er	*Erithacus rubecula* (European robin)
ET	Electron transfer
ETC	Electron transfer chain
FC	Ferricyanide
FAD	Flavin adenine dinucleotide
FMN	Flavin mononucleotide
FWHM	Full width at half maximum
Gg	*Gallus gallus domesticus* (Chicken)
GS	Ground state
GSB	Ground state bleach

HEWL	Hen egg-white lysozyme
HFC	Hyperfine coupling
IR	Infrared
IRF	Instrument response function
K	Lysine
LED	Light emitting diode
LvN	Liouville von Neumann
HFE	High Field Effect
LFE	Low field effect
LMCT	Ligand to metal charge transfer
MARY	Magnetically altered reaction yield
MC	Metal centred
MCP	Microchannel plate
MFE	Magnetic field effect
NMR	Nuclear magnetic resonance
OCTAS	Optical cavity enhanced transient absorption spectroscopy
PIA	Photoinduced absorption
PMT	Photomultiplier tube
PPD	Pump-probe delay
R	Arginine
Rf	Riboflavin
RFR	Random fields relaxation
RP	Radical pair
RPM	Radical pair mechanism
SC	Supercontinuum
ST	Singlet-triplet
STD	Singlet triplet dephasing

SCRP	Spin correlated radical pair
TA	Transient absorption
TEM	Transverse electric mode
UV/Vis	Ultraviolet-Visible light
W	Tryptophan
Y	Tyrosine
μDF-MARY	Microdroplet fluorescence MARY

List of Figures

1 Quantum Robin. vi

2.1 Zeeman interaction for a single $s = 1/2$ spin and composite two $s = 1/2$ spin system. 9
2.2 RPM example photocycle. 16
2.3 Time-dependent singlet probability 18
2.4 Time-dependent singlet probability with recombination 20
2.5 Simulated MARY and time-dependent MFE. 22
2.6 Anisotropic HFC time-dependent singlet probability at different magnetic field orientations. 26
2.7 Time-dependent singlet probability with STD relaxation. 30
2.8 Pigeon cryptochrome 4a crystal structure. 32
2.9 RPM in cryptochrome 4a photocycle. 33

3.1 First four TEM modes of an optical cavity. 38
3.2 Optical cavity stability criteria and stable cavity examples. 39
3.3 Longitudinal modes of light transmitted through an optical cavity. 40
3.4 Pulse of light in an optical cavity schematic. 41
3.5 Schematic of continuous light incident on an optical cavity. 44
3.6 BBCEAS experiment schematic and triggering sequence. 45
3.7 BBCEAS cavity calibration curves and CEF spectra. 47
3.8 Pulsed light in an optical cavity schematic. 49

4.1 *Er*Cry4a, *Cc*Cry4a, *Cl*Cry4a and *Gg*Cry4a 30 mT $\Delta\Delta A$ results. 53
4.2 *Er*Cry4a $\Delta\Delta A$ spectral fit. 54

5.1 *Er*Cry4a WT BBCEAS ΔA spectra with and without 5 mM FC. 60
5.2 BBCEAS ΔA spectra from 5 mM FC in pH 8 tris buffer. 61
5.3 Continuous irradiation experimental set-up schematic. 63
5.4 Ferricyanide and ferrocyanide UV/Vis and IR spectra. 64
5.5 FC in water irradiation results. 65
5.6 FC in tris buffer irradiation results. 67
5.7 FC in 20 % glycerol/water (V/V) irradiation results. 68
5.8 FC photodegradation DFT results. 70
5.9 *Gg*Cry4 W369F homology model. 73
5.10 BBCEAS *Gg*Cry4 W369F ΔA results, O_2 vs FC. 74

5.11 BBCEAS *Gg*Cry4 W369F $\Delta\Delta A$ results, O_2 vs FC 75
5.12 BBCEAS *Gg*Cry4 W369F FC concentration dependence results. 77
5.13 BBCEAS *Gg*Cry4 W369F long-lived radicals ratio as a function of FC concentration. 78
5.14 *Gg*Cry4 W369F photochemical schemes, used for kinetic modelling, under oxygen and in the presence of FC. 80
5.15 *Gg*Cry4 W369F kinetic modelling results, O_2 *vs.* FC. 81
5.16 *Gg*Cry4 W369F Coulombic charge surfaces. 83
5.17 Contour plot of steady state $FADH^{\bullet}/W^{\bullet}$ concentration as a function of k_{fr} and k_{wr}. 84
5.18 Kinetic model simulated *Gg*Cry4 W369F $\Delta\Delta A$ spectra, O_2 *vs* FC. 85
5.19 Simulation results for potentially FC induced spin dynamics mechanisms. . 92

6.1 *Er*Cry4a homology model. 95
6.2 Transient absorption experiment schematic. 98
6.3 *Gg*Cry4a WT, *Gg*Cry4a W369F, *Gg*Cry4a R317C and *Gg*Cry4a E320K UV/Vis spetcra. 100
6.4 *Gg*Cry4a WT, *Gg*Cry4a W369F, *Gg*Cry4a R317C and *Gg*Cry4a E320K TA ΔA spectra. 103
6.5 *Gg*Cry4a WT, *Gg*Cry4a W369F, *Gg*Cry4a R317C and *Gg*Cry4a E320K ΔA kinetics. 104
6.6 *Gg*Cry4a W369F TA ΔA global analysis results. 105
6.7 *Gg*Cry4a W369F TA MFE results. 107
6.8 *Gg*Cry4a WT BBCEAS ΔA global analysis results. 108
6.9 *Gg*Cry4a WT, R317C, E320K and W369F BBCEAS $\Delta\Delta A$ spectra. 109
6.10 *Gg*Cry4a WT, R317C, E320K and W369F BBCEAS MARY results. 110
6.11 *Gg*Cry4a WT, R317C, E320K and W369F continuous irradiation results. . . 112
6.12 *Gg*Cry4a WT, R317C, E320K and W369F simulated MFEs. 115

7.1 *Gg*Cry4a WT homology model with Y319 highlighted. 120
7.2 *Gg*Cry4a W369F Y319F ΔA and MFE TA results. 122
7.3 *Gg*Cry4a W369F Y319F TA ΔA global fit results 123
7.4 BBCEAS ΔA spectra for *Gg*Cry4a W369F and *Gg*Cry4a W369F Y319F. . . . 125
7.5 Time-averaged BBCEAS $\Delta\Delta A$ spectra for *Gg*Cry4a W369F and *Gg*Cry4a W369F Y319F. 127
7.6 *Gg*Cry4a Y319F BBCEAS ΔA spectra and $\Delta\Delta A$ spectrum. 128
7.7 BBCEAS ΔA spectra for *Gg*Cry4a W372F and *Gg*Cry4a W318F. 130
7.8 BBCEAS $\Delta\Delta A$ spectra for *Gg*Cry4a W372F and *Gg*Cry4a W318F. 131

8.1 Simple 4 state RPM. 136
8.2 iCCD schematic. 140
8.3 OCTAS IRF. 143

8.4 OCTAS intracavity FMN fluorescence decay. 144
8.5 OCTAS experiment schematic. 145
8.6 HEWL crystal structure and FMN/HEWL photocycle. 147
8.7 OCTAS FMN/HEWL ΔA results (pulsed excitation). 149
8.8 OCTAS FMN/HEWL $\Delta\Delta A$ results (pulsed excitation). 151
8.9 OCBBCEAS FMN/HEWL ΔA results. 152
8.10 OCTAS FMN/HEWL ΔA results (continuous excitation). 153
8.11 OCTAS FMN/HEWL $\Delta\Delta A$ results (continuous excitation). 154
8.12 FAD photocycle. 155
8.13 OCTAS FAD ΔA results. 156
8.14 OCTAS FAD $\Delta\Delta A$ results. 157
8.15 CPF structure and photocycle. 159
8.16 Spin dynamics simulation of CPF at low and high temperatures. 160
8.17 OCTAS CPF ΔA results. 161
8.18 OCTAS CPF $\Delta\Delta A$ results. 162
8.19 OCTAS *Gg*Cry4a W369F Y319F ΔA results. 164
8.20 OCTAS *Gg*Cry4a W369F Y319F ΔA global analysis results. 165
8.21 OCTAS *Gg*Cry4a W369F Y319F $\Delta\Delta A$ results. 166
8.22 Upgraded OCTAS experiment schematic. 169

9.1 Example microfluidic chip. 173
9.2 Schematics of different microdroplet generation chip geometries. 178
9.3 Droplet PMT signal and microscope image. 183
9.4 μDFM experimental set-up schematic. 186
9.5 μDFM experimental procedure. 187
9.6 Illustrative example of droplet detection algorithm. 189
9.7 Capsule geometry droplet and resulting simulated PMT signal. 192
9.8 FAD microdroplet fluorescence spectra and averaged FAD microdroplet PMT signal. 193
9.9 FAD microdroplet excitation power dependence results, experimental and simulated. 194
9.10 FAD microdroplet excitation power dependent MARY results. 195
9.11 FMN and ascorbic acid structures and FMN/ascorbic acid photocycle. . . . 196
9.12 FMN/ascorbic microdroplet MARY results. 197
9.13 FMN/ascorbic acid microdroplet PMT signal and microdroplet MFE Allan deviation. 198
9.14 Example of flow within a microdroplet and riboflavin structure. 199
9.15 Riboflavin/tryptophan microdroplet diameter dependent MFE results. . . . 200
9.16 Riboflavin/tryptophan microdroplet diameter dependent MARY results. . . 201
9.17 Example of analysis method for cell encapsulated micrdroplets. 204

A.1 *Er*Cry4a, *Cc*Cry4a, *Cl*Cry4a and *Gg*Cry4a BBCEAS ΔA spectra with Fe(III) . 229

A.2 FC 30 mT BBCEAS $\Delta\Delta A$ spectrum 230
A.3 *Er*Cry4a, *Cc*Cry4a, *Cl*Cry4a and *Gg*Cry4a BBCEAS $\Delta\Delta A$ spectral fits with Fe(III) 231
A.4 Amino acid sequence alignment of *Er*Cry4a, *Cc*Cry4a, *Cl*Cry4a and *Gg*Cry4a 232
A.5 Molecular structures of tris and glycerol 233
A.6 DFT simulated IR spectra for potassium ferrocyanide, potassium ferricyanide and its potential photodegradation products 233
A.7 *Gg*Cry4 W369F under an oxygen atmosphere photocycle 234
A.8 *Gg*Cry4 W369F photocycle in the presence of potassium ferricyanide 235
A.9 Atom labels for all HFC constants present in the $FAD^{\bullet-}$ and $WH^{\bullet+}$ radicals . 237
A.10 Trace sampling time dependent MFEs, ΔRP, at several singlet recombination rate constants 241
A.11 Trace sampling time dependent MFEs, ΔRP, with varying $WH^{\bullet+}$ deprotonation rate constants 241
A.12 OCTAS FMN/HEWL global fit results 242
A.13 FAD kinetic cycle 243

List of Tables

4.1 Naming convention for various avian cryptochrome samples. 52

4.2 Results from fitting equation 4.2 to the field dependent $\Delta\Delta A$ data in **Fig. 4.1** with respect to MFE_{Sat} and $B_{1/2}$. MFE_{Sat} is the $\Delta\Delta A$ when $B_0 \rightarrow \infty$ and $B_{1/2}$ is the half width at half maximum. Errors were estimated using the inverse Hessian method. 55

5.1 Known or calculated rate constants used in the kinetic models. $k_{h\nu}$ is the excitation rate and was calculated as a first order process. k_{ET} is the electron transfer rate and was taken from the work of Lacombat *et al.*[58]. k_P is the protonation rate and was estimated by Otsuka *et al.*[126] k_r and k_{DP} were estimated from transient absorption measurements (see **Chapter 6**). Of course these rate constants are estimates and as such their reliability in the context of BBCEAS is debatable. 79

5.2 Optimised rate constants from the kinetic modeling in **Fig. 5.15**. Note, $k_{fr'}$ is the first step in a now two step $FADH^{\bullet}$ recovery (see **Fig. 5.14** and discussion in text). 82

5.3 HFC interactions used in all simulations were taken from Maeda *et al.*[87] . . 91

6.1 Dipolar (D) coupling constants, and thus radical pair separation (r), obtained from out-of-phase electron spin echo envelope modulation spectroscopy. Data measured by DPhil student Tommy Pitcher. Experimental and simulation details can be found in Gravell and Murton *et al.*[117] 101

6.2 TA lifetimes of all four proteins estimated by kinetic fitting of the ΔA decay curves, averaged between 500-550 nm, shown in **Fig. 6.5**. All decays were fit to a biexponential function with a constant offset to account for long-lived photoproducts. 104

6.3 Biexponential fits to the individual species kinetics extracted by global analysis (**Fig. 6.6**). All species evolve on a similar timescale, indicating similar singlet recombination and $WH^{\bullet+}$ deprotonation rate. 106

6.4 Time constants (τ_{rec}) obtained by monoexponential fitting of the $FADH^{\bullet}$ recovery, generated by continuous blue-light illumination, and global analysis of the spectral evolution. Both methods are in broad agreement and reflect FAD_{OX} recovery directly from $FADH^{\bullet}$. 112

7.1 Biexponential fits to the individual species kinetics extracted by global analysis of the *Gg*Cry4a W369F Y319F TA ΔA results (**Fig. 7.3**). All species evolve on a similar timescale, indicating similar singlet recombination and $WH^{\bullet+}$ deprotonation rates. 124

8.1 Summary of the key OCTAS results from model systems in comparison to published results from alternative techniques. A few comments on the benefits of OCTAS in comparison to those techniques are included. 167

9.1 Summary of MARY results. 197
9.2 Summary of the key μDF-MARY results from model systems in comparison to published results, where possible, from alternative fluorescence or microscopy techniques. In the FMN/$AscH_2$ system, LFE/HFE refers to the percentage ratio between the maximum of the LFE and saturation point of the HFE. Refer to Evans *et al.*[242] for a description of the prompt fluorescence MFE experiment. n.a. indicates that there is no relevant published data to compare to. 203

A.1 Rate constants for the SCRP reactions used in the simulations presented in **Fig. 5.19**. 237
A.2 HFC interactions used in all simulations were taken from Hiscock *et al.*[246] Refer to **Fig. A.9** for atom labels. 240
A.3 Rate constants for the FAD fluorescence kinetic modelling done in **Chapter 9**. All values were taken from Antill *et al.*[162,247] or Kattnig *et al.*[123] 244